



**HAL**  
open science

# Commutation of second-order nonlinear optical responses of indolino-oxazolidines : from molecules in solution to functionalized surfaces

Kornelia Pielak

► **To cite this version:**

Kornelia Pielak. Commutation of second-order nonlinear optical responses of indolino-oxazolidines : from molecules in solution to functionalized surfaces. Other. Université de Bordeaux; Université de Namur, 2018. English. NNT : 2018BORD0096 . tel-03199619

**HAL Id: tel-03199619**

**<https://theses.hal.science/tel-03199619>**

Submitted on 15 Apr 2021

**HAL** is a multi-disciplinary open access archive for the deposit and dissemination of scientific research documents, whether they are published or not. The documents may come from teaching and research institutions in France or abroad, or from public or private research centers.

L'archive ouverte pluridisciplinaire **HAL**, est destinée au dépôt et à la diffusion de documents scientifiques de niveau recherche, publiés ou non, émanant des établissements d'enseignement et de recherche français ou étrangers, des laboratoires publics ou privés.



THÈSE  
présentée pour obtenir le Grade de  
**DOCTEUR**  
DE L'UNIVERSITÉ DE BORDEAUX ET DE L'UNIVERSITÉ DE  
NAMUR  
ÉCOLE DOCTORALE DES SCIENCES CHIMIQUES  
SPÉCIALITÉ: CHIMIE PHYSIQUE  
par  
**KORNELIA PIELAK**  
**COMMUTATION DES RÉPONSES OPTIQUES NON  
LINÉAIRES DU SECOND ORDRE DES  
INDOLINO-OXAZOLIDINES: DES MOLÉCULES EN  
SOLUTION AUX SURFACES FONCTIONNALISÉES**

Directeur de thèse: Prof. **Frédéric CASTET** Université de Bordeaux  
Directeur de thèse: Prof. **Benoît CHAMPAGNE** Université de Namur

Soutenue le 3 Juillet, 2018

Devant la commission d'examen formée de:

Prof. <b>Vincent RODRIGUEZ</b>	Université de Bordeaux	Président
Prof. <b>Koen CLAYS</b>	Katholieke Universiteit Leuven	Rapporteur
Prof. <b>Eduard MATITO</b>	Université du Pays Basque	Rapporteur
Prof. <b>Elena CARIATI</b>	Università di Milano	Examineur
Dr. <b>Aurélien PLAQUET</b>	Université de Namur	Examineur





THESIS

submitted to the

UNIVERSITY OF BORDEAUX & UNIVERSITY OF NAMUR  
DOCTORAL SCHOOL OF CHEMICAL SCIENCES

by

**KORNELIA PIELAK**

in fulfillment for the Degree of  
**DOCTOR OF PHILOSOPHY**

in CHEMICAL PHYSICS

**COMMUTATION OF SECOND-ORDER NONLINEAR  
OPTICAL RESPONSES OF INDOLINO-OXAZOLIDINES:  
FROM MOLECULES IN SOLUTION TO  
FUNCTIONALIZED SURFACES**

Thesis Director: Prof. **Frédéric CASTET** University of Bordeaux  
Thesis Director: Prof. **Benoît CHAMPAGNE** University of Namur

Defense date: 3 July 2018.

**Review Committee.**

Prof. <b>Vincent RODRIGUEZ</b>	University of Bordeaux	President
Prof. <b>Koen CLAYS</b>	University of Leuven	Reporter
Prof. <b>Eduard MATITO</b>	University of Basque Country	Reporter
Prof. <b>Elena CARIATI</b>	University of Milan	Examiner
Dr. <b>Aurélié PLAQUET</b>	University of Namur	Examiner



*Pracę dedykuję moim Rodzicom,  
za wsparcie, motywację i niesłabnącą wiarę,  
jaką zawsze mogłam w nich znaleźć.*



# Acknowledgements

---

First and foremost, I would like to express my sincere gratitude to my supervisors Prof. Frédéric Castet and Prof. Benoît Champagne for continuous support during my PhD study, for their patience, motivation, enthusiasm and immense knowledge. Their friendly guidance and expert advices have been invaluable throughout all stages of my work.

Besides my promoters, I would like to warmly thank all the members of my thesis committee: the president Prof. Vincent Rodriguez, the reporters Prof. Koen Clays and Prof. Eduard Matito, and also the examiners Prof. Elena Cariati and Dr. Aurélie Plaquet, for their insightful comments, interesting questions and discussion.

My sincere thanks also goes to Prof. Lionel Sanguinet for experimental synthesizing molecules, which were the matter of my research. Moreover, I would like to thank Dr. Flavie Bondu and Dr. Stefania Righetto for guiding me and a great support during the experimental work.

I would also wish to express my gratitude to Prof. Luca Muccioli and Dr. Claire Tonnelé for their invaluable help during the molecular dynamics simulations and to Jean Deviers for his support in theoretical calculations.

Most importantly, I would like to thank my parents and all my family for their love and help to get through those three years, for understanding and encouragement in many moments of crisis. For their unwavering belief that I can achieve so much and for giving me strength to reach for the stars and chase my dreams.

A very special thanks goes to my supportive fiance Dr. Manoj Gali, without his love, help and positive attitude, I would not have finished this thesis.

In conclusion, I would also like to thank all the members and my friends from the Theoretical Chemistry group at the Institute of Molecular Sciences of the University of Bordeaux and the Laboratory of Theoretical Chemistry of the University of Namur, for a support and a great time together.



# Contents

---

<b>1</b>	<b>Introduction</b>	<b>1</b>
1.1	Nonlinear Optical Phenomena . . . . .	1
1.2	NLO Materials . . . . .	4
1.3	Nonlinear optical Switches . . . . .	6
1.3.1	Indolinoxazolidine Derivatives . . . . .	6
1.4	Switching on Functionalized Surfaces . . . . .	8
1.5	Potential Applications . . . . .	9
1.6	Objectives . . . . .	9
<b>2</b>	<b>Experimental Techniques</b>	<b>17</b>
2.1	UV-vis Spectroscopy . . . . .	17
2.2	Determination of the First Hyperpolarizability . . . . .	19
2.2.1	Electric Field-Induced Second Harmonic Generation . . . . .	19
2.2.2	Hyper-Rayleigh Scattering . . . . .	24
<b>3</b>	<b>Theoretical Methods</b>	<b>31</b>
3.1	Wavefunction Quantum Mechanics Methods . . . . .	31
3.1.1	Schrödinger Equation . . . . .	31
3.1.2	Born-Oppenheimer Approximation . . . . .	32
3.1.3	Hartree-Fock Theory . . . . .	33
3.1.4	Møller-Plesset Perturbation Theory . . . . .	36
3.2	Density Functional Theory . . . . .	38
3.2.1	Hohenberg-Kohn Theorems . . . . .	38
3.2.2	Kohn-Sham Theory . . . . .	39
3.2.3	Exchange-Correlations Functionals . . . . .	40
3.3	Basis Sets . . . . .	42
3.4	Absorption Spectra Calculations . . . . .	43
3.5	Hyperpolarizability Calculations . . . . .	45
3.5.1	Time-Dependent Hartree-Fock . . . . .	45
3.5.2	Time-Dependent Density Functional Theory . . . . .	47

---

3.5.3	Finite Field Method . . . . .	48
3.5.4	Sum-Over-States Method and The Two-State Model . . . . .	49
3.6	Solvent Effects . . . . .	50
3.7	Molecular Dynamics Simulations . . . . .	51
<b>4</b>	<b>Second-Order Nonlinear Optical Properties of Indolino-Oxazolidine Derivatives</b>	<b>61</b>
4.1	Introduction . . . . .	62
4.2	Experimental and Theoretical Methods . . . . .	63
4.2.1	Synthesis . . . . .	63
4.2.2	UV-visible and Hyper-Rayleigh Scattering Measurements . . . . .	64
4.2.3	Quantum Chemical Calculations . . . . .	65
4.3	Results and Discussion . . . . .	66
4.3.1	Structural Properties . . . . .	66
4.3.2	Linear Optical Properties . . . . .	68
4.3.3	Nonlinear Optical Properties . . . . .	72
4.4	Conclusion . . . . .	75
<b>5</b>	<b>Acido-Triggered Switching of the Second-Order Nonlinear Optical Properties of a Ferrocenyl-Containing Indolino-Oxazolidine Derivative</b>	<b>83</b>
5.1	Introduction . . . . .	84
5.2	Experimental and Theoretical Methods . . . . .	85
5.2.1	Synthesis . . . . .	85
5.2.2	UV-visible and hyper-Rayleigh Scattering Measurements . . . . .	86
5.2.3	Quantum Chemical Calculations . . . . .	87
5.3	Results and Discussion . . . . .	88
5.3.1	Structural Properties . . . . .	88
5.3.2	Linear Optical Properties . . . . .	88
5.3.3	Nonlinear Optical Properties . . . . .	91
5.4	Conclusion . . . . .	94
<b>6</b>	<b>Dynamical Behavior and Contrasted Second Harmonic Generation Responses in Acido-Triggered Molecular Switches</b>	<b>101</b>
6.1	Introduction . . . . .	102
6.2	Experimental and Theoretical Methods . . . . .	104
6.2.1	Nonlinear Optics: General Considerations and Definitions . . . . .	104
6.2.2	EFISHG Measurements . . . . .	105
6.2.3	Molecular Dynamics Simulations . . . . .	106

6.2.4	Hyperpolarizability Calculations . . . . .	108
6.3	Results . . . . .	109
6.3.1	MD Simulations and <i>ab initio</i> Calculations . . . . .	109
6.3.2	EFISHG Measurements . . . . .	114
6.4	Further Discussion and Conclusion . . . . .	114
<b>7</b>	<b>Nonlinear Optical Responses of Self-Assembled Monolayers Functionalized with Indolino-Oxazolidine Photoswitches</b>	<b>121</b>
7.1	Introduction . . . . .	122
7.2	Theoretical Methodology . . . . .	123
7.2.1	Molecular Dynamics Simulations . . . . .	123
7.2.2	Quantum Chemical Calculations . . . . .	124
7.3	Results and Discussion . . . . .	125
7.3.1	Morphology of the Self-Assembled Monolayers . . . . .	125
7.3.2	Commutation of the Nonlinear Optical Responses . . . . .	127
7.3.3	Relationships Between Geometrical Structures and NLO Responses . . . . .	130
7.4	Conclusions . . . . .	131
<b>8</b>	<b>Summary, General Conclusions, and Outlook</b>	<b>137</b>
	<b>Appendix A</b>	<b>145</b>
	<b>Appendix B</b>	<b>155</b>
	<b>Appendix C</b>	<b>165</b>
	<b>Appendix D</b>	<b>185</b>



# Introduction

*In this Chapter, the physical and mathematical descriptions of nonlinear optical (NLO) properties of molecules and materials are introduced, focusing on the molecular second-order NLO responses characterized by the first hyperpolarizability, and in particular on the second harmonic generation (SHG) process. Furthermore, various classes of NLO systems are discussed, with special emphasis on indolinooxazolines switches, which can commute in solution between two forms displaying very large differences in their SHG responses. We also briefly introduce examples of photoresponsive self-assembled monolayers (SAMs) based on NLO switches, and the potential applications offered by this kind of systems in the field of optical communications, data processing or storage. The global motivation and objectives of this thesis are then presented at the end of the chapter.*

## 1.1 Nonlinear Optical Phenomena

The nonlinear optical (NLO) phenomenon was discovered in 1875, when Kerr observed the change in the refractive index of a material in response to an applied electric field, known as the Kerr effect. [1] However, the dynamic development of NLO experiments started with the invention of the optical ruby laser by Maiman (1960) [2] and just one year later Franken performed the first second harmonic generation (SHG) experiment. [3] From this time, number of nonlinear phenomena have been observed in a large variety materials.

When an electromagnetic wave propagates through a medium, it induces a polarization as a result of the motion of the electrons and nuclei in response to the external electric field ( $\vec{E}$ ). At the macroscopic level, the polarization ( $\vec{P}$ ) is defined as the vector describing the electric dipole moment per unit volume induced by the external electric fields. For small field intensities, such induced polarization is proportional to the applied fields. The linear susceptibility ( $\chi^{(1)}$ ) is the quantity that

characterizes the response of the material proportional to the field:

$$\vec{P}(\vec{E}) = \vec{P}_0 + \overset{\leftrightarrow}{\chi}^{(1)} \cdot \vec{E} \quad (1.1)$$

However, when the material is subjected to a very high intensity electric field induced by a laser light, the polarization can be driven beyond the usual linear regime. The nonlinear behavior of the polarization is then described by a power series with respect to the external fields:

$$\vec{P}(\vec{E}) = \vec{P}_0 + \overset{\leftrightarrow}{\chi}^{(1)} \cdot \vec{E} + \overset{\leftrightarrow}{\chi}^{(2)} : \vec{E}^2 + \overset{\leftrightarrow}{\chi}^{(3)} : \vec{E}^3 + \dots \quad (1.2)$$

This equation introduces the a second- and a third-order nonlinear optical susceptibilities,  $\overset{\leftrightarrow}{\chi}^{(2)}$  and  $\overset{\leftrightarrow}{\chi}^{(3)}$ , which are third-rank and fourth-rank tensors, respectively.

At the molecular scale, the interaction between the applied electric field and the molecules is described by the electric dipole moment ( $\vec{\mu}$ ). Similarly to the polarization, the electric dipole moment can be expressed as a power series with respect to the external fields, or using a Taylor series expansion:

$$\vec{\mu}(\vec{E}) = \vec{\mu}_0 + \overset{\leftrightarrow}{\alpha} \cdot \vec{E} + \frac{1}{2} \overset{\leftrightarrow}{\beta} : \vec{E}^2 + \frac{1}{6} \overset{\leftrightarrow}{\gamma} : \vec{E}^3 + \dots \quad (1.3)$$

where  $\overset{\leftrightarrow}{\alpha}$  is the linear polarizability,  $\overset{\leftrightarrow}{\beta}$  is the first hyperpolarizability (or second-order polarizability) and  $\overset{\leftrightarrow}{\gamma}$  is the second hyperpolarizability (or third-order polarizability).

As the microscopic analog of the second-order optical susceptibility, the first hyperpolarizability  $\beta$  is a rank-3 tensor, which contains 27 components usually collected within a  $9 \times 3$  matrix:

$$\beta = \begin{bmatrix} \beta_{xxx} & \beta_{xyy} & \beta_{xzz} & \beta_{xyz} & \beta_{xzy} & \beta_{xzx} & \beta_{xxz} & \beta_{xxy} & \beta_{xyx} \\ \beta_{yxx} & \beta_{yyy} & \beta_{yzz} & \beta_{yyz} & \beta_{yzy} & \beta_{yzx} & \beta_{yzx} & \beta_{yyx} & \beta_{yyx} \\ \beta_{zxx} & \beta_{zyy} & \beta_{zzz} & \beta_{zyz} & \beta_{zzy} & \beta_{zxx} & \beta_{zxx} & \beta_{zxy} & \beta_{zyx} \end{bmatrix} \quad (1.4)$$

This large number of tensor elements can be reduced by taking into account the intrinsic permutation symmetry existing in the case of two indiscernible incident photons:  $\beta_{xyz} = \beta_{xzy}$ . Consequently, the number of independent components in the can be reduced from 27 to 18, and collected in a  $6 \times 3$  matrix:

$$\beta = \begin{bmatrix} \beta_{xxx} & \beta_{xyy} & \beta_{xzz} & \beta_{xyz} & \beta_{xzx} & \beta_{xyx} \\ \beta_{yxx} & \beta_{yyy} & \beta_{yzz} & \beta_{yyz} & \beta_{yzx} & \beta_{yyx} \\ \beta_{zxx} & \beta_{zyy} & \beta_{zzz} & \beta_{zyz} & \beta_{zxx} & \beta_{zyx} \end{bmatrix} \quad (1.5)$$

Furthermore, if the frequencies (incident and scattered ones) implied in NLO process are far from any absorption band of the molecule under study, the overall permutation symmetry can be applied on the Cartesian components of the hyper-

polarizability tensor, without any changes of their values. This property is known as the Kleinman's symmetry rule [4]. With  $\beta_{xyz} = \beta_{yzx} = \beta_{zxy} = \beta_{xzy} = \beta_{yxz} = \beta_{zyx}$ , the  $\beta$  tensor can be curtailed to only 10 components:

$$\beta = \begin{bmatrix} \beta_{xxx} & \beta_{xyy} & \beta_{xzz} \\ \beta_{yxx} & \beta_{yyy} & \beta_{yzz} \\ \beta_{zxx} & \beta_{zyy} & \beta_{zzz} \end{bmatrix} + [\beta_{xyz}] \quad (1.6)$$

It is essential to underline that molecules and materials need to be non-centrosymmetric to display second-order NLO response. If they are centrosymmetric, their second-order NLO responses cancel out, and the lowest order nonlinearity is the third order.

Moreover, the linear and nonlinear optical polarizabilities depend on the frequency  $\omega$  of the applied fields:

$$\begin{aligned} \vec{\mu}(\vec{E}) &= \vec{\mu}_0 + \sum_{\omega} \overset{\leftrightarrow}{\alpha}(-\omega, \omega) \cdot \vec{E} (e^{-i\omega t} + c.c.) \\ &+ \frac{1}{2!} \sum_{\omega_1, \omega_2} \overset{\leftrightarrow}{\beta}(-\omega_{\sigma}; \omega_1, \omega_2) : \vec{E} \vec{E} (e^{-i\omega_{\sigma} t} + c.c.) \\ &+ \frac{1}{3!} \sum_{\omega_1, \omega_2, \omega_3} \overset{\leftrightarrow}{\gamma}(-\omega_{\sigma}; \omega_1, \omega_2, \omega_3) : \vec{E} \vec{E} \vec{E} (e^{-i\omega_{\sigma} t} + c.c.) + \dots \end{aligned} \quad (1.7)$$

where the  $\omega_1$ ,  $\omega_2$  and  $\omega_3$  are the frequencies of the applied electric fields,  $\omega_{\sigma}$  is the sum of incident frequencies and *c.c.* denotes the complex conjugate.

## Second Harmonic Generation

Second harmonic generation (SHG, also known as 'frequency doubling') is a nonlinear optical process, in which two photons with the same frequency ( $\omega$ ) interact with a medium and generate a new photon at frequency  $2\omega$ . This phenomena is presented schematically in Figure 1.1. Two photons of the light field excite the ground state. The first photon creates an excitation from the ground state to an intermediate state. The intermediate state can be a virtual state, which is excited during a short time. The second photon can generate the transition from the intermediate state to the final state, which decays by coherent emission of a photon creating the light field.



Figure 1.1: Geometry of second-harmonic generation (left) and energy-level diagram describing second-harmonic generation (right).

## 1.2 NLO Materials

Researches on novel nonlinear optical materials have been a hot topic due to their widespread applications. Generally, NLO materials fall into two classes, either inorganic, which are known to exhibit SHG effect, or organic. Over the last 40 years, the lasers using inorganic matter have been employed as optical devices and consequently inorganic materials have dominated the optical technology. During the 1990's, organic materials were identified as promising candidates for nonlinear optical applications, because they can exhibit extremely large NLO response. [5–7]

Recent studies particularly focused on the design of  $\pi$ -electron conjugated organic materials [8], which exhibit larger optical nonlinearity, faster optical response, higher bandwidth, lower driving voltage more flexible device design and potentially lower processing cost. [9]

According to Oudar and Chemla [10]), in order to exhibit second-order NLO responses, molecules must possess:

- excited electronic states close in energy to the ground state,
- large oscillator strengths - or transition dipole moments - for electronic transitions from the ground state and excited states,
- large difference between ground state and excited state dipole moments.

Those principles are linked via the following equation:

$$\beta \propto \frac{|\mu_{ge}^2| \Delta\mu_{ge}}{\Delta E_{ge}^2} \propto \frac{f_{ge} \Delta\mu_{ge}}{\Delta E_{ge}^3} \quad (1.8)$$

where  $f_{ge}$  is the oscillator strength,  $\mu_{ge}$  and  $\Delta E_{ge}$  are the transition dipole moment and energy gap, respectively, between the ground state ( $g$ ) and the first strongly allowed charge-transfer excited state ( $e$ ) and  $\Delta\mu_{ge} = \mu_{ee} - \mu_{gg}$ .

Many research efforts have been dedicated to the synthesis and design of new materials with efficient nonlinear optical responses, and such requirements (Eq. 1.8) are best met by highly polarizable donor-acceptor chromophores, which are referred to as push-pull systems (Figure 1.2). These organic materials are based on molecular units containing electron donor (D) and electron acceptor (A) groups on opposite sides of a linker containing delocalizable  $\pi$ -electrons. Many efforts have been dedicated to find the optimum combination of a bridge, donor and acceptor groups in order to maximize the NLO responses. Commonly, dithiol, dialkylamino or alkoxy units are used as a donor groups, while nitro, cyano or polycyano units are used as acceptor groups. [11–13]

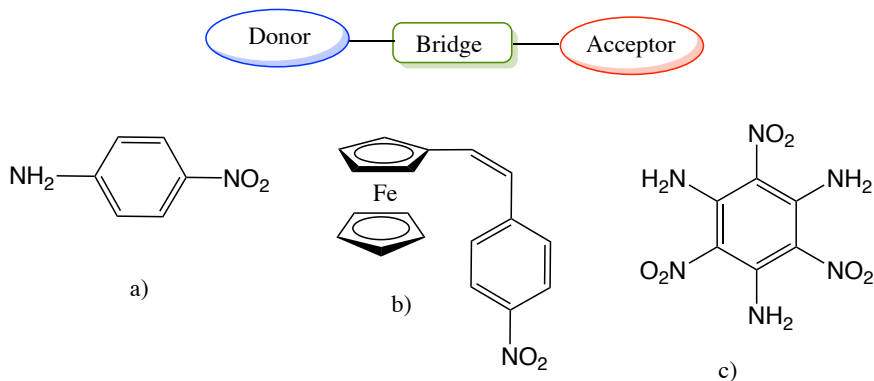


Figure 1.2: Schematic representation of a model Donor- $\pi$ -Acceptor system and representative examples: a) push pull dipolar *p*-nitroaniline ( $\beta = 9.2 \times 10^{-30}$  esu, measured in acetone [17]), b) push-pull molecule involving an organometallic unit (ferrocene donor,  $\beta = 66 \times 10^{-30}$  esu, Kurtz powder measurements at 1064 nm [18]) and c) octupolar 1,3,5-triamino-2,4,6-trinitrobenzene molecule ( $\beta_{333} = 27 \times 10^{-30}$  esu measured in acetone by EFISHG technique [19]) 1 atomic unit =  $3.62 \times 10^{-42}$  m<sup>4</sup> V<sup>-1</sup> =  $8.641 \times 10^{-33}$  esu. [20]

The nature of the bridge has also been widely studied, paying special attention to a structural parameter having a direct impact on the first hyperpolarizability, namely the bond-length alternation (BLA). [14–16] BLA refers to the average difference in length between single and double bonds along the  $\pi$ -conjugated backbone. A BLA value close to 0 indicates that the system is highly conjugated.

In 1987, M. Green [21] reported the first ferrocene derivatives with excellent NLO response, initiating new molecular design developments using metallocenes as donor moieties. Organometallic units can be characterized by low energy metal to ligand (MLCT) or ligand to metal (LMCT) charge transfer excitations, and can exhibit excited state with very low energy and dipole moments. Moreover metallocenes can be used as donor or acceptor groups, or also as polarisable conjugated bridges. [18, 22, 23] In the recent years, many studies reported NLO properties of metal complexes, very often involving ruthenium [24, 25].

In 1990, J. Zyss and co-workers [26–28] introduced a new kind of systems exhibiting high second-order nonlinear optical responses, namely octupolar molecules (Figure 1.2). Octupolar structures are non polar molecules that combine second-order nonlinear optical properties with a strict cancellation of all vector-like observables, including the ground- and excited-state dipole moment. Hence, such systems can not be described by the two-level model because  $\Delta\mu_{ge} = 0$  and must be described using, at least, a three-level model. Octupolar molecules have the advantage to undergo easier noncentrosymmetric crystallization than dipolar molecules. Furthermore, with two or three dimensional charge-transfer transitions, they are able to improve the efficiency-transparency trade-off and stability compared to classical dipolar compounds.

## 1.3 Nonlinear optical Switches

In recent years, along with the development of optoelectronic and photonic technologies, molecular NLO switches received extensive attention. Those species are systems that are reversibly switchable between at least two forms that exhibit very different  $\beta$  responses, and which are stable during at least the measurement time for the readout. [29]. The commutation between different forms can be triggered by using various external stimuli such as a variation of pH [30–32], temperature [33], light [34–38] or redox potential [39].

In 1999, J. Coe [40] categorized different types of molecular switches based on the part of the molecule that is altered during the commutation reaction (Figure 1.3). The most common used type of NLO switches involves the alteration of the  $\pi$  conjugation within the bridge linking the donor and acceptor unit. [41] The figure of merit of such switches is the contrast between the 'ON' state ( $\beta \gg 0$ ) and the 'OFF' state ( $\beta \approx 0$ ).

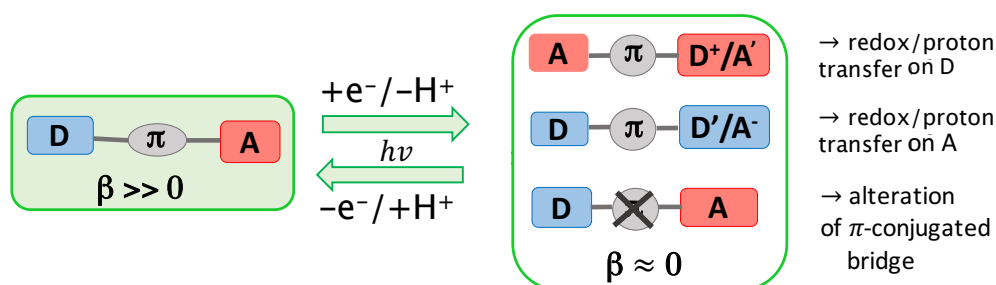


Figure 1.3: Schematic representation of a molecular switches.

### 1.3.1 Indolinooxazolidine Derivatives

Indolinooxazolidine derivatives is the main matter of this thesis. Those compounds come from indolinospiropyrans, which were widely used in photochromism. Indolinooxazolidine species have been discovered in the early 1970s, the first in a form of indolenium salts appeared in patents as useful dyeing agents for wood pulp-based paper, wool, natural acetate silk and polyacrylonitrile fibers. [42] The Figure 1.4 presents the indolinooxazolidine and their related structurally sub-families. The first detailed synthesis of the indolinooxazolidine derivatives in its closed form with  $\pi$ -system was reported later in 1973 by Krongauz. [43]

In the 1990's, studies of the Indolinooxazolidine derivatives have shown that such systems considered as a core, associated with various styrylic residues might act as multiaddressable switches displaying both photo- and acidochromic properties. Due to their switching ability or mild condensation also in condition without solvent, numerous structural variations of this compound could be developed.

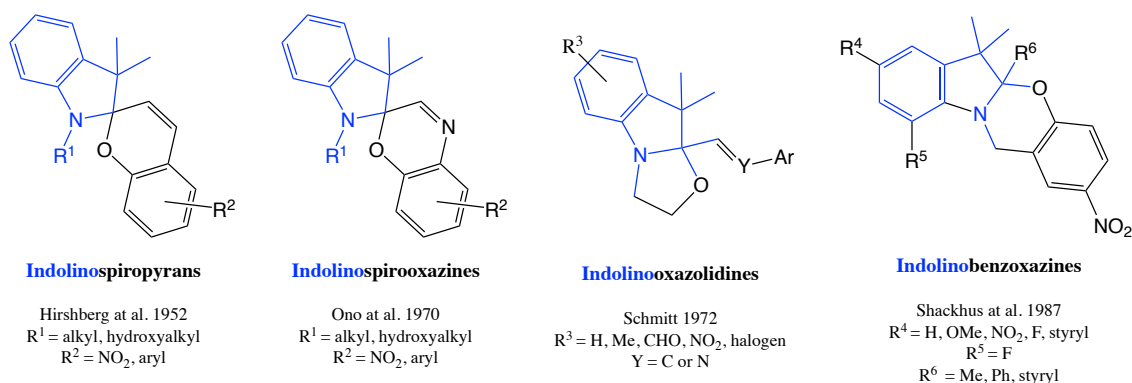


Figure 1.4: Indolinooxazolidines and their related structurally sub-families (from Ref. [42]).

In 2005, Sanguinet at al. [30] reported the synthesis of a new series of multiaddressable chromophores based on the indolinooxazolidine unit, which were shown to exhibit photo- and acido-tunable NLO properties. Since this time, many systems were derived from indolinooxazolidine family. Recently, it has been demonstrated that the association of an indolinooxazolidine core with a bithiophene moiety acting as a redox center leads to a trimodal switch where the interconversion between the colorless closed form and the colored open form can be indifferently triggered by light irradiation, pH variation, or electrical stimulation. Some examples of such compounds with their  $\beta$  response are illustrated on Figure 1.5. Those structures show the huge contrast between the closed and open forms.

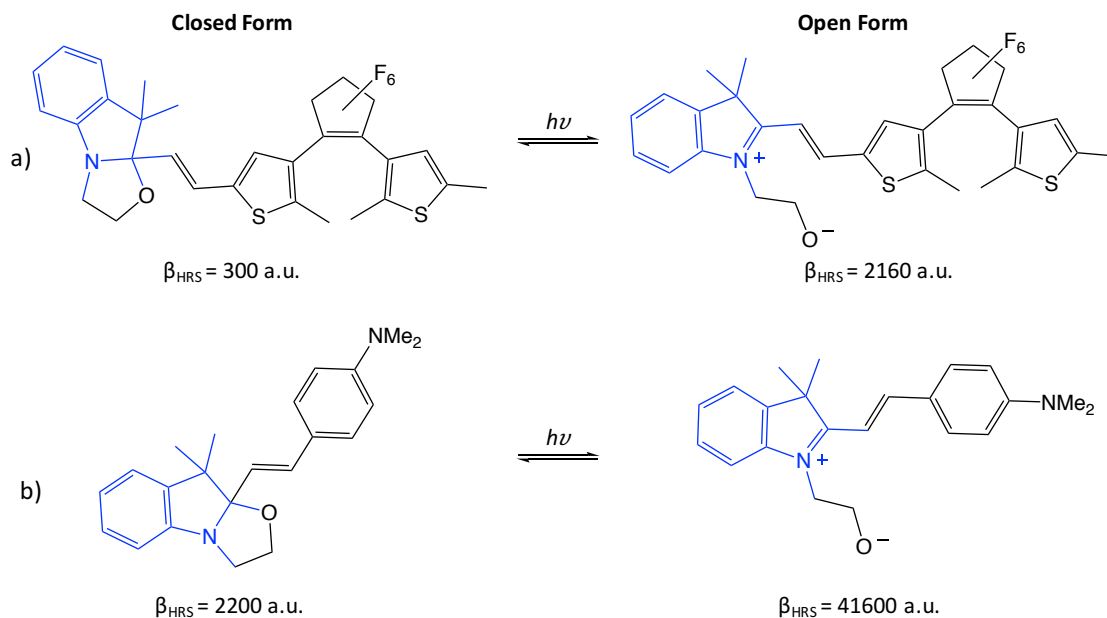


Figure 1.5: Examples of NLO switches based on indolinooxazolidine with their first hyperpolarizability value (from Ref. [44, 45]).

## 1.4 Switching on Functionalized Surfaces

Nowadays, the challenge of designing efficient NLO switches goes beyond the traditional approach of characterizing - by experimental and theoretical means - the molecules in solution. It implies considering the molecules in the solid state or under the form of functionalized surfaces. Literature describes numerous examples of reversible switching molecules grafted on a planar solid surface [46–48]. The first examples of reversible SHG switching on surfaces were demonstrated by using azobenzene [49] and spiropyran containing polymers [50] and later fulgimide moieties [51]. In fact, azobenzene represents the most commonly used and investigated molecular switch for surface functionalization [52–54].

Switching of the second-harmonic generation has been previously demonstrated in poled polymers containing photochromic dyes [50], organic photochromic crystals [36], and Langmuir-Blodgett thin films of organometallic complexes [39]. One of the most versatile approaches for surface engineering and interface design is to use self-assembled monolayers (SAM), which generally denotes a monomolecular thick film of organic compounds on flat metal or semiconductor surfaces. SAMs have been considered as ideal platforms to order and align molecules at surfaces. The potential issue of SAM is that the neighboring molecular switches can influence each other by electronic coupling, but this can be treated by taking care of various spacer groups [55].

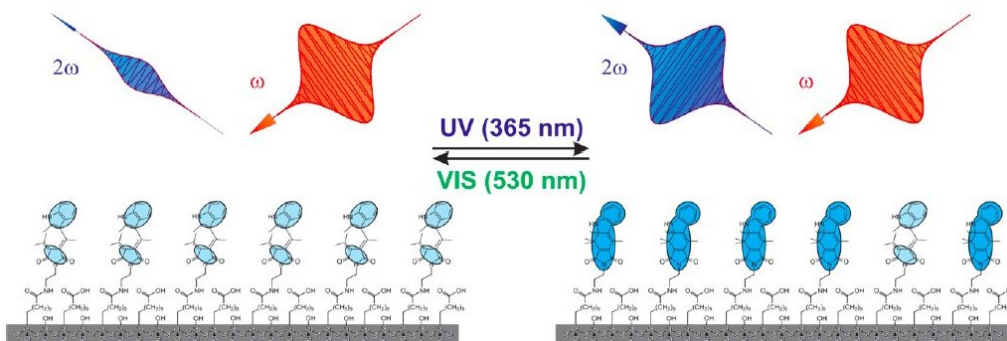


Figure 1.6: Example of the reversible photoswitching of the NLO response in second harmonic generation (from Ref. [51]).

## 1.5 Potential Applications

Intensive research on the novel nonlinear optical materials can be understood, due to their widespread applications in such branches as optical communications, optical data processing and storage [37], electrooptical devices [56, 57]. Based on the principles of nonlinear optics, nonlinear optical fibers [58] and ultrashort pulsed or power tunable lasers [59] have been constructed. Furthermore, the Q-switching, mode-locking technologies [60] and other lasers (pulse compression, frequency conversion, laser transportation) are based on nonlinear optics phenomena. [61] Other branches of applications are information technology, which include optical communicating (*e.g.* semiconductor laser, optical switching, coherent optical communication [62]), computing (*e.g.* optical logic gate) [63] or sensing (*e.g.* fiber sensor). [64] In particular switches with commutable NLO properties are addressed to store and restore information optically, or to deflect light beams. [65] With the emergence of photonic technologies in areas such as telecommunications where information is coded, transported and routed optically, there is a strong technological demand for high-performance NLO materials. [66, 67]

## 1.6 Objectives

The main goal of this thesis is the detailed characterization of the second harmonic generation (SHG) responses of indolinooxazolidine derivatives in different environments. These molecular switches are particularly interesting, because they can commute between a colorless closed form and a colored open form, as a result of various external stimuli, such as light irradiation, pH variation, or electrical stimulation. The two forms display different NLO responses and a huge contrast of their  $\beta$  values, making these systems interesting for applications in molecular-scale memory devices with multiple storage and nondestructive capacity. In this thesis, we evaluate the first hyperpolarizability of both forms and the corresponding contrast for several indolinooxazolidine derivatives that differ by their donor and acceptor groups. For instance, we study the effect of a  $-\text{CH}_3$  versus a  $-\text{NO}_2$  electron-withdrawing group on the indole moiety, as well as of the effect of using a ferrocene organometallic unit instead of a bithiophene donor moiety. Our work adopts a multidisciplinary approach where the NLO properties of the compounds are characterized experimentally and by computational methods, after they have been synthesized by our collaborators.

Experimentally, in order to evaluate the second harmonic generation, we apply the hyper-Rayleigh scattering (HRS) and electric-field induced second harmonic generation (EFISHG) techniques in solution (acetonitrile and chloroform, respectively). The EFISHG method allows the measurements of NLO properties for neutral species only. In such process, NLO switches dissolve in chloroform solution and by the addition of trifluoroacetic acid, the neutral closed form is transformed into a protonated

open form, forming an ion pair with the trifluoroacetate a counterion.

The corresponding theoretical calculations are performed by means of density functional theory (DFT), its time-dependent form (TDDFT), as well as post Hartree-Fock *ab initio* methods, which take into account the electron correlation effects (by combining the Finite Field method with Møller-Plesset Perturbation theory). The influence of the basis set size, of the exchange-correlation functionals and of the solvation model is also investigated. Moreover, for the full understanding of those compounds, it was also valuable to analyze the linear optical properties, *i.e.* the UV-vis absorption spectrum.

Regarding the loosely bound ionic pairs, theoretically, the challenge was then to describe their dynamical behavior. To do that we applied a multiscale computational method, which consists first in molecular dynamics simulations with explicit chloroform molecules and then, for a selection of snapshots, in the calculation of the first hyperpolarizability by using quantum chemical methods with implicit solvent model (PCM). This approach turned out to be useful for addressing several issues related to the EFISHG properties, such as the sign of  $\mu\beta_{//}$  and the amplitude of the second hyperpolarizability ( $\gamma$ ). This also allowed comparing implicit and explicit solvation models.

Besides molecules in solution, computational investigations tackle the second-order nonlinear optical properties of self-assembled monolayers (SAM) based on indolinoxazolidine derivatives. The morphology of various conformations of the monolayers are characterized by using MD simulations. Then, following the multi-step strategy elaborated for switches in solutions, DFT calculations are performed on snapshots extracted from the MD trajectories, providing a global overview on structural disorder induced by thermal effects and steric interactions, and their impact on the SHG responses of both states of the SAM. The sequential MD-QM approach facilitates understanding the relationships between geometrical structures and the NLO properties.

In summary, this PhD addresses the SHG responses and  $\beta$  contrasts of indolinoxazolidine derivatives in different environments. Thus, the strategy of this thesis is going beyond the classical framework of describing NLO responses in solutions using implicit models and deals with multiscale simulations of solutions, as well as of 2D photoresponsive functionalized surfaces.

# Bibliography

---

- [1] J. Kerr. A new relation between electricity and light: Dielectrified media birefringent. *Philosophical Magazine*, **50**:337–348, 1875.
- [2] T. H. Maiman. Stimulated optical radiation in ruby. *Nature*, **187**:493–494, 1960.
- [3] P. A. Franken, A. E. Hill, C. W. Peters, and G. Weinreich. Generation of optical harmonics. *Phys. Rev. Lett.*, **7**(4):118–119, 1961.
- [4] D. A. Kleinman. *Phys. Rev.*, **126**:1977, 1962.
- [5] P. N. Prasad and D. J. Williams. *Introduction to nonlinear optical effects in molecules and polymers*. Wiley: New York,, 1991.
- [6] F. Pan, K. McCallion, and M. Chiappetta. Waveguide fabrication and high-speed in-line intensity modulation in 4-N,N-4-dimethylamino-4-N-methylstilbazolium tosylate. *Appl. Phys. Lett*, **74**(4):492–494, 1999.
- [7] T. Kaino, B. Cai, and K. Takayama. Fabrication of DAST channel optical waveguides. *Adv. Funct. Mater*, **12**(9):599–603, 2002.
- [8] W. Geis, R. Sinta, W. Mowers, S. J. Deneault, M. F. Marchant, K. E. Krohn, S. J. Spector, D. R. Calawa, and T. M. Lyszczarz. Fabrication of crystalline organic waveguides with an exceptionally large electro-optic coefficient. *Appl. Phys. Lett*, **84**(19):3729–3731, 2004.
- [9] L. R. Dalton. Organic electro-optic materials. **76**(2003):1421–1433, 2004.
- [10] J. L. Oudar and D. S. Chemla. Hyperpolarizabilities of the nitroanilines and their relations to the excited state dipole moment. *J. Chem. Phys.*, **66**(6):2664–2668, 1977.
- [11] M. Stahelin, B. Zysset, M. Ahlheim, S. R. Marder, P. V. Bedworth, C. Runser, M. Barzoukas, and A. Fort. Nonlinear optical properties of push-pull polyenes for electro-optics. *J. Opt. Soc. Am*, **13**(11):2401–2407, 1996.

- 
- [12] A. E. De A Machado and A. De S. Arnóbio, Gama. Enhanced optical nonlinearities in push-pull organic systems with polyenic-mesoionic ring mixed bridges. *J. Braz. Chem. Soc.*, **19**(7):1381–1387, 2008.
- [13] N. H. List, R. Zaleśny, N. A. Murugan, J. Kongsted, W. Bartkowiak, and H. Ågren. Relation between nonlinear optical properties of push-pull molecules and metric of charge transfer excitations. *J. Chem. Theory Comput.*, **11**(9):4182–4188, 2015.
- [14] C. B. Gorman and S. R. Marder. An investigation of the interrelationships between linear and nonlinear polarizabilities and bond-length alternation in conjugated organic molecules. *Proc. Natl. Acad. Sci.*, **90**(23):11297–11301, 1993.
- [15] S. R. Marder, C. B. Gorman, F. Meyers, J. W. Perry, G. Bourhill, J.-L. Brédas, and B. M. Pierce. A unified description of linear and nonlinear polarization in organic polymethine dyes. *Science*, **265**(5172):632–635, 1994.
- [16] F. Meyers, S. R. Marder, B. M. Pierce, and J.-L. Brédas. Electric field modulated nonlinear optical properties of donor-acceptor polyenes: sum-over-states investigation of the relationship between molecular polarizabilities ( $\alpha$ ,  $\beta$ , and  $\gamma$ ) and bond length alternation. *J. Am. Chem. Soc.*, **116**(23):10703–10714, 1994.
- [17] L. T. Cheng, W. Tam, S. H. Stevenson, G. R. Meredith, G. Rikken, and S. R. Marder. Experimental investigations of organic molecular nonlinear optical polarizabilities. 1. Methods and results on benzene and stilbene derivatives. *J. Phys. Chem.*, **95**(26):10631–10643, 1991.
- [18] N. J. Long. Organometallic compounds for nonlinear optics. *Angew. Chem. Int. Ed.*, **34**:21–38, 1995.
- [19] T. Verbiest, C. Samyn, A. Persoons, K. Clays, J. Wolff, and D. Reinhoudt. Investigations of the hyperpolarizability in organic molecules from dipolar to octopolar systems. *J. Am. Chem. Soc.*, **116**(20):9320–9323, 1994.
- [20] D. P. Shelton and J. E. Rice. Measurements and calculations of the hyperpolarizabilities of atoms and small molecules in the gas phase. *Chem. Rev.*, **94**(1):3–29, 1994.
- [21] M. L. H. Green, S. R. Marder, M. E. Thompson, J. A. Bandy, D. Bloor, P. V. Kolinsky, and R. J. Jones. Synthesis and structure of (cis)-[1-ferrocenyl-2-(4-nitrophenyl)ethylene], an organotransition metal compound with a large second-order optical nonlinearity. *Nature*, **330**(6146):360–362, 1987.
- [22] H. S. Nalwa. Organometallic materials for nonlinear optics. *Appl. Organomet. Chem.*, **5**(5):349–377, 1991.

- 
- [23] T. Verbiest, S. Houbrechts, M. Kauranen, and K. Clays. Second-order nonlinear optical materials: recent advances in chromophore design. *J. Mater. Chem*, **7**(11):2175–2189, 1997.
- [24] J. B. Coe, A. J. Harris, I. Asselberghs, A. Persoons, C. J. Jeffery, H. L. Rees, T. Gelbrich, and B. M. Hursthouse. Tuning of charge-transfer absorption and molecular quadratic non-linear optical properties in ruthenium(II) ammine complexes. *J. Chem. Soc.*, (20):3617–3625, 1999.
- [25] G. Grelaud, M. P. Cifuentes, F. Paul, and M. G. Humphrey. Group 8 metal alkynyl complexes for nonlinear optics. *J. Organomet. Chem*, **751**:181–200, 2014.
- [26] I. Ledoux, J. Zyss, J. S. L. Siegel, J. Brienne, and J. Lehn. Second-harmonic generation from non-dipolar non-centrosymmetric aromatic charge-transfer molecules. *Chem. Phys. Lett.*, **172**(6):0–4, 1990.
- [27] J. Zyss. *Octupolar organic systems in quadratic nonlinear optics: molecules and materials*. Nonlinear Optics, 1991.
- [28] J. Zyss. Molecular engineering implications of rotational invariance in quadratic nonlinear optics: From dipolar to octupolar molecules and materials. *J. Chem. Phys*, **98**(9):6583–6599, 1993.
- [29] B. L. Feringa and W. R. Browne. *Molecular switches*. Eds. Wiley-VCH: Weinheim, 2nd edition, 2011.
- [30] L. Sanguinet, J.-L. Pozzo, V. Rodriguez, F. Adamietz, F. Castet, L. Ducasse, and B. Champagne. Acido- and photo-triggered NLO properties enhancement. *J. Phys. Chem. B.*, **109**(22):11139–11150, 2005.
- [31] A. Plaquet, B. Champagne, J. Kulhanek, F. Bures, E. Bogdan, F. Castet, L. Ducasse, and V. Rodriguez. Effects of the nature and length of the  $\pi$ -conjugated bridge on the second-order nonlinear optical responses of push-pull molecules including 4,5-dicyanoimidazole and their protonated forms. *ChemPhysChem*, **12**:3245–3252, 2011.
- [32] E. Cariati, C. Dragonetti, E. Lucenti, F. Nisic, S. Righetto, D. Roberto, and E. Tordin. An acido-triggered reversible luminescent and nonlinear optical switch based on a substituted styrylpyridine: EFISH measurements as an unusual method to reveal a protonation-deprotonation NLO contrast. *Chem-Comm*, **50**(13):1608, 2014.
- [33] M. Sliwa, A. Spangenberg, I. Malfant, P. G. Lacroix, R. Métivier, R. B. Pansu, and K. Nakatani. Structural, optical, and theoretical studies of a ther-

- mochromic organic crystal with reversibly variable second harmonic generation. *Chem. Mater.*, **20**(12):4062–4068, 2008.
- [34] G. Berkovic, V. Krongauz, and V. Weiss. Spiropyrans and spirooxazines for memories and switches. *Chem. Rev.*, **100**(5):1741–1754, 2000.
- [35] B. L. Feringa, R. A. van Delden, N. Koumura, and Geertsema E. M. Chiroptical molecular switches. *Chem. Rev.*, **100**:1789–1816, 2000.
- [36] M. Sliwa, S. Létard, I. Malfant, M. Nierlich, P. G. Lacroix, T. Asahi, H. Masuhara, P. Yu, and K. Nakatani. Design, synthesis, structural and nonlinear optical properties of photochromic crystals: Toward reversible molecular switches. *Chem. Mater.*, **17**(18):4727–4735, 2005.
- [37] M. G. Papadopoulos, A. J. Sadlej, and J. Leszczynski. *Non-linear optical properties of matter, from molecules to condensed phases*. Springer: The Netherlands, 2006.
- [38] V. Aubert, V. Guerschais, E. Ishow, K. Hoang-Thi, I. Ledoux, K. Nakatani, and Le Bozec H. Efficient photoswitching of the nonlinear optical properties of dipolar photochromic zinc(II) complexes. *Angew. Chem., Int. Ed.*, **47**:577–580, 2008.
- [39] L. Boubekeur-Lecaque, B. J. Coe, K. Clays, S. Foerier, T. Verbiest, and I. Asselberghs. Redox-switching of nonlinear optical behavior in langmuir-blodgett thin films containing a ruthenium(II) ammine complex. *J. Am. Chem. Soc.*, **130**(11):3286–3287, 2008.
- [40] B. J. Coe. Molecular materials possessing switchable quadratic nonlinear optical properties. *Chem. Eur. J.*, **5**(9):2464–2471, 1999.
- [41] F. Castet, V. Rodriguez, J.-L. Pozzo, L. Ducasse, A. Plaquet, and B. Champagne. Design and characterization of molecular nonlinear optical switches. *Acc. Chem. Res.*, **46**(11):2656–2665, 2013.
- [42] G. Szalóki and L. Sanguinet. *Properties and applications of indolinoxazolines as photo electro and acidochromic*. Springer, 2017.
- [43] El. Zaitseva, Al. Prokhoda, Ln. Kurkovskays, Rr. Shifrina, Ns. Kurdish, Da. Drapkina, and Va. Krongauz. *Photochromy of organic substances. VI. Preoarration of N-methacryloylhydroxyethyl derivatives of indolent spiropyran*s. Khim Geterotsik, 1973.
- [44] J. Quertinmont, B. Champagne, F. Castet, and M. Hidalgo Cardenuto. Explicit versus implicit solvation effects on the first hyperpolarizability of an organic biphotochrome. *J. Phys. Chem. A*, **119**(21):5496–5503, 2015.

- 
- [45] F. Mançois, J.-L. Pozzo, J. Pan, F. Adamietz, V. Rodriguez, L. Ducasse, F. Castet, A. Plaquet, and B. Champagne. Two-way molecular switches with large nonlinear optical contrast. *Chem. Eur. J*, **15**(11):2560–2571, 2009.
- [46] B. C. Bunker, B. I. Kim, J. E. Houston, R. Rosario, A. A. Garcia, M. Hayes, D. Gust, and S. T. Picraux. Direct observation of photo switching in tethered spiropyran using the interfacial force microscope. *Nano Lett.*, **3**(12):1723–1727, 2003.
- [47] Y. Sheng, J. Leszczynski, A. A. Garcia, R. Rosario, D. Gust, and J. Springer. Comprehensive theoretical study of the conversion reactions of spiropyran: Substituent and solvent effects. *J. Phys. Chem. B*, **108**(41):16233–16243, 2004.
- [48] R. Rosario, D. Gust, M. Hayes, J. Springer, and A. A. Garcia. Solvatochromic study of the microenvironment of surface-bound spiropyran. *Langmuir*, **19**(21):8801–8806, 2003.
- [49] R. Loucif-Saïbi, K. Nakatani, J. A. Delaire, M. Dumont, and Z. Sekkat. Photoisomerization and second harmonic generation in disperse red one-doped and -functionalized poly(methyl methacrylate) films. *Chem. Mater*, **5**(2):229–236, 1993.
- [50] Y. Atassi, J. A. Delaire, and K. Nakatani. Coupling between photochromism and second-harmonic generation in spiropyran- and spirooxazine-doped polymer films. *J. Phys. Chem. A*, **99**(44):16320–16326, 1995.
- [51] M. Schulze, M. Utecht, A. Hebert, K. Rück-Braun, P. Saalfrank, and P. Tegeder. Reversible photoswitching of the interfacial nonlinear optical response. *J. Phys. Chem. Lett*, **6**(3):505–509, 2015.
- [52] C. Gahl, R. Schmidt, D. Brete, E. R. McNellis, W. Freyer, R. Carley, K. Reuter, and M. Weinelt. Structure and excitonic coupling in self-assembled monolayers of azobenzene-functionalized alkanethiols. *J. Am. Chem. Soc*, **132**(6):1831–1838, 2010.
- [53] M. Schulze, M. Utecht, T. Moldt, D. Przyrembel, C. Gahl, M. Weinelt, P. Saalfrank, and P. Tegeder. Nonlinear optical response of photochromic azobenzene-functionalized self-assembled monolayers. *Phys. Chem. Chem. Phys.*, **17**(27):18079–18086, 2015.
- [54] T. Moldt, D. Brete, D. Przyrembel, S. Das, J. R. Goldman, P. K. Kundu, C. Gahl, R. Klajn, and M. Weinelt. Tailoring the properties of surface-immobilized azobenzenes by monolayer dilution and surface curvature. *Langmuir*, **31**(3):1048–1057, 2015.

- 
- [55] N. Katsonis, M. Lubomska, M. M. Pollard, B. L. Feringa, and P. Rudolf. Synthetic light-activated molecular switches and motors on surfaces. *Progress in Surface Science*, **82**(7-8):407–434, 2007.
- [56] J. M. Hales, J. Matichak, S. Barlow, S. Ohira, K. Yesudas, J.-L. Brédas, J. W. Perry, and S. R. Marder. Design of polymethine dyes with large third-order optical nonlinearities and loss figures of merit. *Science*, **327**(5972):1485–1488, 2010.
- [57] S. Mukhopadhyay, C. Risko, S. R. Marder, and Brédas J.-L. Polymethine dyes for all-optical switching applications: A quantum-chemical characterization of counter-ion and aggregation effects on the third-order nonlinear optical response. *Chem. Sci.*, **4**(207890):3906–3911, 2012.
- [58] G. Agrawal. Nonlinear fiber optics: its history and recent progress. *Josa B*, **28**(12):0–1, 2011.
- [59] A. M. Heidt, J. P. Burger, J.-N. Maran, and N. Traynor. High power and high energy ultrashort pulse generation with a frequency shifted feedback fiber laser. *Opt. Express*, **15**(24):15892–15897, 2007.
- [60] H. Ahmad, M. Dernaika, and S. W. Harun. All-fiber dual wavelength passive Q-switched fiber laser using a dispersion-decreasing taper fiber in a nonlinear loop mirror. *Opt. Express*, **22**(19):22794, 2014.
- [61] R. Boyd. Nonlinear Optics. *J. Chem. Inf. Model.*, **53**:1689–1699, 2013.
- [62] G. Li. Recent advances in coherent optical communication. *Adva. Opt. Photo.*, **1**(2):279, 2009.
- [63] P. Singh, D. Kr. Tripathi, S. Jaiswal, and H. K. Dixit. All-optical logic gates: Designs, classification, and comparison. *Adv. Opt. Tech.*, **2014**, 2014.
- [64] Yili Guo. *Nonlinear photonics: nonlinearities in optics, optoelectronics, and fiber communications*. Chinese University Press, 2002.
- [65] G. Bouwhuis and J. H. Spruit. Optical storage read-out of nonlinear disks. *Appl. Opt.*, **29**(26):3766–3774, 1990.
- [66] E. Garmire. Nonlinear optics in daily life. *Opt. Express*, **21**(25):30532, 2013.
- [67] M. Samoc, N. Gauthier, M. P. Cifuentes, F. Paul, C. Lapinte, and M. G. Humphrey. Electrochemical switching of the cubic nonlinear optical properties of an aryldiethynyl-linked heterobimetallic complex between three distinct states. *Angew. Chem. Int. Ed*, **45**(44):7376–7379, 2006.

## Experimental Techniques

*This chapter describes the principles of the experimental techniques, which were employed to measure the linear and nonlinear optical responses of NLO switches in solution. The experimental determination of the first hyperpolarizability was achieved by means of the Hyper-Rayleigh scattering (HRS) technique, at the ISM of the University of Bordeaux, as well as by the Electric Field-Induced Second Harmonic Generation (EFISHG) technique, available at the ISTM-CNR of the University of Milan. The linear optical properties of the NLO switches were described by using the most common method, namely UV-vis absorption spectroscopy and these measurements were performed at both Universities.*

### 2.1 UV-vis Spectroscopy

Molecular spectroscopies study the interactions of electromagnetic waves with matter. Molecules can absorb photons of energy  $E = h\nu = hc/\lambda$ , where  $\nu$  is the frequency,  $\lambda$  the corresponding wavelength, and the  $c$  the speed of light in vacuum. The Ultraviolet-Visible (UV-vis) spectroscopy is a useful technique to characterize the absorption, transmission and reflectivity of a variety of compounds in the 190-780 nm range of the electromagnetic spectrum. [1] UV-vis spectroscopy allows to describe the color of molecules, as well as to unravel the relationships between the color and the structure of compounds. It is routinely used for the quantitative determination of specific chemical species.

Upon irradiation in the UV-vis range the molecule is electronically excited. This process is usually described by the promotion of one electron from an occupied orbital (usually a bonding  $\sigma$ ,  $\pi$  or non-bonding  $n$ ) to an unoccupied one (an anti-bonding  $\pi^*$  or  $\sigma^*$  orbital) with higher energy. Typical transitions from the ground state to higher levels are presented in Figure 2.1.

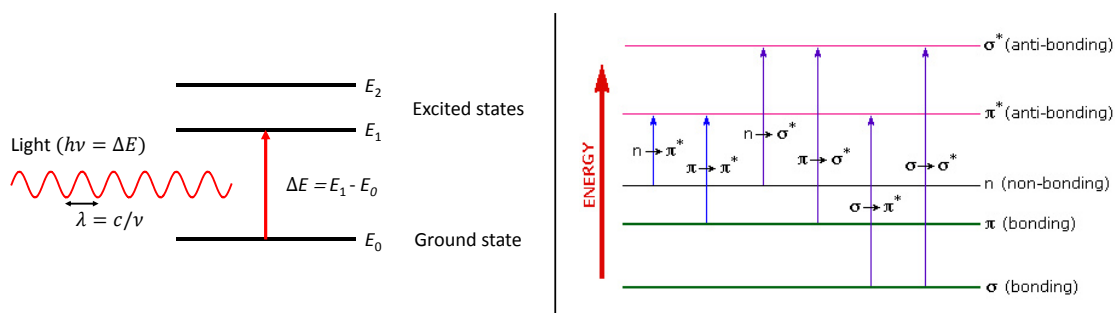


Figure 2.1: Energy changes upon electronic transition from the ground to excited states (left) and different types of electronic transitions (right).

### Beer-Lambert Law

One of the most common applications of UV-vis spectroscopy is to monitor the concentration of chromophores by using the *Beer-Lambert Law*, which describes the linear relationship between absorbance and concentration of an absorbing species [2]. This rule can be expressed via the equation:

$$A = \log \frac{I_0}{I} = \varepsilon [c] l \quad (2.1)$$

where  $A$  is the absorbance of the sample,  $I_0$  and  $I$  are the incident and transmitted intensities, respectively,  $l$  is the path length of the absorbing solution,  $[c]$  is the concentration of the absorbing species and  $\varepsilon$  is characteristic of each absorbing material, known as the molar absorption coefficient. The  $\varepsilon$  value varies with the wavelength and depends on the intrinsic property of chemical species *i.e.* on its chemical composition. The other useful parameter is the wavelength at which the maximum absorption occurs ( $\lambda_{max}$ ), which also depends on the nature of the chromophores. When  $\varepsilon$  and  $\lambda_{max}$  are known, the concentration of its solution can be calculated. The maximum value of the molar absorption coefficient ( $\varepsilon_{max}$ ), at wavelength  $\lambda_{max}$ , is an indicator of the intensity of the electronic transition, although the absorption band can spread across a range of wavelengths, so that a single wavenumber may not reflect the true intensity of the transition. The integrated absorption coefficient ( $\alpha$ ) is the integral of the molar absorption coefficient over the entire band, which therefore corresponds to the area under the curve plot of molar absorption coefficient as a function of the wavenumber ( $\tilde{\nu}$ ):

$$\alpha = \int_{band} \varepsilon(\tilde{\nu}) d\tilde{\nu} \quad (2.2)$$

The area of the absorption band in solution can be characterized by its width at half maximum ( $\Delta\tilde{\nu}_{1/2}$ ). This is the width at which  $\varepsilon = \varepsilon_{max}/2$ . By assuming a

symmetrical band,  $\varepsilon$  is then given by:

$$\int_{band} \varepsilon(\tilde{\nu}) d\tilde{\nu} \approx \varepsilon_{max} \Delta\tilde{\nu}_{1/2} \quad (2.3)$$

The experimental intensity of a UV-vis absorption band can be compared with simulations using the oscillator strength parameter ( $f$ ), which determines the probability of the light absorption through electronic transitions between energy levels:

$$f = \frac{4m_e c \varepsilon_0 \ln 10}{N_A e^2} \int_{band} \varepsilon(\tilde{\nu}) d\tilde{\nu} \quad (2.4)$$

where  $m_e$  is the mass of the electron,  $c$  is the speed of the light in vacuum,  $\varepsilon_0$  is vacuum permittivity,  $N_A$  is the Avogadro number and  $e$  is the electric charge of the electron.

## 2.2 Determination of the First Hyperpolarizability

### 2.2.1 Electric Field-Induced Second Harmonic Generation

#### General Principle

Electric field-induced second harmonic generation (EFISHG) has been first observed in solids (1962) [3] and few years later also in gases (1971) [4, 5]. In case of liquids, Levine and Bethea (1975) [6, 7] have performed EFISHG experiments to determine the first hyperpolarizability  $\beta$  of chromophores solutions. For liquids and gases the centrosymmetry is broken by applying a static external electric field  $\vec{E}$ , due to its interaction with the permanent dipole moments  $\vec{\mu}$  of the molecules, leading to the following energy contribution ( $U$ ):

$$U = -\vec{\mu} \cdot \vec{E} = -\|\vec{\mu}\| \|\vec{E}\| \cos \theta \quad (2.5)$$

where  $\theta$  is the angle between the dipole moment and the applied electric field. This external electric field necessary to align the molecules, imposes some restrictions on the EFISHG technique:

- a permanent molecular dipole moment is necessary (the first hyperpolarizability can not be obtained independently from the dipole moment), so that it can not be applied for octupolar molecules, even though their  $\beta$  is non-zero,
- EFISHG is not applicable to ionic species,
- compounds of interest are generally polar so they require polar solvents (the most commonly used solvents are dichloromethane and chloroform) [8].

EFISHG is categorized as a third-order nonlinear optical process and the incident polarization is propagated along the direction of the external static electric field, so that the second harmonic polarization  $P_{2\omega}$  (at frequency  $2\omega$ ) reads:

$$P_{2\omega} = \Gamma E_0 (E_\omega)^2 \quad (2.6)$$

where  $\Gamma$  is the macroscopic third-order nonlinearity,  $E_0$  is the amplitude of the static electric field and  $E_\omega$  is the amplitude of the laser field at frequency  $\omega$ . The  $\Gamma$  quantity is related to the molecular effective second hyperpolarizability  $\gamma_{EFISHG}$ , by the equation:

$$\Gamma = N f_0 (f_\omega)^2 f_{2\omega} \gamma_{EFISHG} \quad (2.7)$$

$N$  is the number of molecules per unit volume and  $f_0$  is known as a Onsager local field factor (1936) [9], which accounts for the effects of the permanent dipole moment of the surrounding molecules:

$$f_0 = \frac{\varepsilon_0 (n_{2\omega}^2 + 2)}{n_{2\omega}^2 + 2\varepsilon_0} \quad (2.8)$$

where  $\varepsilon_0$  is the static dielectric constant and  $n_{2\omega}$  is the refractive index at frequency  $2\omega$ .  $f_\omega$  and  $f_{2\omega}$  are the Lorentz-Lorenz (1952) [10] local field factors, which account for the effects of induced dipoles in the medium through electronic polarizations:

$$f_\omega = \frac{n_\omega^2 + 2}{3} \quad \text{and} \quad f_{2\omega} = \frac{n_{2\omega}^2 + 2}{3} \quad (2.9)$$

where  $n_\omega$  is the refractive index at frequency  $\omega$ . In Eq. 2.7,  $\gamma_{EFISHG}$  is in fact an effective second hyperpolarizability, which involves both quadratic ( $\beta$ ) and cubic ( $\gamma$ ) response contributions:

$$\gamma_{EFISHG} = \gamma + \frac{\mu\beta}{5k_B T} \quad (2.10)$$

$\mu$  is the molecular dipole moment and  $\beta$  the projection of the vectorial component of the  $\beta$  tensor on the dipole moment axis.  $k_B$  is the Boltzmann's constant,  $T$  is the temperature (K) and  $\gamma$  is the second hyperpolarizability, which is usually neglected in the interpretation of experimental measurements. Thus, the EFISHG technique, often provides the value of the scalar product between  $\vec{\mu}$  and  $\vec{\beta}$ . On the other hand, the total SHG responses in EFISHG reads:

$$\begin{aligned} \gamma_{EFISHG} &= \langle \gamma(-2\omega; \omega, \omega, 0) \rangle \\ &= \gamma_{//}(-2\omega, \omega, \omega, 0) + \frac{\mu\beta_{//}(-2\omega; \omega, \omega)}{3k_B T} = \frac{[\mu\beta_{//}(-2\omega; \omega, \omega)]_{eff}}{3k_B T} \end{aligned} \quad (2.11)$$

with  $\beta_{//}(-2\omega; \omega, \omega)$ , the so-called parallel  $\beta$ , corresponds to 3/5 times the projection

of the vector component of the  $\beta$  tensor on the dipole moment axis:

$$\beta_{//}(-2\omega; \omega, \omega) = \frac{3}{5} \sum_i \frac{\mu_i \beta_i}{\mu} \quad (2.12)$$

where  $\mu$  is the norm of dipole moment and  $\mu_i$  its  $i^{\text{th}}$  Cartesian component. The  $\mu\beta_{//}/3k_B T$  term is the dipolar orientational second-order contribution to EFISHG while  $\gamma(-2\omega; \omega, \omega, 0)$  is a third-order term corresponding to the mixing of two optical fields at  $\omega$  with the dc poling field at  $\omega = 0$ .

### Experimental Setup

The schematic diagram in Figure 2.2 shows the classical EFISHG setup. The experiments were carried out with an incident wavelength of 1907 nm, obtained by Raman shifting the fundamental 1064 nm wavelength produced by a Q-switched, mode-locked Nd<sup>3+</sup>:YAG laser. The input polarization is controlled by a half-wave plate (HWP) and a polarizer (P1). Molecules are aligned by a pulsed high voltage synchronized with the laser beam pulse to the wedge-shaped cell. A static electric field is applied to break the statistical centrosymmetry of the solution by dipolar orientation of solvent and chromophore molecules. The cell is translated in the  $z$ -direction to vary the path length. The interaction between the laser and the sample generates two output radiations: the transmitted fundamental beam ( $\omega$ ) and its second harmonics ( $2\omega$ ). The fundamental radiation is removed by filters (P2 is a second polarizer and IR is an infra-red blocking filter), so that at the end, only the second harmonic radiation is detected by a photomultiplier tube (PMT). Collected data are then extracted to calculate the  $\vec{\mu} \cdot \vec{\beta}$  value of the molecules.

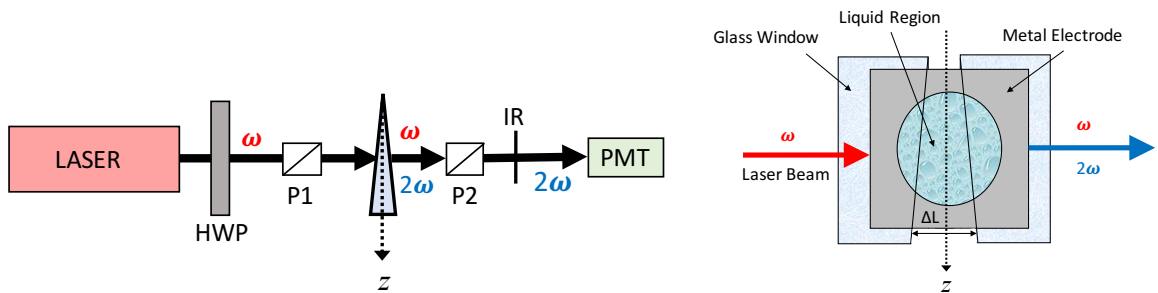


Figure 2.2: EFISHG setup designed for measuring the hyperpolarizabilities (left) and top view of the wedge cell (right).

Since the wedge-shaped cell is translated perpendicularly to the incident laser beam (along the  $z$ -direction) in order to induce a periodic second harmonic generation signal (Maker fringes [11], see Figure 2.3), the width and the periodicity of the fringes are correlated to the macroscopic susceptibility  $\Gamma(S)$  of the solution, which depends on the intensity of the second harmonic light  $I_{2\omega}$  and on the coherence length  $l_c$ , according to:

$$\Gamma(S) = \frac{1}{l_c} \left[ A \sqrt{\frac{I_{2\omega}(S)}{I_{2\omega}(0)} \frac{E_0(0)}{E_0(S)} + B} \right] 10^{-12} \quad (2.13)$$

$E_0$  is the amplitude of the dc-electric field.  $S$  refers to the chromophores solution while 0 to the solvent only.  $A$  and  $B$  are constants depending on the solvent and the cell windows. The microscopic  $\gamma_{EFISHG}$  value is then inferred from the macroscopic susceptibilities of the solvent  $\Gamma(0)$  and of the solute  $\Gamma(S)$ , via the equation:

$$\gamma_{EFISHG} = \frac{M}{\rho N_A f x} [(1+x)\Gamma(S) - \Gamma(0)] \quad (2.14)$$

where  $N_A$  is the Avogadro number,  $M$  the molecular weight of the compound,  $\rho$  the density of the solution,  $x$  the molar fraction of the compound and  $f$  a local field correction factor ( $f = f_0(f_\omega)^2 f_{2\omega}$ , Eqs. 2.7, 2.8 and 3.3).

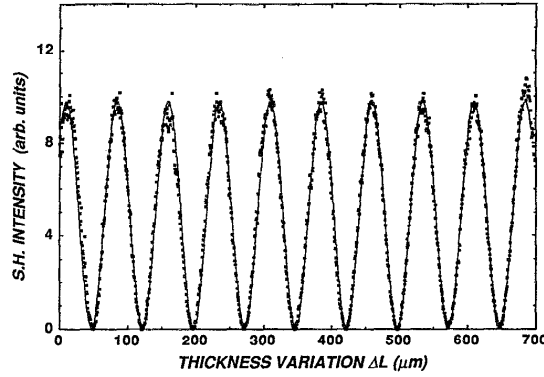


Figure 2.3: Example of the Maker fringes measured in an EFISHG experiment (from Ref. [12]).

### Conventions and Units in EFISHG

In order to compare the experimental values with the theoretical results, it is necessary to remind the relationships between the *T convention* (used in the calculations) and the phenomenological or *X convention* (used in the measurements), which were presented by Willetts (1992) [13] by considering the following equations:

$$\frac{\Delta\mu(2\omega)}{E_0 E_\omega^2 \cos(2\omega t)} = \frac{1}{4} \left[ \gamma_{//}^T(-2\omega; \omega, \omega, 0) + \frac{\mu\beta_{//}^T(-2\omega; \omega, \omega)}{3k_B T} \right] \quad (2.15a)$$

$$= \frac{1}{4} \left[ \gamma_{//}^T(-2\omega; \omega, \omega, 0) + \frac{\mu\beta_z^T(-2\omega; \omega, \omega)}{5k_B T} \right] \quad (2.15b)$$

$$= \left[ \gamma_{//}^X(-2\omega; \omega, \omega, 0) + \frac{\mu\beta_z^X(-2\omega; \omega, \omega)}{5k_B T} \right] \quad (2.15c)$$

where the second equation was obtained by assuming that the dipole moment is oriented along the  $z$  axis (*i.e.*  $\mu_x = \mu_y = 0$  and  $\mu = \mu_z$ ). Within *convention T*, the relationship between the  $z$  component of the  $\beta$  vector and the so-called parallel component of  $\beta$  reads:

$$\beta_{//}^T(-2\omega; \omega, \omega) = \frac{3}{5}\beta_z^T(-2\omega; \omega, \omega) \quad (2.16)$$

Then, combining Eqs. 2.15b and 2.15c:

$$\frac{\mu\beta_{//}^T(-2\omega; \omega, \omega)}{4(3k_B T)} = \frac{\mu\beta_z^X(-2\omega; \omega, \omega)}{5k_B T} \quad (2.17)$$

so that

$$\mu\beta_{//}^T(-2\omega; \omega, \omega) = \frac{12}{5}\mu\beta_z^X(-2\omega; \omega, \omega) \quad (2.18)$$

and

$$\gamma_{//}^T(-2\omega; \omega, \omega, 0) = 4\gamma_{//}^X(-2\omega; \omega, \omega, 0) \quad (2.19)$$

Experimentally, the whole (second- and third-order terms) response is measured and this response is often referred to as a  $\mu\beta$  quantity. As a matter of fact, since the third-order term is not necessarily zero, the whole response corresponds to an effective  $\mu\beta$ :

$$\frac{[\mu\beta_z^X(-2\omega; \omega, \omega)]_{eff}}{5k_B T} = \gamma_{//}^X(-2\omega; \omega, \omega, 0) + \frac{\mu\beta_z^X(-2\omega; \omega, \omega)}{5k_B T} \quad (2.20)$$

$$[\mu\beta_z^X(-2\omega; \omega, \omega)]_{eff} = 5k_B T \times \gamma_{//}^X(-2\omega; \omega, \omega, 0) + \mu\beta_z^X(-2\omega; \omega, \omega) \quad (2.21)$$

similarly:

$$\frac{[\mu\beta_{//}^T(-2\omega; \omega, \omega)]_{eff}}{3k_B T} = \gamma_{//}^T(-2\omega; \omega, \omega, 0) + \frac{\mu\beta_{//}^T(-2\omega; \omega, \omega)}{3k_B T} \quad (2.22)$$

or

$$[\mu\beta_{//}^T(-2\omega; \omega, \omega)]_{eff} = 3k_B T \times \gamma_{//}^T(-2\omega; \omega, \omega, 0) + \mu\beta_{//}^T(-2\omega; \omega, \omega) \quad (2.23)$$

It might be useful to assess the relative amplitude of the two contributions. So was defined the  $R_{3/2}$  ratio between the third- and second-order contributions to EFISHG:

$$R_{3/2} = \frac{3k_B T \times \gamma_{//}^T(-2\omega; \omega, \omega, 0)}{\mu\beta_{//}^T(-2\omega; \omega, \omega)} = \frac{5k_B T \times \gamma_{//}^X(-2\omega; \omega, \omega, 0)}{\mu\beta_z^X(-2\omega; \omega, \omega)} \quad (2.24)$$

Those relationships show, as expected, that no matter which convention is used, this ratio is the same, *i.e.* the ratio between the third- and second-order terms of the square brackets of the initial expressions (Eqs. 2.15).

In EFISHG technique the value of  $\mu\beta$  is often expressed by using esu units. From Shelton and J. E. Rice [14], 1 atomic unit of dipole moment is equal to  $2.5418 \times 10^{-18}$  esu ( $8.478358 \times 10^{-30}$  C m). Similarly 1 atomic unit of first hyperpolarizability corresponds to  $8.6392 \times 10^{-33}$  esu ( $3.206361 \times 10^{-53}$  C<sup>3</sup> m<sup>3</sup> J<sup>-2</sup>). So that, a  $\mu\beta$  value of 45.539 a.u. corresponds to  $10^{-48}$  esu.

## 2.2.2 Hyper-Rayleigh Scattering

### General Principle

Hyper-Rayleigh scattering (HRS) was first observed in 1965 [15], and is also called harmonic light scattering (HLS). Contrary to EFISHG, it is a non-coherent phenomena. In this technique, the sample is irradiated by a incident light beam at frequency  $\omega$  and the intensity of the scattered light beam at frequency  $2\omega$  is measured. [16–20] For a single molecule this intensity  $I_{2\omega}$  can be calculated from the intensity of the incident light beam  $I_\omega$  and the averaged square of the first hyperpolarizability, by the equation:

$$I_{2\omega} = \frac{32\pi^2}{c\epsilon_0^3\lambda^4r^2} N f_\omega^4 f_{2\omega}^2 \langle \beta_{HRS}^2 \rangle I_\omega^2 \quad (2.25)$$

where the brackets indicates the orientational averaging,  $c$  is the speed of light in vacuum,  $\epsilon_0$  is the permittivity of vacuum,  $r$  is the sample-detector distance,  $N$  is the concentration of the chromophore and  $f_\omega$  and  $f_{2\omega}$  are the local field factors, as defined in Eq. (3.3).

The relationships between  $\beta_{HRS}$  and the molecular tensor components  $\beta_{ijk}$  is determined by the scattering geometry and the polarization state of the fundamental and the harmonic light beams. In hyper-Rayleigh scattering experiments, the elliptical polarization of the incident light can be obtained, as well as linear horizontal (H, 0°) and vertical (V, 90°) polarizations but also left and right circular polarizations (45°). The experimental setup is constructed such that the incident fundamental light beam is propagating in the Y-direction and the scattered light is collected in the X-direction. Note that, it is necessary to distinguish between the system of the laboratory coordinates: X, Y and Z, and the molecular coordinates: x, y and z. In the case of an incident light polarized in the Z direction (vertical geometry) and a scattered light collected using the same polarization, the relationships between the orientationally averaged tensor quantities and the molecular tensor components read [21]:

$$\begin{aligned}
 \langle \beta_{ZZZ}^2 \rangle &= \frac{1}{7} \sum_i^{x,y,z} \beta_{iii}^2 + \frac{4}{35} \sum_{i \neq j}^{x,y,z} \beta_{iij}^2 + \frac{2}{35} \sum_{i \neq j}^{x,y,z} \beta_{iii} \beta_{ijj} + \frac{4}{35} \sum_{i \neq j}^{x,y,z} \beta_{jii} \beta_{iij} + \frac{4}{35} \sum_{i \neq j}^{x,y,z} \beta_{iii} \beta_{jji} \\
 &+ \frac{1}{35} \sum_{i \neq j}^{x,y,z} \beta_{jii}^2 + \frac{4}{105} \sum_{i \neq j \neq k}^{x,y,z} \beta_{iij} \beta_{jkk} + \frac{1}{105} \sum_{i \neq j \neq k}^{x,y,z} \beta_{jii} \beta_{jkk} \\
 &+ \frac{4}{105} \sum_{i \neq j \neq k}^{x,y,z} \beta_{ijk} \beta_{kkj} + \frac{2}{105} \sum_{i \neq j \neq k}^{x,y,z} \beta_{ijk}^2 + \frac{4}{105} \sum_{i \neq j \neq k}^{x,y,z} \beta_{ijk} \beta_{jik}
 \end{aligned} \tag{2.26}$$

In the case of an incident light polarized along the X direction (horizontal geometry) and a scattered light collected using a polarization along Z:

$$\begin{aligned}
 \langle \beta_{ZXX}^2 \rangle &= \frac{1}{35} \sum_i^{x,y,z} \beta_{iii}^2 + \frac{4}{105} \sum_{i \neq j}^{x,y,z} \beta_{iii} \beta_{ijj} - \frac{2}{35} \sum_{i \neq j}^{x,y,z} \beta_{iii} \beta_{jji} + \frac{8}{105} \sum_{i \neq j}^{x,y,z} \beta_{iij}^2 + \frac{3}{35} \sum_{i \neq j}^{x,y,z} \beta_{ijj}^2 \\
 &- \frac{2}{35} \sum_{i \neq j}^{x,y,z} \beta_{iij} \beta_{jii} + \frac{1}{35} \sum_{i \neq j \neq k}^{x,y,z} \beta_{iij} \beta_{ikk} - \frac{2}{105} \sum_{i \neq j \neq k}^{x,y,z} \beta_{iik} \beta_{jjk} \\
 &- \frac{2}{105} \sum_{i \neq j \neq k}^{x,y,z} \beta_{iij} \beta_{jkk} + \frac{2}{35} \sum_{i \neq j \neq k}^{x,y,z} \beta_{ijk}^2 - \frac{2}{105} \sum_{i \neq j \neq k}^{x,y,z} \beta_{ijk} \beta_{jik}
 \end{aligned} \tag{2.27}$$

The two polarizations are detected with the same sensitivity and then the total HRS response is the sum of both contributions:

$$\langle \beta_{HRS}^2 \rangle = \langle \beta_{ZZZ}^2 \rangle + \langle \beta_{ZXX}^2 \rangle \tag{2.28}$$

The ratio between the HRS intensities is called the depolarization ratio (DR), which can be expressed as:

$$DR = \frac{\langle \beta_{ZZZ}^2 \rangle}{\langle \beta_{ZXX}^2 \rangle} \tag{2.29}$$

The depolarization ratio can achieve different values depending on the part of the molecules responsible for the NLO response. For one-dimensional push-pull  $\pi$ -conjugated molecules, for which the  $\beta$  tensor is dominated by one diagonal tensor component  $\beta_{zzz}$ :

$$\langle \beta_{ZZZ}^2 \rangle = \frac{1}{7} \beta_{zzz}^2 \quad \text{and} \quad \langle \beta_{ZXX}^2 \rangle = \frac{1}{35} \beta_{zzz}^2 \quad \text{so, that} \quad DR = \frac{35}{7} = 5 \tag{2.30}$$

On the other hand, for octupolar molecules, only  $\beta_{xyz} \neq 0$ , so that:

$$\langle \beta_{ZZZ}^2 \rangle = \frac{36}{105} \beta_{xyz}^2 \quad \text{and} \quad \langle \beta_{ZXX}^2 \rangle = \frac{24}{105} \beta_{xyz}^2 \quad \text{so, that} \quad DR = \frac{36}{24} = 1.5 \tag{2.31}$$

The HRS hyperpolarizabilities can also be interpreted by using the spherical representation of the  $\beta$  tensor, where the dipolar (J=1) and octupolar (J=3) contributions to  $\beta_{HRS}$  are determined from the Cartesian components of  $\beta$ . [22, 23] In the

molecular frame, by assuming Kleinman's symmetry (defined in Chapter 1), the two contributions read:

$$|\beta_{J=1}|^2 = \frac{3}{5} \sum_i^{x,y,z} \beta_{iii}^2 + \frac{6}{5} \sum_{i \neq j}^{x,y,z} \beta_{iii} \beta_{ijj} + \frac{3}{5} \sum_{i \neq j}^{x,y,z} \beta_{jii}^2 + \frac{3}{5} \sum_{i \neq j \neq k}^{x,y,z} \beta_{jii} \beta_{jkk} \quad (2.32)$$

$$|\beta_{J=3}|^2 = \frac{2}{5} \sum_i^{x,y,z} \beta_{iii}^2 - \frac{6}{5} \sum_{i \neq j}^{x,y,z} \beta_{iii} \beta_{ijj} + \frac{12}{5} \sum_{i \neq j}^{x,y,z} \beta_{jii}^2 - \frac{3}{5} \sum_{i \neq j \neq k}^{x,y,z} \beta_{jii} \beta_{jkk} + \sum_{i \neq j \neq k}^{x,y,z} \beta_{ijk}^2 \quad (2.33)$$

From those, relations with the HRS brackets can be defined as:

$$\langle \beta_{ZZZ}^2 \rangle = \frac{9}{45} |\beta_{J=1}|^2 + \frac{6}{105} |\beta_{J=3}|^2 \quad (2.34)$$

$$\langle \beta_{ZXX}^2 \rangle = \frac{1}{45} |\beta_{J=1}|^2 + \frac{4}{105} |\beta_{J=3}|^2 \quad (2.35)$$

The ratio between the octupolar and dipolar contributions to the first hyperpolarizability is called the nonlinear anisotropy factor ( $\rho$ ):

$$\rho = |\beta_{J=3}| / |\beta_{J=1}| \quad (2.36)$$

The anisotropy factor can be linked to  $\beta_{HRS}$  and DR by the following equations:

$$\beta_{HRS} = \sqrt{\frac{10}{45} |\beta_{J=1}|^2 + \frac{10}{105} |\beta_{J=3}|^2} = |\beta_{J=1}| \sqrt{\frac{2}{3} \left( \frac{1}{3} + \frac{1}{7} \rho^2 \right)} \quad (2.37)$$

$$DR = 9 \frac{\left( 1 + \frac{2}{7} \rho^2 \right)}{\left( 1 + \frac{12}{7} \rho^2 \right)} \quad (2.38)$$

## Experimental Setup

The experiments were carried out with an incident radiation at 1064 nm, obtained from a passively mode-locked Nd:YVO<sub>4</sub> laser. The setup of the devices was configured in a classical 90° scattering geometry. Figure 2.4 shows the schematic setup of the HRS measurements. The incident light beam is transmitted via two crossed polarizers (P1, P2), between which a half-wave plate (HWP) is localized in order to control the intensities of the fundamental laser beam. Before the incident light is focused to the cell, the light beam is split in two: one part of the intensity is splitted (BS, beam split) and detected by photo-diode (PD), while the other one is focused through the lens (FL, L) and concave mirror (M). As a consequence, the second harmonic signal, which passes the interference filter (IF) can be collected by the photomultiplier (PMT) perpendicularly to the incident light beam direction, avoiding possible interferences of the laser with the measured signal.

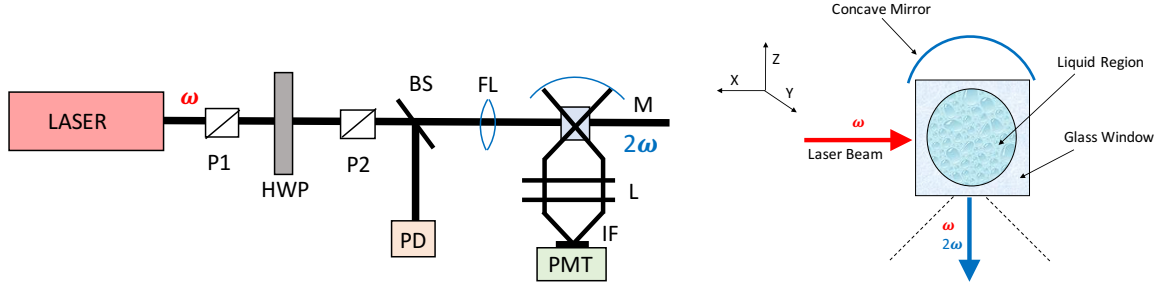


Figure 2.4: HRS setup designed for measurements of the first hyperpolarizabilities (left) and top view of the cell (right).

The total harmonic scattered light for a solution of two components, the solvent (S) and a solute (X), is given by:

$$I_{\Psi V}^{2\omega} = G f_L^2 \{ C_S [|\beta_{J=1}|^2 C_{\Psi V}]_S + C_X [|\beta_{J=1}|^2 C_{\Psi V}]_X \} \times 10^{-a_X^{2\omega}} C_X (I^\omega)^2 \quad (2.39)$$

where  $G$  includes all experimental factors,  $C$  is the molarity of the solvent or solute (in  $\text{molL}^{-1}$ ) and  $f_L^2$  is the local field factor ( $f_L^2 = f_\omega^4 f_{2\omega}^2$ , from Eq. 2.25).  $I^\omega$  is the incident light intensity and  $a_X^{2\omega}$  accounts for the one-photon absorption of the chromophore at the second harmonic frequency.  $|\beta_{J=1}|$  and  $|\beta_{J=3}|$  are respectively the dipolar and octupolar (vide infra) components (see Eqs. 2.32 and 2.33), while  $C_{\Psi V}$  is the orientational average of the molecular spherical components of the first hyperpolarizability of the solute (or solvent), which can be expressed as:

$$C_{\Psi V} = \left( \frac{9}{45} + \frac{6}{105} \rho^2 \right) + \left( -\frac{20}{45} + \frac{10}{105} \rho^2 \right) \cos^2 \Psi + \left( \frac{12}{45} - \frac{12}{105} \rho^2 \right) \cos^4 \Psi \quad (2.40)$$

In summary of this chapter, the advantages of HRS over the EFISHG technique include:

- the knowledge of the dipole moment is not necessary to extract the  $\beta$  response,
- $\beta_{HRS}$  of ionic molecules can be measured, because no external field is needed,
- similarly,  $\beta_{HRS}$  of octupolar molecules can be investigated,
- furthermore, the depolarization ratio (DR) can give information about the geometry of the NLOphore.

Despite so many benefits, HRS possesses also a few disadvantages:

- because, it is an incoherent signal, the scattered second harmonic light is weak and requires sensitive detection,
- the technique can overestimate the  $\beta$  value because HRS incoherent light scattering can not be distinguished from 2-photon fluorescence [24–26]. Nevertheless, solutions have been proposed to remove 2-photon fluorescence from the total signal. [27]

# Bibliography

---

- [1] Heinz-Helmut Perkampus. *UV-vis Spectroscopy and its application*. Springer Laboratory, 1992.
- [2] D. F. Swinehart. The Beer-Lambert Law. *J. Chem. Educ.*, **39**(7):333–335, 1962.
- [3] R. W. Terhune, P. D. Maker, and C. M. Savage. Optical harmonic generation in calcite. *Phys. Rev. Lett.*, **8**(404):2550–2136, 1962.
- [4] R. S. Finn, J. F. Ward, F. Ward, and R. S. Finn. DC-induced optical second-harmonic generation in the inert gases. *Phys. Rev. Lett.*, **26**(6):285–289, 1971.
- [5] G. Hauchecorne, F. Kerhervé, and G. Mayer. Measurement of light wave interactions in various substances. *J. Phys. (France)*, **32**:47–62, 1971.
- [6] B. F. Levine and C. G. Bethea. Molecular hyperpolarizabilities determined from conjugated and nonconjugated organic liquids. *App. Phys. Lett.*, **24**(9):445–447, 1974.
- [7] B. F. Levine and C. G. Bethea. Second and third order hyperpolarizabilities of organic molecules. *J. Chem. Phys.*, **63**(6):2666–2682, 1975.
- [8] R. Dworzak and D. Kieslinger. Electric field induced second harmonic generation (EFISH) experiments in the swivel cell: New aspects of an established method. *Phys. Chem. Chem. Phys.*, **2**:5057–5064, 2000.
- [9] L. Onsager. Electric moments of molecules in liquids. *J. Am. Chem. Soc.*, **58**(8):1486–1493, 1936.
- [10] H. A. Lorentz. *The theory of the electrons and its applications to the phenomena of light and radiant heat*. Dover Publications, Inc., New York, 2nd edition, 1952.
- [11] P. D. Maker, R. Terhune, M. Nisenoff, and C. M. Savage. Effects of dispersion and focusing on the production of optical harmonics. *Phys. Rev. Lett.*, **8**:21–23, 1962.

- 
- [12] C. Bosshard, G. Knöpfle, P. Prêtre, and P. Günter. Second-order polarizabilities of nitropyridine derivatives determined with electric-field-induced second-harmonic generation and a solvatochromic method: A comparative study. *J. Appl. Phys.*, **71**(4):1594–1605, 1992.
- [13] A. Willetts, J. E. Rice, D. M. Burland, and D. P. Shelton. Problems in the comparison of theoretical and experimental hyperpolarizabilities. *J. Chem. Phys.*, **97**(10):7590–7599, 1992.
- [14] D. P. Shelton and J. E. Rice. Measurements and calculations of the hyperpolarizabilities of atoms and small molecules in the gas phase. *Chem. Rev.*, **94**(1):3–29, 1994.
- [15] R. W. Terhune, P. D. Maker, and C. M. Savage. Measurements of nonlinear light scattering. *Phys. Rev. Lett.*, **14**(17):681–684, 1965.
- [16] K. Clays and A. Persoons. Hyper-Rayleigh scattering in solution. *Phys. Rev. Lett.*, **66**(23):2980–2983, 1991.
- [17] T. Verbiest, C. Samyn, A. Persoons, K. Clays, J. Wolff, and D. Reinhoudt. Investigations of the hyperpolarizability in organic molecules from dipolar to octopolar systems. *J. Am. Chem. Soc.*, **116**(20):9320–9323, 1994.
- [18] M. A. Pauley, H. W. Guan, C. H. Wang, and Alex K.Y. Jen. Determination of first hyperpolarizability of nonlinear optical chromophores by second harmonic scattering using an external reference. *J. Chem. Phys.*, **104**(20):7821–7829, 1996.
- [19] T. Verbiest, K. Clays, and V. Rodriguez. *Second-order nonlinear optical characterisations techniques: an introduction*. CRC Press, New York, 2009.
- [20] E. Hendrickx, K. Clays, and A. Persoons. Hyper-Rayleigh scattering in isotropic solution. *Acc. Chem. Res.*, **31**(10):675–683, 1998.
- [21] R. Bersohn, Yoh-Han Pao, and H. L. Frisch. Double-quantum light scattering by molecules. *J. Chem. Phys.*, **45**(9):3184–3198, 1966.
- [22] S. Brasselet and J. Zyss. Multipolar molecules and multipolar fields: probing and controlling the tensorial nature of nonlinear molecular media. *J. Opt. Soc. Am. B*, **15**(1):257–288, 1998.
- [23] V. Rodriguez, J. Grondin, F. Adamietz, and Y. Danten. Local structure in ionic liquids investigated by hyper-Rayleigh scattering. *J. Phys. Chem. B*, **114**(46):15057–15065, 2010.

- [24] M. C. Flipse, R. de Jonge, R. H. Woudenberg, A. W. Marsman, C. A. van Walree, and L. W. Jenneskens. The determination of first hyperpolarizabilities  $\beta$  using hyper-Rayleigh scattering: a caveat. *Chem. Phys. Lett.*, **245**(3):297–303, 1995.
- [25] I. D. Morrison, R. G. Denning, W. M. Laidlaw, and M. A. Stammers. Measurement of first hyperpolarizabilities by hyper-Rayleigh scattering. *Rev. Sci. Instrum.*, **67**(4):1445–1453, 1996.
- [26] N. W. Song, T. I. Kang, S. C. Jeoung, S. J. Jeon, B. R. Cho, and D. Kim. Improved method for measuring the first-order hyperpolarizability of organic NLO materials in solution by using the hyper-Rayleigh scattering technique. *Chem. Phys. Lett.*, **261**(3):307–312, 1996.
- [27] G. Olbrechts, R. Strobbe, K. Clays, and A. Persoons. High-frequency demodulation of multi-photon fluorescence in hyper-Rayleigh scattering. *Rev. Sci. Instrum.*, **69**:2233–2241, 1998.

## Theoretical Methods

*This chapter reviews the theoretical models based on quantum mechanics and classical dynamics, which are employed in this thesis. The principles of the methods and the key equations are given to facilitate the understanding. First, the wavefunction methods are introduced from the Schrödinger equation, then one of the earliest methods, the Hartree-Fock (HF) method, is described followed by models that account for electron correlation, such as Møller-Plesset Perturbation Theory (MP2) and then Density Functional Theory (DFT). The excitation energies and excited state properties were determined by using Time-Dependent (TD) DFT. Then, methods to evaluate and analyze the second-order NLO properties are presented, the TDHF approach, its DFT equivalent (TDDFT), and the Finite Field (FF) approach. At the end, the principles of classical Molecular Dynamics (MD) simulation and solution models are presented.*

### 3.1 Wavefunction Quantum Mechanics Methods

#### 3.1.1 Schrödinger Equation

The development of quantum chemistry was initiated in 1926, when Erwin Schrödinger proposed the eponymous equation, which contains the information about the structure and energy of the system. [1, 2] This equation in its time independent (properties do not change in time) non-relativistic form reads:

$$\widehat{H}\Psi = E\Psi \tag{3.1}$$

where  $\Psi$  is the wavefunction, which is a function of the space and spin coordinates of all the particles of the system and contains all the information about the system.  $E$  is the total energy of the system. The state with lowest energy is called the ground state ( $\Psi_0$ ) and its energy is the ground state energy ( $E_0$ ). The Hamiltonian operator

$\widehat{H}$  is the sum of the kinetic energy operator  $\widehat{T}$  and the potential energy operator  $\widehat{V}$ :

$$\widehat{H} = \widehat{T} + \widehat{V} \quad (3.2)$$

$$\widehat{T} = -\frac{1}{2} \sum_{I=1}^L \frac{1}{m_I} \nabla_I^2 \quad \text{and} \quad \widehat{V} = \sum_{I=1}^L \sum_{J>I}^L \frac{Z_I Z_J}{|r_{IJ}|} \quad (3.3)$$

where  $m_I$  is the mass of the  $I^{\text{th}}$  particle,  $L$  is the number of particles,  $|r_{IJ}|$  is the distance between the  $I$  and  $J$  particles and  $Z_I, Z_J$  are the charges of them.  $\nabla_I^2$  is the Laplacian operator, which in Cartesian coordinates reads:

$$\nabla_I^2 = \frac{\partial^2}{\partial x_I^2} + \frac{\partial^2}{\partial y_I^2} + \frac{\partial^2}{\partial z_I^2} \quad (3.4)$$

For *molecular* systems, the Schrödinger equation makes the distinction between the particles,  $M$  atoms (nuclei) and  $N$  electrons:

$$\widehat{H} = \underbrace{-\frac{1}{2} \sum_{i=1}^N \nabla_i^2}_{\widehat{T}_e} - \underbrace{\frac{1}{2} \sum_{A=1}^M \frac{1}{M_A} \nabla_A^2}_{\widehat{T}_n} - \underbrace{\sum_{i=1}^N \sum_{A=1}^M \frac{Z_A}{|r_{iA}|}}_{\widehat{V}_{ne}} + \underbrace{\sum_{i=1}^N \sum_{j>1}^N \frac{1}{|r_{ij}|}}_{\widehat{V}_{ee}} + \underbrace{\sum_{A=1}^M \sum_{B>A}^M \frac{Z_A Z_B}{|R_{AB}|}}_{\widehat{V}_{nn}} \quad (3.5)$$

The first two terms are the kinetic energy operators of the electrons ( $\widehat{T}_e$ ) and the nuclei ( $\widehat{T}_n$ ), respectively. The remaining three terms represent the Coulomb potential operators of the particles, which include the attraction between the electrons and the nuclei ( $\widehat{V}_{ne}$ ), the repulsion between the electrons ( $\widehat{V}_{ee}$ ), and the repulsion between the nuclei ( $\widehat{V}_{nn}$ ).

### 3.1.2 Born-Oppenheimer Approximation

The difficulties of solving Schrödinger equation comes from the fact that the wavefunction  $\Psi$  depends on a large number of variables. Since, the nuclei are much heavier than the electrons (nuclei are approximately  $10^3$  to  $10^5$  times heavier), their motion is generally much slower and the characteristic time scales of electronic processes are much smaller. Due to this knowledge, in 1927, Max Born and J. Robert Oppenheimer [3] considered the nuclei as having a fixed geometry with respect to electrons, so that when studying the electronic motions, the second term of Eq. 3.5 can be neglected. For the same reason, the nucleus-nucleus repulsion potential is assumed to be constant. Thus, the remaining electronic Hamiltonian becomes:

$$\widehat{H} = -\frac{1}{2} \sum_{i=1}^N \nabla_i^2 - \sum_{i=1}^N \sum_{A=1}^M \frac{Z_A}{|r_{iA}|} + \sum_{i=1}^N \sum_{j>1}^N \frac{1}{|r_{ij}|} \quad (3.6)$$

### 3.1.3 Hartree-Fock Theory

Despite the Born-Oppenheimer approach, the electronic Schrödinger equation could be solved exactly only for the hydrogen atom. For other atoms containing many electrons obtaining highly accurate wavefunctions is still intractable and further approximations are required. In 1926 Heisenberg [4] and Dirac [5] independently proposed that the electronic wavefunction should be antisymmetric with respect to the interchange of two particle coordinates, in order to satisfy the Pauli [6] principle. Then, Slater [7] proposed that these antisymmetric wavefunctions are written under the form of normalized determinants built from spinorbitals  $\chi_a(\vec{x}_a)$ .

In 1930, Fock [8] employed the Slater determinant to the *ab initio* self consistent field (SCF) method developed by Hartree [9] and proposed the Hartree-Fock (HF) method, which gives an approximation to the Schrödinger equation and is one of the most fundamental theories in quantum chemistry. So, in HF theory, the wavefunction, reads:

$$\Psi(\vec{x}_1, \vec{x}_2, \dots, \vec{x}_N) = \frac{1}{\sqrt{N!}} \begin{vmatrix} \chi_1(\vec{x}_1) & \chi_2(\vec{x}_1) & \cdots & \chi_N(\vec{x}_1) \\ \chi_1(\vec{x}_2) & \chi_2(\vec{x}_2) & \cdots & \chi_N(\vec{x}_2) \\ \vdots & \vdots & \ddots & \vdots \\ \chi_1(\vec{x}_N) & \chi_2(\vec{x}_N) & \cdots & \chi_N(\vec{x}_N) \end{vmatrix} \quad (3.7)$$

where the rows of the determinant are associated with the  $N$  electrons and the columns with the  $N$  spinorbitals.  $1/\sqrt{N!}$  is the normalization factor. The spinorbitals are orthonormal:

$$\langle \chi_a | \chi_b \rangle = \delta_{ab} \quad (3.8)$$

The spinorbitals are products of spin and spatial orbitals:

$$\chi_a(\vec{x}) = \begin{cases} \psi_a(\vec{r})\alpha(\omega) \\ \text{or} \\ \psi_a(\vec{r})\beta(\omega) \end{cases} \quad (3.9)$$

where  $\vec{x}_N$  includes spatial ( $\vec{r}$ ) and spin ( $\omega$ ) coordinates. The spatial orbital  $\psi_a(\vec{r})$  is a function of the position vector  $\vec{r}$ , while the orthonormal spin functions  $\alpha(\omega)$  and  $\beta(\omega)$  correspond to spin up ( $\uparrow$ ) and spin down ( $\downarrow$ ). According to the Slater determinant, two electrons with the same spin can not occupy the same spatial orbital.

The spatial and spin coordinates integrals in Dirac notation (denotes with the angle brackets  $\langle \rangle$ ), for one-electron integrals reads:

$$\langle a | \hat{h} | a \rangle = \langle \chi_a | \hat{h} | \chi_a \rangle = \int d\vec{x}_1 \chi_a^*(\vec{x}_1) \hat{h} \chi_a(\vec{x}_1) \quad (3.10)$$

where  $\hat{h}$  is the one-electron operator, defined as:

$$\hat{h}(1) = -\frac{1}{2}\nabla_1^2 - \sum_{A=1}^M \frac{Z_A}{r_{1A}} \quad (3.11)$$

and for two-electron integrals:

$$\begin{aligned} \langle ab||ab \rangle &= \langle ab|ab \rangle - \langle ab|ba \rangle \\ &= \int d\vec{x}_1 d\vec{x}_2 \chi_a^*(\vec{x}_1) \chi_b^*(\vec{x}_2) \frac{1}{r_{12}} \chi_a(\vec{x}_1) \chi_b(\vec{x}_2) \\ &\quad - \int d\vec{x}_1 d\vec{x}_2 \chi_a^*(\vec{x}_1) \chi_b^*(\vec{x}_2) \frac{1}{r_{12}} \chi_b(\vec{x}_1) \chi_a(\vec{x}_2) \end{aligned} \quad (3.12)$$

$r_{12}$  is the distance between electrons 1 and 2 and the  $a$  and  $b$  indices refer to occupied spinorbitals.

The HF method is based on the *variational* principle, stating that the best determinant gives the lowest electronic ground state energy:

$$E_0 = \langle \Psi_0 | \hat{H} | \Psi_0 \rangle \quad (3.13)$$

Now, by developing this expansion in terms of one- and two-electron integrals, it reads:

$$E_0 = \sum_a \langle a | \hat{h} | a \rangle + \frac{1}{2} \sum_{ab} \langle ab || ab \rangle \quad (3.14)$$

Optimization of the ground state wavefunction relies on minimizing the electronic energy with respect to the set of one-electron spinorbitals  $\chi(\vec{x})$ , via the so-called HF equation:

$$\hat{f}(i) |\chi_n(\vec{x})\rangle = \varepsilon_n |\chi_n(\vec{x})\rangle \quad (3.15)$$

where  $\varepsilon_n$  is the energy of the spin-orbital  $\chi_n(\vec{x})$  and  $\hat{f}(i)$  is an effective one-electron operator, called the Fock operator, which has the form:

$$\hat{f}(i) = \hat{h}(i) + V^{HF}(i) \quad (3.16)$$

$V^{HF}(i)$  is the effective Hartree-Fock potential, which accounts for the average potential experienced by the  $i^{th}$  electron in the environment of all (other) electrons.  $\hat{f}(i)$  can be rewritten to express  $V^{HF}(i)$  explicitly as the sum of the Coulomb [ $\hat{J}_b(i)$ ] and exchange [ $\hat{K}_b(i)$ ] operators:

$$V^{HF}(i) = \sum_b^{occ} \hat{J}_b(i) - \sum_b^{occ} \hat{K}_b(i) \quad (3.17)$$

where

$$\hat{J}_b(\vec{x}_1) |\chi_a(\vec{x}_1)\rangle = \left[ \int d\vec{x}_2 \chi_b^*(\vec{x}_2) \frac{1}{r_{12}} \chi_b(\vec{x}_2) \right] \chi_a(\vec{x}_1) \quad (3.18)$$

$$\widehat{K}_b(\vec{x}_1)|\chi_a(\vec{x}_1)\rangle = \left[ \int d\vec{x}_2 \chi_b^*(\vec{x}_2) \frac{1}{r_{12}} \chi_a(\vec{x}_2) \right] \chi_b(\vec{x}_1) \quad (3.19)$$

In the HF method one can distinguish between two type of systems. When, at least, one spatial orbital contains a single electron, the system is referred to be *open shell*, while when all spatial orbitals are doubly occupied, it is a *closed-shell*. Generally, there is a large energy difference between the highest occupied molecular orbital (HOMO) and the lowest unoccupied molecular orbital (LUMO). The unoccupied molecular orbitals are called *virtual orbitals*. An open-shell system is described by using unrestricted determinants (unrestricted Hartee-Fock UHF) while closed-shell by means of restricted determinants (restricted Hartee-Fock RHF).

In the LCAO method, each molecular orbital is presented as a linear combination of the atomic orbitals:

$$|\psi_a\rangle = \sum_{\mu=1}^K C_{\mu a} |\phi_\mu\rangle \quad (3.20)$$

where the  $C_{\mu a}$  are the expansion LCAO coefficients,  $\phi_\mu$  are the atomic orbitals and  $K$  is their number. The sets of the AOs used in the LCAO expansions are called basis sets. The details are presented in the Basis Sets section 3.3.

Eq. 3.15 can be rewritten under matrix form after accounting for the LCAO approximation. Two matrices are introduced: the overlap ( $S$ ) and the Fock ( $F$ ) matrices of dimension  $K \times K$ . The  $S_{\mu\nu}$  overlap matrix element reads:

$$S_{\mu\nu} = \int d\vec{r}_1 \phi_\mu^*(\vec{r}_1) \phi_\nu(\vec{r}_1) \quad (3.21)$$

while, the Fock element matrix is defined as:

$$F_{\mu\nu} = \int d\vec{r}_1 \phi_\mu^*(\vec{r}_1) \widehat{f}(1) \phi_\nu(\vec{r}_1) \quad (3.22)$$

Then, following Roothaan and Hall (1951) [10, 11], equation 3.15 becomes:

$$\sum_{\nu=1}^K F_{\mu\nu} C_{\nu n} = \varepsilon_n \sum_{\nu=1}^K S_{\mu\nu} C_{\nu n} \quad (3.23)$$

or even more simply, the Roothaan matrix equation:

$$FC = SC\epsilon \quad (3.24)$$

where  $\epsilon$  is a diagonal matrix, containing the orbital energies  $\varepsilon_n$ .

The general HF computational procedure consists of the following steps: 1) an initial set of spinorbitals is used to calculate the starting HF potential ( $V^{HF}$ ) 2) the eigenvalue problem is solved (Eq. 3.24) and a new set of orbitals is generated and compared with those of the initial step, then 3) if the numerical convergence criteria are satisfied the solution is obtained, but if they are not satisfied, the procedure

is repeated iteratively until the convergence is reached. That cycle is called the self-consistent field (SCF) method.

### 3.1.4 Møller-Plesset Perturbation Theory

Other methods to solve the Schrödinger equation take into account electron correlation, which are not included in HF. There are many post-Hartree-Fock methods that include explicit electron-electron interactions, such as the configuration interaction (CI) method, the multi-configurational self-consistent field (MCSCF) method, or the Møller-Plesset perturbation theory (MP). Only the last one was applied in this thesis and the principles are described below.

The MP method is based on the Rayleigh-Schrödinger perturbation theory. It treats electron correlation as a perturbation to the zero<sup>th</sup>-order Hartree-Fock Hamiltonian. The total Hamiltonian is divided into the zero<sup>th</sup>-order part ( $\widehat{H}_0$ ) and the perturbation term  $\zeta\widehat{H}'$ , as follows:

$$\widehat{H} = \sum_{i=1} \widehat{h}(i) + \sum_{j>i} \frac{1}{|r_{ij}|} = \widehat{H}_0 + \zeta\widehat{H}' \quad (3.25)$$

where  $\zeta$  is an ordering parameter that is eventually set equal to 1 and  $\zeta\widehat{H}'$  is small with respect to  $\widehat{H}_0$ :

$$\widehat{H}_0 = \sum_{i=1}^N \widehat{f}(\vec{x}_i) = \widehat{h}(\vec{x}_i) + V^{HF}(\vec{x}_i) \quad (3.26)$$

Thus, the perturbation  $\zeta\widehat{H}'$  is the difference between the true electronic Hamiltonian and the HF Hamiltonian. From the Schrödinger equation, the problem to be solved is:

$$(\widehat{H}_0 + \zeta\widehat{H}')|\Psi\rangle = E|\Psi\rangle \quad (3.27)$$

According to the Rayleigh-Schrödinger perturbation theory, the energy and wavefunction can be expanded in Taylor series of  $\zeta$ :

$$|\Psi\rangle = |\Psi^{(0)}\rangle + \zeta|\Psi^{(1)}\rangle + \zeta^2|\Psi^{(2)}\rangle + \dots \quad (3.28)$$

$$E = E^{(0)} + \zeta E^{(1)} + \zeta^2 E^{(2)} + \dots \quad (3.29)$$

For non-degenerate states the  $n^{\text{th}}$ -order energy terms ( $E^{(n)}$ ) is expressed in terms of the  $n-1^{\text{th}}$  order wavefunctions  $|\Psi^{n-1}\rangle$ , which can be written as a function of orbital energies and integrals:

$$E^{(0)} = \langle \Psi^{(0)} | \widehat{H}_0 | \Psi^{(0)} \rangle = \sum_a^{\text{occ}} \varepsilon_a \quad (3.30)$$

$$E^{(1)} = \langle \Psi^{(0)} | \zeta\widehat{H}' | \Psi^{(0)} \rangle = -\frac{1}{2} \sum_{ab}^{\text{occ}} \langle ab || ab \rangle \quad (3.31)$$

$$E^{(2)} = \langle \Psi^{(0)} | \zeta \widehat{H}' | \Psi^{(1)} \rangle \quad (3.32)$$

...

The sum of the zero<sup>th</sup>- and first-order energies reads:

$$E_{HF} = E^{(0)} + E^{(1)} = \sum_a^{occu} \varepsilon_a - \frac{1}{2} \sum_{ab}^{occu} \langle ab || ab \rangle \quad (3.33)$$

which corresponds the Hartree-Fock ground state energy. The first improvement to the HF energy, and the dominant one, is the second-order energy  $E^{(2)}$ :

$$E^{(2)} = \sum_{n \neq 0} \frac{|\langle 0 | \zeta \widehat{H}' | n \rangle|^2}{E_0^{(0)} - E_n^{(0)}} \quad (3.34)$$

or:

$$E^{(2)} = \sum_{a>b;r>s} \frac{|\langle ab || rs \rangle|^2}{\varepsilon_a + \varepsilon_b - \varepsilon_r - \varepsilon_s} \quad (3.35)$$

where  $a, b$  and  $r, s$  correspond to occupied and virtual spinorbitals, respectively (see Eq. 3.12). Therefore the MP2 energy is finally given by a sum of two terms:

$$E_{MP2} = E_{HF} + E^{(2)} \quad (3.36)$$

MP $n$  methods (MP2 and higher orders: MP3, MP4, ...) are known to demonstrate an oscillatory convergence behavior while the MP $n$  energies can either underestimate or overestimate the exact energy (see Figure 3.1).

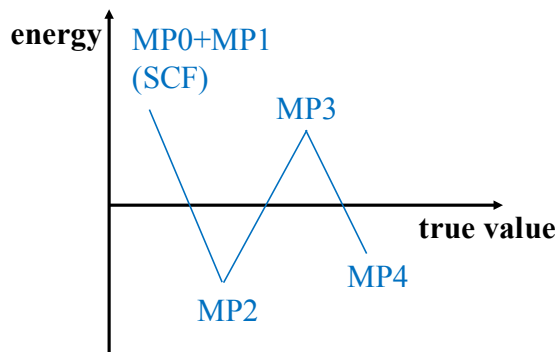


Figure 3.1: Oscillating convergence behavior of the total ground state energy obtained with MP $n$  methods. The true energy is the exact non-relativistic electronic energy in the Born-Oppenheimer approximation (Figure inspired from Ref. [12]).

## 3.2 Density Functional Theory

Another method, which can be seen as an extension of the Hartree-Fock method is the Density Functional Theory (DFT). Nowadays, it is one of the most extensively used methods in computational chemistry, due to its simplicity and good accuracy/cost ratio. DFT is based on the electron density  $\rho(\vec{r})$ , which replaces the wavefunction and contains the same information about the system. The electron density reads:

$$\rho(\vec{r}) = N \int \cdots \int |\Psi(\vec{x}_1, \vec{x}_2 \cdots \vec{x}_N)|^2 d\omega d\vec{x}_2 \cdots d\vec{x}_N \quad (3.37)$$

The state of  $\Psi$  is determined, as well as the probability of finding any of the  $N$  electrons within the volume element  $d\vec{r}$  with arbitrary spin and  $N - 1$  electrons with arbitrary positions and spins. The total number of electrons is obtained by integrating  $\rho(\vec{r})$  over the whole space:

$$N = \int \rho(\vec{r}) d\vec{r} \quad (3.38)$$

where  $\rho(\vec{r})d\vec{r}$  is the probability of finding any electron in the volume element  $d\vec{r}$  at the position  $\vec{r}$ , independent of the positions of the other electrons.

### 3.2.1 Hohenberg-Kohn Theorems

The theoretical basis for DFT was provided by Hohenberg and Kohn in 1964 [13], when they published their two theorems. According to the first Hohenberg-Kohn theorem: *the external potential  $V_{ext}(\vec{r})$  is determined, within a trivial additive constant, by the electron density  $\rho(\vec{r})$* . Consequently, the ground state energy can be written exactly as a functional of the electron density,  $E = E[\rho]$ :

$$E_0[\rho_0] = T_e[\rho_0] + E_{ee}[\rho_0] + E_{Ne}[\rho_0] \quad (3.39)$$

where  $T_e[\rho_0]$  is kinetic energy of electrons,  $E_{ee}[\rho_0]$  is the electron-electron interaction energy functional, and the external potential energy  $E_{Ne}[\rho_0]$  corresponds to the nuclei-electron attraction. All quantities can be written explicitly in terms of the ground state density  $[\rho_0]$ :

$$E_0[\rho_0] = \underbrace{T_e[\rho_0] + E_{ee}[\rho_0]}_{F_{HK}[\rho]} + \underbrace{\int \rho_0(\vec{r}) V_{Ne}(\vec{r}) d\vec{r}}_{\text{system dependent}} \quad (3.40)$$

The independent parts are gathered into a Hohenberg-Kohn functional ( $F_{HK}[\rho]$ ):

$$F_{HK}[\rho] = T_e[\rho] + E_{ee}[\rho] = \langle \Psi | \hat{T}_e + \hat{V}_{ee} | \Psi \rangle \quad (3.41)$$

If the functional  $F_{HK}$  was known, then  $E_0$  could also be known exactly. However, its explicit form is unknown. Thus, in order to solve this, the  $E_{ee}$  term has to be separated in two terms:

$$E_{ee}[\rho] = J[\rho] + E_{ncl}[\rho] = \frac{1}{2} \int \int \frac{\rho(\vec{r}_1)\rho(\vec{r}_2)}{r_{12}} d\vec{r}_1 d\vec{r}_2 + E_{ncl} \quad (3.42)$$

where  $J[\rho]$  is the classical Coulomb repulsion and  $E_{ncl}$  gathers the non-classical contributions of the self interaction, exchange, and electron correlation.

According to the second Hohenberg-Kohn theorem: *the correct ground state density of the system is the one that minimizes the total energy through the functional.* Based on this variational principle, any approximate electronic density  $[\tilde{\rho}]$ , associated with an external potential, gives always an energy that is greater or equal to the exact ground state energy:

$$E_0 \leq E[\tilde{\rho}] = T_e[\tilde{\rho}] + E_{ee}[\tilde{\rho}] + E_{Ne}[\tilde{\rho}] \quad (3.43)$$

### 3.2.2 Kohn-Sham Theory

In 1965, Kohn and Sham [14] realized that most of the problems in finding  $\rho(\vec{r})$  are related to defining an accurate functional for the kinetic energy. In order to solve this issue, they proposed introducing the idea of a fictitious system (KS scheme) build from a set of orbitals (one-electron functions), where the electrons are non-interacting. The electron density is expressed as the the sum of the squares of the occupied orbitals  $\psi_a(\vec{r})$  in the Kohn-Sham determinant:

$$\rho(\vec{r}) = \sum_a^N |\psi_a(\vec{r})|^2 \quad (3.44)$$

The total energy:

$$E[\rho(\vec{r})] = T_S[\rho(\vec{r})] + \int [\hat{V}_{ext}(\vec{r}) + \hat{J}(\vec{r})]\rho(\vec{r})d\vec{r} + E_{XC}[\rho] \quad (3.45)$$

where  $T_S[\rho(\vec{r})]$  corresponds to the kinetic energy of the non-interacting electrons,  $\hat{J}(\vec{r})$  represents the classical Coulomb interaction between the electrons and  $\hat{V}_{ext}(\vec{r})$  is the potential arising from the nuclei. The kinetic energy for a system of non-interacting electrons, which reproduce the true ground state density is expressed in terms of one electron functions:

$$T_S[\rho(\vec{r})] = -\frac{1}{2} \sum_a^N \langle \psi_a | \nabla^2 | \psi_a \rangle \quad (3.46)$$

where the  $|\psi_a\rangle$  are the Kohn-Sham orbitals. In addition, Kohn and Sham introduced a universal functional  $F[\rho(\vec{r})]$ :

$$F[\rho(\vec{r})] = T_S[\rho(\vec{r})] + J[\rho(\vec{r})] + E_{XC}[\rho(\vec{r})] \quad (3.47)$$

where  $E_{XC}$  is the exchange-correlation energy functional:

$$E_{XC}[\rho(\vec{r})] = T_c[\rho(\vec{r})] + E_{ncI}[\rho(\vec{r})] \quad (3.48)$$

where  $T_c[\rho(\vec{r})]$  is the residual part of the kinetic energy.  $E_{XC}$  encompasses all the other contributions to the energy which are not accounted for in the previous terms, such as the electron exchange, correlation energy and correction for the self-interaction included in the Coulomb term, as well as the portion of the kinetic energy which corresponds to the differences between the non-interacting and the real system.

### 3.2.3 Exchange-Correlations Functionals

Development of new functionals is an ongoing and active area of research. It is common to distinguish the exchange-correlation energy functional into a functional for exchange ( $X$ ) and a component for correlation ( $C$ ). The most simplified form for  $E_{XC}$  is given by the Local Density Approximation (LDA), where the exchange and correlation energies originate from the homogeneous electron gas:

$$E_{XC}^{LDA}[\rho] = \int \rho(\vec{r}) \varepsilon_{XC}[\rho(\vec{r})] d\vec{r} \quad (3.49)$$

where  $\varepsilon_{XC}$  is the exchange-correlation energy per particle. The example of the LDA functional is SVWN [15], which combines Slater exchange with Vosko, Wilk and Nusair correlation expressions. An improvement to LDA exchange-correlation functionals is the called Generalized Gradient Approximation (GGA). This approximation takes also into account the dependence with the gradient of the electronic density ( $\vec{\nabla}\rho(\vec{r})$ ):

$$E_{XC}^{GGA}[\rho] = \int \rho(\vec{r}) \varepsilon_{XC}[\rho(\vec{r}), \vec{\nabla}\rho(\vec{r})] d\vec{r} \quad (3.50)$$

GGA functionals achieve good results for ground state energies and dissociation energies or bond lengths. The examples of GGA XC are BLYP (Becke [16], Lee Yang and Parr [17]), PW91 (Perdew and Wang) or PBE (Perdew, Burke and Ernzerhof) functionals. The meta-GGA (mGGAs) functionals (*e.g.* TPSS, Tao, Perdew, Staroverov and Scuseria) are extension GGA's. They include Laplacian of the electron density or the local kinetic energy. Some properties are improved with respect to GGA, such atomic or H-bond dissociation energies.

Those types of functionals very poorly describe the exchange part, which is exactly defined by the HF form. Thus, Becke proposed a combination GGA XC with HF exchange, which is non-local and presents the exact  $-1/r$  asymptotic behavior. That strategy gives hybrid functionals with the most popular B3LYP XC [18, 19], called also global hybrids, because the % of the HF exchange is constant for any inter-electronic distances. In B3LYP, the three parameters were determined to best fit the experimental data. B3LYP classified as a hybrid exchange-correlation functional with 20% of HF exchange:

$$E_{XC}^{B3LYP} = (1 - a)E_X^{HF} + aE_X^{Slater} + bE_X^{Becke} + cE_C^{LYP} + (1 - c)E_c^{VWN} \quad (3.51)$$

where  $a = 0.80$ ,  $b = 0.72$  and  $c = 0.81$ .

The CAM-B3LYP functional [20] belongs to the class of range separated functionals, meaning that the exchange interaction is described by different mechanisms for short and long inter-electron distances (with 65% of HF). In long range corrected functionals the electron repulsion operator  $1/r_{12}$  split into short- and long- range part by applying a standard error function:

$$\frac{1}{r_{12}} = \frac{1 - \text{erf}(\mu r_{12})}{r_{12}} + \frac{\text{erf}(\mu r_{12})}{r_{12}} \quad (3.52)$$

where the first term is related to short-range interaction and is described with GGA functional, while the second term corresponds to the long-range interaction and combination with HF functional.  $\mu$  is a range-separation parameter. The CAM-B3LYP can be successfully applied for excitations energies with charge transfer calculations and also in estimating hyperpolarizabilities.

The long-range corrected BLYP (LC-BLYP) functional has also been used for calculating optical excitations and hyperpolarizabilities. [21] Some of these studies encompassed the tuning of the range separation parameter  $\mu$ . However, some previous studies evidenced that the long-range correction does not appear to be the key element to improve the description of hyperpolarizabilities by LC-DFT. Rather, the inclusion of substantial amounts of Hartree-Fock exchange, which reduces the many-electron self-interaction error, appears as responsible for the good results afforded by range separated hybrids. [22].

The M06 [23] functional belongs to the family of M05 [24] exchange functionals. M06 has 27% of HF exchange and M06-2X 54%, respectively. They are good functionals for main group of atoms, organometallics, kinetics, thermochemistry and non-covalent bonds. Many studies in the literature have shown the importance of the choice of the exchange correlation functionals for the calculations of nonlinear optical properties. (see e.g. [25])

In this thesis, the B3LYP and hybrid meta-generalized gradient-approximations (hybrid meta-GGAs) M06 functionals were used for structural geometry optimization.

M06-2X [23] (the same family as M06), CAM-B3LYP or B3PW91 [26] functionals were applied for predicting the linear and nonlinear optical properties.

### 3.3 Basis Sets

The basis sets of atomic orbitals are the sets of functions (called basis functions) that are used to represent the electronic wavefunction in all *ab initio* methods. The general equation for basis functions reads:

$$\eta = f(x, y, z) \exp(-\xi r^n) \quad (3.53)$$

where  $f(x, y, z)$  is a polynomial the atomic orbital is localized around the origin (0,0,0). In case of  $n = 1$ , we have Slater-type orbitals (STOs) [27], while  $n = 2$  we obtain the basis sets, which were proposed by Boys in 1950 [28], called Gaussian-type orbitals (GTOs). The Slater-type orbitals basis sets are not efficient to compute a large numbers of integrals, because of the expansion functions. Many years ago, replacing STOs by the Gaussian-type orbitals caused a great progress in quantum chemistry.

In order to decide on the type of the basis sets, the most essential factor is the number of functions to be used. In the *minimal basis set*, a single basis function is used for each atomic orbital on each free atom. The first improvement of the basis set consist in doubling the number of basis functions to produce a *double zeta* (DZ) type basis. The *triple zeta* (TZ) is the same as double one, but contains three times as many functions as the minimum basis. Also *quadruple zeta* (QZ), *quintuple zeta* (5Z) and so on. In most cases, in order to describe the electron correlation higher-angular momentum atomic orbitals are essential and those functionals are called *polarization functions*. Polarization functions are added to the chosen *sp*-basis. A single set of *p*-polarization functions can be added to the hydrogens (6-31G(p)) and *d*-functions on heavy atoms (6-31G(d, p)). Another common extension of the basis sets is the inclusion of *diffuse* functions, denoted by + (addition of four functions: s, p<sub>x</sub>, p<sub>y</sub>, p<sub>z</sub>, (6-31+G)) for each non-hydrogen atoms and ++ diffuse function added also to the light atoms (hydrogen and helium (6-31++G)).

In the frame of accurate prediction of the electron correlation a new category of basis sets has been developed: they are called *correlation consistent* basis sets, and are denoted as cc-pVXZ, where "cc" means correlation consistent, "p" indicates the polarization functions on all atoms, the VXZ stands for valence with the cardinal number X=D, T, Q ... indicates double-, triple- or quadruple- zeta. The diffuse functions are added by means of augmented correlation-consistent basis sets, aug-cc-pVXZ. Nevertheless in this thesis, in most cases the 6-311+G(d) or 6-311G(d) basis sets were used, because they are sufficient for the methods and systems which were studied.

### 3.4 Absorption Spectra Calculations

The development of the computer technology and the increased efficiency of the electronic structure methods allowed to simulate the absorption spectra. The computational UV-vis spectrum become a complementary tool to experimental measurements. In this thesis, the theoretical calculations have been performed by using time-dependent density functional theory (TDDFT).

TDDFT based on the Runge and Gross theorem (1984) [29] that the densities  $\rho(\vec{r}, t)$  and  $\rho'(\vec{r}, t)$  evolving from the same initial state  $\Psi_0 = \Psi(t = t_0)$  under the influence of the two potentials  $V(\vec{r}, t)$  and  $V'(\vec{r}, t)$  (both expandable in Taylor series around the initial time  $t = t_0$ ), are always different:

$$V(\vec{r}, t) - V^*(\vec{r}, t) \neq c(t) \quad (3.54)$$

The Runge-Gross theorem is a similar way to the Kohn-Sham construction for the ground state density (see Eq. 3.37). By construction, the density of the interacting system can be calculated from the Kohn-Sham orbitals:

$$\rho(\vec{r}, t) = \sum_a^N \psi_a^*(\vec{r}, t) \psi_a(\vec{r}, t) \quad (3.55)$$

In the time-dependent Kohn-Sham equation, the potential is written as the sum of the three terms:

$$V_{KS}[\rho](\vec{r}, t) = V_{ext}(\vec{r}, t) + J[\rho](\vec{r}, t) + V_{XC}[\rho](\vec{r}, t) \quad (3.56)$$

The first term is the external potential ( $V_{ext}(\vec{r}, t)$ ), whereas the second term accounts for the classical electrostatic interaction between the electrons:

$$J[\rho](\vec{r}, t) = \int d\vec{r}' \frac{\rho(\vec{r}', t)}{|\vec{r} - \vec{r}'|} \quad (3.57)$$

In the third term, the exchange correlation potential ( $V_{XC}[\rho](\vec{r}, t)$ ) includes all the nontrivial many-body effects and its extreme complex functional depends on the density. In the time-dependent KS equation, the exchange correlation potential by adiabatic local density approximation is given by:

$$V_{XC}[\rho](\vec{r}, t) = \frac{\delta E_{XC}[\rho(\vec{r}, t)]}{\delta \rho(\vec{r}, t)} \quad (3.58)$$

where  $E_{XC}[\rho](\vec{r}, t)$  is the exchange-correlation energy functional (see Eq. 3.48).

In the linear response theory, a small external perturbation (spin dependent)  $\delta V_{ext}(\vec{r}, \omega)$  induces a density response  $\delta \rho(\vec{r}, \omega)$  and this is linearly related to the density response

function  $\chi(\vec{r}, \vec{r}', \omega)$ :

$$\delta\rho(\vec{r}, \omega) = \int d\vec{r}' \chi(\vec{r}, \vec{r}', \omega) \delta V_{ext}(\vec{r}, \omega) \quad (3.59)$$

Also, induced change in the density can be calculated in the Kohn-Sham system by virtue of the Runge-Gross theorem:

$$\delta\rho(\vec{r}, \omega) = \int d\vec{r}' \chi_{KS}(\vec{r}, \vec{r}', \omega) \delta V_{KS}(\vec{r}, \omega) \quad (3.60)$$

where  $\chi_{KS}$  is the Kohn-Sham response function. Accordingly to the Eqs. 3.56, 3.57 and 3.58 the variation of the Kohn-Sham potential, reads:

$$\delta V_{KS}(\vec{r}, \omega) = \delta V_{ext}(\vec{r}, \omega) + \int d\vec{r}' \frac{\delta\rho(\vec{r}', \omega)}{|\vec{r} - \vec{r}'|} + \int d\vec{r}' \frac{\delta V_{XC}(\vec{r}')}{\delta\rho(\vec{r}')} \delta\rho(\vec{r}') \quad (3.61)$$

The idea of calculating excitation energies within the linear response regime of time-dependent density functional theory is based on the frequency-dependent linear density response of an interacting system has poles at the exact excitation energies of the system. For the interacting response function Dyson-like equation:

$$\begin{aligned} \chi(\vec{r}, \vec{r}'; \omega) &= \chi_{KS}(\vec{r}, \vec{r}'; \omega) + \int d\vec{r} \int d\vec{r}' \chi_{KS}(\vec{r}, \vec{r}'; \omega) \\ &\times \left[ \frac{1}{|\vec{r} - \vec{r}'|} + f_{XC}(\vec{r}, \vec{r}'; \omega) \right] \chi(\vec{r}, \vec{r}'; \omega) \end{aligned} \quad (3.62)$$

where  $f_{XC}(\vec{r}, \vec{r}'; \omega)$  is the time-dependent exchange-correlation kernel. The exchange-correlation kernel leads to corrections for the transitions from the KS values to the 'true' values, although the response of the ground-state KS part usually stays dominant.

Moreover, the linear response  $[\rho^1(\vec{r}, \omega)]$  obtained by the Fourier transformation, can be expressed in terms of summation over all possible single-excitations, where the  $P_{ra}(\omega)$  quantities are unknown:

$$\rho^1(\vec{r}, \omega) = \sum_a^{occ} \sum_r^{unocc} \psi_a^*(\vec{r}) \psi_r(\vec{r}) P_{ra}(\omega) + \psi_a(\vec{r}) \psi_a^*(\vec{r}) P_{ar}(\omega) \quad (3.63)$$

The variations of  $P$  can be expressed in terms of the variation in  $\nu^1$ , which contains the vector elements of the external perturbations at frequency  $\omega$ :

$$\begin{pmatrix} P(\omega) \\ P^*(\omega) \end{pmatrix} = \left[ \begin{pmatrix} A & B \\ B^* & A^* \end{pmatrix} - \omega \begin{pmatrix} 1 & 0 \\ 0 & -1 \end{pmatrix} \right]^{-1} \begin{pmatrix} -\nu^1(\omega) \\ \nu^{1,*}(\omega) \end{pmatrix} \quad (3.64)$$

where,

$$A_{ai,bj} = \delta_{ij} \delta_{ab} (\varepsilon_a - \varepsilon_i) + K_{ai,bj} \quad (3.65)$$

$$B_{ai,bj} = K_{ai,jb} \quad (3.66)$$

The  $A$  and  $B$  matrices are the dimensions  $(occ \times unocc) \times (occ \times unocc)$ . Only the single-excited states are treated when  $\omega$ -dependence of  $K$  is removed.  $K$  is the coupling matrix including a Coulomb term and an exchange correlation term:

$$K_{ai,bj} = \int d\vec{r} \int d\vec{r}' \psi_a^*(\vec{r}) \psi_i(\vec{r}) \left[ \frac{1}{|\vec{r} - \vec{r}'|} + f_{XC}(\vec{r}, \vec{r}') \right] \psi_b^*(\vec{r}') \psi_j(\vec{r}') \quad (3.67)$$

For TDDFT calculations of excitation energies is needed selection of an XC potential, in order to obtain ground state wavefunction, density or energy, as well as XC kernel for expressing the  $K$  matrix elements.

The vertical excitation energies of the system correspond to the poles of the linear response, when the matrix to invert is singular. The excitation energies are evaluated as a solution of a non-Hermitian equation:

$$(A - B)^{1/2}(A + B)(A - B)^{1/2}T = \omega^2 T \quad (3.68)$$

where  $T = (A - B)^{-1/2}(X + Y)$  The  $X$  and  $Y$  matrices are associated with the electronic excitations and deexcitations of the system. After obtaining the excitation energies from the  $X + Y$  matrices, the oscillator strengths  $f$  can be evaluated and often compared with the experimental line shapes of UV-vis spectrum (see Chapter 2).

The detailed procedure which allows to define the charge transfer (CT) model e.g. the CT distance, the transferred charge and the dipole moment variation has been described in Ref. [30].

## 3.5 Hyperpolarizability Calculations

Different quantum chemical approaches can be applied in order to predict and interpret the first hyperpolarizability. The time-dependent Hartee-Fock (TDHF), TDDFT and the Finite Field (FF) methods are presented in this section. Although other approaches also allow to evaluate the nonlinear optical properties, such a MP2, which the principle of the methodology have been described in previous section.

### 3.5.1 Time-Dependent Hartee-Fock

The Time-Dependent Hartee-Fock (TDHF) (1963) [31] method allows to determine analytically the successive dipole moment derivatives with respect to external electric fields, such as the first hyperpolarizabilities:

$$\beta_{ijk} = (-\omega_\sigma; \omega_1, \omega_2) = -2 \sum_{\mu, \nu}^K M_{\mu\nu}^i D_{\mu\nu}^{jk}(\omega_1, \omega_2) \quad (3.69)$$

where  $M_{\mu\nu}^i$  is the element of dipole moment matrix along the  $i$ -axis,  $D_{\mu\nu}^{jk}$  is the second-order derivatives of the density matrix with respect to the external oscillating fields oriented along the  $j$  and  $k$ -Cartesian axes and of pulsations  $\omega_1$  and  $\omega_2$  and  $\omega_\sigma = \omega_1, \omega_2$ . Now the HF equation (Eq. 3.24) is replaced by the time-dependent Hartee-Fock form:

$$FC = -i\frac{\partial}{\partial t}SC = SC\varepsilon \quad (3.70)$$

And matrices are determined:

$$C^\dagger SC = 1 \quad (3.71)$$

$$D = CnC^\dagger \quad (3.72)$$

$F$  is the the Fock matrix,  $C$  is the LCAO martix,  $S$  is the overlap matrix,  $D$  is the density matrix and  $\varepsilon$  is the energy matrix.  $n$  is a diagonal matrix with elements equal to 1 and 0 for an occupied and an unoccupied orbitals, respectively. In TDHF scheme, the first step is to consider two perturbations  $\lambda^i$  at pulsations  $\omega$  and  $-\omega$ , which are complex-conjugate of each other:

$$\lambda^i(\omega) = E^i e^{-i\omega t} \quad (3.73)$$

$$\lambda^i(-\omega) = E^i e^{i\omega t} = (\lambda^i(\omega))^* \quad (3.74)$$

where  $E_i$  is the amplitude and  $\omega$  its pulsation. The matrices are expanded in terms of power series expansions of both perturbations. The example of the LCAO matrix:

$$C(\omega) = C + \lambda^i(\omega)C^i(\omega) + \lambda^i(-\omega)C^i(-\omega) + \dots \quad (3.75)$$

$$C(\omega)^\dagger = C^\dagger + \lambda^i(-\omega)C^{i\dagger}(\omega) + \lambda^i(\omega)C^{i\dagger}(-\omega) + \dots \quad (3.76)$$

At first order, in the perturbation of Equations 3.70, 3.71 and 3.72, give:

$$F^i(\omega)C + FC^i(\omega) + \omega SC^i(\omega) = SC^i(\omega)\varepsilon + SC\varepsilon^i(\omega) \quad (3.77)$$

$$C^{i\dagger}(-\omega)SC + C^\dagger SC^i(\omega) = 0 \quad (3.78)$$

$$D^i(\omega) = C^i(\omega)nC^\dagger + CnC^{i\dagger}(-\omega) \quad (3.79)$$

Thus, the determination of  $D^i$  matrix requires the knowledge of the perturbed LCAO matrices  $C^i(\omega)$  and  $C^i(-\omega)$ . In order to do this, new unitary matrices,  $U^i(\omega)$  and  $U^i(-\omega)$ , are introduced:

$$C^i(\omega) = CU^i(\omega) \quad \text{and} \quad C^i(-\omega) = CU^i(-\omega) \quad (3.80)$$

by considering Eq. 3.71, and after inserting unitary matrices in Eq. 3.78, one gets:

$$U^{i\dagger}(-\omega)C^\dagger SC + C^\dagger SCU^i(\omega) = 0 \quad (3.81)$$

$$U^{i\dagger}(-\omega) + U^i(\omega) = 0 \quad (3.82)$$

Accordingly,

$$C^i(-\omega) = CU^i(-\omega) \Rightarrow C^i(-\omega) = -CU^{i\dagger}(\omega) \quad (3.83)$$

This relationship illustrates that For the  $D^i(\omega)$  matrix elements depend on the occ-occ and unocc-occ of the  $U^i(\omega)$  and  $U^i(-\omega)$  matrices:

$$D_{\mu\nu}^i(\omega) = \sum_{a=1}^{occ} \sum_{r=1}^{unocc} C_{\mu r} U_{ra}^i(\omega) C_{av}^\dagger + C_{\mu a} U_{ar}^{i\dagger}(-\omega) C_{rv}^\dagger \quad (3.84)$$

which are evaluated from the general expression:

$$C^\dagger F^i(\omega) C + \varepsilon U^i(\omega) + \omega U^i = U^i(\omega) \varepsilon + \varepsilon^i(\omega) \quad (3.85)$$

$$G_{ar}^i(\omega) + \varepsilon_a U_{ar}^i(\omega) + \omega U_{ar}^i(\omega) = U_{ar}^i(\omega) \varepsilon_r \quad (3.86)$$

where  $G_{ar}^i = (C^\dagger F^i(\omega) C)_{ia}$ . Finally:

$$U_{ar}^i(\omega) = \frac{G_{ar}^i(\omega)}{\varepsilon_r - \varepsilon_a - \omega} \quad (3.87)$$

Knowing  $U^i(\omega)$ , can determine the perturbed LCAO matrices  $C^i(\omega)$  can be evaluated and, as a consequence, the first-order derivative of the density matrices. The TDHF scheme is an iterative procedure, which means that uses an initial guess to generate a sequence of improving approximate solutions for a class of problems, in which the  $n^{th}$  approximation is derived from the previous ones.

The first hyperpolarizability, which is the third-order response of the energy with respect to the external field, can be determined by applying the '2n+1' rule [32], thus  $\beta$  became the first-order derivatives of the wavefunction:

$$\begin{aligned} \beta_{ijk} = & -Tr \left[ n \left\{ U^i G^j U^k + U^k G^j U^i + U^j G^k U^i + U^i G^k U^j + U^k G^i U^j + U^j G^i U^k + \right\} \right] \\ & - Tr \left[ n \left\{ U^i U^k \varepsilon^j + U^k U^i \varepsilon^j + U^j U^i \varepsilon^k + U^i U^j \varepsilon^k + U^k U^j \varepsilon^i + U^j U^k \varepsilon^i \right\} \right] \end{aligned} \quad (3.88)$$

The static limit of the electric field, the TDHF scheme reduces to the couple-perturbed Hartee-Fock (CPHF) method [33].

### 3.5.2 Time-Dependent Density Functional Theory

The first hyperpolarizability can be evaluated by using TDDFT method [34], which the detailed principle was presented is Section 3.4. In order to obtain  $\beta$ , the procedure is similar as in TDHF theory. The unitary matrix  $U$  is also used to evaluate the first order LCAO coefficient matrix (Eq. 3.80), which is obtained from

Eq. 3.87, where  $G_{KSar}^{(i)}(\omega)$  is replaced by the TDDFT counterpart:

$$G_{KSar}^{(i)}(\omega) = \langle \psi_a | \mu_i F_i(\omega) + V_{Coul}^{(i)} + V_{XC}^{(i)} | \psi_r \rangle \quad (3.89)$$

where all the matrix elements are evaluated by numerical integration. And similarly to TDHF, by applying '2n+1' rule, the first hyperpolarizability is obtained:

$$\begin{aligned} \beta_{ijk} = & -Tr \left[ n \left\{ U^i G^j U^k + U^k G^j U^i + U^j G^k U^i + U^i G^k U^j + U^k G^i U^j + U^j G^i U^k + \right\} \right] \\ & - Tr \left[ n \left\{ U^i U^k \varepsilon^j + U^k U^i \varepsilon^j + U^j U^i \varepsilon^k + U^i U^j \varepsilon^k + U^k U^j \varepsilon^i + U^j U^k \varepsilon^i \right\} \right] \\ & + Tr(g_{XC} D^{(a)} D^{(b)} D^{(c)}) \end{aligned} \quad (3.90)$$

where  $g_{XC}$  is the exchange-correlation kernel related with the second-order response functions of the time-dependent exchange-correlation potential with respect to the TD density.

In the literature the TDDFT approach showed a good results for computing molecular hyperpolarizabilities [35] without being computationally demanding compared to high level correlated methods. However, the critical point is the choice of an appropriate functional. As mentioned before, functionals with a significant amount of HF exact exchange like M06-2X should be selected.

### 3.5.3 Finite Field Method

The optical response can be also determined by applying a numerical technique, the Finite Field (FF) (1965) [36], where different tensor components, like the first hyperpolarizability, can be determined as a derivatives of the dipole moment or of the energy with respect to the external electric field (see also Chapter 1, Eq. 1.3), according to the expression:

$$\begin{aligned} \beta &= - \left( \frac{\partial^3 W}{\partial \vec{E}^3} \right)_{\vec{E}=0} = - \lim_{E \rightarrow 0} \frac{W(2\vec{E}) - W(-2\vec{E}) - 2[W(\vec{E}) - W(-\vec{E})]}{2\vec{E}^3} \\ &= - \left( \frac{\partial^2 \mu}{\partial \vec{E}^2} \right)_{\vec{E}=0} = - \lim_{\mu \rightarrow 0} \frac{\mu(\vec{E}) + \mu(-2\vec{E}) - 2\mu(0)}{2\vec{E}^2} \end{aligned} \quad (3.91)$$

where  $W(\vec{E})$  is the energy of the system computed in the presence of an electric field of strength  $\vec{E}$ . An intermediate approach combines the analytical and numerical derivatives if the second derivatives of the energy is obtained as the first derivatives of the dipole moment  $\mu$ . The finite field method has some limits and drawbacks. It is limited to the calculation of static response properties, because time-dependent fields are too complicated to be handled in a straightforward manner. Another problem is that calculated FF properties need further refinements to eliminate contributions from the higher-order derivatives in the Taylor expansion. In order to remove higher-

order contamination in the FF differentiation, the Romberg procedure (1927) [37, 38] has been applied with field amplitudes:

$$\beta_k^n = \frac{4^n \beta_k^{n-1} - \beta_{k+1}^{n-1}}{4^n - 1} \quad (3.92)$$

where  $k$  defines the field amplitudes  $\vec{E}_k = \vec{E}_0 2^{k-1}$  and  $n$  is the order of the iteration. The Romberg procedure based on the different sets of the electric field amplitudes, which are calculated by using a triangle. This procedure can support monitoring of the convergence of numerical differentiations (see Figure 3.2).

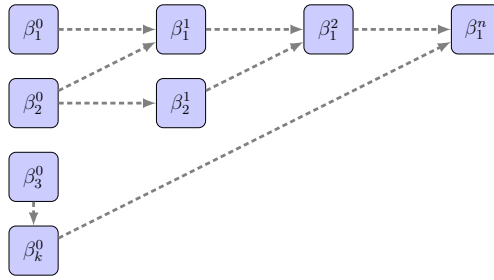


Figure 3.2: Scheme of the Romberg's procedure.

The finite field method is a fast and easy to implement numerical technique that is widely used for calculating the static dipole polarizabilities and hyperpolarizabilities of molecules and polymers. This method is broadly applicable at many levels of approximations, including MP2.

### 3.5.4 Sum-Over-States Method and The Two-State Model

$\beta$  can also be evaluated using the SOS (Sum-Over-States) perturbation theory method. In such a case  $\beta$  is expressed as a function of spectroscopic quantities ( $\Delta E, \mu, \Delta\mu$ ). For instance  $\alpha$  is calculated by evaluating the transition dipoles ( $\mu_i^{0n}$ ) and the excitation energies ( $E_n^0 - E_0^0$ ) for all the excited states in the molecule.

$$\alpha_{ij} = 2 \sum_{n \neq 0} \frac{\langle 0 | \mu_i | n \rangle \langle n | \mu_j | 0 \rangle}{E_n^0 - E_0^0} = 2 \sum_{n \neq 0} \frac{\mu_i^{0n} \mu_j^{n0}}{E_n^0 - E_0^0} \quad (3.93)$$

The  $\beta$  expression is slightly more complex:

$$\beta_{ijk} = \sum_{n, m \neq 0} \frac{\langle 0 | \mu_i | n \rangle \langle n | \mu_j | m \rangle \langle m | \mu_k | 0 \rangle}{(E_n^0 - E_0^0)} - \langle 0 | \mu_i | 0 \rangle \sum_n \frac{\langle \mu_j | n \rangle \langle n | \mu_k | 0 \rangle}{[E_n^0 - E_0^0]^2} \quad (3.94)$$

The SOS expressions are very appealing for interpreting the  $\beta$  responses but, in many cases, the summations (in Eqs. 3.93 and 3.94) converge slowly. In particular, provided the expansion functions do not cover the energy continuum, the result is incomplete. The above expressions concern the static quantities but they can easily be extended to the dynamic ones, as well as to account for damping of the

response (the finite time of the excited states). In the case of push-pull  $\pi$ -conjugated compounds Oudar and Chemla [39] showed that one low-energy charge-transfer excited state often provides a dominant contribution to  $\beta$ . The two-state simplified expression can be used to describe the frequency dispersion of  $\beta$  and, in particular, to extrapolate dynamic  $\beta$  values measured typically at 1064 nm to the static limit or to another wavelength.

The frequency dispersion factor  $F(\Delta E_{ge}, \omega, \Gamma)$  reads:

$$F(\Delta E_{ge}, \omega, \Gamma) = \frac{\beta(-2\omega; \omega, \omega)}{\beta(0; 0, 0)} = \frac{\Delta E_{ge}^2 (\Delta E_{ge} - i\Gamma)^2}{\left([\Delta E_{ge} - i\Gamma]^2 - (\hbar\omega)^2\right) \left([\Delta E_{ge} - i\Gamma]^2 - 4(\hbar\omega)^2\right)} \quad (3.95)$$

where  $\Delta E_{ge}$  is the dipole-allowed excitation energy,  $\hbar\omega$  is the photon energy of the incident beam and  $\Gamma$  the homogeneous damping parameter. A typical value for  $\Gamma$  is  $1000 \text{ cm}^{-1}$ .

### 3.6 Solvent Effects

There are two fundamentally different ways to take into account the solvent effects: the implicit and the explicit methods. Continuum approaches or implicit solvent models are the most commonly used. These include Onsager (1936) [40] reaction field model or the more sophisticated polarizable continuum model (PCM) [41] in its integral equation formalism (IEF-PCM) [42]. The discrete or explicit solvent models begin usually with a MD simulation step where the solvent molecules, represented explicitly, are distributed around the solute molecules. Then, for selected snapshots, the properties of the solute and its solvent environment are calculated using supermolecular approaches or embedding schemes. Such discrete solvation treatments are especially useful when hydrogen bonds between the solute and the solvent play an important role. In addition, continuum and discrete models can be mixed together to form so-called semi-continuum model or quantum mechanical/molecular mechanical (QM/MM) method.

In PCM models the solvents environment is represented by a homogeneous dielec-

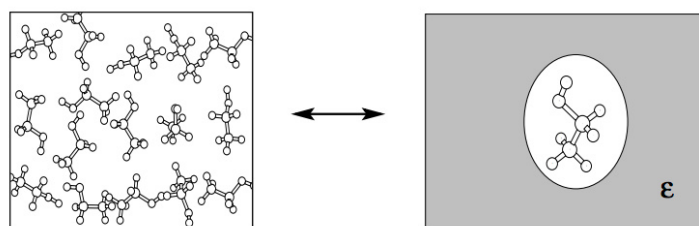


Figure 3.3: Discrete models (right) versus continuum (left) for solutions.

tric characterized by its dielectric constant  $\varepsilon$ , while the solute molecule is immersed inside a cavity and is described by using quantum chemistry methods. The cavity is defined as interlocking atomic spheres with radius close to the van der Waals values. The physical picture of the electrostatic solute-solvent interactions is simple: 1°) the charge distribution of the solute polarizes the dielectric continuum; this polarization is described by (partial) charges on the surface of the cavity, 2°) in turn these charges polarize the solute and its wavefunction; 3°) the new solute charges polarize the solvent and so on until 4°) the equilibrium is reached. Going into some details, the surface density reads:

$$\sigma(\vec{s}) = -\frac{\varepsilon - 1}{4\pi\varepsilon} \vec{E} \cdot \vec{n} \quad (3.96)$$

where  $\vec{E}$  is the total electric field evaluated on the surface of the cavity and  $\vec{n}$  is a unitary vector perpendicular to the outside surface. The total electric field has two components: one depending on the charge distribution of the solute  $\rho_S(\vec{r})$  and the second relative to the apparent surface charge  $\sigma(\vec{s})$  related to the solvent:

$$\sigma(\vec{s}) = -\frac{\varepsilon - 1}{4\pi\varepsilon} (\vec{E}_\rho + \vec{E}_\sigma) \cdot \vec{n} \quad (3.97)$$

This formula can be rewritten by considering the directional derivatives of the electrostatic potential:

$$\sigma(\vec{s}) = -\frac{\varepsilon - 1}{4\pi\varepsilon} \frac{\partial}{\partial \vec{n}} (V_\rho + V_\sigma) \quad (3.98)$$

where

$$V_\rho(\vec{r}) = \int \frac{\rho_S(\vec{r}')}{|\vec{r}' - \vec{r}|} d\vec{r}' \quad (3.99)$$

The cavity of the surface is approximated in terms of a set of finite elements, called tesserae.  $\sigma(\vec{s})$  is considered constant within each tesserae, so that the corresponding  $q_k$  charge is given by product of that density  $\sigma(\vec{s}_k)$  by the area of the tesserae  $A_k$ . Consequently, the potential becomes:

$$V_\sigma(\vec{r}) = \sum_k \frac{\sigma(\vec{s}_k) A_k}{|\vec{r} - \vec{s}_k|} = \sum_k \frac{q_k}{|\vec{r} - \vec{s}_k|} \quad (3.100)$$

The explicit solvent models molecules are more expensive but also more accurate, because they account for specific solute-solvent interactions, while the implicit solvent models are faster and, to a given extent, less precise because the solvent is described by a dielectrics.

## 3.7 Molecular Dynamics Simulations

Molecular Dynamics (MD) (originally developed in the late 1950s) [43–45] is a computer simulation technique, in which the time evolution of a set of interacting atoms can be followed by integrating their equations of motion. In many aspects,

the MD simulations can imitate the real experiment. This technique was developed to enable studies of the properties of material volumes containing even billions of atoms with effective inter atomic potential.

There exist two different kind of the MD, which could be categorized as an *ab initio* MD and a classical MD. In *ab initio* MD method the electronic behavior can be obtained from the first principles by using a quantum mechanical methodology, such a DFT. Although *ab initio* calculations provide important information that is not available from classical MD methods, such as density of electronic states and chemical reactions, but due to the cost of treating the electronic degrees of freedom, the computational cost of this simulation is much higher than classical MD. Consequently, *ab initio* MD is limited to smaller systems and shorter periods of time. The classic MD technique consists of the numerical solution of the classical equations of motion. The force field defines the potential energy  $V(\vec{R})$  of the acting on atom  $A$ :

$$\vec{F}(\vec{R}_A) = -\Delta V(\vec{R}_A) \quad (3.101)$$

From Newton's second law:

$$\vec{F}(\vec{R}_A) = M_A \vec{a}_A = M_A \frac{d^2 \vec{R}_A(t)}{dt^2} \quad (3.102)$$

where  $M_A$  is the mass of the atom,  $t$  is the time and  $\vec{a}_A$  is the acceleration of the molecule. The simplest and the most used solution for this equation of motion is Verlet algorithm [46]. The basic formula for this algorithm is derived from the Taylor expansions for the positions ( $\vec{R}_A(t)$ ):

$$\vec{R}_A(t + \Delta t) = 2\vec{R}_A(t) - \vec{R}_A(t - \Delta t) + \vec{a}(t)\Delta t^2 \quad (3.103)$$

It can be accurate up to terms of the fourth power in  $\Delta t$ . Velocities can be calculated from the positions or propagated explicitly as in alternative velocity Verlet schemes [47], which are determined:

$$\vec{R}_A(t + \Delta t) = \vec{R}_A(t) + \vec{v}_A(t)\Delta t + \frac{\vec{a}(t)}{2}\Delta t^2 \quad (3.104)$$

$$\vec{v}_A(t + \Delta t) = \vec{v}_A(t) + \frac{\vec{a}(t + \Delta t) + \vec{a}(t)}{2}\Delta t \quad (3.105)$$

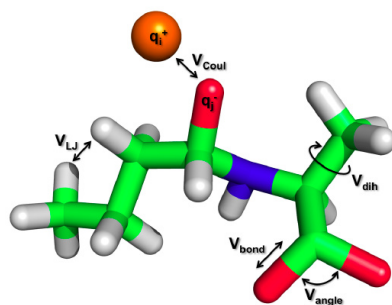
Thus, the position of the atoms  $\vec{R}_A$ , velocities  $\vec{v}_A$  and other dynamical information at time  $t$  can be attempted to obtain the new positions at the later time  $t + \Delta t$ .

In MD procedure, each atom move with a constant velocity  $\vec{v}$  in the time step  $\Delta t$ , and the new position  $\vec{R}'$  can be produced. Then the potential energy, forces and the velocities are calculated for a new position. This is repeated for a great number of a time steps. The positions and velocities evolve with time and the trajectory of the system can be used to calculate the macroscopic observables by time-averaging.

## Force Field Parametrization

In classical MD, the main interactions between particles are described by the parametrization of so-called Force Field (FF). A force consists of data specifying charges of atoms, bonded and non-bonded parameters. Different sets of parameters are available, but in this thesis the AMBER force field [43] has been used. There are also many tools available for carrying out molecular dynamics simulation such as GROMACS [48], CHARMM [49] and many more, but here NAMD [50] was employed. The potential energy that includes the intra- and inter-molecular interactions can be modeled approximately by a classical molecular mechanical force field with the following form:

$$\begin{aligned}
 V(R) &= V_{bond} + V_{angle} + V_{torsion} + V_{vdw} + V_{elect} \\
 &= \sum_{bonds} \frac{1}{2} k_l (l - l_{eq})^2 \\
 &+ \sum_{angles} \frac{1}{2} k_\theta (\theta - \theta_{eq})^2 \\
 &+ \sum_{dihedrals} \frac{V_n}{2} (1 + \cos(n\Phi - \delta)) \\
 &+ \sum_{pairs_{A,B}} 4\epsilon_{AB} \left[ \left( \frac{\sigma_{AB}}{R_{AB}} \right)^{12} - \left( \frac{\sigma_{AB}}{R_{AB}} \right)^6 \right] + \frac{q_A q_B}{R_{AB}}
 \end{aligned}$$



The bonded energy terms describe bond stretching ( $V_{bond}$ ), angle bending ( $V_{angle}$ ) and torsion around dihedral angles ( $V_{torsion}$ ). The non-bonded terms are the van der Waals interaction ( $V_{vdw}$ ) and electrostatic ( $V_{elect}$ ) potentials. Where,  $l_{eq}$  and  $\theta_{eq}$  are the equilibration bond length and the bond angle parameters. The parameters  $k_l$  and  $k_\theta$  are the force constant. The torsion potential is described by multiplicity  $n$ , its barrier height  $V_n$  and its phase  $\delta$ . Non-bonded energies are calculated using two terms, the first is the Leonard-Jones (LJ) term describing the van der Waals interaction. The particles at a certain distance  $R$  from each other are initially attracted towards each other and are then abruptly repelled, where  $1/R^{12}$  is the repulsion term and  $1/R^6$  is the attraction term. The  $\epsilon_{AB}$  governs the strength of the interaction and the  $\sigma_{AB}$  defines a length scale related to the equilibrium separation of a pair of atoms. The energy potential curve of the LJ potential is presented in Figure 3.4 on the left.

The second non-bonded term is the Coulomb interactions dealing with the electrostatic interactions of partial charges of the atoms  $q_{A,B}$ . In fact, the most time consuming step in MD simulations is calculation of the non-bonded interactions. In order to reduce the number of particles pairs that need to be calculate, the Periodic Boundary Conditions (PBC) can be applied. PBC is one the most widely used method, which allows to simulate properties of materials by using only a few thousands of atoms. PBC means that atom which passes over the cell boundary comes

back on the other side. Imposing PBC to the simulated system is exactly replicated in three dimensions and providing a periodic lattice. In general, concerned with molecular systems with a size much larger than the system can be afford to simulate. The implementations of the periodic boundary conditions reduces the computational costs of a simulations because computations involves intermolecular separations greater than the length of the computational box are not included (see Figure 3.4 on the right).

A common rule used in periodic boundary conditions is a neighbor list method, in which around a particular atom exists the cutoff radius  $r_{cut}$ , which truncates non-bonded interactions. Outside the potential cutoff sphere, a larger sphere radius is constructed for including a rest of all the neighbor atoms. In MD, beyond  $r_{cut}$  particles simply do not see each other. However, in case of long range Coulomb atomic interaction the cutoff radius can not be applied. In 1921 Ewald [52] proposed the idea of transforming the full Coulomb potential into two quickly-converging terms that can be evaluated in real space and Fourier space. Therefore, the Ewald summation provides a practical approach for evaluating long-range electrostatic potentials. Unfortunately, its computational cost is on the order of  $M^2$  or  $M^{3/2}$  and the method becomes very inefficient for stimulating large systems. Then, the Particle Mesh Ewald (PME) method [53, 54] was developed to improve the performance of the conventional Ewald summation. In PME, the atomic charges are interpolated on grid points which are then transformed by using the fast Fourier transformation algorithm and the computational cost of the PME method becomes on the order  $M \cdot \log M$ . Therefore, the PME method is much more efficient than the conventional Ewald summation, and has so been widely used in large-scale MD.

### Microcanonical and Canonical Ensembles

An Ensemble is a theoretical tool which is used for analyzing the evolution of the thermodynamic system. MD simulations generate sequence of points in space as a function of time which belong to the same ensemble. They correspond to the different conformations of the system, which an be distinguish:

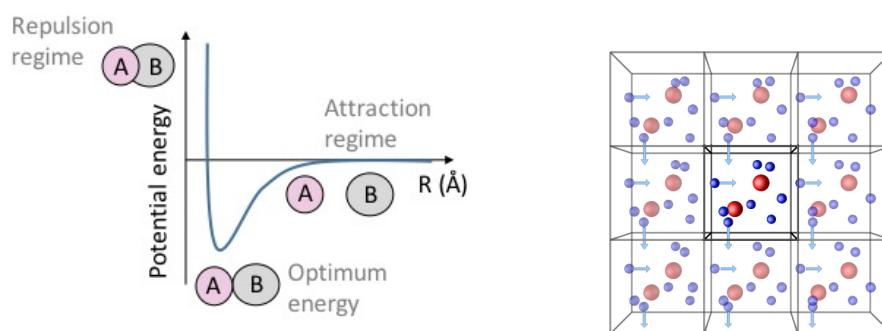


Figure 3.4: Schematic of Leonard-Jones potential of a single pair of atoms (left) and the periodic boundary conditions in the simulation box (right, inspired from [51]).

- canonical ensemble (NVT) is a thermodynamically non isolated system- constant the number of the particles (N), the volume (V) and the temperature (T). Energy is exchanged with a thermostat.
- microcanonical ensemble (NVE) is a thermodynamically isolated system- fixed number of atoms (N), the volume (V) and the energy (E) of the system.
- (NPT) ensemble- constant the number of the particles (N) the pressure (P) and the temperature (T). The mechanism to keep the pressure and temperature constant is the barostat and the thermostat, respectively.

Based on the positions and velocities it is possible to calculate statistical quantities such as temperature. Temperature is a statistical quantity which has to be expressed as a function of position and momenta of all particles in the system. For a system containing large enough number of atoms the temperature can be estimated from the kinetic energy:

$$\left\langle \frac{1}{2}mv^2 \right\rangle = \frac{1}{2}M_f k_B T \quad (3.106)$$

where  $M_f$  is the number of the degree of freedom in the system with  $M$  particles (atoms) and  $k_B$  is a Boltzmann constant. Temperature depends on time because positions and velocities depend on time:

$$T(t) = \sum_{A=1}^M \frac{m_A v_A^2(t)}{k_B M_f} \quad (3.107)$$

And the pressure of a pair potential is determined:

$$PV = M k_B T + \frac{1}{3} \left\langle \sum_{A \neq B}^M r_{AB} \cdot f_{AB} \right\rangle \quad (3.108)$$

where  $r_{AB}$  and  $f_{AB}$  is the force on particle  $A$  exerted by particle  $B$ .

Thus, MD allows to study interactions on a microscopic level, such as the influence of ions on the stability of a biomolecule, and their coordination behavior towards a solute. Techniques like selective deprotonation or protonation of side chains can be applied to investigate protein stability as a function of charge distribution along the molecule. The number of applications of MD simulation is large, and with increasing computer power this number will become even larger.

# Bibliography

---

- [1] E. Schrödinger. An undulatory theory of the mechanics of atoms and molecules. *Phys. Rev.*, **28**(6):1049–1070, 1926.
- [2] E. Schrödinger. *Collected papers on wave mechanics*. Blackie and Son Limited, 1928.
- [3] M. Born and R. Oppenheimer. Zur quantentheorie der molekeln. *Annalen der Physik*, **389**(20):457–484, 1927.
- [4] W. Heisenberg. Über quantentheoretische umdeutung kinematischer und mechanischer beziehungen. *Z. Phys.*, **38**:411–426, 1926.
- [5] P. A. M. Dirac. On the theory of quantum mechanics. *Proc. R. Soc. Lond. A*, **100**:661–677, 1926.
- [6] W. Pauli. Über den zusammenhang des abschlusses der elektronengruppen im atom mit der komplexstruktur der spektren. *Z. Phys.*, **31**:765–783, 1925.
- [7] J. C. Slater. The theory of complex spectra. *Phys. Rev.*, **34**:1293–1322, 1929.
- [8] V. Fock. Bemerkung zum virialsatz. *Z. Phys.*, **61**:126–148, 1930.
- [9] D. R. Hartree. The wave mechanics of an atom with a non-coulomb central field. part i. theory and methods. *Proc. Cambridge Phil. Soc.*, **24**:89–132, 1928.
- [10] C. C. J. Roothaan. New developments in molecular orbital theory. *Rev. Mod. Phys.*, **23**:69–89, 1951.
- [11] G. G. Hall. The molecular orbital theory of chemical valency. viii - a method of calculating ionization potentials. *Proc. Roy. Soc. (London) Ser. A*, **205**(6):541, 1951.
- [12] D. Cremer. Møller-Plesset perturbation theory: From small molecule methods to methods for thousands of atoms. *Comp. Mol. Sci.*, **1**(4):509–530, 2011.
- [13] P. Hohenberg and W. Kohn. Inhomogeneous electron gas. *Phys. Rev.*, **136**:864–871, 1964.

- 
- [14] W. Kohn and L. J. Sham. Self-consistent equations including exchange and correlation effects. *Phys. Rev.*, **140**:1133–1138, 1965.
- [15] S. H. Vosko, L. Wilk, and M. Nusair. Accurate spin-dependent electron liquid correlation energies for local spin density calculations: a critical analysis. *Canadian J. Phys.*, **58**(8):1200–1211, 1980.
- [16] A. D. Becke. Density-functional exchange-energy approximation with correct asymptotic behavior. *Phys. Rev. A*, **38**(6):3098–3100, 1988.
- [17] C. Lee, W. Yang, and R. G. Parr. Development of the Colle-Salvetti correlation-energy formula into a functional of the electron density. *Phys. Rev. B*, **37**(2):785–789, 1988.
- [18] A. D. Becke. Density-functional thermochemistry. III. The role of exact exchange. *J. Chem. Phys.*, **98**(7):5648–5652, 1993.
- [19] P. J. Stephens, F. J. Devlin, C. F. Chabalowski, and M. J. Frisch. Ab initio calculation of vibrational absorption and circular dichroism spectra using density functional force fields. *J. Phys. Chem.*, **98**(45):11623–11627, 1994.
- [20] T. Yanai, D. P. Tew, and N. C. Handy. A new hybrid exchange-correlation functional using the Coulomb-attenuating method (CAM-B3LYP). *Chem. Phys. Lett.*, **393**(1-3):51–57, 2004.
- [21] L. E. Johnson, L. R. Dalton, and B. H. Robinson. Optimizing calculations of electronic excitations and relative hyperpolarizabilities of electrooptic chromophores. *Acc. Chem. Res.*, **47**(11):3258–3265, 2014.
- [22] A. J. Garza, N. A. Wazzan, A. M. Asiri, and G. E. Scuseria. Can short- and middle-range hybrids describe the hyperpolarizabilities of long-range charge-transfer compounds? *J. Phys. Chem. A*, **118**(50):11787–11796, 2014.
- [23] Y. Zhao and D. G. Truhlar. The M06 suite of density functionals for main group thermochemistry, thermochemical kinetics, noncovalent interactions, excited states, and transition elements: two new functionals and systematic testing of four M06-class functionals and 12 other functionals. *Theor. Chem. Acc.*, **120**:215–241, 2008.
- [24] Y. Zhao, N. E. Schultz, and D. G. Truhlar. Exchange-correlation functional with broad accuracy for metallic and nonmetallic compounds, kinetics, and noncovalent interactions. *J. Chem. Phys.*, **123**(16):1–4, 2005.
- [25] S. J. A. Van Gisbergen, J. G. Snijders, and E. J. Baerends. Accurate density functional calculations on frequency-dependent hyperpolarizabilities of small

- molecules Accurate density functional calculations on frequency-dependent hyperpolarizabilities of small molecules. **109**(124), 1988.
- [26] J. P. Perdew and Y. Wang. Accurate and simple analytic representation of the electron-gas correlation energy. *Phys. Rev. B*, **45**(23):244–249, 1992.
- [27] W. J. Hehre, R. F. Stewart, and J. A. Pople. Self-consistent molecular-orbital methods. I. Use of gaussian expansions of slater-type atomic orbitals. *J. Chem. Phys.*, **51**(6):2657–2664, 1969.
- [28] S. F. Boys. Electronic wave functions. I. a general method of calculation for the stationary states of any molecular system. *Proceedings of the Royal Society A: Mathematical, Physical and Engineering Sciences*, **200**(1063):542–554, 1950.
- [29] E. Runge and E. K.U. Gross. Density-functional theory for time-dependent systems. *Phys. Rev. Lett.*, **52**(12):997–1000, 1984.
- [30] D. Jacquemin, T. L. Bahers, C. Adamo, and I. Ciofini. What is the best atomic charge model to describe through-space charge-transfer excitations? *Phys. Chem. Chem. Phys.*, **14**(16):5383, 2012.
- [31] M. A. Ball and McLachlan A. D. Time-dependent Hartree-Fock theory. II. The electron-pair bond. *Mol. Phys.*, **7**:501–513, 1963.
- [32] J. N. Silverman and J. C. van Leuven. Perturbational-variational approach to the calculation of variational wavefunctions. I. theory. *Phys. Rev.*, **162**:1175–1182, 1962.
- [33] P. W. Langhoff, M. Karplus, and R. P. Hurst. Approximations to Hartree-Fock perturbation theory. *J. Chem. Phys.*, **44**:505–514, 1966.
- [34] S. J. A. van Gisbergen, J. G. Snijders, and E. J. Baerends. Calculating frequency-dependent hyperpolarizabilities using time-dependent density functional theory. *J. Chem. Phys.*, **2**:10644–10656, 1998.
- [35] N. Kobko, A. Masunov, and S. Tretiak. Calculations of the third-order nonlinear optical responses in push-pull chromophores with a time-dependent density functional theory. *Chem. Phys. Lett.*, **392**(4-6):444–451, 2004.
- [36] H. D. Cohen and C. C. Roothan. Electric dipole polarizability of atoms by the hartree-fock method. i. theory for closed-shell systems. *J. Chem. Phys.*, **43**:S34–S38, 1965.
- [37] L. F. Richardson and J. A. Gaunt. Philosophical transactions of the Royal Society of London. Series A, Containing papers of a mathematical or physical character. **344**:299–349, 1927.

- 
- [38] M. De Wergifosse, V. Liégeois, and B. Champagne. Evaluation of the molecular static and dynamic first hyperpolarizabilities. *Int. J. Quant. Chem.*, **114**(14):900–910, 2014.
- [39] J. L. Oudar and D. S. Chemla. Hyperpolarizabilities of the nitroanilines and their relations to the excited state dipole moment. *J. Chem. Phys.*, **66**(6):2664–2668, 1977.
- [40] L. Onsager. Electric moments of molecules in liquids. *J. Am. Chem. Soc.*, **58**:1486–1492, 1936.
- [41] S. Mietus, E. Scrocco, and J. Tomasi. Electrostatic interaction of a solute with a continuum. a direct utilization of ab initio molecular potentials for the prevision of solvent effects. *J. Chem. Phys.*, **55**:117–129, 1981.
- [42] B. Mennucci, R. Cammi, and J. Mennucci. Medium effects on the properties of chemical systems: Electric and magnetic response of donor-acceptor systems within the polarizable continuum model. *Int. J. Quantum Chem.*, **75**(4-5):767–781, 1999.
- [43] E. Fermi, J. Pasta, and S. Ulam. Studies of nonlinear problems. *Los Alamos report LA-1940*, 1955.
- [44] B. J. Alder and T. E. Wainwright. Studies in molecular dynamics. I. General method. *J. Chem. Phys.*, **31**:459–466, 1959.
- [45] B. J. Alder and T. E. Wainwright. Studies in molecular dynamics. II. Behavior of a small number of elastic spheres. *J. Chem. Phys.*, **33**(5):1439–1451, 1960.
- [46] L. Verlet. Computer experiments on classical fluids. I. Thermodynamical properties of Lennard-Jones molecules. *Phys. Rev.*, **159**(5):1, 1967.
- [47] W. C. Swope, H. C. Andersen, P. H. Berens, and K. R. Wilson. A computer simulation method for the calculation of equilibrium constants for the formation of physical clusters of molecules: Application to small water clusters. *J. Chem. Phys.*, **76**(1):637–649, 1982.
- [48] D. Van Der Spoel, E. Lindahl, B. Hess, G. Groenhof, A. E. Mark, and H. J. Berendsen. GROMACS: fast, flexible, and free. *J. Comput. Chem.*, **26**:1701–1718, 2005.
- [49] B. R. Brooks, R. E. Bruccoleri, B. D. Olafson, D. J. States, S. Swaminathan, and M. Karplus. CHARMM: A program for macromolecular energy, minimization, and dynamics calculations. *J. Comput. Chem.*, **4**:187–217, 1983.

- [50] M. Nelson, W. Humphrey, R. Kufrin, A. Gursoy, A. Dalke, L. Kale, R. Skeel, and K. Schulten. MDSCOPE- a visual computing environment for structural biology. *Comput. Phys. Comm.*, **4**:111–133, 1995.
- [51] Model box periodic boundary conditions - p.b.c. <http://isaacs.sourceforge.net/phys/psc.html>, 2018.
- [52] P. P. Ewald. Die Berechnung optischer und elektrostatischer Gitterpotentiale. *Annalen der Physik*, **369**(3):253–287, 1921.
- [53] R. W. Hockney and J. W. Eastwood. *Computer simulation using particles*. McGraw-Hill, NY., 1981.
- [54] T. Darden, L. Perera, L. Li, and P. Lee. New tricks for modelers from the crystallography toolkit: The particle mesh Ewald algorithm and its use in nucleic acid simulations. *Structure*, **7**(3):55–60, 1999.

# Second-Order Nonlinear Optical Properties of Indolino-Oxazolidine Derivatives

K. Pielak, F. Bondu, L. Sanguinet, V. Rodriguez, B. Champagne and F. Castet.  
*J. Phys. Chem. C* **121**:1851-1860, 2017.

*In this chapter the linear and nonlinear optical properties of two novel indolinooxazolidine derivatives acting as multiaddressable switches are presented. The second-order hyperpolarizability contrasts upon commutation between their non conjugated closed (CF) and a  $\pi$ -conjugated open (POF) forms were characterized using hyper-Rayleigh scattering measurements, and rationalized by means of density functional theory and post Hartree-Fock ab initio calculations. The study was conducted for compounds bearing two different substituents on the indolinoxazolidine moiety, namely **1**:  $R=CH_3$ , and **2**:  $R=NO_2$ . The HRS experiments and theoretical calculations showed that the addition of a withdrawing substituent on the indolinic subunit leads to a more effective photoinduced charge transfer while decreasing the transition energy of the  $S_0 \rightarrow S_1$  transition, which induces a significant enhancement of the HRS response of the open form. This substitution is however detrimental to the NLO contrast, due to the concomitant increase of the HRS response of the closed form.*

In this chapter, I was responsible for the all theoretical calculations and carried out the HRS experiments of compound **2**.

## 4.1 Introduction

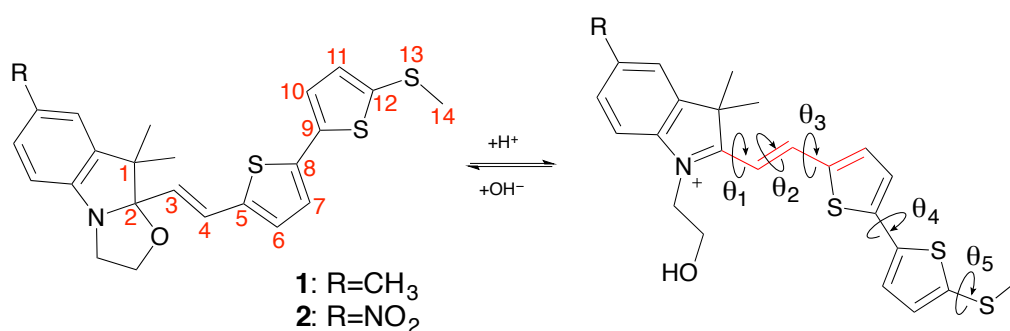
Organic compounds exhibiting commutable optical properties are widely studied for their potential applications in the design of novel photonic and optoelectronic devices such as logic gates or high-density optical memories. [1] The switching events can be triggered in many ways, leading to a broad variety of molecular switches that can be classified following their addressability as photochromes, acidochromes, halochromes, thermochromes, or electrochromes. [2] Besides modifications of the linear optical properties of the molecules, these various stimuli can also induce variation of the nonlinear optical (NLO) properties such as second-harmonic generation (SHG), two-photon absorption (TPA), and third-harmonic generation (THG). Molecular switches that undergo large quadratic hyperpolarizability ( $\beta$ ) changes within their interconversion network are of particular interest for designing molecular-scale memory devices with multiple storage and nondestructive capacity. Indeed, exploiting nonlinear optics to probe the electronic states of the system enables the reading of stored information outside the absorption band of the compounds, thereby avoiding uncontrolled conversions and losses of information during the reading processes (cross-talk). As reviewed recently, [3] examples of molecular NLO switches abound in literature. NLO contrasts have been evidenced upon photo-induced intramolecular proton transfer in keto-enol tautomers, [4–7] upon cyclization/decyclization processes in dithiazolylenes, [8] dihydroazulene-vinylheptafulvenes, [9] fulgides, [10] spiropyrans, [11] or oxazines, [12] upon acid/base protonation/deprotonation in azafulleroids, [13] styrylpyridine derivatives, [14] and other pH-switchable dyes, [15, 16] as well as upon redox stimuli in organometallic complexes. [17–20]

Beyond single-unit NLO switches, recent work in the field has been directed towards systems incorporating  $n$  switchable units coupled within a single structure, thereby allowing theoretically a total of  $2^n$  possible states and offering platforms for the development of optical memories with enhanced storage capacity. [21–23] Diversifying the addressability of molecular systems by introducing switchable units that can be triggered indifferently by using various stimuli constitutes an additional way to extend the functionalities of the devices. Among multifunctional systems designed for NLO, benzazolo-oxazolidine derivatives incorporating either an indole, a benzimidazole, or a benzothiazole heterocycle were shown to exhibit versatile switching properties, ensuring both photo- and acido-addressable conversion associated to large changes in the first hyperpolarizability. [24–27]

Recently, have been demonstrated that the association of an indolino-oxazolidine core with a bithiophene moiety acting as a redox center (compound **(1)**, Scheme 4.1) leads to a trimodal switch where the interconversion between the colorless closed form and the colored open form can be indifferently triggered by light irradiation, pH variation, or electrical stimulation. [28, 29] Hyper-Rayleigh scattering (HRS) experi-

ments conducted in dilute solutions demonstrated that the protonated, oxidized and irradiated open forms exhibit the same NLO features, with a huge enhancement of the first hyperpolarizability upon commutation between the closed and open forms. Based on these systems, a new compact electrochemical cell was designed in order to monitor in situ the HRS response of the chromophore upon electrochemical stimulation. Large and reversible NLO contrasts were observed during oxidation/reduction cycles, making compound **1** an attractive multiresponsive system for further applications in devices. [30]

In the quest for optimizing the NLO performances of these derivatives, previous investigations also demonstrated that grafting electron-withdrawing substituents onto the indolinic residue could further induce a significant enhancement of the NLO response of the open form, thanks to an increased photo-induced charge transfer between the indolinic core and the associated styrylic residues. [27] Following these guidelines, this chapter reports the synthesis and the NLO properties of a new derivative of the same family, bearing a nitro substituent on its indolinic moiety (compound (**2**), in Scheme 4.1). The first hyperpolarizability of the closed and open forms, determined experimentally by means of HRS measurements performed in acetonitrile, are rationalized in the light of quantum chemical calculations and compared to compound **1**, which bears a methyl in place of the nitro group on the indolinic unit.



Scheme 4.1: Closed form (CF) and protonated open form (POF) of the indolinooxazolidine derivatives (**1**) and (**2**). The rotational angles  $\theta_{1-5}$  are displayed ( $\theta_1 = C_1 - C_2 - C_3 - C_4$ ;  $\theta_2 = C_2 - C_3 - C_4 - C_5$ ;  $\theta_3 = C_3 - C_4 - C_5 - C_6$ ;  $\theta_4 = C_7 - C_8 - C_9 - C_{10}$ ;  $\theta_5 = C_{11} - C_{12} - S_{13} - C_{14}$ ), as well as (in red) the conjugated segment considered for the calculation of the BLA.

## 4.2 Experimental and Theoretical Methods

### 4.2.1 Synthesis

The preparation of compound **1** was already reported in Ref. [30] and lays down on a two-steps linear synthesis consisting in condensation between 2,3,3,5-tetramethylindolino[2,1-b]oxazolidine and 5-bromo-2-thiophenecarboxaldehyde, followed by an extension of the  $\pi$ -conjugated system using a Suzuki coupling. If similar

strategy could be reasonably envisioned for the preparation of compound **2**, we have preferred in this study a more convergent synthetic pathway involving the condensation between 5'-thiomethyl-[2,2'-bithiophen]-5-carboxaldehyde and the appropriate (nitro or methylated) indolinooxazolidine compound (see the Appendix A for details).

## 4.2.2 UV-visible and Hyper-Rayleigh Scattering Measurements

The linear and nonlinear optical properties of compound **1** were reported in Ref. [30] UV-vis spectroscopy measurements of compound **2** in acetonitrile were carried out on a PerkinElmer Lambda 650 spectrophotometer in the visible region (300-800 nm). Hyper-Rayleigh scattering measurements were performed at 1064 nm in diluted acetonitrile solutions with chromophore concentrations ranging from  $10^{-3}$  to  $10^{-4}$  M for the closed forms, and from  $\sim 6 \times 10^{-5}$  to  $10^{-5}$  M for the open forms. All solutions were centrifuged during 20 minutes to prevent spurious scattering from particles. The open form of **2** was obtained by adding vapor of trifluoroacetic acid (TFA). The details of the experimental set up can be found in Refs. [31, 32]. Thus, we only recall here the general principles of HRS as well as the quantities of interest in this study.

The total harmonic scattered light for a diluted binary solution composed of a solvent ( $S$ ) (the contribution of TFA to the HRS signal is considered negligible owing to its very small concentration as vapor and weak intrinsic response) and a solute ( $X$ ) is given by:

$$I_{\Psi V}^{2\omega} = G f_L^2 \{ C_S [|\beta_{J=1}|^2 C_{\Psi V}]_S + C_X [|\beta_{J=1}|^2 C_{\Psi V}]_X \} \times 10^{-a_X^{2\omega} C_X} (I^\omega)^2 \quad (4.1)$$

where  $G$  is a constant containing geometrical, optical, and electrical factors of the experimental setup,  $C$  is the molarity of the solvent or solute (in  $\text{molL}^{-1}$ ), and  $f_L$  is a local field correction approximated using the high frequency Lorentz-Lorenz spherical cavity expression.  $I^\omega$  is the incident intensity, and  $a_X^{2\omega}$  accounts for the one-photon absorption of the chromophore at the second harmonic frequency.  $|\beta_{J=1}|$  and  $|\beta_{J=3}|$  are respectively the dipolar and octupolar (vide infra) components of the total HRS first hyperpolarizability ( $\beta_{HRS}$ ) using the irreducible spherical representation of the  $\beta$  tensor, [33, 34] while  $C_{\Psi V}$  is the orientational average of the molecular spherical components of the hyperpolarizability of the solute (or solvent), which can be expressed as:

$$C_{\Psi V} = \left( \frac{9}{45} + \frac{6}{105} \rho^2 \right) + \left( -\frac{20}{45} + \frac{10}{105} \rho^2 \right) \cos^2 \Psi + \left( \frac{12}{45} - \frac{12}{105} \rho^2 \right) \cos^4 \Psi \quad (4.2)$$

where  $\rho = |\beta_{J=3}|/|\beta_{J=1}|$  is the nonlinear anisotropy ratio, which is related to  $\beta_{HRS}$  and the depolarization ratio (DR) as:

$$\beta_{HRS} = \sqrt{\langle \beta_{HRS}^2 \rangle} = \sqrt{\frac{10}{45}|\beta_{J=1}|^2 + \frac{10}{105}|\beta_{J=3}|^2} = |\beta_{J=1}| \sqrt{\frac{2}{3} \left( \frac{1}{3} + \frac{1}{7}\rho^2 \right)} \quad (4.3)$$

$$DR = 9 \frac{1 + \frac{2}{7}\rho^2}{1 + \frac{12}{7}\rho^2} \quad (4.4)$$

### 4.2.3 Quantum Chemical Calculations

Molecular structures were optimized using density functional theory (DFT) together with the M06 [35] exchange-correlation functional (XCF) and the 6-311G(d) basis set. Each structure was characterized as a minimum of the potential energy surface based on its real harmonic vibrational frequencies. Vertical excitation energies and excited state properties were determined using time-dependent (TD) DFT with the M06-2X [36] XCF and the same 6-311G(d) basis set. The components of the static and dynamic (frequency-dependent) first hyperpolarizability tensors were calculated at the TDDFT/M06-2X/6-311+G(d) level, using incident wavelengths of 1907 and 1064 nm without assuming Kleinman’s symmetry conditions. [37] The dipolar and octupolar contributions to the HRS hyperpolarizability were eventually determined from the Cartesian components of  $\beta$  calculated in the molecular frame by using the following expression assuming Kleinman’s symmetry:

$$|\beta_{J=1}|^2 = \frac{3}{5} \sum_{\zeta}^{x,y,z} \beta_{\zeta\zeta\zeta}^2 + \frac{6}{5} \sum_{\zeta \neq \eta}^{x,y,z} \beta_{\zeta\zeta\zeta} \beta_{\zeta\eta\eta} + \frac{3}{5} \sum_{\zeta \neq \eta}^{x,y,z} \beta_{\eta\zeta\zeta}^2 + \frac{3}{5} \sum_{\zeta \neq \eta \neq \xi}^{x,y,z} \beta_{\eta\zeta\zeta} \beta_{\eta\xi\xi} \quad (4.5)$$

$$|\beta_{J=3}|^2 = \frac{2}{5} \sum_{\zeta}^{x,y,z} \beta_{\zeta\zeta\zeta}^2 - \frac{6}{5} \sum_{\zeta \neq \eta}^{x,y,z} \beta_{\zeta\zeta\zeta} \beta_{\zeta\eta\eta} + \frac{12}{5} \sum_{\zeta \neq \eta}^{x,y,z} \beta_{\eta\zeta\zeta}^2 - \frac{3}{5} \sum_{\zeta \neq \eta \neq \xi}^{x,y,z} \beta_{\eta\zeta\zeta} \beta_{\eta\xi\xi} + \sum_{\zeta \neq \eta \neq \xi}^{x,y,z} \beta_{\zeta\eta\xi}^2 \quad (4.6)$$

The M06-2X XCF has been selected owing to its good performance for calculating the second-order NLO properties of a large variety of organic chromophores, [38] including the relative first hyperpolarizabilities of closed and open forms of indolino-oxazolidine [30] and oxazine [12] derivatives, of which the electronic excitations present small- and medium-range charge transfer character, respectively. For comparison purposes, the NLO properties of compounds **1** and **2** were also calculated using the CAM-B3LYP XCF, which adds a long-range correction using the Coulomb-attenuating method and includes 19% of Hartree-Fock (HF) exchange at short range and 65% at long range (with a range separating parameter  $\mu = 0.33 a_0^{-1}$ ). [39] In addition, the coupled-perturbed Hartree-Fock (CPHF) and the second-order Møller-Plesset perturbation theory (MP2) approaches were also employed in order to further size up the electron correlation effects. Indeed, several investigations on push-pull  $\pi$ -conjugated systems have shown that the largest part of electron correlation ef-

fects is included at the MP2 level. [40–42] The MP2 values were calculated using a finite field (FF) procedure [43] implying a fully automatized Romberg procedure to improve the accuracy on the numerical derivatives. [44, 45] Solvent effects (acetonitrile) were included in all calculations (geometry optimizations, thermochemistry, computations of linear and nonlinear optical properties) by using the Polarizable Continuum Model in its Integral Equation Formalism (IEF-PCM). [46, 47] This model approximates the solvent as a structureless polarizable continuum characterized by its macroscopic dielectric permittivity, which depends on the frequency of the applied electric field. For acetonitrile, the dielectric constants in the static limit ( $\epsilon_0$ ) and at infinite frequency ( $\epsilon_\infty$ ) are respectively equal to 35.688 and 1.807. The good performance of IEF-PCM in describing the NLO contrasts along the conversion pathways of a hybrid system incorporating an indolino-oxazolidine moiety coupled to a dithienylethene was recently addressed by comparison to an explicit approach combining quantum chemical calculations and Monte Carlo simulations. [48] All quantum chemical calculations were performed using the Gaussian 09 package. [49]

## 4.3 Results and Discussion

### 4.3.1 Structural Properties

For both compounds **1** and **2**, a search for the most stable conformers was achieved by considering several starting geometries with different values of the torsion angles along the single bonds ( $\theta_1, \theta_3 - \theta_5$ ) reported on Scheme 4.1. Only *trans* conformers with respect to the  $C_3 - C_4$  double bond ( $\theta_2 \sim \pm 180^\circ$ ) were considered, since previous investigations have demonstrated that, regardless of the form, the thermal populations of the *cis* isomers are negligible in these derivatives. [23] The geometrical parameters characterizing the degree of conjugation within the various isomers in their closed and protonated open forms, namely the torsion angles  $\theta_1 - \theta_5$  and the averaged bond-length alternation (BLA) along the  $C_2 - C_6$  conjugated chain (red segment in Scheme 4.1), are gathered in Tables 4.1 and 4.2, together with the relative Gibbs energies and Maxwell-Boltzmann statistical populations, calculated using the standard temperature and pressure conditions (298.15 K, 1 atm).

As shown in Table 4.1, compound **1** ( $R = \text{CH}_3$ ) in its closed form possesses a single conformer with significant population (conformer VII, 87%), the other ones being less stable with populations not exceeding 11%. A similar situation is observed for compound **2** ( $R = \text{NO}_2$ ).  $\theta_1$  is similar (around  $110 - 115^\circ$ ) for all structures. For all conformers of the two compounds, the carbons  $C_2, C_3, C_4$  and  $C_5$  lie almost in the same plane since  $\theta_2$  is equal to  $\sim \pm 180^\circ$ . Increasing  $\theta_3$  from  $\sim 0^\circ$  to  $\sim 180^\circ$  (*i.e.* the orientation of the bithiophene with respect to the conjugated linker) stabilizes the structure by about 1 kcal/mol. Varying the rotational angle  $\theta_4$  from  $\sim 20^\circ$  to  $\sim 160^\circ$  (*i.e.* going from a *syn* to a alternate configuration of the bithiophene) de-

Table 4.1: Torsional angles ( $^{\circ}$ ) and bond length alternation (BLA,  $\text{\AA}$ ) of the various conformers of compounds **1** and **2** in their closed forms, as optimized at the M06/6-311G(d) level in acetonitrile. Last columns: Relative Gibbs free energies ( $\Delta G^{\ominus}$ , kcal/mol) and populations (%) estimated using a Boltzmann statistics at room temperature.

<i>Conf.</i>	$\theta_1$	$\theta_2$	$\theta_3$	$\theta_4$	$\theta_5$	<i>BLA</i>	$\Delta G^{\ominus}$	%
<b>1: R=CH<sub>3</sub></b>								
I	114.6	-179.8	4.6	160.1	1.2	0.138	4.15	0.1
II	112.5	-178.7	6.5	163.7	102.7	0.138	1.24	10.7
III	113.6	-178.7	11.3	-23.6	-100.8	0.138	3.96	0.1
IV	113.5	179.6	178.5	22.6	99.2	0.136	2.58	1.1
V	112.4	-179.7	-0.9	24.8	103.4	0.138	3.42	0.3
VI	112.5	-179.6	-178.1	-23.8	1.6	0.135	2.92	0.6
VII	112.8	-179.8	-178.1	162.2	104	0.136	0.00	87.1
<b>2: R=NO<sub>2</sub></b>								
I	110.7	-178.2	5.7	159.2	0.4	0.137	2.70	0.8
II	112.7	-178.7	8.5	165.5	104.4	0.138	1.05	13.5
III	112.2	-179.5	2.0	24.6	0.7	0.137	3.64	0.2
IV	111.8	179.8	178.6	22.4	99.7	0.135	1.67	4.7
V	109.3	-177.7	4.3	-24.9	100.3	0.138	2.42	1.3
VI	111.8	-179.4	-177.8	-23.3	4.1	0.134	2.79	0.7
VII	111.1	-179.6	-178.7	161.7	102.0	0.135	0.00	78.8

creases the energy by 2.2-2.6 kcal/mol in compound **1** (III $\rightarrow$  II, V $\rightarrow$ II, IV $\rightarrow$ VII), and by 0.9-1.4 kcal/mol in compound **2** (III $\rightarrow$ I, V $\rightarrow$ II). The orientation of the terminal thiomethyl group also influences the total energy: varying  $\theta_5$  from  $\sim 0^{\circ}$  to  $\sim 100^{\circ}$  lowers the energy (by 0.3 up to 2.9 kcal/mol) in both compounds. For all conformers of both compounds, the BLA values lie around 0.14  $\text{\AA}$ , with negligible influence of the substituent R. Open forms of compounds **1** and **2** (Table 4.2) possess several conformers with significant population at room temperature. For compound **1**, conformers with  $\theta_3 \sim 0^{\circ}$  (I-V) have populations smaller than 5%. Conformers with  $\theta_3 \sim \pm 180^{\circ}$  are the most stable, except IX. Similar conclusion holds for compound **2** although the relative population of conformer II is  $\sim 12\%$ . The angle  $\theta_1$ , similar in all closed forms, can adopt either a value of  $\sim 0^{\circ}$  or  $\sim 180^{\circ}$  in the open forms. Conformers with  $\theta_1 \sim 0^{\circ}$  are in most cases stabilized compared to those with  $\theta_1 \sim 180^{\circ}$ , although they might be isoenergetic in compound **1**. Increasing  $\theta_3$  from  $\sim 0^{\circ}$  to  $\sim 180^{\circ}$  also lowers the Gibbs energies, by 0.4 to 1.9 kcal/mol depending on the other torsion angles. As in closed forms, the *alternate* conformation of the bithiophene is more stable than *syn* one. So, varying the rotational angle  $\theta_4$  from  $\sim 0^{\circ}$  to  $\sim 180^{\circ}$  stabilizes the system by 0.1 to 0.8 kcal/mol. In contrast to the closed forms, the terminal thiomethyl group lies in (or is close to) the mean plane of the molecule in the most stable structures, and the variation of the torsion angle defining the orientation of the terminal methyl group, from about  $0^{\circ}$  to  $180^{\circ}$  results in an

Table 4.2: Torsional angles ( $^{\circ}$ ) and bond length alternation (BLA,  $\text{\AA}$ ) of the various conformers of compounds **1** and **2** in their protonated open forms, as optimized at the M06/6-311G(d) level in acetonitrile. Last columns: Relative Gibb’s free energies ( $\Delta G^{\ominus}$ , kcal/mol) and populations (%) estimated using a Boltzmann statistics at room temperature.

<i>Conf.</i>	$\theta_1$	$\theta_2$	$\theta_3$	$\theta_4$	$\theta_5$	<i>BLA</i>	$\Delta G^{\ominus}$	%
<b>1: R=CH<sub>3</sub></b>								
I	0.2	179.8	-0.1	179.7	-178.5	0.032	1.65	2.2
II	-0.3	-179.3	-1.2	178.8	0.0	0.035	1.28	4.0
III	0.1	-179.4	-0.8	-1.6	0.4	0.032	1.90	1.4
IV	1.6	179.4	-0.8	178.7	179.9	0.029	2.06	1.1
V	-160.0	-179.2	6.1	1.7	0.3	0.036	1.87	1.5
VI	-159.0	179.0	-175.1	177.9	-0.1	0.037	0.00	35.3
VII	3.9	-173.3	-177.5	179.9	-27.8	0.043	0.09	30.1
VIII	0.2	179.3	-179.9	-2.8	0.3	0.030	0.22	24.3
IX	-172.4	179.6	-178.1	-1.8	1.9	0.030	4.02	0.0
<b>2: R=NO<sub>2</sub></b>								
I	0.6	179.7	-0.2	179.2	178.3	0.011	1.73	2.5
II	0.3	-179.3	-0.3	179.5	-0.2	0.015	0.82	11.6
III	0.3	-179.5	-1.2	-1.1	2.5	0.012	1.18	6.2
IV	2.0	179.1	-0.5	178	178.7	0.008	2.40	0.8
V	-162.8	-178.0	5.7	1.3	0.8	0.015	2.10	1.3
VI	-162.1	-179.1	-175.3	179.3	1.2	0.017	0.52	19.2
VII	0.6	-179.4	179.3	179.8	-1.2	0.012	0.00	46.0
VIII	0.2	178.7	-180.0	-1.9	0.5	0.010	0.79	12.1
IX	-174.0	-179.1	-178.6	0.3	2.0	0.010	2.88	0.4

increase of the energy of the order of 1 kcal/mol. As expected, the BLA of the open forms is one order of magnitude smaller than that of the closed forms, since opening of the oxazolidine ring strengthens the electron conjugation along the molecule. In contrast to what observed in closed forms, the R substituent impacts the value of the BLA, which is smaller for compound **2** than for compound **1**. Therefore, introducing an electron-withdrawing NO<sub>2</sub> group on the indolinoxazolidine unit increases the electron conjugation, and is expected to impact the linear and nonlinear optical properties (*vide infra*).

### 4.3.2 Linear Optical Properties

The UV-visible spectra measured in acetonitrile and calculated at the TD/M06-2X/6-311G(d) level for compounds **1** and **2** in their closed and protonated open forms are reported in Figure 4.1, while the characteristics of the main optical transitions are gathered in Table 4.3. In addition to the theoretical transition wavelengths and oscillator strengths, the dipole moment variation between the ground state and the optically active excited state ( $\Delta\mu = |\vec{\mu}_e - \vec{\mu}_g|$ ) is also reported. From the

analysis of the total electron densities of the two electronic states,  $\Delta\mu$  is further decomposed as  $\Delta\mu = d^{CT} \times q^{CT}$  where  $q^{CT}$  is the photo-induced charge transfer *i.e.* the global amount of charge transfer upon electronic excitation, and  $d^{CT}$  is the distance over which this charge is transferred. [50, 51] Note that the spectroscopic quantities reported in Table 4.3 correspond to the weighted sum of the properties of the different conformers. The data for the complete set of conformers listed in Tables 4.1 and 4.2 are provided in the Appendix A (Table A.1).

For both compounds, the opening of the indolino-oxazine ring induces a large shift of the main absorption band from the near UV to the visible region. The closed forms are almost colorless and characterized by a maximal absorption wavelength ( $\lambda_{max}$ ) centered at 360 nm, with no impact of the substituent R. The open form of compound **1** absorbs at 521 nm, while the main absorption band of compound **2** is centered at 562 nm, indicating that the nitro substituent enhances the electron conjugation within the molecule. The computed absorption wavelengths of the closed forms quantitatively agree with the experimental ones. Although those of open forms are overestimated compared to experiments, the redshift induced by the addition of the nitro substituent is very well described, with a computed value of 44 nm compared to 38 nm observed experimentally. TDDFT calculations further reveal that the dipole moment variation  $\Delta\mu$  between the ground state and the first excited state is very small in the closed forms ( $< 1$  D), while it is larger than 10 D in the open forms, due to a larger extent of the photo-induced charge transfer as shown by the larger  $q^{CT}$  and  $d^{CT}$  values (Table 4.3). This strong difference in  $\Delta\mu$  between the closed and open forms is one of the necessary requirements to obtain high NLO contrasts, and can be rationalized from the analysis of the molecular orbitals (MOs) implied in the main absorption band (Figure 4.3). In the closed forms of both compounds, both the occupied and unoccupied MOs involved in the  $S_0 \rightarrow S_1$  transition are localized on the bithiophene unit and on the ethylenic bridge, with no delocalization on the indolino-oxazolidine part, which explains the weak charge transfer ( $q^{CT} \approx 0.4 |e|$ ,  $d^{CT} \approx 0.2 \text{ \AA}$ ) and the small change in dipole moment ( $\Delta\mu \approx 0.4 \text{ D}$ ). In the open form of compound **1**, the two MOs are spread over the whole molecule. The HOMO is mostly delocalized over the bithiophene moiety and the conjugated linker, while the LUMO extends more on the indolino-oxazolidine part. Therefore, the excitation-induced charge transfer is much more pronounced than in the closed form, with  $q^{CT} \approx 0.6 |e|$ ,  $d^{CT} \approx 3.6 \text{ \AA}$  and  $\Delta\mu \approx 10.4 \text{ D}$ .

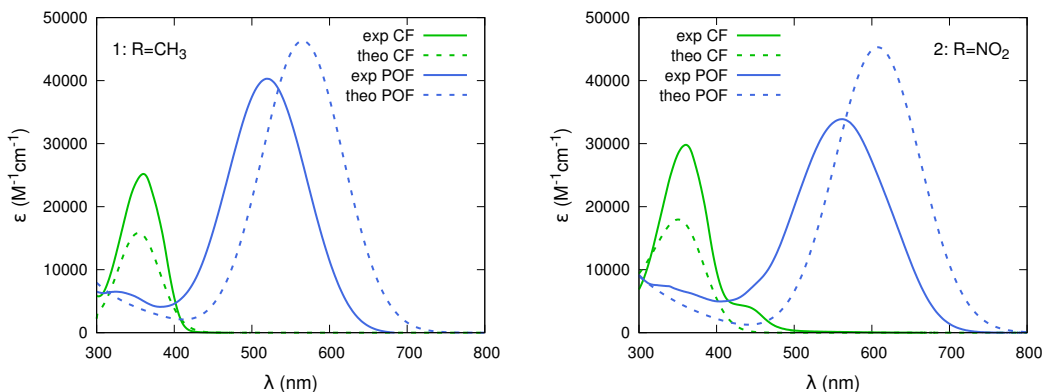


Figure 4.1: UV-vis absorption spectra measured and calculated in acetonitrile for compounds **1** (left) and **2** (right) in their closed and protonated open forms.

Table 4.3: Experimental maximum absorption wavelengths ( $\lambda_{max}$ , nm), molar extinction coefficients ( $\epsilon$ ,  $M^{-1} \cdot cm^{-1}$ ), full width at half maximum (FWHM,  $cm^{-1}$ ) and oscillator strengths ( $f$ ). As well as, theoretical averaged transition wavelengths ( $\lambda_{ge}$ , nm) and energies ( $\Delta E_{ge}$ , eV), oscillator strengths ( $f_{ge}$ ), dipole moment variations ( $\Delta\mu = |\vec{\mu}_e - \vec{\mu}_g|$ , D), charge transfers ( $q^{CT}$ ,  $|e|$ ) and charge transfer distances ( $d^{CT}$ , Å), calculated at the M06-2X/6-311G(d) level in acetonitrile for the  $S_0 \rightarrow S_1$  transition of compounds **1** and **2** in their closed and open forms.

Comp.	$\lambda_{max}$	$\epsilon$	FWHM	$f^{[a]}$	Theoretical					
					$\lambda_{ge}$	$\Delta E_{ge}$	$f_{ge}$	$\Delta\mu$	$q^{CT}$	$d^{CT}$
	Experimental									
<b>1</b> CF	360	25000	5000	0.537	357	3.478	1.237	0.444	0.392	0.234
<b>1</b> POF	521	40000	4600	0.791	565	2.193	1.869	10.364	0.609	3.535
<b>2</b> CF	360	30000	5500	0.709	356	3.481	1.316	0.437	0.391	0.226
<b>2</b> POF	562	33900	4500	0.656	608	2.044	2.005	10.926	0.592	3.845

[a] estimated using  $f \approx 4.3 \times \epsilon \times FWHM$

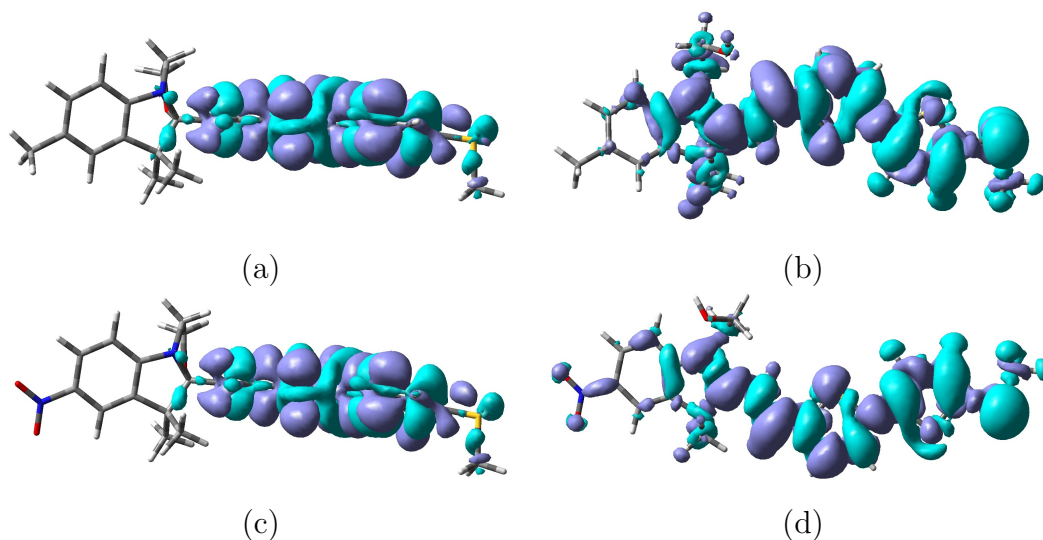


Figure 4.2: Electron density difference between the lowest excited state and the ground state for compounds **1** and **2** in the most stable closed and protonated open forms, as calculated at the M06-2X/6-311G(d) level in acetonitrile (isovalues = 0.0004). Blue (violet) lobes are associated with negative (positive) values. (a) **1**: R=CH<sub>3</sub> CF (conf. VII); (b) **1**: R=CH<sub>3</sub> POF (conf. VI); (c) **2**: R=NO<sub>2</sub> CF (conf. VII); (d) **2**: R=NO<sub>2</sub> POF (conf. VII).

The addition of a nitro group in compound **2** leads to a localization of the LUMO on the indolinooxazolidine part, which further increases  $d^{CT}$  to 3.8 Å and  $\Delta\mu$  to 10.9 D. Similar conclusions can be drawn from the analysis of the density difference maps (Figure 4.2), which illustrate the difference in the total electron density between the ground and first excited states:  $\Delta\rho = \rho(S_1) - \rho(S_0)$ . TDDFT calculations also predict that the oscillator strengths associated to the  $S_0 \rightarrow S_1$  transition are slightly larger in the open forms of both compounds, which is not observed experimentally for compound **2** although the molar extinction coefficient increases upon the CF  $\rightarrow$  POF commutation. UV-vis. spectra also evidence a more intense  $S_0 \rightarrow S_1$  transition in the open form of compound **1** compared to that of compound **2**, which is not reproduced by the calculations.

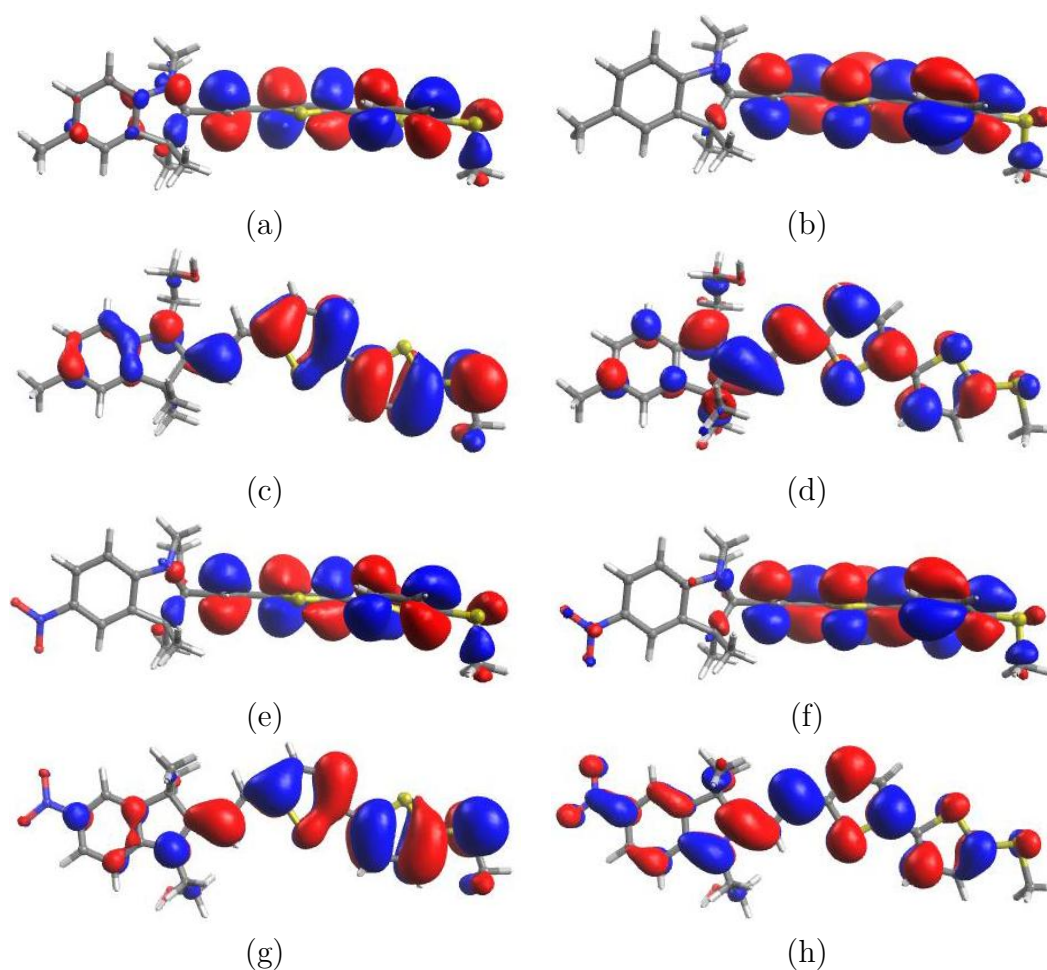


Figure 4.3: Shape of the molecular orbitals involved in the  $S_0 \rightarrow S_1$  transition for the boths compounds, as calculated at the M06-2X/6-311G(d) level in acetonitrile. (a) **1**: R=CH<sub>3</sub> CF: HOMO (conf. VII); (b) **1**: R=CH<sub>3</sub> CF: LUMO (conf. VII); (c) **1**: R=CH<sub>3</sub> POF: HOMO (conf. VI); (d) **1**: R=CH<sub>3</sub> POF: LUMO (conf. VI); (e) **2**: R=NO<sub>2</sub> CF: HOMO (conf. VII); (f) **2**: R=NO<sub>2</sub> CF: LUMO+1 (conf. VII); (g) **2**: R=NO<sub>2</sub> POF: HOMO (conf. VII); (h) **2**: R=NO<sub>2</sub> POF: LUMO (conf. VII)

### 4.3.3 Nonlinear Optical Properties

The total HRS hyperpolarizabilities ( $\beta_{HRS}$ ), the dipolar ( $|\beta_{J=1}|$ ) and octupolar ( $|\beta_{J=3}|$ ) components, as well as the associated depolarization (DR) and anisotropy ( $\rho$ ) ratios measured in acetonitrile, are reported in Table 4.4. 3D representations of the HRS responses of compounds **1** and **2** in their closed and open forms as a function of the incident power and concentration, as well as polarization curves, are reported in Figures A.1 and A.2 (see Appendix A). To overcome frequency resonance effects and allow reliable comparisons between experimental and computed NLO responses, the  $\beta_{HRS}$  values measured at 1064 nm were extrapolated to  $\lambda = 1907$  nm and to the static limit ( $\lambda = \infty$ ), by using the homogeneously damped two-level model [52] (see Chapter 3).

In both compounds, the opening of the indolino-oxazolidine moiety induces a large enhancement of  $\beta_{HRS}$ . In compound **1**, the measured open/closed  $\beta_{HRS}$  contrast ratio is equal to 38, and it remains as large as 27-30 when extrapolated out of resonance conditions. This enhancement is accompanied by a significant increase of the DR from 3.5 to 4.7, very close to the value of 5, which is typical of ideal 1D systems, *i.e.* with a single non zero diagonal component in the Cartesian  $\beta$  tensor. The reinforcement of the 1D character of the NLO chromophore is also characterized by the decrease of the anisotropy ratio  $\rho$  from 1.28 (indicating a dominant octupolar character) to 0.88 (indicating a dominant dipolar character). In contrast, the DR and  $\rho$  values do not change significantly between the closed and open form of compound **2**, due to the presence of the NO<sub>2</sub> group that reduces the octupolar character of the closed form. The nitro group also enhances the HRS response of both forms of compound **2** compared to compound **1**. The open form of compound **2** displays the largest  $\beta_{HRS}$  due to smaller transition energy and larger dipole moment variation from the ground to the excited state. However, compound **2** exhibits smaller  $\beta_{HRS}$  contrasts upon the CF  $\rightarrow$  POF commutation, essentially due to the larger enhancement of the HRS response of its closed form.

The averaged NLO properties calculated at the M06-2X/6-311+G(d) level are listed in Table 4.5. The data for the whole set of conformers are provided in the Appendix A (Tables A.2-A.4). As can be observed in Table 4.5, the dynamic  $\beta_{HRS}$  values calculated at 1064 nm for the open form of **1** (and to a lesser extent for **2**) are contaminated by electronic excitation resonance due to the overlap between the maximum absorption band of the compound ( $\lambda_{ge} = 564$  nm) and the second harmonic wavelength ( $\lambda = 532$  nm). Therefore, the discussion below will concentrate on the NLO properties calculated far from resonance, *i.e.* at  $\lambda = 1907$  nm and in the static limit. Besides, theoretical results obtained at the CAM-B3LYP/6-311+G(d) level (Tables A.5-A.7) are fully consistent and lead to the same conclusions as those obtained using M06-2X. Consistently with experimental measurements, the  $\beta_{HRS}$  response calculated for the closed form of **1** is weak and dominated by its octupolar

component ( $\rho > 1$ ), which indicates a non-planar (rather 3D) geometry. In the POF, the increase of the conjugation length gives rise to an enhancement of  $\beta_{HRS}$  by two orders of magnitude, together with an increase of DR, as expected for a more planar molecule probed close to resonance. The addition of a nitro group on the indolino-oxazolidine moiety in **2** induces an increase of the  $\beta_{HRS}$  response of the closed form by a factor of  $\sim 6$  with respect to compound **1**, as well as an increase of the dipolar character of the compound (DR being closer to 5, and  $\rho$  smaller than 1). The  $\beta_{HRS}$  contrast upon the CF $\rightarrow$ POF commutation is four times smaller for **2** than for **1** and lies around  $\sim 20$ , which agrees with HRS experiments, where a smaller  $\beta_{HRS}$  contrast for the nitro-derivative is also observed. The enhancement of the HRS response of the open forms due to the addition of the nitro substituent, quantified by the  $\beta_{HRS}(\mathbf{2})/\beta_{HRS}(\mathbf{1})$  ratio, amounts to 1.4-1.6, in quantitative agreement with experiments (1.7-1.8). MP2 calculations (Table 4.6) provide very similar trends, substantiating the good performance of TDDFT calculations. As typically expected, electron correlation effects as determined at the MP2 level account for an increase of  $\beta_{HRS}$  by a factor of  $\sim 2$  or more in comparison to uncorrelated HF calculations.

Finally, Figure 4.4 illustrates the static  $\beta_{HRS}$  contrast upon the CF $\rightarrow$ POF commutation for both compounds, as extrapolated from the dynamic experimental values and as calculated using the various levels of approximation selected in this study. Clearly, all levels of theory overestimate the  $\beta_{HRS}$  contrasts, in particular that of compound **1**, but reproduce the larger enhancement of the NLO response of compound **1**.

Table 4.4:  $\beta_{HRS}$  and  $\beta_J$  values (with relative accuracy *ca* 5% and expressed in atomic units<sup>[a]</sup> using *convention T*), as well as  $\rho$  and DR deduced from HRS measurements. The last lines report  $\beta_{HRS}$  values extrapolated to a 1907 nm wavelength ( $\beta_{HRS,1907}$ ) and to the static limit ( $\beta_{HRS,0}$ ). The  $\beta_{HRS}$  contrasts upon the CF $\rightarrow$ POF commutation are given in parentheses.

	<b>1: R=CH<sub>3</sub></b>		<b>2: R=NO<sub>2</sub></b>	
	CF	POF	CF	POF
$\beta_{HRS,1064}$	2800	106000 (37.8)	14800	173000 (11.7)
D.R.	3.50	4.70	4.19	4.12
$ \beta_{J=1} $	4600	194000	26000	300000
$ \beta_{J=3} $	5900	172000	26600	320000
$\rho$	$1.28 \pm 0.06$	$0.88 \pm 0.02$	$1.02 \pm 0.01$	$1.04 \pm 0.02$
$\beta_{HRS,1907}$	1800	55000 (30.6)	9700	100000 (10.3)
$\beta_{HRS,0}$	1600	42000 (27.3)	8500	73000 (8.6)

<sup>a</sup> 1 atomic unit =  $3.62 \times 10^{-42} m^4 V^{-1} = 8.641 \times 10^{-33}$  esu.

Table 4.5: Averaged  $\beta_{HRS}$  and  $\beta_J$  values, as well as  $\rho$  and DR calculated for compounds **1** and **2** in their closed and protonated open forms, as calculated at the M06-2X/6-311+G(d) level in acetonitrile, using wavelengths of 1064 and 1907 nm and in the static limit ( $\lambda = \infty$ ).  $\beta_{HRS}$  contrasts upon the CF $\rightarrow$ POF commutation are given in parenthesis.

Comp.	$\beta_{HRS}$	D.R.	$ \beta_{J=1} $	$ \beta_{J=3} $	$\rho$
$\lambda = 1064$ nm					
<b>1</b> CF	394	3.28	629	835	1.39
<b>1</b> POF	1179784	4.94	2196476	1832036	0.83
<b>2</b> CF	2653	4.66	4865	4318	0.89
<b>2</b> POF	6337367	4.95	1181719	979019	0.83
$\lambda = 1907$ nm					
<b>1</b> CF	290	3.53	478	589	1.26
<b>1</b> POF	32560 (112.3)	4.91	60611	53025	0.83
<b>2</b> CF	2238	4.59	4080	3705	0.91
<b>2</b> POF	52369 (23.4)	4.94	97574	81100	0.83
$\lambda = \infty$ nm					
<b>1</b> CF	376	3.75	636	727	1.18
<b>1</b> POF	39560 (105.2)	4.86	73384	62184	0.85
<b>2</b> CF	2832	4.49	5125	4783	0.94
<b>2</b> POF	63593 (22.5)	4.87	117987	99867	0.85

Table 4.6: Averaged static  $\beta_{HRS}$  and  $\beta_J$  values, as well as  $\rho$  and DR calculated for compounds **1** and **2** in their closed and protonated open forms, as calculated at the HF and MP2 levels in acetonitrile using the 6-311+G(d) basis set.  $\beta_{HRS}$  contrasts upon the CF $\rightarrow$ POF commutation are given in parenthesis.

Comp.	$\beta_{HRS}$	D.R.	$ \beta_{J=1} $	$ \beta_{J=3} $	$\rho$
HF					
<b>1</b> CF	249	3.09	384	549	1.49
<b>1</b> POF	19660 (78.9)	4.61	35857	32519	0.91
<b>2</b> CF	1491	3.61	2473	3007	1.23
<b>2</b> POF	30808 (20.6)	4.62	56154	51005	0.91
MP2					
<b>1</b> CF	409	3.82	385	962	2.50
<b>1</b> POF	48424 (118.4)	5.02	94307	62202	0.66
<b>2</b> CF	3104	4.71	5756	4612	0.80
<b>2</b> POF	77049 (24.8)	4.95	149114	102110	0.68

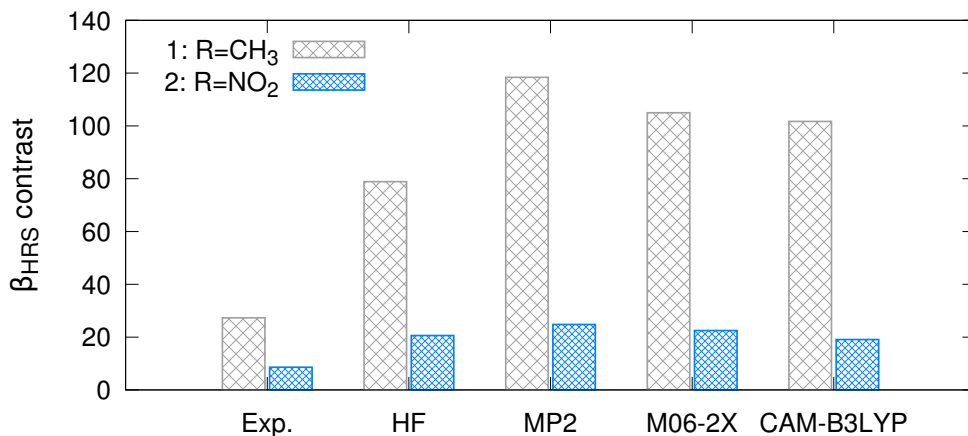


Figure 4.4: Static  $\beta_{HRS}$  contrasts upon the CF $\rightarrow$ POF commutation of compounds **1** and **2** calculated using various levels of calculation using the 6-311+G(d) basis set, and compared to the extrapolated experimental value.

## 4.4 Conclusion

The structural, linear and nonlinear optical properties of two indolino-oxazolidine derivatives differing by a methyl or a nitro substitution on the indolinic core have been investigated by using UV-vis spectroscopy and hyper-Rayleigh scattering measurements in combination with systematic first principles calculations accounting for all possible geometrical conformations of the compounds. The large second-order hyperpolarizability contrasts measured upon commutation between the closed and open forms demonstrate that the two compounds act as highly efficient NLO switches. Both experimental and theoretical results consistently evidence that nitro substitution has a negligible impact on the UV-vis absorption spectrum of the closed form, while it induces a bathochromic shift of the lowest-energy band of the open form. The decrease of the transition energy of the  $S_0 \rightarrow S_1$  transition, associated to a larger change in the dipole moment, induces a significant enhancement of the HRS response of the open form. A smaller  $\beta$  contrast is nevertheless observed in the nitro-substituted derivative compared to the methylated one, due to the concomitant exaltation of the HRS response of the closed form. These experimental observations are fully supported by the quantum chemical results. Although HF, DFT and MP2 calculations overestimate the  $\beta(\text{open})/\beta(\text{closed})$  contrast ratios, all levels of approximation reproduce and rationalize the reduction of the  $\beta$  contrast induced by nitro-substitution.

# Bibliography

---

- [1] J. Andréasson and U. Pischel. Molecules with a sense of logic: a progress report. *Chem. Soc. Rev.*, **44**(5):1053–1069, 2015.
- [2] B. L. Feringa and W. R. Browne. *Molecular switches*. Eds. Wiley-VCH: Weinheim, 2nd edition, 2011.
- [3] F. Castet, V. Rodriguez, J. L. Pozzo, L. Ducasse, A. Plaquet, and B. Champagne. Design and characterization of molecular nonlinear optical switches. *Acc. Chem. Res.*, **46**(11):2656–2665, 2013.
- [4] M. Sliwa, S. Létard, I. Malfant, M. Nierlich, P. G. Lacroix, T. Asahi, H. Masuhara, P. Yu, and K. Nakatani. Design, synthesis, structural and nonlinear optical properties of photochromic crystals: Toward reversible molecular switches. *Chem. Mater.*, **17**(18):4727–4735, 2005.
- [5] A. Bogdan, E. Plaquet, L. Antonov, V. Rodriguez, and L. Ducasse. Solvent effects on the second-order nonlinear optical responses in the Keto-Enol equilibrium of a 2-hydroxy-1-naphthaldehyde derivative. *J. Phys. Chem. C*, **114**:12760–12768, 2010.
- [6] S. De, M. Ray, Pati Y. A., and Das K. P. Base triggered enhancement of the first hyperpolarizability of a Keto-Enol tautomer. *J. Phys. Chem. B.*, **117**:15086–15092, 2013.
- [7] Castet F. and Champagne B. Switching of the nonlinear optical responses of anil derivatives: from dilute solutions to the solid state. In *Tautomerism: Concepts and Application in Science and Technology*. Antonov L., Ed.; Wiley, 2016.
- [8] M. Giraud, A. Léaustic, R. Guillot, P. Yu, P. G. Lacroix, K. Nakatani, R. Pansu, and F. Maurel. Dithiazolyethene-based molecular switches for nonlinear optical properties and fluorescence: synthesis, crystal structure and ligating properties. *J. Mater. Chem.*, **17**(41):4414, 2007.

- 
- [9] A. Plaquet, B. Champagne, F. Castet, L. Ducasse, E. Bogdan, V. Rodriguez, and J. Pozzo. Theoretical investigation of the dynamic first hyperpolarizability of DHA-VHF molecular switches. *New J. Chem.*, **33**(6):1349, 2009.
- [10] A. J. Garza, O. I. Osman, N. A. Wazzan, S. B. Khan, G. E. Scuseria, and A. M. Asiri. Photochromic and nonlinear optical properties of fulgides: A density functional theory study. *Comput. Theor. Chem.*, **1022**:82–85, 2013.
- [11] A. Plaquet, M. Guillaume, B. Champagne, F. Castet, L. Ducasse, J.-L. Pozzo, and V. Rodriguez. In silico optimization of merocyanine-spiropyran compounds as second-order nonlinear optical molecular switches. *Phys. Chem. Chem. Phys.*, **10**(41):6223–32, 2008.
- [12] P. Beaujean, F. Bondu, A. Plaquet, J. Garcia-Amorós, J. Cusido, F. M. Raymo, F. Castet, V. Rodriguez, and B. Champagne. Oxazines: A new class of second-order nonlinear optical switches. *J. Am. Chem. Soc.*, **138**(15):5052–5062, 2016.
- [13] I. Asselberghs, Y. Zhao, K. Clays, A. Persoons, A. Comito, and Y. Rubin. Reversible switching of molecular second-order nonlinear optical polarizability through proton-transfer. *Chem. Phys. Lett.*, **364**(3-4):279–283, 2002.
- [14] E. Cariati, C. Dragonetti, E. Lucenti, F. Nisic, S. Righetto, D. Roberto, and E. Tordin. An acido-triggered reversible luminescent and nonlinear optical switch based on a substituted styrylpyridine: EFISH measurements as an unusual method to reveal a protonation-deprotonation NLO contrast. *Chem. Commun.*, **50**(13):1608, 2014.
- [15] A. Plaquet, B. Champagne, J. Kulhanek, F. Bures, E. Bogdan, F. Castet, L. Ducasse, and V. Rodriguez. Effects of the nature and length of the  $\pi$ -conjugated bridge on the second-order nonlinear optical responses of push-pull molecules including 4,5-dicyanoimidazole and their protonated forms. *ChemPhysChem*, **12**:3245–3252, 2011.
- [16] S. van Bezouw, J. Campo, S. H. Lee, O. P. Kwon, and W. Wenseleers. Organic compounds with large and high-contrast pH-switchable nonlinear optical response. *J. Phys. Chem. C*, **119**(37):21658–21663, 2015.
- [17] B. J. Coe, S. Houbrechts, I. Asselberghs, and A. Persoons. Efficient reversible redox-switching of molecular first hyperpolarizabilities in ruthenium(II) complexes possessing large quadratic optical nonlinearities. *Angew. Chem., Int. Ed.*, **38**(9):366–369, 1999.
- [18] V. Aubert, V. Guerchais, E. Ishow, K. Hoang-Thi, I. Ledoux, K. Nakatani, and Le Bozec H. Efficient photoswitching of the nonlinear optical properties of

- dipolar photochromic zinc(II) complexes. *Angew. Chem., Int. Ed.*, **47**:577–580, 2008.
- [19] J. Boixel, V. Guerschais, H. Le Bozec, D. Chantzis, A. and Jacquemin, A. Colombo, C. Dragonetti, D. Marinotto, and D. Roberto. Sequential double second-order nonlinear optical switch by an acido-triggered photochromic cyclometallated platinum (II) complex. *Chem. Commun*, **51**:7805–7808, 2015.
- [20] W. Y. Wang, N. N. Ma, S. L. Sun, and Y. Q. Qiu. Impact of redox stimuli on ferrocene-buckybowl complexes: Switchable optoelectronic and nonlinear optical properties. *Organometallics*, **33**(13):3341–3352, 2014.
- [21] K. J. Chen, A. D. Laurent, and D. Jacquemin. Strategies for designing diarylethenes as efficient nonlinear optical switches. *J. Phys. Chem. C*, **118**(8):4334–4345, 2014.
- [22] F. Castet, B. Champagne, F. Pina, and V. Rodriguez. A multistate pH-triggered nonlinear optical switch. *ChemPhysChem*, **15**(11):2221–2224, 2014.
- [23] F. Bondu, J. Quertinmont, V. Rodriguez, J.-L. Pozzo, A. Plaquet, B. Champagne, and F. Castet. Second-order nonlinear optical properties of a dithienylethene-indolinooxazolidine hybrid: a joint experimental and theoretical investigation. *Chem.-Eur. J.*, **21**(51):18749–18757, 2015.
- [24] L. Sanguinet, J. L. Pozzo, V. Rodriguez, F. Adamietz, F. Castet, L. Ducasse, and B. Champagne. Acido- and phototriggered NLO properties enhancement. *J. Phys. Chem. B*, **109**(22):11139–11150, 2005.
- [25] L. Sanguinet, J.-L. Pozzo, M. Guillaume, B. Champagne, F. Castet, L. Ducasse, E. Maury, J. Soulié, F. Mançois, F. Adamietz, and V. Rodriguez. Acid-switchable NLO-phores; Benzimidazolo[2,3-b]oxazolidines. *J. Phys. Chem. B*, **110**(22):10672–10682, 2006.
- [26] F. Mançois, L. Sanguinet, J.-L. Pozzo, M. Guillaume, B. Champagne, V. Rodriguez, F. Adamietz, L. Ducasse, and F. Castet. Acido-triggered nonlinear optical switches: Benzazolo-oxazolidines. *J. Phys. Chem. B*, **111**(33):9795–9802, 2007.
- [27] F. Mançois, J.-L. Pozzo, J. Pan, F. Adamietz, V. Rodriguez, L. Ducasse, F. Castet, A. Plaquet, and B. Champagne. Two-way molecular switches with large nonlinear optical contrast. *Chem. - Eur. J. 2009*, **15**(11):2560–2571, 2009.
- [28] G. Szalóki, O. Alévêque, J.-L. Pozzo, R. Hadji, E. Levillain, and L. Sanguinet. Indolinooxazolidine: A versatile switchable unit. *J. Phys. Chem. B*, **119**(1):307–315, 2015.

- [29] R. Hadji, G. Szalóki, O. Alévêque, E. Levillain, and L. Sanguinet. The step-wise oxidation of indolino[2,1-b]oxazolidine derivatives. *J. Electroanal. Chem.*, **749**:1–9, 2015.
- [30] F. Bondu, R. Hadji, G. Szalóki, O. Alévêque, L. Sanguinet, J. L. Pozzo, T. Cavnagnat, D. Buffeteau, and V. Rodriguez. Huge electro-/photo-/acidinduced second-order nonlinear contrasts from multiaddressable indolinooxazolodine. *J. Phys. Chem. B*, **119**(22):6758–6765, 2015.
- [31] F. Castet, E. Bogdan, A. Plaquet, L. Ducasse, B. Champagne, and V. Rodriguez. Reference molecules for nonlinear optics: A joint experimental and theoretical investigation. *J. Chem. Phys.*, **136**(2):024506, jan 2012.
- [32] F. Castet, F. Blanchard-Desce, M. Adamietz, Y. M. Poronik, D. T. Gryko, and V. Rodriguez. Experimental and theoretical investigation of the first-order hyperpolarizability of octupolar merocyanine dyes. *ChemPhysChem*, **15**(12):2575–2581, 2014.
- [33] S. Brasselet and J. Zyss. Multipolar molecules and multipolar fields: probing and controlling the tensorial nature of nonlinear molecular media. *J. Opt. Soc. Am. B*, **15**(1):257, 1998.
- [34] V Rodriguez, J Grondin, F Adamietz, and Y Danten. Local structure in ionic liquids investigated by hyper-Rayleigh scattering. *J. Phys. Chem. B*, **114**(46):15057–65, 2010.
- [35] Y. Zhao and D. G. Truhlar. The M06 suite of density functionals for main group thermochemistry, thermochemical kinetics, noncovalent interactions, excited states, and transition elements: Two new functionals and systematic testing of four M06-class functionals and 12 other functionals. *Theor. Chem. Acc.*, **120**(1-3):215–241, 2008.
- [36] R. Li and D. G Truhlar. Density functional approximations for charge transfer excitations with intermediate spatial overlap. *Phys. Chem. Chem. Phys.*, **12**:12697–12701, 2010.
- [37] R. Bersohn, Y. H. Pao, and H. L. Frisch. Double-quantum light scattering by molecules. *J. Chem. Phys.*, **45**(9):3184–3198, 1966.
- [38] L. E. Johnson, L. R. Dalton, and B. H. Robinson. Optimizing calculations of electronic excitations and relative hyperpolarizabilities of electrooptic chromophores. *Acc. Chem. Res.*, **47**(11):3258–3265, 2014.
- [39] T. Yanai, D. P. Tew, and N. C. Handy. A new hybrid exchange-correlation functional using the Coulomb-attenuating method (CAM-B3LYP). *Chem. Phys. Lett.*, **393**(1-3):51–57, 2004.

- 
- [40] B. Champagne and B. Kirtman. Evaluation of alternative sum-over-states expressions for the first hyperpolarizability of push-pull  $\pi$ -conjugated systems. *J. Chem. Phys.*, **125**(2), 2006.
- [41] M. de Wergifosse and B. Champagne. Electron correlation effects on the first hyperpolarizability of push-pull  $\pi$ -conjugated systems. *J. Chem. Phys.*, **134**(7):074113, 2011.
- [42] M. Hidalgo Cardenuto and B. Champagne. The first hyperpolarizability of nitrobenzene in benzene solutions: investigation of the effects of electron correlation within the sequential QM/MM approach. *Phys. Chem. Chem. Phys.*, **17**(36):23634–23642, 2015.
- [43] H. D. Cohen and C. C. J. Roothaan. Electric dipole polarizability of atoms by the Hartree-Fock method. I. Theory for closed-shell systems. *J. Chem. Phys.*, **43**(10):S34–S39, 1965.
- [44] A. A K Mohammed, P. A. Limacher, and B. Champagne. Finding optimal finite field strengths allowing for a maximum of precision in the calculation of polarizabilities and hyperpolarizabilities. *J. Comput. Chem.*, **34**(17):1497–1507, 2013.
- [45] M. De Wergifosse, V. Liégeois, and B. Champagne. Evaluation of the molecular static and dynamic first hyperpolarizabilities. *Int. J. Quantum Chem.*, **114**(14):900–910, 2014.
- [46] B. Mennucci, R. Cammi, and J. Mennucci. Medium effects on the properties of chemical systems: Electric and magnetic response of donor-acceptor systems within the polarizable continuum model. *Int. J. Quantum Chem.*, **75**(4-5):767–781, 1999.
- [47] J. Tomasi, B. Mennucci, and R. Cammi. Quantum mechanical continuum solvation models. *Chem. Rev.*, **105**(8):2999–3093, 2005.
- [48] J. Quertinmont, B. Champagne, F. Castet, and M. Hidalgo Cardenuto. Explicit versus implicit solvation effects on the first hyperpolarizability of an organic biphotochrome. *J. Phys. Chem. A*, **119**(21):5496–5503, 2015.
- [49] M. J. Frisch, G. W. Trucks, H. B. Schlegel, G. E. Scuseria, M. A. Robb, J. R. Cheeseman, G. Scalmani, V. Barone, B. Mennucci, G. A. Petersson, H. Nakatsuji, M. Caricato, X. Li, H. P. Hratchian, A. F. Izmaylov, et al. Gaussian 09 revision d01. Gaussian Inc. Wallingford CT 2009.
- [50] T. Le Bahers, C. Adamo, and I. Ciofini. A qualitative index of spatial extent in charge-transfer excitations. *J. Chem. Theory Comput.*, **7**(8):2498–2506, 2011.

- [51] D. Jacquemin, T. Le Bahers, C. Adamo, and I. Ciofini. What is the 'best' atomic charge model to describe through-space charge-transfer excitations? *Phys. Chem. Chem. Phys.*, **14**(16):5383, 2012.
- [52] J. L. Oudar and D. S. Chemla. Hyperpolarizabilities of the nitroanilines and their relations to the excited state dipole moment. *J. Chem. Phys.*, **66**(6):2664–2668, 1977.



# Acido-Triggered Switching of the Second-Order Nonlinear Optical Properties of a Ferrocenyl-Containing Indolino-Oxazolidine Derivative

K. Pielak, F. Bondu, L. Sanguinet, V. Rodriguez, B. Champagne and F. Castet.  
*Dyes and Pigments* **160**:641-646, 2019.

*The synthesis and the characterization of the linear and second-order nonlinear optical properties are reported for a new derivative of the indolino-oxazolidine family, which exploits the strong donor capacity of the ferrocenyl unit. Hyper-Rayleigh scattering experiments show that the pH-triggered commutation between the closed and protonated open form of this compound enhances the first hyperpolarizability by roughly a factor 5, as a result of the increase of the push-pull  $\pi$ -electron conjugation within the molecule, between the donor ferrocenyl unit and the acceptor indoleninium moiety. Although derivatives exhibiting larger  $\beta$  responses in their nonlinear optical active form and larger  $\beta_{POF}/\beta_{CF}$  contrasts were previously reported within this class of materials, the figure of merit of this ferrocenyl-based compound is high enough for device application. Quantum chemical calculations of the linear and nonlinear optical properties are at least in qualitative agreement with the experimental trends. Calculations also show that  $\beta$  of the protonated open form originates from two low-lying excited states, of which the contributions partly cancel each other due to the opposite directions of the photo-excited charge transfer.*

In this chapter, I was responsible for the all theoretical calculations, analyzing the data and prepare the manuscript.

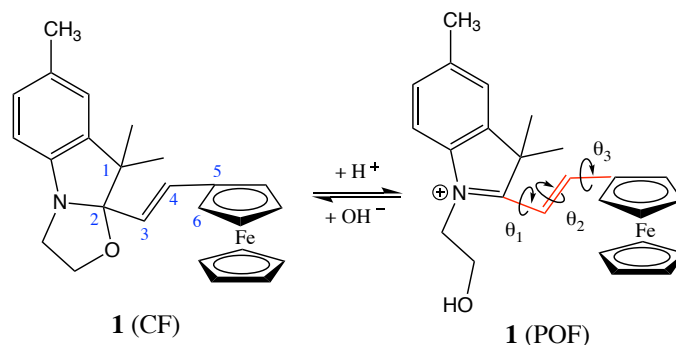
## 5.1 Introduction

The last two decades have witnessed a growing interest in developing organic materials that exhibit switchable second-order nonlinear optical (NLO) responses, owing to their potential applications in the field of photonics, optoelectronics, data storage, imaging, or optical communication. [1–4] Most of the systems synthesized to date are based on push-pull molecules, built by connecting strong electron-donor (D) and electron-acceptor (A) substituents through a  $\pi$ -conjugated chemical bridge. [5] The commutation of the NLO properties in such systems can be achieved by reversibly altering the efficiency of the donor, of the acceptor, or still the electronic conjugation along the linker. The switching process can be triggered by using a variety of external perturbations such as light irradiation, pH variation, temperature, ion trapping, or electrical stimulation. Since light constitutes a fast, non-invasive and low-cost way to remotely control the state of a system, photochromic molecules constitute the most appropriate candidates for practical applications. However, recent works aiming at diversifying the device addressability has motivated the design of versatile systems, whose commutation can be triggered by using different orthogonal stimuli. [6] Moreover, the quest for high density storage devices also pushed molecular engineering developments towards multistate systems, which include several switchable units. [7–10]

In this regard, previous studies carried out in our groups have shown that push-pull compounds containing an indolino-oxazolidine (IND) unit, which can interconvert between a colorless closed form and a colored open one, display marked variations in their first hyperpolarizability ( $\beta$ ) upon switching. [11, 12] Moreover, the indolino-oxazolidine core was demonstrated to be 3-way addressable using optical, chemical, and electrical stimuli, [13, 14] while its combination with a dithienylethene unit was reported to behave as an effective 4-state NLO switch. [15]

Aiming at optimizing the NLO performances of this class of materials, we report here the synthesis, as well as the linear and NLO properties of a new derivative, involving an IND unit linked to a ferrocenyl (Fc) donor group through a vinylic bridge (compound **1**, Scheme 5.1). Since the discovery of Fc in 1951, [16] and the elucidation of its structure one year later, [17] numerous investigations have been carried out to take advantage of Fc donor properties, leading to unique optical, electrical, magnetic, and redox properties associated to high chemical and thermal stability. [18–22] Moreover, the ferrocenyl donor moiety is also an efficient building block to achieve large second-order NLO responses, [23–31] and, owing to its redox properties, to display redox-triggered NLO contrasts. [24, 28, 29] Compounds incorporating the Fc unit have also been investigated for their third-order NLO responses. [32] The present contribution focuses on the acido-triggered conversion of compound **1**. Here, the oxidation state of Fc remains unchanged upon switching but the push-pull  $\pi$ -conjugated character is strongly varied, leading to variations of linear and nonlinear

optical properties. The first hyperpolarizabilities of the closed form (CF) and protonated open form (POF) are determined by using the hyper-Rayleigh Scattering (HRS) technique, in combination with quantum chemical calculations. These joint experimental/theoretical characterizations provide a detailed understanding of the second-order NLO responses of the two forms, in relation with their geometrical and electronic structures in the ground and relevant excited states.

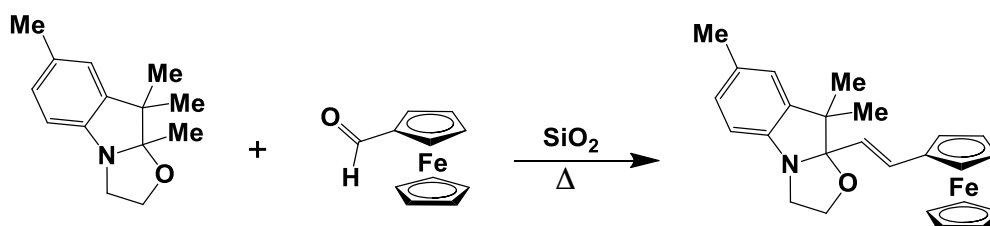


Scheme 5.1: Structure of the closed and protonated open forms of the IND-Fc derivative. The torsional angles  $\theta_{1-3}$  are displayed ( $\theta_1 = C_1 - C_2 - C_3 - C_4$ ;  $\theta_2 = C_2 - C_3 - C_4 - C_5$ ;  $\theta_3 = C_3 - C_4 - C_5 - C_6$ ), as well as (in red) the  $\pi$ -conjugated segment considered for the calculation of the bond length alternation.

## 5.2 Experimental and Theoretical Methods

### 5.2.1 Synthesis

The preparation of the indolino-oxazolidine derivatives is straightforward and can be resumed to a condensation between an aromatic aldehyde and the 2,3,3-trimethylindolinoxazolidine classically carried out in boiling ethanol. In the case of ferrocenylcarboxaldehyde, these classical experimental conditions are ineffective and the starting material was recovered after one night at reflux. If acidic or basic conditions are sometimes used to facilitate the condensation, in the present case, it leads to the formation of the corresponding diethyl acetal in place of the desired indolino-oxazolidine. Nevertheless, the indolinoxazolidine-ferrocenyl dyad can be easily obtained in moderate yield of 35% following the silica-mediated synthesis reported recently [33]. More details are provided in the Appendix B.



## 5.2.2 UV-visible and hyper-Rayleigh Scattering Measurements

Absorption spectra of acetonitrile solutions were recorded in the 300-800 nm region using a PerkinElmer Lambda 650 spectrophotometer. HRS measurements were performed using a 1064 nm incident wavelength, in acetonitrile solutions in the range of concentration  $3.8 \times 10^{-3}$  M for the closed form and  $4.0 \times 10^{-4}$  M for the protonated open form. The open form was obtained by adding vapor of trifluoroacetic acid. The details about the experimental procedure are described in previous reports. [34, 35] The HRS measurements were analyzed by decomposing the second-order NLO responses into dipolar ( $|\beta_{J=1}|$ ) and octupolar ( $|\beta_{J=3}|$ ) components. [34, 36] Within this multipolar description, the total harmonic scattered light for a binary solution (solvent/chromophore) in the diluted regime is given by:

$$I_{\Psi V}^{2\omega} = G f_L^2 \{ C_S [|\beta_{J=1}|^2 C_{\Psi V}]_S + C_X [|\beta_{J=1}|^2 C_{\Psi V}]_X \} \times 10^{-a_X^{2\omega} C_X} (I^\omega)^2 \quad (5.1)$$

where subscripts S and X are related to the solvent and chromophore, respectively. G is a constant containing geometrical, optical, and electrical factors of the experimental setup, C is the concentration (molarity) of the solvent or solute, and  $f_L$  is a local field correction approximated using the high frequency Lorentz-Lorenz spherical cavity expression.  $I^\omega$  is the incident intensity,  $a_X^{2\omega}$  accounts for the one-photon absorption of the total second-harmonic response from the chromophore.  $C_{\Psi V}$  is the orientational average of the molecular spherical components of the hyperpolarizability of the solute or solvent, expressed as:

$$C_{\Psi V} = \left( \frac{9}{45} + \frac{6}{105} \rho^2 \right) + \left( -\frac{20}{45} + \frac{10}{105} \rho^2 \right) \cos^2 \Psi + \left( \frac{12}{45} - \frac{12}{105} \rho^2 \right) \cos^4 \Psi \quad (5.2)$$

where  $\rho = |\beta_{J=3}|/|\beta_{J=1}|$  is the nonlinear anisotropy ratio. The total HRS hyperpolarizability ( $\beta_{HRS}$ ) and the depolarization ratio (DR) are given by the expressions:

$$\beta_{HRS} = \sqrt{\langle \beta_{HRS}^2 \rangle} = \sqrt{\frac{10}{45} |\beta_{J=1}|^2 + \frac{10}{105} |\beta_{J=3}|^2} = |\beta_{J=1}| \sqrt{\frac{2}{3} \left( \frac{1}{3} + \frac{1}{7} \rho^2 \right)} \quad (5.3)$$

$$DR = 9 \frac{1 + \frac{2}{7} \rho^2}{1 + \frac{12}{7} \rho^2} \quad (5.4)$$

By assuming Kleinman's conditions, [37] the dipolar and octupolar contributions to  $\beta_{HRS}$  read as follows:

$$|\beta_{J=1}|^2 = \frac{3}{5} \sum_{\zeta}^{x,y,z} \beta_{\zeta\zeta\zeta}^2 + \frac{6}{5} \sum_{\zeta \neq \eta}^{x,y,z} \beta_{\zeta\zeta\zeta} \beta_{\zeta\eta\eta} + \frac{3}{5} \sum_{\zeta \neq \eta}^{x,y,z} \beta_{\eta\zeta\zeta}^2 \quad (5.5)$$

$$|\beta_{J=3}|^2 = \frac{2}{5} \sum_{\zeta}^{x,y,z} \beta_{\zeta\zeta\zeta}^2 - \frac{6}{5} \sum_{\zeta \neq \eta}^{x,y,z} \beta_{\zeta\zeta\zeta} \beta_{\zeta\eta\eta} + \frac{12}{5} \sum_{\zeta \neq \eta}^{x,y,z} \beta_{\eta\zeta\zeta}^2 - \frac{3}{5} \sum_{\zeta \neq \eta \neq \xi}^{x,y,z} \beta_{\eta\zeta\zeta} \beta_{\eta\xi\xi} + \sum_{\zeta \neq \eta \neq \xi}^{x,y,z} \beta_{\zeta\eta\xi}^2 \quad (5.6)$$

where  $\beta_{\zeta\eta\xi}$  is one of the  $\beta$ -tensor components in the molecular frame.

### 5.2.3 Quantum Chemical Calculations

Geometrical structures of both forms of compound **1**, as well as their linear and nonlinear optical properties, were determined using methods based on density functional theory (DFT). The choice of exchange-correlation functionals (XCFs) and basis set was made on the basis of former studies on metallocenes. [20, 27, 30, 31] So, full geometry optimizations were performed using the B3LYP [38, 39] XCF, together with the 6-311G(d) basis set. All optimized structures correspond to stationary points on the potential energy surfaces, as confirmed by only real vibrational frequencies. Linear optical properties were determined at the time-dependent (TD) DFT level, using the B3PW91 functional [40] and the 6-311G(d) basis set. The static and dynamic second-order NLO properties were also calculated using TDDFT, in combination with the range-separated CAM-B3LYP functional [41] and the larger 6-311+G(d) basis set, which includes an additional set of diffuse Gaussian functions on the valence shell. Moreover, to gauge the magnitude of electron correlation effects, additional XCFs (B3LYP, BPW91, and M06-2X [42]) as well as the coupled-perturbed Hartree-Fock (CPHF) and the second-order Møller-Plesset perturbation theory (MP2) approaches were further employed to compute the first hyperpolarizabilities of the closed and open forms, as well as their contrasts. These level of approximation were shown to be well suited for computing the first hyperpolarizabilities of  $\pi$ -conjugated organic chromophores, including indolinooxazolidine derivatives. [4, 14] Solvent (acetonitrile) effects were included in all calculations by means of the polarizable continuum model in its integral equation formalism (IEF-PCM). [43, 44] All theoretical calculations were carried out by using the Gaussian 09 package [45]. All  $\beta$  values are reported within the Taylor series formalism (T convention), and are given in atomic units (1 au of  $\beta = 3.6310^{-42} \text{ m}^4\text{V}^{-1} = 3.2063 \times 10^{-53} \text{ C}^3\text{m}^3\text{J}^{-2} = 8.641 \times 10^{-33} \text{ esu}$ ).

## 5.3 Results and Discussion

### 5.3.1 Structural Properties

As presented in Table 5.1, both forms of compound **1** possess several stable conformers characterized by different torsion angles and bond length alternation (BLA) along the  $\pi$ -conjugated vinylic bridge (in red in Scheme 5.1). The relative populations of each conformer were estimated using a Boltzmann statistics at room temperature on the basis of the relative Gibbs free energies ( $\Delta G^\ominus$ ). The optimized structures of the conformers of both forms are presented in Figures B.1 and B.2 (Appendix B).

For the closed form, the possible variations of  $\theta_2$  and  $\theta_3$  give rise to four different conformers, while the absolute value of the torsion angle  $\theta_1$  lie around  $100^\circ$  in all cases. Conformers displaying  $\theta_2$  values close to  $180^\circ$  (I, IV) are more stable by about 6-7 kcal/mol than those for which  $|\theta_2| \approx 0^\circ$  (II, III). Increasing  $\theta_3$  from  $\sim 14^\circ$  (IV) to  $\sim 163^\circ$  (I) further destabilizes the compound by 1 kcal/mol. Therefore, only conformers I and IV achieve significant populations, of 15% and 85%, respectively. All values of BLA lie around 0.15 Å.

For the protonated open form, five stable conformers are found. Contrary to the case of the closed form, the  $\theta_1$  angle can adopt different values, with a significant influence on  $\Delta G^\ominus$  and therefore on the conformer populations. Conformers for which  $\theta_1$  is close to zero (IV, V) are the most stable ones, and quasi isoenergetic. Increasing  $|\theta_1|$  from  $\sim 0^\circ$  to  $\sim 160^\circ$  (I, II) increases  $\Delta G^\ominus$  to 2-3 kcal/mol. The conformer III, for which  $\theta_2 \sim 9^\circ$  (which corresponds to a *cis*-configuration of the vinylic bridge), is much higher in energy and is not populated. Only conformers IV and V exist at room temperature, with relative populations of 30% and 68%. The BLA values of the POFs are about twice smaller than those of closed forms, due to the increased  $\pi$ -electron conjugation along the molecule, from the Fc to IND moieties. On the other hand, the opening of the oxazolidine ring has no influence on the Fc structure, which displays similar distances between the Fe atom and the ferrocenyl plane ( $\sim 1.68$  Å), as well as similar BLA within the cyclopentadienyl rings in both closed and open forms.

### 5.3.2 Linear Optical Properties

Experimental and theoretical UV-visible absorption spectra in acetonitrile are shown in Figure 5.1 for both forms of compound **1**, together with the electron density difference between the ground and photo-excited states. A more detailed comparison between the calculated vertical excitation energies and experimental absorption maxima is given in Tables 5.2 and 5.3. The photo-induced charge displacement ( $q^{CT}$ ) and the charge transfer distance ( $d^{CT}$ ), [46, 47] as well as the dipole moment variation between the ground and excited states ( $\Delta\mu_{ge} = |\vec{\mu}_e - \vec{\mu}_g| = q^{CT} \times d^{CT}$ ) are

Table 5.1: Torsion angles ( $\theta_{1-3}$ , degrees) and bond length alternation (BLA, Å) of the various conformers of the closed and protonated open forms, as calculated at the B3LYP/6-311G(d) level in acetonitrile. Last columns: Relative Gibbs free energies ( $\Delta G^\ominus$ , kcal/mol) and populations (%) estimated using a Boltzmann statistics at room temperature.

<i>Conf.</i>	$\theta_1$	$\theta_2$	$\theta_3$	<i>BLA</i>	$\Delta G^\ominus$	%
Closed Form (CF)						
I	-110.7	-177.5	163.1	0.148	1.0	15.3
II	110.1	-1.8	156.9	0.146	6.6	0.0
III	88.8	-1.5	17.4	0.146	6.8	0.0
IV	112.5	-179.7	14.2	0.148	0.0	84.7
Protonated Open Form (POF)						
I	162.4	-179.3	8.0	0.059	3.3	0.2
II	156.0	-178.4	171.3	0.060	2.1	2.0
III	-133.7	8.9	25.8	0.088	11.4	0.0
IV	-4.1	-179.9	9.8	0.057	0.5	30.0
V	-2.8	178.6	176.9	0.058	0.0	67.8

also reported. The topologies of the molecular orbitals (MOs) involved in the main electronic transitions are depicted in the Appendix B (Figures B.3 and B.4) while the spectroscopic quantities for all conformers are given in Table B.1.

Experimentally, the visible absorption band of the closed form exhibits one weak maxima at 425 nm, which is assigned to a metal-to-ligand charge transfer (MLCT) transition (*i.e.* from the Fe atom to the cyclopentadienyl rings). The computed spectrum globally shows a similar shape and intensity, the main absorption band being shifted to larger wavelengths with respect to experiment. The absorption band in the 450-600 nm region is constituted of two electronic transitions,  $S_0 \rightarrow S_3$  at 495 nm and  $S_0 \rightarrow S_2$  at 556 nm, characterized by weak oscillator strengths. In both cases, the dipole moment variation between the ground and excited states is very small (0.52 D and 0.40 D, respectively), consistently with the shape of the MOs involved in the electronic excitations and with the density difference maps (Figure 5.1, a and b). These latter show indeed that the photo-induced density variations

Table 5.2: Maximum absorption wavelengths ( $\lambda_{max}$ , nm), molar extinction coefficients ( $\varepsilon_{max}$ ,  $M^{-1} cm^{-1}$ ), full width at half maximum (FWHM,  $cm^{-1}$ ), and oscillator strengths ( $f^a$ ) measured in acetonitrile, for the closed (CF) and protonated open forms (POF) of compound **1**.

Form	$\lambda_{max}$	$\varepsilon_{max}$	FWHM	$f^a$
CF	425	680	7500	0.021
POF	407	23000	4600	0.433
	606	8100	3600	0.119

<sup>a</sup> estimated using  $4.3 \times 10^{-9} \times \varepsilon_{max} \times FWHM$

Table 5.3: Vertical transition wavelengths ( $\lambda_{ge}$ , nm), energies ( $\Delta E_{ge}$ , eV), oscillator strengths ( $f_{ge}$ ), dipole moment variations ( $\Delta\mu_{ge}$ , D), charge transfers ( $q^{CT}$ , |e|), charge transfer distances ( $d^{CT}$ , Å), and dominant one-electron transitions (and their % weights) for the lowest-energy dipole-allowed excitations  $S_0 \rightarrow S_N$  of the closed (CF) and protonated open forms (POF) of compound **1**, as calculated at the TDDFT/B3PW91/6-311G(d) level in acetonitrile and averaged over the various conformers.

Form	Transition	$\lambda_{ge}$	$\Delta E_{ge}$	$f_{ge}$	$\Delta\mu_{ge}$	$q^{CT}$	$d^{CT}$	Excitation % comp.
CF	$S_0 \rightarrow S_3$	495	2.506	0.002	0.517	0.554	0.194	H-1→L+2 (31); H-3→L (21) H-3→L+2 (12)
	$S_0 \rightarrow S_2$	556	2.219	0.003	0.398	0.485	0.170	H→L (29); H-1→L+2 (27) H-1→L+3 (14)
POF	$S_0 \rightarrow S_7$	433	2.872	1.097	1.923	0.528	0.761	H-2→L (75)
	$S_0 \rightarrow S_2$	675	1.843	0.124	7.207	0.753	1.995	H→L (69); H-1→L+2 (15)

are localized on the Fc unit and the vinylic chain with no delocalization on the indolino-oxazolidine part, thus giving rise to small CT distances ( $d^{CT} < 0.20$  Å).

The absorption spectrum of the protonated open form exhibits two absorption bands, whose wavelengths, although red-shifted, are well reproduced by the TDDFT calculations. The relative intensity of the two bands is also qualitatively reproduced by the calculations, although the intensity of the high-energy band is overestimated. The less intense band at larger wavelength (exp. 606 nm, theo. 675 nm,  $S_0 \rightarrow S_2$ ) is attributed to a MLCT transition, while the most intense one, located at smaller wavelength (exp. 407 nm, theo. 433 nm,  $S_0 \rightarrow S_7$ ), is ascribed to a delocalized  $\pi - \pi^*$  charge transfer transition. Compared to the closed form, owing to  $\pi$ -electron conjugation, the opening of the indolino-oxazolidine ring induces a large increase of the charge transfer distance upon photo-excitation ( $d^{CT}$ ), which translates into large dipole moment differences  $\Delta\mu_{ge}$  between the ground and excited states: 7.20 D and

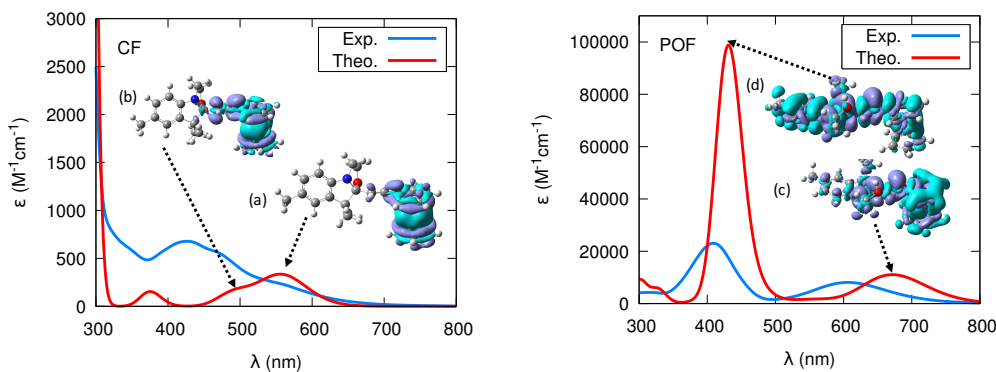


Figure 5.1: UV-vis absorption spectra measured and calculated at the TDDFT/B3PW91/6-311G(d) level in acetonitrile for closed (left) and protonated open (right) forms, and electron density difference (isoval. = 0.02 a.u.) between the ground and dipole-allowed excited states. The purple-colored regions indicate the regions in which the electron density increases upon excitation while the blue-colored regions indicate those in which the electron density decreases.

1.92 D for the  $S_0 \rightarrow S_2$  and  $S_0 \rightarrow S_7$  transitions, respectively. Moreover, the charge transfer directions of these two electronic transitions are almost opposite, with an angle of 168 degrees between their  $\Delta\mu_{ge}$  vectors, so that their contributions to the first hyperpolarizability cancel each other. Those enhancements and opposite charge transfer directions can be observed on the density difference maps (Figure 5.1, c and d), where in the case of the  $S_0 \rightarrow S_2$  transition ( $d^{CT} \sim 2.0 \text{ \AA}$ ), the electron density goes from the ferrocenyl unit to the ethylenic bridge, and to a lesser extent to the indolinoxazolidine moiety. In the case of the  $S_0 \rightarrow S_7$  transition, the density variation further delocalizes over the whole molecule, with a global displacement from the indolinoxazolidine moiety to the ethylene bridge and density reorganization in the ferrocenyl unit. This gives rise to a CT distance ( $d^{CT} \sim 0.8 \text{ \AA}$ ), larger than for the CF but smaller than for the  $S_0 \rightarrow S_2$  transition of the POF.

### 5.3.3 Nonlinear Optical Properties

The three-dimensional (3D) evolution of the HRS intensity as a function of the incident power and concentration is presented in Figure 5.2 for both forms of compound **1**. These plots evidence the linear evolution of the intensity of scattered second harmonic light with respect to the chromophore concentration, as well as its quadratic behavior with respect to the intensity of the incident beam. Polarization curves, also displayed in Figure 5.2, show that both CF and POF behave as typical 1D NLO scatterers, [34] for which the first hyperpolarizability tensor is dominated by one single diagonal component.

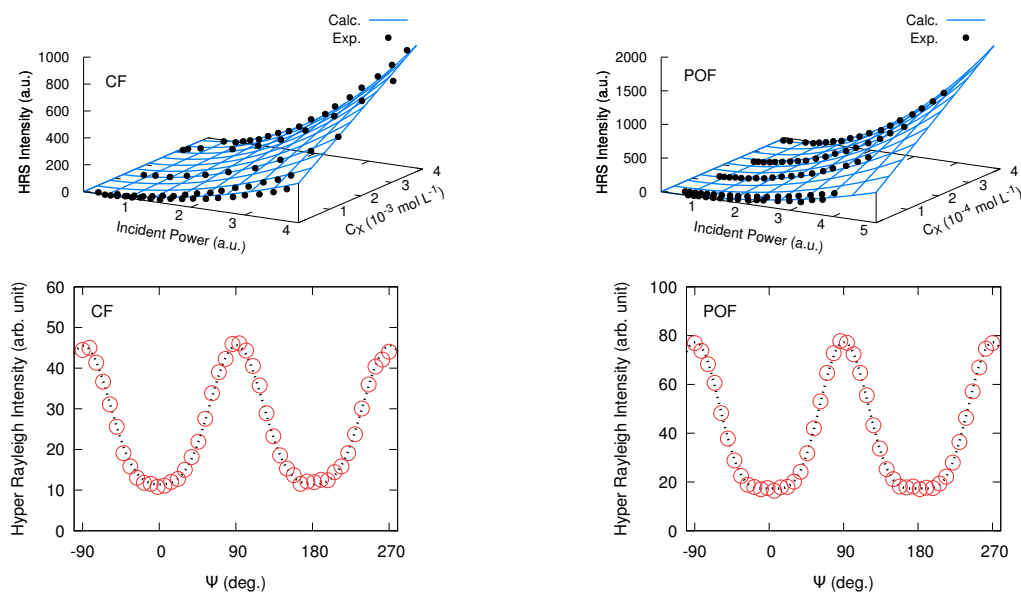


Figure 5.2: HRS responses of the closed (left) and protonated open (right) forms in acetonitrile. Top: 3D representation of the HRS intensity ( $I^{2\omega}$ ) as a function of the incident power ( $I^\omega$ ) and concentration. Bottom: polarization profiles.

The second-order nonlinear responses of the CF and POF are summarized in Table 5.4. The reported quantities include the total HRS hyperpolarizabilities ( $\beta_{HRS}$ ), the dipolar ( $|\beta_{J=1}|$ ) and octupolar ( $|\beta_{J=3}|$ ) components, as well as their associated depolarization (DR) and nonlinear anisotropy ratios ( $\rho$ ). Moreover, to get rid of frequency dispersion effects and facilitate the comparisons with the calculations, the HRS hyperpolarizabilities measured at  $\lambda = 1064$  nm were extrapolated to the 1907 nm wavelength, which is out of resonant conditions, as well as to the static limit ( $\lambda = \infty$ ). However, the simple two-state approximation (TSA) [48] cannot be employed because i) for the CF, the experimental second harmonic wavelength (532 nm) falls in the tail of the absorption band and is therefore in resonance and ii) for the POF, this wavelength falls in between two excited states, of which the  $\beta$  contributions have opposite signs and partly cancel each other. Therefore, for the CF, following previous investigations, [49, 50] an extension of the TSA model including homogeneous broadening has been employed. On the other hand, for the POF, in addition to homogeneous broadening the two lowest-energy excited states were included in the treatment. Then, the  $\beta_{HRS}$  values computed at the CAM-B3LYP/6-311+G(d) level using the different wavelengths, and averaged over the various conformers, are also reported. The detailed values for the different conformers of both forms are given in Table B.2 (Appendix B).

As observed for all derivatives of this family, the increase of the  $\pi$ -electron conjugation associated to the opening of the indolino-oxazolidine ring strongly enhances the  $\beta_{HRS,1064}$  response, here by a factor 4.7. The  $\beta_{POF}/\beta_{CF}$  ratio decreases (1.9)

Table 5.4: HRS hyperpolarizability ( $\beta_{HRS,1064}$ ), dipolar ( $|\beta_{J=1}|$ ) and octupolar ( $|\beta_{J=3}|$ ) contributions, as well as depolarization (DR) and  $\rho$  ratios, deduced from HRS measurements at 1064 nm, and the corresponding static and dynamic (at 1907 nm) extrapolated values,  $\beta_{HRS,\infty}$  and  $\beta_{HRS,1907}$ , in comparison to the CAM-B3LYP/6-311+G(d) values calculated at the same wavelengths and averaged over the various conformers. The  $\beta_{POF}/\beta_{CF}$  contrasts are given in parentheses. All  $\beta$  values are given in atomic units using the T convention.

	Exp.		Theo.	
	CF	POF	CF	POF
$\beta_{HRS,1064}$	3600 <sup>a</sup>	16800 <sup>a</sup> (4.7)	458	32246 (67.8)
$ \beta_{J=1} $	6400 <sup>a</sup>	31000 <sup>a</sup>	865	59604
$ \beta_{J=3} $	6600 <sup>a</sup>	26600 <sup>a</sup>	701	51269
DR	4.41	4.81	5.00	4.80
$\rho$	1.04 $\pm$ 0.01	0.86 $\pm$ 0.01	0.80	0.86
$\beta_{HRS,1907}$	1400 <sup>b</sup>	2700 <sup>c</sup> (1.9)	378	3422 (9.1)
$\beta_{HRS,\infty}$	900 <sup>b</sup>	1300 <sup>c</sup> (1.4)	475	4243 (8.9)

<sup>a</sup> With relative accuracy of *ca* 5%.

<sup>b</sup> Using a FWHM value of 0.33 eV.

<sup>c</sup> Using FWHM values of 0.44 and 0.56 eV for the first and second absorption bands, respectively.

when considering  $\beta_{HRS}$  values extrapolated to 1907 nm. The TDDFT calculations reproduce these trends, though the  $\beta_{POF}/\beta_{CF}$  ratios are overestimated. At 1907 nm, the agreement between the calculated and experimental  $\beta_{HRS}$  values is good for the POF but not for the CF, which highlights the difficulty of extrapolating  $\beta_{HRS,1064}$  due to the strong resonance effects. Note that the experimental and calculated static values are not comparable because in the calculations the static and dynamic dielectric constants - used in the PCM calculations - differ much whereas all experimental values refer to optical dielectric constants. All DR values are close to 5, evidencing that the chromophores can be considered as 1D NLOphores with one dominant diagonal component in the  $\beta$  tensor.

Finally, to get further insights on the impact of the level of calculation on the NLO responses, additional TDDFT calculations were performed using a selection of XCFs. CPHF and FF/MP2 results were also carried out, in order to size up the magnitude of electron correlation effects. The results are collected in Tables B.3 and B.4 (Appendix B), while the  $\beta_{POF}/\beta_{CF}$  ratios are compared in Figure 5.3. The results show that all levels of calculation overestimate the variation of the  $\beta_{HRS,1064}$  response upon the CF $\rightarrow$ POF commutation, as already found for other derivatives of this family. [14] This overestimation is particularly marked with CAM-B3LYP, and to a lesser extent with BPW91. Going from CPHF to MP2 enhances the static  $\beta_{HRS}$  values by a factor 1.7 for the closed form, and by a factor 3 for the open form, leading to an increase of the  $\beta$  contrast by roughly a factor 2.

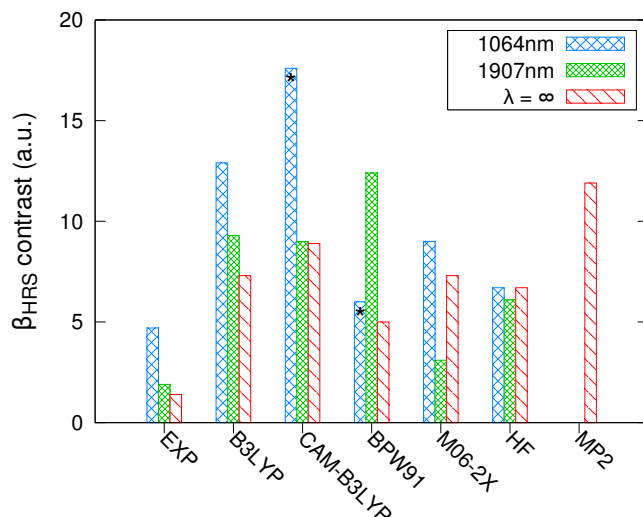


Figure 5.3:  $\beta_{HRS}$  contrasts between the CF and POF, calculated in acetonitrile using different functionals and methods in association with the 6-311+G(d) basis set (\*value divided by 4).

## 5.4 Conclusion

This paper has reported the synthesis and the characterization of the linear and second-order nonlinear optical properties of a new derivative of the indolino-oxazolidine family, which exploits the strong donor capacity of the ferrocenyl unit. HRS experiments show that the pH-triggered commutation between the closed and protonated open form of this compound enhances the first hyperpolarizability by roughly a factor 5, as a result of the increase of the electron conjugation within the molecule. Although derivatives exhibiting larger  $\beta$  responses in their nonlinear optical active form and larger  $\beta_{POF}/\beta_{CF}$  contrasts were previously reported within this class of materials, [11, 12], the figure of merit of this ferrocenyl-based compound is high enough for device application, since the measured contrast is sufficiently large to allow unambiguous distinction between the two forms. Quantum chemical calculations of the linear and nonlinear optical properties are at least in qualitative agreement with the experimental trends. They show that  $\beta$  of the protonated open form originates from two low-energy excited states, of which the contributions partly cancel each other due to the opposite directions of the photo-excited charge transfer.

# Bibliography

---

- [1] B. J. Coe. Molecular materials possessing switchable quadratic nonlinear optical properties. *Chem. Eur. J.*, **5**(9):2464–2471, 1999.
- [2] J. A. Delaire and K. Nakatani. Linear and nonlinear optical properties of photochromic molecules and materials. *Chem. Rev.*, **100**(5):1817–1846, 2000.
- [3] I. Asselberghs, K. Clays, A. Persoons, M. D. Ward, and J. McCleverty. Switching of molecular second-order polarizability in solution. *J. Mater. Chem.*, **14**:2831–2839, 2004.
- [4] F. Castet, V. Rodriguez, J.-L. Pozzo, L. Ducasse, A. Plaquet, and B. Champagne. Design and characterization of molecular nonlinear optical switches. *Acc. Chem. Res.*, **46**(11):2656–2665, 2013.
- [5] T. Verbiest, S. Houbrechts, M. Kauranen, and K. Clays. Second-order nonlinear optical materials: recent advances in chromophore design. *J. Mater. Chem.*, **7**(11):2175–2189, 1997.
- [6] P. Beaujean, F. Bondu, A. Plaquet, J. Garcia-Amorós, J. Cusido, F. M. Raymo, F. Castet, V. Rodriguez, and B. Champagne. Oxazines: a new class of second-order nonlinear optical switches. *J. Am. Chem. Soc.*, **138**(15):5052–5062, 2016.
- [7] G. Szalóki, G. Sevez, G. Berthet, J.-L. Pozzo, and S. Delbaere. A simple molecule-based octastate switch. *J. Am. Chem. Soc.*, **136**:13510–13513, 2014.
- [8] J. Quertinmont, B. Champagne, F. Castet, and M. Hidalgo Cardenuto. Explicit versus implicit solvation effects on the first hyperpolarizability of an organic biphotochrome. *J. Phys. Chem. A*, **119**(21):5496–5503, 2015.
- [9] J. Yuan, Y. Yuan, X. Tian, J. Sun, and Y. Ge. Spirooxazine-fulgide biphotochromic molecular switches with nonlinear optical responses across four states. *J. Phys. Chem. C*, **120**(27):14840–14853, 2016.

- [10] S. Hadj Mohamed, J. Quertinmont, S. Delbaere, L. Sanguinet, and B. Champagne. Assessing the structure of octastate molecular switches using 1H NMR density functional theory calculations. *J. Phys. Chem. C*, **122**:1800–1808, 2018.
- [11] L. Sanguinet, J.-L. Pozzo, V. Rodriguez, F. Adamietz, F. Castet, L. Ducasse, and B. Champagne. Acido- and photo-triggered NLO properties enhancement. *J. Phys. Chem. B*, **109**(22):11139–11150, 2005.
- [12] F. Mançois, J.-L. Pozzo, J. Pan, F. Adamietz, V. Rodriguez, L. Ducasse, F. Castet, A. Plaquet, and B. Champagne. Two-way molecular switches with large nonlinear optical contrast. *Chem.-Eur. J.*, **15**(11):2560–2571, 2009.
- [13] F. Bondu, R. Hadji, G. Szalóki, O. Alévêque, L. Sanguinet, J.-L. Pozzo, D. Cavnagnat, T. Buffeteau, and V. Rodriguez. Huge electro-/photo-/acidoinduced second-order nonlinear contrasts from multiaddressable indolinooxazolodine. *J. Phys. Chem. B*, **119**(22):6758–6765, 2015.
- [14] K. Pielak, F. Bondu, L. Sanguinet, V. Rodriguez, B. Champagne, and F. Castet. Second-order nonlinear optical properties of multiaddressable indolinooxazolodine derivatives: joint computational and hyper-Rayleigh scattering investigations. *J. Phys. Chem. C*, **121**(3):1851–1860, 2017.
- [15] F. Bondu, J. Quertinmont, V. Rodriguez, J.-L. Pozzo, A. Plaquet, B. Champagne, and F. Castet. Second-order nonlinear optical properties of a dithienylethene-indolinooxazolodine hybrid: a joint experimental and theoretical investigation. *Chem. Eur. J.*, **21**(51):18749–18757, 2015.
- [16] P. L. Pauson and T. J. Kealy. A new type of organo-iron compound. *Nature*, **168**:1039–1040, 1951.
- [17] G. Wilkinson, M. Rosenblum, M. C. Whiting, and R. B. Woodward. The structure of iron bis-cyclopentadienyl. *J. Am. Chem. Soc.*, **74**:2125–2126, 1952.
- [18] N. G. Connelly and W. E. Geiger. Chemical redox agents for organometallic chemistry. *Chem. Rev.*, **96**:877–910, 1996.
- [19] R. Horikoshi and T. Mochida. Ferrocene-containing coordination polymers: ligand design and assembled structures. *Eur. J. Inorg. Chem.*, **2010**(34):5355–5371, 2010.
- [20] A. Moore, K. Shufelt, B. G. Janesko, and K. N. Green. Ligand effects on the redox behavior of bimetallic tungsten(0)/ferrocene(II) complexes. *Polyhedron*, **72**:50–55, 2014.

- [21] P. Chinapang, V. Ruangpornvisuti, M. Sukwattanasinitt, and P. Rashatasakhon. Ferrocenyl derivative of 1,8-naphthalimide as a new turn-on fluorescent sensor for Au(III) ion. *Dyes Pigm.*, **112**:236–238, 2015.
- [22] J. Xiang, T.-K. Wang, Q. Zhao, W. Huang, C.-L. Ho, and W.-Y. Wong. Ferrocene-containing poly(fluorenylethynylene)s for nonvolatile resistive memory devices. *J. Mater. Chem. C*, **4**(5):921–928, 2016.
- [23] S. Barlow, H. E. Bunting, C. Ringham, J. C. Green, G. U. Bublitz, S. G. Boxer, J. W. Perry, and S. R. Marder. Studies of the electronic structure of metallocene-based second-order nonlinear optical dyes. *J. Am. Chem. Soc.*, **115**(121):3715–3723, 1999.
- [24] I. Asselberghs, K. Clays, A. Persoons, A. M. McDonagh, M. D. Ward, and J. McCleverty. In situ reversible electrochemical switching of the molecular first hyperpolarizability. *Chem. Phys. Lett.*, **368**:408–411, 2003.
- [25] N. Tsuboya, R. Hamasaki, M. Ito, M. Mitsuishi, T. Miyashita, and Y. Yamamoto. Nonlinear optical properties of novel fullerene-ferrocene hybrid molecules. *J. Mater. Chem.*, **13**(3):511–513, 2003.
- [26] A. M. Asiri, G. A. Baghaffar, M. S. Al-Amoudi, and A. G. Al-Sehemi. Synthesis, characterization, thermal stability and nonlinear optical properties of push-pull chromophores containing ferrocene donor group. *Optoelectron. Adv. Mat.*, **3**(4):364–370, 2009.
- [27] S. Salman, J.-L. Brédas, S. R. Marder, V. Coropceanu, and S. Barlow. Dipolar ferrocene and ruthenocene second-order nonlinear optical chromophores: a time-dependent density functional theory investigation of their absorption spectra. *Organometallics*, **32**(20):6061–6068, 2013.
- [28] W.-Y. Wang, S.-L. Sun, and Y.-Q. Qiu. Redox control of ferrocene-based complexes with systematically extended  $\pi$ -conjugated connectors: switchable and tailorable second order nonlinear. *Phys. Chem. Chem. Phys.*, **10**:4900–4910, 2014.
- [29] S. Kaur, S. Dhoun, G. Depotter, P. Kaur, K. Clays, and K. Singh. Synthesis, linear and nonlinear optical properties of thermally stable ferrocene-diketopyrrolopyrrole dyads. *RSC Adv.*, **5**:84643–84656, 2014.
- [30] W.-Y. Wang, L. Wang, N.-N. Ma, C.-L. Zhu, and Y.-Q. Qiu. Ferrocene/fullerene hybrids showing large second-order nonlinear optical activities: impact of the cage unit size. *Dalton Trans.*, **44**(21):10078–10088, 2015.

- [31] S. J. Wang, Y. F. Wang, and C. Cai. Multidecker sandwich complexes  $V_n\text{Ben}_{n+1}$  ( $n = 1, 2, 3$ ) as stronger electron donor relative to ferrocene for designing high-performance organometallic second-order NLO chromophores: evident layer effect on the first hyperpolarizability and two-dimensional NLO character. *J. Phys. Chem. C*, **119**(10):5589–5595, 2015.
- [32] Y. Shi, L. Xiao, D. Wu, F. Li, D. Li, J. Zhang, S. Li, H. Zhou, J. Wu, and Y. Tian. Synthesis, crystal structure, electrochemistry and third-order nonlinear optical properties of two novel ferrocene derivatives. *J. Organomet. Chem.*, **817**:36–42, 2016.
- [33] G. Szalóki and L. Sanguinet. Silica-mediated synthesis of indolinooxazolidine-based molecular switches. *J. Org. Chem.*, **80**(8):3949–3956, 2015.
- [34] F. Castet, E. Bogdan, A. Plaquet, L. Ducasse, B. Champagne, and V. Rodriguez. Reference molecules for nonlinear optics: a joint experimental and theoretical investigation. *J. Chem. Phys.*, **136**(2):024506, 2012.
- [35] F. Castet, M. Blanchard-Desce, F. Adamietz, Y. M. Poronik, D. T. Gryko, and V. Rodriguez. Experimental and theoretical investigation of the first-order hyperpolarizability of octupolar merocyanine dyes. *ChemPhysChem*, **15**(12):2575–2581, 2014.
- [36] V. Rodriguez, J. Grondin, F. Adamietz, and Y. Danten. Local structure in ionic liquids investigated by hyper-Rayleigh scattering. *J. Phys. Chem. B*, **114**(46):15057–15065, 2010.
- [37] D. A. Kleinman. Nonlinear dielectric polarization in optical media. *Phys. Rev.*, **126**:1977–1979, 1962.
- [38] A. D. Becke. Density-functional thermochemistry. III. The role of exact exchange. *J. Chem. Phys.*, **98**(7):5648–5652, 1993.
- [39] P. J. Stephens, F. J. Devlin, C. F. Chabalowski, and M. J. Frisch. Ab initio calculation of vibrational absorption and circular dichroism spectra using density functional force fields. *J. Phys. Chem.*, **98**(45):11623–11627, 1994.
- [40] J. P. Perdew and Y. Wang. Accurate and simple analytic representation of the electron-gas correlation energy. **45**(23):244–249, 1992.
- [41] T. Yanai, D. P. Tew, and N. C. Handy. A new hybrid exchange-correlation functional using the coulomb-attenuating method (CAM-B3LYP). *Chem. Phys. Lett.*, **393**(1-3):51–57, 2004.

- [42] Y. Zhao and D. G. Truhlar. The M06 suite of density functionals for main group thermochemistry, thermochemical kinetics, noncovalent interactions, excited states, and transition elements: two new functionals and systematic testing of four M06-class functionals and 12 other functionals. *Theor. Chem. Acc.*, **120**:215–241, 2008.
- [43] B. Mennucci, R. Cammi, and J. Tomasi. Medium effects on the properties of chemical systems: electric and magnetic response of donor-acceptor systems within the polarizable continuum model. *Int. J. Quantum Chem.*, **75**(4-5):767–781, 1999.
- [44] J. Tomasi, B. Mennucci, and R. Cammi. Quantum mechanical continuum solvation models. *Chem. Rev.*, **105**(8):2999–3093, 2005.
- [45] M. J. Frisch, G. W. Trucks, H. B. Schlegel, G. E. Scuseria, M. A. Robb, J. R. Cheeseman, G. Scalmani, V. Barone, B. Mennucci, G. A. Petersson, H. Nakatsuji, M. Caricato, X. Li, H. P. Hratchian, A. F. Izmaylov, et al. Gaussian 09 revision d01. Gaussian Inc. Wallingford CT 2009.
- [46] T. Le Bahers, C. Adamo, and I. Ciofini. A qualitative index of spatial extent in charge-transfer excitations. *J. Chem. Theory Comput.*, **7**(8):2498–2506, 2011.
- [47] D. Jacquemin, T. L. Bahers, C. Adamo, and I. Ciofini. What is the est’ atomic charge model to describe through-space charge-transfer excitations? *Phys. Chem. Chem. Phys.*, **14**(16):5383, 2012.
- [48] J. L. Oudar and D. S. Chemla. Hyperpolarizabilities of the nitroanilines and their relations to the excited state dipole moment. *J. Chem. Phys.*, **66**(6):2664–2668, 1977.
- [49] J. Campo, W. Wenseleers, E. Goovaerts, M. Szablewski, and G. Cross. Accurate determination and modeling of the dispersion of the first hyperpolarizability of an efficient zwitterionic nonlinear optical chromophore by tunable wavelength hyper-Rayleigh scattering. *J. Phys. Chem. C*, **112**:287–296, 2008.
- [50] E. De Meulenaere, I. Asselberghs, M. de Wergifosse, E. Botek, S. Spaepen, B. Champagne, J. Vanderleyden, and K. Clays. Second-order nonlinear optical properties of fluorescent proteins for second harmonic imaging. *J. Mater. Chem.*, **19**:7514–7519, 2009.



# Dynamical Behavior and Contrasted Second Harmonic Generation Responses in Acido-Triggered Molecular Switches

K. Pielak, C. Tonnelé, L. Sanguinet, E. Cariati, S. Righetto, L. Muccioli, F. Castet and B. Champagne. *J. Phys. Chem. C*, Accepted

*Second-order nonlinear optical molecular switches are systems displaying marked variations of their second harmonic generation (SHG) responses upon external stimulation. This chapter shows a combination of a multiscale computational method and experimental characterizations to provide a full description of the SHG responses of molecular switches built from the association of the indolinooxazolidine unit to a bithiophene donor. In chloroform solutions, the addition of trifluoroacetic acid triggers the switching from a neutral closed form to a protonated open form, making an ion pair with the trifluoroacetate counterion and induces a strong enhancement of the SHG responses. The numerical simulations i) evidence how the large and rapid thermally induced geometrical fluctuations lead to broadening the SHG responses distributions, making even difficult the determination of their sign, ii) rationalize the variations of these responses as a function of the closure/opening of the oxazolidine ring and of the nature of its chemical substitution, and iii) call into question common assumptions employed when analyzing the experimental SHG responses.*

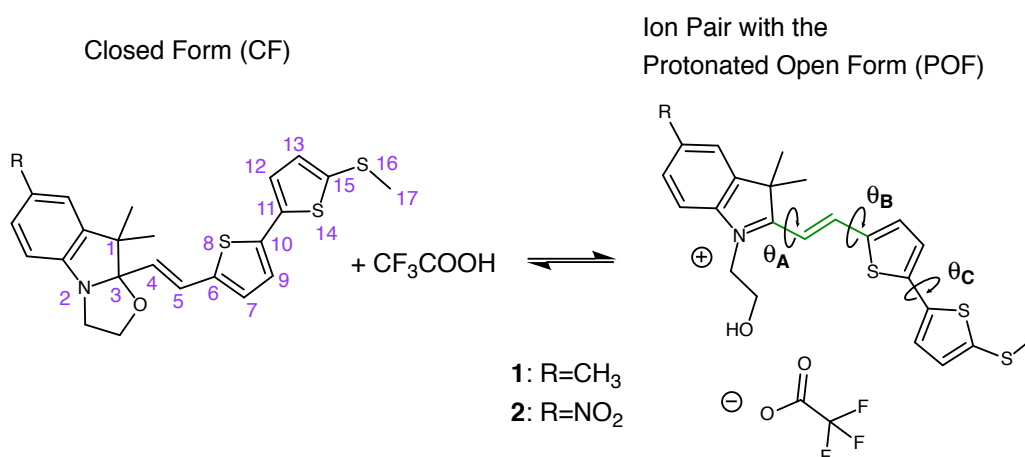
In this chapter, I performed the MD modelling and *ab initio* simulations, as well as carried out the EFISHG experiments.

## 6.1 Introduction

Molecular optical switches are systems displaying marked contrast in their optical properties upon chemical transformations triggered either by photonic, chemical, or electrochemical signals. As such, these molecular systems constitute the building units of nanoscale devices allowing switchable logic functions or data storage, [1, 2] in which different types of optical responses can be exploited to probe the electronic state of the system. In the last years, a number of studies have concentrated on organic compounds exhibiting contrasts of nonlinear optical (NLO) properties between their metastable states, [3–5] which offer the possibility of reading the stored information without altering it. Optimizing the performances of such systems, in terms of efficiency of the switching process and amplitude of the NLO contrasts between the NLO-active (ON) and NLO-inactive (OFF) states, requires multidisciplinary approaches combining molecular synthesis, spectroscopic characterizations, and numerical simulations. These techniques enabled establishing design guidelines to achieve large NLO responses and contrasts in push-pull  $\pi$ -conjugated systems, by a controlled tuning of the relative strength of the donor and acceptor moieties, or a modulation of their electronic communication through alteration of the  $\pi$ -conjugated linker. [3–18] Besides these traditional transformations, some of these switches, like poly(phenanthrene), exhibit dynamical changes from coil to helical conformation by varying the nature of the solvent, which further modify the  $\pi$ -conjugation and therefore of the second-order NLO responses. [19] Modulation of the second harmonic generation (SHG) response has also been reported in metal-organic frameworks, where the uptake/release of CO<sub>2</sub> induces a reversible cell expansion and a change of the (non)centrosymmetric structure. [20] However, although the importance of dynamical geometrical fluctuations on the second-order NLO properties was previously evidenced in flexible pyridine-pyrimidine and hydrazine-pyrimidine helical strands [21], as well as in recent investigations focusing on the impact of concentration on the first hyperpolarizability of solutions of nitrobenzene in benzene [22], the dynamical behavior of molecular switches and its impact on their NLO contrasts have never been studied. Most of theoretical investigations reported so far assume the switching mechanism to occur between stationary states, leaving largely unexplored the dynamical nature of the systems. Moreover, although a few of these works have addressed the immobilization of NLO switches on surfaces [23, 24] or their behavior in the solid state, [25, 26] most of them are carried out in solutions, where structural fluctuations are facilitated and might significantly impact the optical contrasts.

In this work, the dynamical nature of the second harmonic generation (SHG) response is characterized for two molecular switches resulting from the association of an indolino-oxazolidine switchable unit bearing either a methyl (**1**) or a nitro (**2**) group in position 5, and of a bithiophene donor moiety substituted by a thiomethyl

group (Scheme 6.1). These systems were shown to exhibit versatile switching properties and can interconvert between a colorless closed form (CF) and a colored open form in a trimodal way, *i.e.* under light irradiation, pH variations, and redox potential variations. [27] In this study we focus on the switching upon trifluoroacetic acid addition in chloroform solution. In these conditions, the opening of the oxazolidine ring with the formation of an indoleninium moiety leads to the formation of an ion pair, constituted by the corresponding protonated open form (POF) of each derivative **1** and **2** associated to the trifluoroacetate (TFA) counteranion. The electrical neutrality of the POF/TFA pair enables to characterize its NLO response by means of electric field induced second harmonic generation (EFISHG) technique. However, the loose nature of the interactions between the two molecular ions, as well as the difficulty in interpreting experimental measurements, call for methods going beyond the traditional stationary state characterizations where single point calculations are performed for the chromophore in solution using *ab initio* quantum mechanical (QM) methods combined with polarizable continuum solvation models, and requires implementing computational approaches accounting for the dynamical behavior of the ion pair within an explicit solvent environment. Adapting the framework used in Refs. [21] and [22], the structures of chloroform-solvated ion pairs were first generated using classical molecular dynamics (MD) simulations, and eventually extracted at regular time steps of the trajectories to calculate their EFISHG responses by means of density functional theory (DFT). MD simulations enable to exhaustively sample the multiple geometrical conformations these NLO switches can adopt, in both their closed and open forms, including the position of the counteranion in the case of the open form. In complement to the EFISHG responses, the sequential MD-then-QM approach is also used to predict the hyper-Rayleigh



Scheme 6.1: Indolino-oxazolidine derivatives **1** and **2** in their closed and protonated open forms. Atom labels, definition of the torsion angles  $\theta_A = N_2 - C_3 - C_4 - C_5$ ,  $\theta_B = C_4 - C_5 - C_6 - S_8$ , and  $\theta_C = S_8 - C_{10} - C_{11} - S_{14}$ , and  $\pi$ -conjugated path used to define the bond length alternation (BLA, green).

scattering (HRS) responses of the switches, HRS being a widespread technique to determine the second-order NLO properties of neutral and charged compounds. These simulations and the accompanying measurements thus provide the first complete description of the SHG responses of molecular switches in solution. Owing to the inclusion of dynamical effects, this multiscale methodology also calls into question common assumptions employed when analyzing second harmonic generation responses. In particular, as highlighted in the Methods Section, the total EFISHG response ( $\gamma_{EFISHG} = \gamma_{//} + \mu\beta_{//}/3k_B T$ ) of  $\pi$ -conjugated systems is expressed as the sum of two NLO contributions: a second-order one, the SHG first hyperpolarizability ( $\beta_{//}$ ), and a third-order one, the EFISHG second hyperpolarizability ( $\gamma_{//}$ ). Traditionally, the EFISHG response of push-pull  $\pi$ -conjugated systems is attributed to the second-order term, whereas the third-order contribution is neglected. [28] This assumption is tested here by addressing how the relative amplitude of these two terms depends on the open or closed state of the molecule, as well as on the nature of the substituent on the phenyl ring.

## 6.2 Experimental and Theoretical Methods

### 6.2.1 Nonlinear Optics: General Considerations and Definitions

The molecular properties known as the (electric-dipole) polarizability ( $\alpha$ ), first ( $\beta$ ), and second ( $\gamma$ ) hyperpolarizabilities are defined by an equation describing the variations in the electric dipole moment upon application of external electric fields:

$$\begin{aligned} \Delta\mu_{\zeta}(-\omega_{\sigma}) &= \sum_{\eta}^{x,y,z} \alpha_{\zeta\eta}(-\omega_{\sigma}; \omega_1) E_{\eta}(\omega_1) + \frac{1}{2!} \sum_{\eta,\chi}^{x,y,z} \beta_{\zeta\eta\chi}(-\omega_{\sigma}; \omega_1, \omega_2) E_{\eta}(\omega_1) E_{\chi}(\omega_2) \\ &+ \frac{1}{3!} \sum_{\eta,\chi,\xi}^{x,y,z} \gamma_{\zeta\eta\chi\xi}(-\omega_{\sigma}; \omega_1, \omega_2, \omega_3) E_{\eta}(\omega_1) E_{\chi}(\omega_2) E_{\xi}(\omega_3) + \dots \end{aligned} \quad (6.1)$$

where the use of T convention is recognized,  $E_{\eta}(\omega_1)$  is the amplitude of the field oscillating at angular frequency  $\omega_1$  applied in the  $\eta$  direction and  $\omega_{\sigma} = \sum_i \omega_i$ .  $\beta(\gamma)$  is a rank 3 (4) tensor, defined in the molecular axes coordinates ( $\eta, \chi, \dots = x, y, z$ ). The study concentrates on the SHG responses,  $\beta_{EFISHG}(-2\omega; \omega, \omega) = \beta_{//}(-2\omega; \omega, \omega) = \beta_{//}$ ,  $\gamma_{//}(-2\omega; \omega, \omega, 0) = \gamma_{EFISHG}$  and  $\beta_{HRS}(-2\omega; \omega, \omega) = \beta_{HRS}$ , which are defined from the following quantities.

On the one hand, in EFISHG, the total SHG response reads:

$$\begin{aligned} \gamma_{EFISHG} &= \langle \gamma(-2\omega; \omega, \omega, 0) \rangle \\ &= \gamma_{//}(-2\omega, \omega, \omega, 0) + \frac{\mu\beta_{//}(-2\omega; \omega, \omega)}{3k_B T} = \frac{[\mu\beta_{//}(-2\omega; \omega, \omega)]_{eff}}{3k_B T} \end{aligned} \quad (6.2)$$

with  $\beta_{//}(-2\omega; \omega, \omega)$ , the so-called parallel  $\beta$ , which corresponds to 3/5 times the projection of the vector component of the  $\beta$  tensor ( $\vec{\beta}$  in Figure 6.4) on the dipole moment axis:

$$\beta_{//}(-2\omega; \omega, \omega) = \frac{1}{5} \sum_i \frac{\mu_i}{\mu} \sum_j (\beta_{ijj} + \beta_{jij} + \beta_{jji}) = \frac{3}{5} \sum_i \frac{\mu_i \beta_i}{\mu} \quad (6.3)$$

where  $\mu$  is the norm of dipole moment and  $\mu_i$  its  $i^{\text{th}}$  Cartesian component,  $k_B$  the Boltzmann constant,  $T$  the temperature. The  $\mu\beta_{//}/3k_B T$  term is the dipolar orientational second-order contribution to EFISHG while  $\gamma_{//}(-2\omega; \omega, \omega, 0)$  is a third-order term corresponding to the mixing of two optical fields at  $\omega$  with the dc poling field at  $\omega = 0$ . For push-pull  $\pi$ -conjugated compounds, the  $\gamma_{//}$  term is usually smaller than the second-order NLO contribution and is often ignored, although this approximation is not justified for compounds with small  $\beta$  responses like **1**. An effective  $\mu\beta_{//}$  response, regrouping both second- and third-order NLO contributions to EFISHG, was therefore defined in Eq. 6.2, allowing a direct comparison with experiment. Indeed, when the measurements are not carried out at different temperatures to disentangle the two contributions, they only provide the global EFISHG response, which is here given under the form of an effective  $\mu\beta_{//}$  value,  $[\mu\beta_{//}]_{eff}$ .

On the other hand, in HRS, for a non-polarized incident light, the SHG intensity of the vertically polarized (along the Z axis of the laboratory frame) signal scattered at  $90^\circ$  with respect to the propagation direction (Y axis) is proportional to the square of  $\beta_{HRS}(-2\omega; \omega, \omega)$ , which involves ensemble averages over the molecular orientations:

$$\beta_{HRS}(-2\omega; \omega, \omega) = \sqrt{\langle \beta_{ZZZ}^2 \rangle + \langle \beta_{XZZ}^2 \rangle} = \sqrt{\langle \beta_{ZZZ}^2 \rangle + \left(1 + \frac{1}{DR}\right)} \quad (6.4)$$

The depolarization ratio DR, which depends on the chromophore shape, is the ratio between the scattered intensities obtained when the incident light is vertically ( $\langle \beta_{ZZZ}^2 \rangle$ ) and horizontally ( $\langle \beta_{XZZ}^2 \rangle$ ) polarized, respectively. The relationships between these orientational averages (in the laboratory frame) and the molecular tensor components (in the molecular frame) are described in a previous paper [29] and in Chapter 2 (Eqs. 2.26 and 2.27). Further details on EFISHG and HRS can be found in Ref. [30].

### 6.2.2 EFISHG Measurements

$\text{CHCl}_3$  solutions of **1** and **2** POF were prepared by exposure of solutions of the corresponding CF forms to  $\text{CF}_3\text{COOH}$  vapors for about 1 h, monitoring the transformation by UV-vis absorption spectroscopy (Figure C.28 in Appendix C). For each compound, two concentrations were used,  $10^{-3}$  and  $5 \times 10^{-4}$  M for **1** and  $5 \times 10^{-4}$  and  $4.4 \times 10^{-4}$  M for **2**.

The molecular first hyperpolarizabilities of the compounds were measured by the solution phase dc EFISHG method, [31] which can provide direct information on the intrinsic molecular SHG responses,  $\gamma_{EFISHG}$  (Eq. 6.2). During the EFISHG measurements, upon cell translation, the intensity of the second harmonic radiation is modulated as interference fringes (Maker fringes). As detailed in Chapter 2, the width and the periodicity of the fringes are correlated to the macroscopic susceptibility  $\Gamma(S)$  of the solution, which depends on the intensity of the second harmonic light  $I_{2\omega}$  and on the coherence length  $l_c$ , according to:

$$\Gamma(S) = \frac{1}{l_c} \left[ A \sqrt{\frac{I_{2\omega}(S) E_0(0)}{I_{2\omega}(0) E_0(S)}} + B \right] 10^{-12} \quad (6.5)$$

$E_0$  is the amplitude of the dc-electric field. S refers to the chromophore solution while 0 to the solvent only.  $A$  and  $B$  are constants depending on the solvent and the cell windows. The microscopic  $\gamma_{EFISHG}$  value is then inferred from the macroscopic susceptibilities of the solvent  $\Gamma(0)$  and of the solution  $\Gamma(S)$ , via the equation:

$$\gamma_{EFISHG} = \frac{M}{\rho N_A f x} [(1+x)\Gamma(S) - \Gamma(0)] \quad (6.6)$$

where  $N_A$  is the Avogadro number,  $M$  the molecular weight of the compound,  $\rho$  the density of the solution,  $x$  the molar fraction of the compound and  $f$  a local field correction factor. All EFISHG measurements were carried out in  $\text{CHCl}_3$  solutions, working with a non-resonant incident wavelength of 1907 nm, obtained by Raman shifting the fundamental 1064 nm wavelength produced by a Q-switched, mode locked  $\text{Nd}^{3+}$ :YAG laser. The  $[\mu\beta_{//}]_{eff}$  values, which are reported instead of  $\gamma_{EFISHG}$  [ $3k_B T \gamma_{EFISHG} = [\mu\beta_{//}]_{eff}$ ], are the mean values of 8 successive measurements performed on the same sample and their standard deviations.

Note that usually it is common knowledge that the EFISHG technique can only be applied to characterize molecules while it fails for ionic species because of the dc electric field necessary to break centrosymmetry leads to migration of the ions. However, we confirm here that the technique can also be used for the determination of the NLO responses of ions in solution, provided the measurements are carried out in a solvent with a low dielectric constant such as  $\text{CHCl}_3$ , which favors ions pairing with suitable counterions. This concept was demonstrated first in 2000 for amphiphilic polyenic push-pull chromophores [32] and more recently applied to derivatives of 4'-dimethylamino-N-methyl-4-stilbazolium with a range of counteranions. [33]

### 6.2.3 Molecular Dynamics Simulations

*Simulation Details.* MD simulations of the different indolino-oxazolidine CF and POF conformers of derivatives **1** and **2** were conducted in  $\text{CHCl}_3$  solvent, using square boxes containing either one neutral CF molecule or one neutral pair

formed by a positively charged POF and a perfluoroacetate anion, and 1600  $\text{CHCl}_3$  molecules. All simulations started from a low-density box with side of 120 Å and were equilibrated for 10 ns in the NPT ensemble ( $p=1$  atm and  $T=298.15$  K) prior to proceeding to production runs of 20 ns. All simulations were carried out using the NAMD code [34] and analyzed with VMD. [35] A time step of 1 fs was used, controlling temperature by rescaling velocities every 100 steps, and pressure with a weak-coupling thermostat. Intermolecular interactions were calculated using 3D periodic boundary conditions, a cutoff of 12 Å for Lennard-Jones and short-range electrostatic interactions, and the Smooth Particle Mesh Ewald method (SPME) [36] for long-range electrostatic interactions.

*Force field parameterization.* The general AMBER Force Field parameters [37] were partially modified in order to obtain a non-transferable force field (FF) aimed at specifically reproducing the equilibrium geometry and the torsional degrees of freedom of the target compounds in chloroform. Hence i) three specific parameter sets were obtained for **1** and **2** CFs, **1** POF, and **2** POF ii) both solvent and solutes electrostatic potential fitting atomic charges were calculated at the IEF-PCM/M06/6-311G(d) level of theory (solvent: chloroform) and used as is in the simulations; iii) AMBER FF bond lengths were adjusted so as to reproduce closely M06 bond lengths and bond length alternation at the corresponding minimum energy geometries with a mean absolute error of 0.005 Å; iv) FF dihedral potentials for torsions around the single  $C_3-C_4$  ( $\theta_A$ ),  $C_5-C_6$  ( $\theta_B$ ), and  $C_{10}-C_{11}$  ( $\theta_C$ ) bonds (Scheme 6.1) were also refitted to M06 values as obtained by constrained optimizations. The procedure for fitting the dihedrals is described in detail in reference [38]; it is worth mentioning here that the gas phase FF dihedral potentials reported in this work correspond to free energy profiles obtained with adaptive biasing force [39] runs at 298.15 K, for boxes containing one CF or POF molecule and 40 Ar atoms in a constant volume of 125 000 Å<sup>3</sup>. The use of shared parameters (with exception of atomic charges) for **1** and **2** CFs is justified by the similarity of DFT-calculated bond lengths and dihedral potentials, apparently only weakly impacted by the  $-\text{CH}_3$  and  $-\text{NO}_2$  substituents (Figure C.1 in Appendix C). Concerning the quality of the description of the solvent, we verified that the simulated density of the pure system (1600  $\text{CHCl}_3$ , 1 atm, 298.15 K) is very close to the experimental one (1.468  $\text{g}\cdot\text{cm}^{-3}$  versus an experimental value of 1.477  $\text{g}\cdot\text{cm}^{-3}$  [40]).

*Conformational sampling.* MD simulations were performed by considering different starting geometries for both forms of the two compounds, in order to ensure a complete sampling of the various conformers in solution. As detailed in Figure C.8 (in Appendix C), four different starting geometries were used to scan all possible structural conformations for closed and open forms. The distributions of the torsional angles over the 20 000 frames extracted from each trajectory are provided in Figure C.2-C.5 (in Appendix C) together with the associated potential energy curves.

For each MD run, one CF or one (POF+counterion) instantaneous geometry was extracted every 100 ps along the production trajectory of 20 ns, for a total of 200 snapshots. The corresponding internal energies (intra plus intermolecular), whose averages are reported in Table C.1 (in Appendix C), were calculated at molecular mechanics level as the difference between the total internal energy of the solvent+solute(s) system minus the energy of the solvent alone. To properly take into account periodic interactions, in particular the ones hidden in the details of the SPME method, both quantities were calculated with NAMD in the same simulation cell.

The geometries were employed for structural analysis and subsequent DFT calculations of the NLO properties. Distributions of the torsional angles calculated using these 200 snapshots are similar to those obtained using the 20 000 frames (Figures C.6-C.7, in Appendix C), evidencing that the reduction of the number of structures reasonably preserves the completeness of the conformational sampling. Boltzmann-averaged values of structural and optical properties are obtained by weighting the value calculated for each snapshot by the Boltzmann statistical weight at 298.15 K calculated from the average conformer internal energies in Table C.1 (in Appendix C).

#### 6.2.4 Hyperpolarizability Calculations

The SHG  $\beta$  and  $\gamma$  tensor components were calculated on geometries extracted from the MD runs using the time-dependent DFT (TDDFT) method [41, 42] with the M06-2X XC functional, [43] and the 6-311+G(d) basis set, for an incident wavelength of 1907 nm. Solvent (chloroform) effects were included by using the integral equation formalism (IEF) of the polarizable continuum model (PCM). The  $\beta$  and  $\gamma$  tensor components were then employed to evaluate the target quantities, *i.e.* i)  $\beta_{\parallel\parallel}(-2\omega; \omega, \omega)$ ,  $\gamma_{\parallel\parallel}(-2\omega; \omega, \omega, 0)$  and  $[\mu\beta_{\parallel\parallel}(-2\omega; \omega, \omega)]_{eff}$  for EFISHG and ii)  $\beta_{HRS}(-2\omega; \omega, \omega)$  and DR for HRS. The M06-2X XC is reliable to calculate hyperpolarizabilities, owing to its substantial amount (54%) of long-range Hartree-Fock exchange, as demonstrated in previous investigations where the performance of DFT XC functionals was assessed with respect to benchmark wavefunction values. [5, 44–46] The IEF-PCM scheme [47, 48] approximates the solvent as a structureless polarizable continuum characterized by its macroscopic dielectric permittivity, which depends on the frequency of the applied electric field. For chloroform, the dielectric constants in the static limit ( $\epsilon_0$ ) and at infinite frequency ( $\epsilon_\infty$ ) are equal to 4.71 and 2.09, respectively. All calculations were carried out using the Gaussian09 package. [49]

Table 6.1: Average geometrical parameters. Average values and standard deviations of bond length alternation (BLA, Å), anion-cation distance ( $d_{AC}$ , Å), hydrogen bond distance ( $d_{OH}$ , Å), and hydrogen bond angle ( $\alpha_{OHO}$ , °) obtained by MD simulations. BLA values of the structures obtained by geometry optimizations at the IEF-PCM/M06/6-311G(d) level, which were used to parameterize the AMBER FF, are given in parentheses in the 3<sup>rd</sup> column (Å).

	BLA	$d_{AC}$	$d_{OH}$	$\alpha_{OHO}$
<b>1</b> CF	0.141 ± 0.022 (0.137)	/	/	/
<b>1</b> POF	0.038 ± 0.019 (0.030)	4.990 ± 0.491	1.603 ± 0.068	166.4 ± 4.4
<b>2</b> CF	0.138 ± 0.019 (0.136)	/	/	/
<b>2</b> POF	0.012 ± 0.019 (0.012)	5.172 ± 0.393	1.596 ± 0.067	167.9 ± 4.3

## 6.3 Results

### 6.3.1 MD Simulations and *ab initio* Calculations

MD simulations afforded insights into the preferred geometries of both compounds in chloroform solutions. The average values of representative structural parameters are gathered in Table 6.1, while detailed results are presented in the Appendix C (Tables C.2-C.4, Figures C.9-C.4). Since both the linear and nonlinear optical responses of push-pull systems are strongly impacted by the strength of  $\pi$ -electron conjugation, reliable simulations of these properties require an accurate description of bond length alternation (BLA) along the central vinylic bridge of the compounds (Scheme 6.1), and thus the derivation of appropriate force fields for both closed and open forms (see Methods Section). MD simulations show that the BLA is one order of magnitude smaller for the open forms than for the closed forms, consistently with the DFT geometries used in the force field parameterization. This effect is further enhanced by nitro substitution in the open form, as indicated by the decrease of the BLA by a factor 3 from compound **1** to compound **2**. For both compounds, MD simulations revealed the existence of a hydrogen bond between the terminal hydroxyl group of the protonated open forms and one of the oxygen atoms of the trifluoroacetate anion, with typical O<sup>-</sup>...H distances of 1.6 Å and O<sup>-</sup>...H-O angles close to 180°. The time evolution of the O<sup>-</sup>...H distance and O<sup>-</sup>...H-O angle shows that the nature of this interaction is highly dynamical, with the hydroxyl H atom alternatively bonding one of the two trifluoroacetate oxygens.

Figure 6.1 illustrates how the trifluoroacetate anion is fluctuating around the terminal hydroxyl group of the POF for 200 selected snapshots extracted from the MD simulations. The average distances ( $d_{AC}$ ) between the centers of mass of the POF (cation) and of the anion, reported in Table 6.1, are similar for both compounds within the amplitudes of their standard deviations. Still, a detailed analysis of the time evolution of this distance (Figures C.13-C.15, in Appendix C) shows infrequent and short-lived changes in the  $d_{AC}$  values, arising from sudden changes

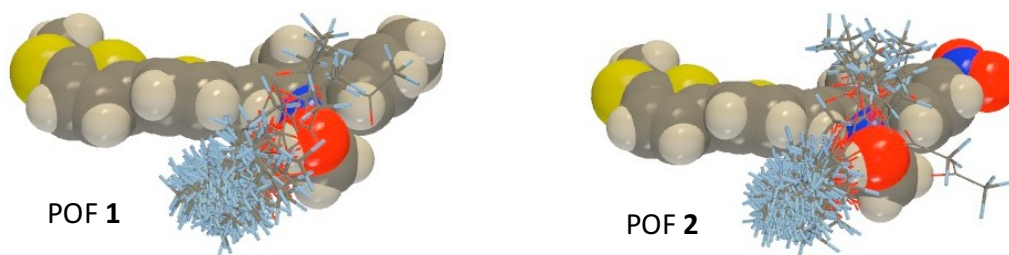


Figure 6.1: Relative position of the trifluoroacetate anion around the POF. Results are given for compounds **1** (left) and **2** (right). The geometry at time zero is used for the POF (represented using atomic van der Waals spheres) whereas 200 snapshots are superimposed for the trifluoroacetate anion (represented using sticks).

in the orientation of the hydroxylated arm and of the counterion with respect to the oxazolidine moiety.

Calculations of the NLO properties were then performed at the TDDFT level for a selection of 200 snapshots equally distributed over the 20 ns production time. Their time evolutions along the MD trajectories are presented in Figures C.16-C.23 (in Appendix C), while Figures 6.2 and 6.3 (Figures C.24- C.27) illustrate the distribution of the  $[\mu\beta_{//}]_{eff}$ ,  $\beta_{HRS}$ ,  $\mu\beta_{//}$ , and  $\gamma_{//}$  values, respectively. The average values of the second-order NLO responses and related quantities are reported Table 6.2, together with their standard deviations, while Table 6.3 lists the EFISHG quantities and their second- and third-order contributions.

The fast geometrical fluctuations of the chromophores, as well as of the relative position of the POF and TFA ions, lead to broad distributions of both the EFISHG and HRS responses, characterized by large standard deviations in theoretical calculations, thus highlighting the importance of dynamic structural changes on the SHG properties of  $\pi$ -conjugated systems in solution. These broad distributions are striking observations for chromophores **1** and **2**, which have much more rigid structures than the previously-studied pyridine-pyrimidine and hydrazine-pyrimidine helical strands. [21] Going into details, the standard deviations amount to about 700 a.u. for both  $\beta_{//}$  and  $\beta_{HRS}$  of compounds **1** and **2** in their closed form, and they are one order of magnitude larger for their protonated open forms. Remarkably, for both CF and POF of compound **1**, standard deviations of  $\beta_{//}$  are several times larger than their corresponding average values, making difficult even the determination of their sign. Conversely, the relative standard deviations on  $\beta_{//}$  are much smaller for **2** (both for CF and POF), probably because the  $\beta_{//}$  values are larger. The same situation is observed for the  $\beta_{HRS}$  and  $\gamma_{//}$  responses of **1** and **2**, but still with standard deviations reaching 1/6 to 2/3 of the corresponding average value. In fact, in the case of  $\gamma_{//}$ , the thermal fluctuations lead to standard deviations of about  $10^5$  a.u. for the CFs of both compounds and, like for the  $\beta$  quantities, they increase by one order of magnitude in POFs. From the simulations, there is no evidence

that the standard deviations would be larger, percentagewise, for the third-order responses than for second-order ones, despite the former being known to be more sensitive to molecular geometries. On the other hand, the larger dispersion of the NLO responses of the POFs compared to the CFs can be related to the fluctuations of the anion position and to the anion-induced electric field, which polarizes the chromophore electronic structure and modulates its  $\beta$  and  $\gamma$  values.

Figures 6.2 and 6.3 also evidence large variations of the average second- and third-order NLO responses between compounds **1** and **2**, as well as between the

Table 6.2: Average first hyperpolarizabilities. Average  $\mu\beta_{//}$  ( $10^3$  a.u.),  $\beta_{//}$  (a.u.), and  $\beta_{HRS}$  (a.u.) values for a wavelength of 1907 nm, norm of the dipole moment  $\mu$  (a.u), angle ( $^\circ$ ) between the dipole moment and vector component of  $\beta$ ,  $\theta(\mu\beta)$ , and depolarization ratio (DR) of the HRS response, given with their standard deviations, calculated at the IEF-PCM/M06-2X/6-311+G(d) level of approximation.

	$\mu\beta_{//}$	$\beta_{//}$	$\mu$	$\theta(\mu\beta)$	$\beta_{HRS}$	DR
<b>1</b> CF	$-0.02 \pm 0.64$	$-176 \pm 781$	$1.04 \pm 0.21$	$93.8 \pm 28.8$	$1000 \pm 631$	$4.91 \pm 0.63$
<b>1</b> POF	$-5.19 \pm 31.8$	$-2652 \pm 6367$	$6.76 \pm 0.69$	$93.5 \pm 8.0$	$32294 \pm 6356$	$4.82 \pm 0.07$
<b>2</b> CF	$4.46 \pm 1.82$	$2444 \pm 797$	$2.71 \pm 0.39$	$44.1 \pm 11.6$	$2431 \pm 615$	$5.70 \pm 0.43$
<b>2</b> POF	$133 \pm 49$	$29102 \pm 8178$	$6.56 \pm 0.83$	$54.9 \pm 6.40$	$37406 \pm 5720$	$4.93 \pm 0.07$

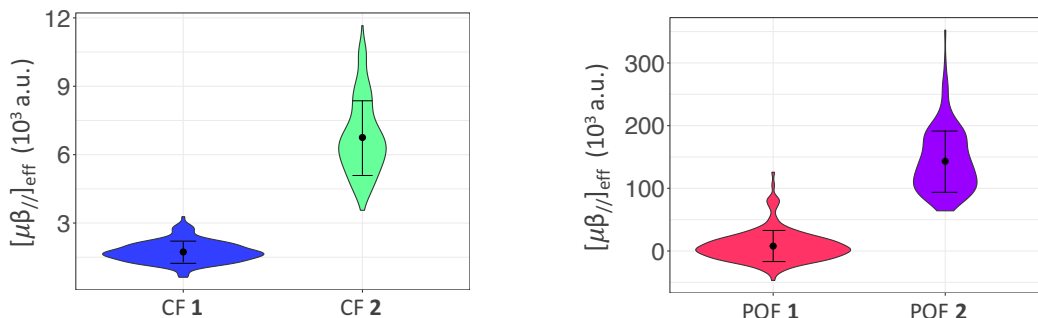


Figure 6.2:  $[\mu\beta_{//}]_{eff}$  violin distribution plots, including their averages (black dots) and standard deviations. Results are given for the closed forms (left) and for the POF/TFA pair (right).

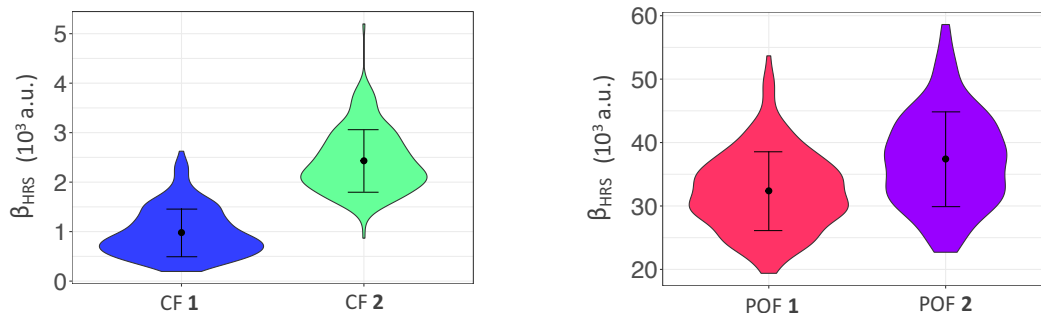


Figure 6.3:  $\beta_{HRS}$  violin distribution plots, including their averages (black dots) and standard deviations. Results are given for the closed forms (left) and for the POF/TFA pair (right).

two forms of a same compound. Compound **1** displays small  $\mu\beta_{||}$  and  $\beta_{||}$  values in its protonated open form, which become negligible after closure of the oxazolidine ring. The weakness of the  $\mu\beta_{||}$  responses of the POF form finds its origin in the almost perpendicular orientation of the dipole moment vector with respect to the vector component of the first hyperpolarizability. In addition to a similar detrimental orientation between the  $\mu$  and  $\beta$  vectors shown in Figure 6.4, the  $\mu\beta_{||}$  responses are further reduced in the closed form of **1** due to the loss of conjugation between the bithiophene donor and the indoleninium acceptor, cancelling out the intrinsic second-order response. The difficulty of determining the sign of  $\mu\beta_{||}$  and  $\beta_{||}$  of **1** is therefore explained by the  $\theta(\mu\beta)$  values that display large fluctuations around  $90^\circ$ . On the other hand, because they are isotropic averages independent on the dipole moment orientation, the  $\beta_{HRS}$  responses are much larger than the  $\beta_{||}$  ones. This is particularly true for the POF, which exhibits a large  $\beta_{HRS}$  response due to its strong  $\pi$ -conjugated push-pull character.

In compound **2**, the replacement of the terminal methyl group present in **1** by an electron-withdrawing nitro substituent leads to contrasting effects on the different quantities. The  $\theta(\mu\beta)$  angles strongly deviate from  $90^\circ$  (Figure 6.4), which dramatically enhances the  $\mu\beta_{||}$  and  $\beta_{||}$  values of both forms. The nitro-substitution also increases the HRS hyperpolarizabilities, with a larger impact for the CF (+140 % from **1** to **2**) than for the POF (+16 %). This asymmetrical enhancement is detrimental to the  $\beta_{HRS}$  contrast, as already evidenced in a previous joint experimental-theoretical study. [50]

For all compounds and forms, the  $\beta$  response is mostly dipolar, and the depolarization ratios (DR) are close to the ideal value of one-dimensional push-pull compounds (DR = 5), for which the  $\beta$  tensor is dominated by a single diagonal tensor component  $\beta_{iii}$  (with  $i$  being also the direction of the excitation-induced charge transfer axis). Still, narrower distributions of the DR values are obtained in the case of the POFs. It is however noteworthy that all the  $\beta_{||}/\beta_{HRS}$  ratios are far from the value of  $\sim 1.45$  expected for ideal dimensional push-pull systems, in particular for compound **1** for which  $\beta_{||}/\beta_{HRS}$  amounts to -0.18 for the CF and -0.08 for the POF/TFA pair. Interestingly, this simple rule commonly used to compare second-order NLO responses obtained from EFISHG and HRS techniques is broken here due to the nature of the systems, which is responsible for those  $\theta(\mu, \beta)$  angles that strongly differ from  $0^\circ$ .

Turning now to the third-order response, opening the oxazolidine ring also leads to a substantial increase of  $\gamma_{||}$  by almost an order of magnitude while the differences between the methyl- and nitro-substituted species are not representative in comparison to the standard deviations on  $\gamma_{||}$ . The large opening-induced augmentation highlights the strong impact of  $\pi$ -conjugation on the third-order responses, as already observed for the second-order responses, while substituting the periph-

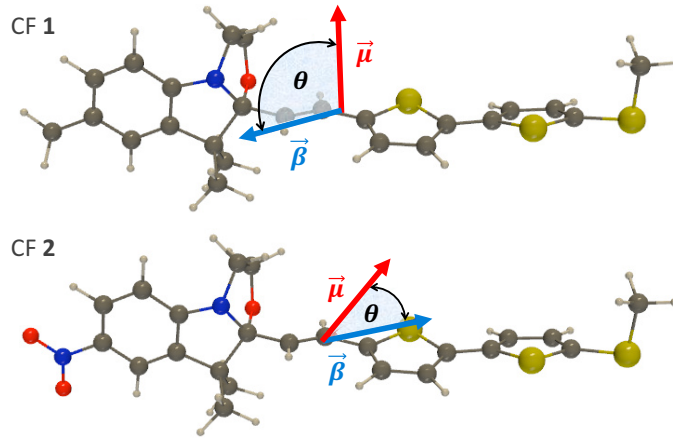


Figure 6.4: Schematic representations of the average angle ( $\theta$ ) between the dipole moment ( $\mu$ ) and the vector component of  $\beta$  of **1** (top) and **2** (bottom) in closed form. The represented geometry corresponds to the most stable conformer as obtained from DFT calculations.

eral methyl by a nitro group has a lower effect (Table 6.3). With the exception of the POF of **2**, the  $\gamma_{//}$  contributions to the EFISHG response are not negligible and should be accounted for when making comparisons with experiments. This is in marked contrast to what is generally assumed, [28] and mostly results from the small second-order NLO responses, as discussed above. For both forms of compound **1**, the values of  $\gamma_{//}$  are in fact larger than their second-order  $\mu\beta_{//}/3k_B T$  counterparts, with a ratio between the third- and second-order contributions to EFISHG,  $R_{3/2}$ , which attains -131 for CF(**1**) and decreases by a factor of 50 (-2.7) for POF(**1**). Moreover, in the latter case,  $\gamma_{//}$  and  $\mu\beta_{//}/3k_B T$  are of similar magnitude but of opposite sign, which results in a reduced global EFISHG response. This also holds for CF(**1**), but in this case  $\mu\beta_{//}/3k_B T$  is negligible. Conversely, for CF(**2**), both contributions have the same sign and the second-order part is about twice as large as the third-order one, but again the standard  $\gamma_{//} \sim 0$  assumption is not valid. Finally, the second-order contribution is dominant in POF(**2**), being one order of magnitude larger than the third-order one, which corresponds to the assumed most traditional case.

Table 6.3: Experimental and calculated EFISHG responses. The  $[\mu\beta_{//}]_{eff}$  values are reported in  $10^3$  a.u. and the  $\mu\beta_{//}/3k_B T$  in  $10^4$  a.u.. The ratios between the third- and second-order contributions to  $\gamma_{EFISHG}$ ,  $R_{3/2} = [3k_B T \times \gamma_{//}]/[\mu\beta_{//}]$  are given in parentheses in the 4<sup>th</sup> column. At  $T = 298.15$  K,  $3k_B T = 2.833 \cdot 10^{-3}$  a.u..

	Calculations				Experiment
	$\mu\beta_{//}/3k_B T$	$\gamma_{//}$	$\gamma_{EFISHG}(R_{3/2})$	$[\mu\beta_{//}]_{eff}$	$[\mu\beta_{//}]_{eff}$
<b>1</b> CF	$-0.5 \pm 22.7$	$63.4 \pm 9.6$	$62.4 \pm 22.6$ (-131)	$1.76 \pm 0.64$	$30.0 \pm 70$
<b>1</b> POF	$-183 \pm 1124$	$493 \pm 194$	$277 \pm 867$ (-2.7)	$7.82 \pm 24.47$	$60 \pm 60$
<b>2</b> CF	$158 \pm 64$	$73.6 \pm 10.2$	$242 \pm 68$ (0.47)	$6.84 \pm 1.93$	$64 \pm 26$
<b>2</b> POF	$4707 \pm 1744$	$428 \pm 110$	$5073 \pm 1742$ (0.091)	$143 \pm 49$	$153 \pm 45$

### 6.3.2 EFISHG Measurements

The NLO responses deduced from EFISHG measurements at different concentrations in  $\text{CHCl}_3$  solutions, as well as their averages, are collected in Table C.5. For both compounds, the uncertainties are large so that the sign of  $[\mu\beta_{//}]_{eff}$  for **1** in its CF and POF cannot be determined and the  $[\mu\beta_{//}]_{eff}$  variations upon the ring opening of the indolino-oxazolidine moiety cannot be predicted. In its POF, **2** presents the largest  $[\mu\beta_{//}]_{eff}$  value due to its nitro substitution. Moreover, a  $[\mu\beta_{//}]_{eff}(\text{POF}(\mathbf{2}))/[\mu\beta_{//}]_{eff}(\text{CF}(\mathbf{2}))$  contrast ratio of 3 can be deduced, in agreement with the increased electron conjugation between the bithiophene and indoleninium moieties.

## 6.4 Further Discussion and Conclusion

In this work it is reported a complete theoretical-experimental investigation of the SHG properties of indolino-oxazolidine molecular switches that can switch between a closed form and a protonated open form upon trifluoroacetic acid addition. Both EFISHG and HRS responses were characterized and shown to be complementary for addressing and rationalizing the SHG responses and their contrast upon switching. In particular, experimental measurements of EFISHG responses were made possible by the electric neutrality of the pairs formed, in chloroform, by the POF cations and the trifluoroacetate anion. On the other hand, the loose nature of these ion pairs calls for theoretical methods accounting for their dynamical behavior. This challenge was successfully met by employing a sequential 'Molecular Mechanics-Quantum Mechanics' approach to describe the geometrical fluctuations of the chromophores and ion pairs, and to highlight their impact on the NLO responses, opening the way to fully *in silico* characterizations of the SHG activity of NLO switches in solution.

The agreement between theory and measurements (Table 6.3) is quantitative for **2** in its POF, which displays the largest response among the four species and the smallest relative error bars/standard deviations. For the other species, the comparison is made difficult by the large relative experimental uncertainties as well as by the fact that the standard deviations for POF(**1**) are larger than the corresponding average values. Experimentally, these large error bars are related to the very small  $\beta_{//}$  and  $\mu\beta_{//}$  values, which, for **1**, originate from the almost perfect orthogonality between the vectorial component of  $\beta$  and the dipole moment, as shown in the calculations. This contrasts with the  $\beta_{HRS}$  results reported in Ref. [50], which do not depend on other properties ( $\mu$  and  $\gamma$ ). Moreover, calculations demonstrate that the inclusion of the third-order contribution to  $\gamma_{EFISHG}$  can strongly modify the predicted value and generally improves the agreement with experiment. Then, our calculations – and to some extent, experiment – demonstrate an increase of the EFISHG responses

i) when substituting the Me group (compound **1**) on the indoline moiety by a NO<sub>2</sub> acceptor group (compound **2**), *i.e.* when going from POF(**1**) to POF(**2**) and from CF(**1**) to CF(**2**) as well as ii) when opening the oxazolidine ring, *i.e.* when going from CF(**1**) to POF(**1**) and from CF(**2**) to POF(**2**).

Exploiting the calculation results enables to shed light on new phenomena and interpretations. Namely, i) the huge effect of geometrical fluctuations on the SHG responses, leads to large standard deviations on both the HRS and EFISHG responses, in particular on the latter. ii) There is no simple relationship between the EFISHG  $\beta_{//}$  and HRS  $\beta_{HRS}$  amplitudes, the complexity originating from the strong impact of the substituent on the relative orientation of the dipole moment with respect to the vector component of the first hyperpolarizability. iii) The third-order contribution to EFISHG ( $\gamma_{//}$ ), which is often neglected in both calculations and experimental data analysis, should not be omitted because it can be large, or even dominant, with respect to its second-order counterpart ( $\mu\beta_{//}/3k_B T$ ) and, for the purpose of optimizing NLO switches, it can strongly influence the POF/CF contrast ratios.

# Bibliography

---

- [1] J. Andréasson and U. Pischel. Molecules with a sense of logic: a progress report. *Chem. Soc. Rev.*, **44**:1053–1069, 2015.
- [2] B. L. Feringa and W. R. Browne. *Molecular switches*. Eds. Wiley-VCH: Weinheim, 2nd edition, 2011.
- [3] B. J. Coe. Molecular materials possessing switchable quadratic nonlinear optical properties. *Chem. Eur. J.*, **5**:2464–2471, 1999.
- [4] J. A. Delaire and K. Nakatani. Linear and nonlinear optical properties of photochromic molecules and materials. *Chem. Rev.*, **100**(5):1817–1846, 2000.
- [5] F. Castet, V. Rodriguez, J.-L. Pozzo, L. Ducasse, A. Plaquet, and B. Champagne. Design and characterization of molecular nonlinear optical switches. *Acc. Chem. Res.*, **46**(11):2656–2665, 2013.
- [6] S. L. Gilat, S. H. Kawai, and J.-M. Lehn. Light-triggered molecular devices: photochemical switching of optical and electrochemical properties in molecular wire type diarylethene species. *Chem. Eur. J.*, **1**(5):275–284, 1995.
- [7] V. Aubert, V. Guerchais, E. Ishow, K. Hoang-Thi, I. Ledoux, K. Nakatani, and Le Bozec H. Efficient photoswitching of the nonlinear optical properties of dipolar photochromic zinc(II) complexes. *Angew. Chem., Int. Ed.*, **47**:577–580, 2008.
- [8] I. Asselberghs, C. Flors, L. Ferrighi, E. Botek, B. Champagne, H. Mizuno, R. Ando, A. Miyawaki, J. Hofkens, M. Van Der Auweraer, and K. Clays. Second-harmonic generation in GFP-like proteins. *J. Am. Chem. Soc.*, **130**(13):15713–15719, 2008.
- [9] F. Mançois, J.-L. Pozzo, J. Pan, F. Adamietz, V. Rodriguez, L. Ducasse, F. Castet, A. Plaquet, and B. Champagne. Multi-addressable molecular switches with large nonlinear optical contrast. *Chem. Eur. J.*, **15**(11):2560–2571, 2009.

- [10] L. Boubekeur-Lecaque, B. J. Coe, J. A. Harris, M. Helliwell, I. Asselberghs, K. Clays, S. Foerier, and T. Verbiest. Incorporation of amphiphilic ruthenium(II) ammine complexes into langmuir-blodgett thin films with switchable quadratic nonlinear optical behavior. *Inorg. Chem.*, **50**(24):12886–12899, 2011.
- [11] N. Gauthier, G. Argouarch, F. Paul, L. Toupet, A. Ladjarafi, K. Costuas, J. F. Halet, M. Samoc, M. P. Cifuentes, T. C. Corkery, and M. G. Humphrey. Electron-rich iron/ruthenium arylalkynyl complexes for third-order nonlinear optics: Redox-switching between three states. *Chem. Eur. J.*, **17**(20):5561–5577, 2011.
- [12] K. A. Green, M. P. Cifuentes, M. Samoc, and M. G. Humphrey. Metal alkynyl complexes as switchable NLO systems. *Coord. Chem. Rev.*, **255**(21-22):2530–2541, 2011.
- [13] S. De, M. Ray, Pati Y. A., and Das K. P. Base triggered enhancement of the first hyperpolarizability of a Keto-Enol tautomer. *J. Phys. Chem. B.*, **117**:15086–15092, 2013.
- [14] E. Cariati, C. Dragonetti, E. Lucenti, F. Nisic, S. Righetto, and E. Roberto, D. and Tordin. An acido-triggered reversible luminescent and nonlinear optical switch based on a substituted styrylpyridine: EFISH measurements as an unusual method to reveal a protonation–deprotonation NLO contrast. *Chem. Commun.*, **50**:1608–1610, 2014.
- [15] K. Matczyszyn, J. Olesiak-Banska, K. Nakatani, P. Yu, N. A. Murugan, R. Zalesny, A. Roztoczyńska, J. Bednarska, W. Bartkowiak, J. Kongsted, H. Ågren, and M. Samoć. One- and two-photon absorption of a spiropyran - merocyanine system: Experimental and theoretical studies. *J. Phys. Chem. B*, **119**(4):1515–1522, 2015.
- [16] J. Boixel, V. Guerchais, H. Le Bozec, A. Chantzis, D. Jacquemin, A. Colombo, C. Dragonetti, D. Marinotto, and D. Roberto. Sequential double second-order nonlinear optical switch by an acido-triggered photochromic cyclometallated platinum (II) complex. *Chem. Commun.*, **51**:7805–7808, 2015.
- [17] S. van Bezouw, J. Campo, S. H. Lee, O. P. Kwon, and W. Wenseleers. Organic compounds with large and high-contrast pH-switchable nonlinear optical response. *J. Phys. Chem. C*, **119**(37):21658–21663, 2015.
- [18] P. Beaujean, F. Bondu, A. Plaquet, J. Garcia-Amorós, J. Cusido, F. M. Raymo, F. Castet, V. Rodriguez, and B. Champagne. Oxazines: a new Class of second-order nonlinear optical switches. *J. Am. Chem. Soc.*, **138**(15):5052–5062, apr 2016.

- [19] S. Van Cleuvenbergen, I. Asselberghs, W. Vanormelingen, T. Verbiest, E. Franz, K. Clays, M.G. Kuzyk, and G. Koeckelberghs. Record-high hyperpolarizabilities in conjugated polymers. *J. Mater. Chem. C*, **2**:4533–4538, 2014.
- [20] P. Serra-Crespo, M. A. Van Der Veen, E. Gobechiya, K. Houthoofd, Y. Filinchuk, C. E.A. Kirschhock, J. A. Martens, B. F. Sels, D. E. De Vos, F. Kapteijn, and J. Gascon. NH<sub>2</sub>-MIL-53(Al): A high-contrast reversible solid-state nonlinear optical switch. *J. Am. Chem. Soc.*, **134**(20):8314–8317, 2012.
- [21] R. Méreau, F. Castet, E. Botek, and B. Champagne. Effect of the dynamical disorder on the second-order nonlinear optical responses of. *J. Phys. Chem. A*, **113**(24):6552–6554, 2009.
- [22] B. Hidalgo Cardenuto, M.; Champagne. QM/MM Investigation of the concentration effects on the second-order nonlinear optical responses of solutions. *J. Chem. Phys.*, **141**:234104, 2014.
- [23] B Nénon, S.; Champagne. SCC-DFTB calculation of the static First hyperpolarizability: From gas phase molecules to functionalized surfaces. *J. Chem. Phys.*, **138**:204107, 2013.
- [24] M. Schulze, M. Utecht, A. Hebert, K. Rück-Braun, P. Saalfrank, and P. Tegeder. Reversible photoswitching of the interfacial nonlinear optical response. *J. Phys. Chem. Lett.*, **6**(3):505–509, 2015.
- [25] M. Sliwa, S. Létard, I. Malfant, M. Nierlich, P. G. Lacroix, T. Asahi, H. Masuhara, P. Yu, and K. Nakatani. Design, synthesis, structural and nonlinear optical properties of photochromic crystals: Toward reversible molecular switches. *Chem. Mater.*, **17**(18):4727–4735, 2005.
- [26] P.X. Li, M.S. Wang, M.J. Zhang, C.S. Lin, L.Z. Cai, S.P. Guo, and G.C. Guo. Electron-transfer photochromism to switch bulk second-order nonlinear optical properties with high contrast. *Angew. Chem. Int. Ed.*, **53**:11529–11531, 2014.
- [27] G. Szalóki, O. Alévêque, J.-L. Pozzo, R. Hadji, E. Levillain, and L. Sanguinet. Indolinoxazolidine: A versatile switchable unit. *J. Phys. Chem. B*, **119**(1):307–315, 2015.
- [28] M. Barzoukas, D. Josse, P. Fremaux, J. Zyss, J.F. Nicoud, and J.O. Morley. Quadratic nonlinear properties of N-(4-nitrophenyl)-L-prolinol and of a newly engineered molecular compound N-(4-nitrophenyl)-N-methylaminoacetonitrile: a comparative study. *J. Opt. Soc. Am. B*, **4**:977–986, 1987.

- [29] F. Castet, E. Bogdan, A. Plaquet, L. Ducasse, B. Champagne, and V. Rodriguez. Reference molecules for nonlinear optics: a joint experimental and theoretical investigation. *J. Chem. Phys.*, **136**(2), 2012.
- [30] T. Verbiest, K. Clays, and V. Rodriguez. *Second-order nonlinear optical characterisations techniques: an introduction*. CRC Press, New York, 2009.
- [31] I. Ledoux and J. Zyss. Influence of the molecular environment in solution measurements of the second-order optical susceptibility for urea and derivatives. *Chem. Phys.*, **73**(9):203–213, 1982.
- [32] V. Alain, M. Blanchard-Desce, I. Ledoux-Rak, and J. Zyss. Amphiphilic polyenic push-pull chromophores for nonlinear optical applications. *ChemComm*, **0**:353–354, 2000.
- [33] F. Tessore, E. Cariati, F. Cariati, D. Roberto, R. Ugo, P. Mussini, C. Zuccaccia, and A. Macchioni. The role of ion pairs in the second-order NLO response of 4-X-1-methylpyridinium salts. *ChemPhysChem*, **11**:495–508, 2010.
- [34] J. C. Phillips, R. Braun, W. Wang, J. Gumbart, E. Tajkhorshid, E. Villa, C. Chipot, R. D. Skeel, L. Kalé, and K. Schulten. Scalable molecular dynamics with NAMD. *J. Comput. Chem.*, **26**(16):1781–1802, 2005.
- [35] W. Humphrey, A. Dalke, and K. Schulten. Vmd: Visual molecular dynamics. *J. Mol. Graph.*, (1):33–38.
- [36] U. Essmann, L. Perera, and M.L. Berkowitz. A smooth particle mesh Ewald method. *J. Chem. Phys.*, **103**:8577–8592, 1995.
- [37] J. M. Wang, R. M. Wolf, J. W. Caldwell, P. Kollman, and D. Case. Development and testing of a general amber force field. *J. Comput. Chem.*, **25**(9):1157–1174, 2004.
- [38] A. Pizzirusso, M.E. Di Pietro, G. De Luca, G. Celebre, M. Longeri, L. Muccioli, and C. Zannoni. Order and conformation of biphenyl in cyanobiphenyl liquid crystals: a combined atomistic molecular dynamics and <sup>1</sup>H NMR study. *ChemPhysChem*, **15**:1356–1367, 2014.
- [39] J. Comer, J. C. Gumbart, J. Hénin, T. Lelievre, A. Pohorille, and C. Chipot. The adaptive biasing force method: Everything you always wanted to know but were afraid to ask. *J. Phys. Chem. B*, **119**(3):1129–1151, 2015.
- [40] Density of chloroform. [http://www.ddbst.com/en/EED/PCP/DEN\\_C47.php](http://www.ddbst.com/en/EED/PCP/DEN_C47.php), 2017.

- 
- [41] S. J. A. van Gisbergen, J. G. Snijders, and E. J. Baerends. Calculating frequency-dependent hyperpolarizabilities using time-dependent density functional theory. *J. Chem. Phys.*, **109**:10644–10656, 1998.
- [42] T. Helgaker, S. Coriani, P. Jørgensen, K. Kristensen, J. Olsen, and K. Ruud. Recent advances in wave function-based methods of molecular-property calculations. *Chem. Rev.*, **112**(1):543–631, 2012.
- [43] Y. Zhao and D. G. Truhlar. The M06 suite of density functionals for main group thermochemistry, thermochemical kinetics, noncovalent interactions, excited states, and transition elements: Two new functionals and systematic testing of four M06-class functionals and 12 other functionals. *Theor. Chem. Acc.*, **120**(1-3):215–241, 2008.
- [44] M. de Wergifosse and B. Champagne. Electron correlation effects on the first hyperpolarizability of push-pull  $\pi$ -conjugated systems. *J. Chem. Phys.*, **134**(7):074113, 2011.
- [45] L. E. Johnson, L. R. Dalton, and B. H. Robinson. Optimizing calculations of electronic excitations and relative hyperpolarizabilities of electrooptic chromophores. *Acc. Chem. Res.*, **47**(11):3258–3265, 2014.
- [46] K. Garrett, X. Sosa Vazquez, S. B. Egri, J. Wilmer, L. E. Johnson, B. H. Robinson, and C. M. Isborn. Optimum exchange for calculation of excitation energies and hyperpolarizabilities of organic electro-optic chromophores. *J. Chem. Theory Comput.*, **10**(9):3821–3831, 2014.
- [47] B. Mennucci, R. Cammi, and J. Mennucci. Medium effects on the properties of chemical systems: Electric and magnetic response of donor-acceptor systems within the polarizable continuum model. *Int. J. Quantum Chem.*, **75**(4-5):767–781, 1999.
- [48] J. Tomasi, B. Mennucci, and R. Cammi. Quantum mechanical continuum solvation models. *Chem. Rev.*, **105**(8):2999–3093, 2005.
- [49] M. J. Frisch, G. W. Trucks, H. B. Schlegel, G. E. Scuseria, M. A. Robb, J. R. Cheeseman, G. Scalmani, V. Barone, B. Mennucci, G. A. Petersson, et al. Gaussian 09 revision d01, 2009. Gaussian Inc. Wallingford CT 2009.
- [50] K. Pielak, F. Bondu, L. Sanguinet, V. Rodriguez, B. Champagne, and F. Castet. Second-order nonlinear optical properties of multiaddressable Indolinoxazolidine derivatives: joint computational and hyper-Rayleigh scattering investigations. *J. Phys. Chem. C*, **121**(3):1851–1860, 2017.

# Nonlinear Optical Responses of Self-Assembled Monolayers Functionalized with Indolino-Oxazolidine Photoswitches

C. Tonnelé, K. Pielak, J. Deviers, L. Muccioli, B. Champagne and F. Castet  
*Phys. Chem. Chem. Phys.* **20**:21590-21597, 2018.

*In this chapter, a computational approach combining molecular dynamic simulations and density functional theory (DFT) calculations is implemented to evaluate the second-order nonlinear optical (NLO) responses of photoresponsive self-assembled monolayers (SAMs) based on indolino-oxazolidine molecular switches. These numerical simulations provide a complete atomistic picture of the morphology of the SAMs, revealing a high degree of positional disorder and an almost isotropic orientation of the chromophores. Subsequent DFT calculations, carried out to evaluate the average first hyperpolarizability of indolino-oxazolidine switches within the SAM, predict that the structural disorder does not significantly reduce the NLO contrast compared to that of the isolated molecules. Chromophores in the SAM can assume a limited number of specific conformers, due to the high rotational barrier that characterize the conjugated bonds along the indolino/oxazolidine-diene-thiophene sequence. A notable exception is the rotation about the thiophene-thioalkyl bond, which is not only almost free, but also strongly correlated with the magnitude of the first hyperpolarizability. Controlling this rotation by chemical design could thus be a viable strategy to optimize the SAMs NLO response and the performance of photoresponsive devices based on indolino/oxazolidine switches.*

My contribution to this chapter was my participation to the supervision of the master internship of J. Deviers on the DFT calculations of molecular hyperpolarizabilities, and to the analysis of the results.

## 7.1 Introduction

Organic photochromic compounds have been extensively studied in the last decades, owing to their possible integration into a large variety of photonic and optoelectronic applications. [1–3] Surface functionalization with molecular photo-switches yields 2D materials responding to light in a controlled way. [4] One of the most versatile approaches for surface engineering and interface design is to use self-assembled monolayers (SAMs), [5] in which highly efficient and selective 'click' reactions can be exploited to introduce a wide range of organic functionalities on well-defined base monolayers, typically consisting in azide-terminated alkylsilanes grafted on commercially available silica substrates. [6–8] Thus, the design of photoresponsive SAMs opens the way for virtually endless materials for applications in optical data storage and signal processing.

While effective in writing the information by switching the chromophores between one (meta)stable state to another, the use of linear absorption spectroscopy to probe the system often results in a destructive readout process, since the state of the photochromic molecules can be altered upon irradiation. Exploiting second-order non-linear optical (NLO) properties instead provides a strategy for non-destructive readout ability to the system, since NLO responses are revealed using near-infrared wavelengths not energetic enough to trigger uncontrolled photoconversions. Molecules exhibiting large and photoswitchable first hyperpolarizability are thus ideal candidates for photonic technologies with multiple storage and non-destructive readout capacity. [9–11]

Filling the gap between isolated molecular switches and photoresponsive materials nevertheless remains a quite challenging task, which requires anchoring the molecular photochromes on a 2D substrate while preserving i) the reversibility of the switching process, and ii) the NLO responses of the switching states, as well as their contrast. Indeed, experiments showing effective photoswitchable NLO SAMs based on fulgimide or azobenzene derivatives have been recently reported, [12, 13] but addressing the aforementioned challenges from a computational point of view has never been tackled. Yet, by offering a microscopic picture of the relationships between the supramolecular structure and NLO properties of the system, numerical simulations have the potential of providing highly useful guidelines to rationally control the NLO responses of the SAMs.

The present work constitutes a first attempt towards the theoretical design of such complex architectures, focusing on indolino-oxazolidine (IND) compounds anchored onto an amorphous  $\text{SiO}_2$  surface. IND derivatives (Scheme 7.1) exhibit reversible photo-conversion between a colorless closed form (CF) and a colored open form (OF) associated with large changes in the first hyperpolarizability. [14–16] To mimic the experimental preparation of indolino-oxazolidine SAMs by click chemistry, [6] IND units were anchored to the silica surface using a two-step process, in which the  $\text{SiO}_2$

surface is first grafted with azidoalkyl linkers, and subsequently some of the linkers are functionalized with photoswitchable IND units (Scheme 7.1). Then, a sequential approach combining classical molecular dynamics (MD) and quantum mechanics (QM) was employed to evaluate the dynamical behavior and second harmonic generation (SHG) responses of the photoresponsive SAMs. MD simulations gave access to the morphology of the NLO-active layer at the atomistic level, and allowed the exhaustive statistical sampling of the multiple geometrical conformations spanned by the chromophores. Finally, DFT calculations performed on individual molecular fragments extracted from the MD trajectories provided a molecular interpretation on how dynamical geometry distortions, induced by thermal and steric effects, impact the SHG responses of both states of the SAM.

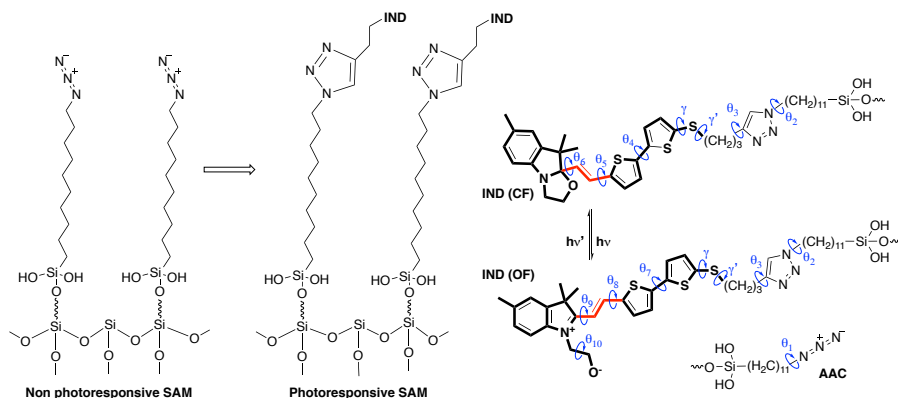


Figure 7.1: SiO<sub>2</sub> surface functionalized with azidoalkyl chains (left) and with the photoresponsive molecules (middle). A similar scheme was adopted for constructing the SAM geometries in the MD simulations. Right: photochromic reaction between the closed form (CF) and open form (OF) of the indolino-oxazolidine derivative (IND, in bold), and azidoalkyl chain (AAC). FF parameters have been derived for torsions  $\theta_1$  to  $\theta_{10}$  (see Appendix D for the definition of the dihedral angles).

## 7.2 Theoretical Methodology

### 7.2.1 Molecular Dynamics Simulations

As detailed in the electronic supporting information (see Appendix D), modified versions of the General AMBER Force Field [17] (FF) were used to specifically reproduce the equilibrium geometries of the azidoalkyl linkers and of the complete NLO molecule (Scheme 7.1). Distinct sets of parameters were derived for describing the open and closed forms of IND. Electrostatic potential-fitted (ESP) atomic charges and torsional potentials around the  $\theta_1 - \theta_{10}$  dihedrals were calculated at the M06/6-311G(d) level, and inserted in the force field with the methodology described in reference [18]. In addition, since reliable simulations of NLO responses of push-pull systems require an accurate description of the  $\pi$ -electron conjugation, [16] AMBER FF bond lengths were adjusted for both states of the switch so as to closely

reproduce DFT bond lengths at the corresponding equilibrium geometries (within a maximum absolute error of 0.006 Å), as well as the bond length alternation (BLA) along the central vinyl bridge (red segments in Scheme 7.1). The amorphous SiO<sub>2</sub> surface of dimensions 52.044 × 51.119 Å<sup>2</sup> and thickness of about 30 Å was constructed following the scheme described in Appendix D. IND-functionalized SAMs were subsequently prepared using a strategy mimicking the experimental sample preparation. In a first step, a densely packed SAM of 120 azido-undecylsilane chains, corresponding to a coverage of 4.5 molecules/nm<sup>2</sup>, was generated to serve as a basis for grafting the NLO molecules. These long non conjugated linkers are used experimentally to electronically decouple the photochromic units from the substrate. This first sample, referred hereafter to as the "non photoresponsive SAM" (see Scheme 7.1), was equilibrated for 80 ns keeping fixed the position of the grafting oxygen of each azidoalkyl chain. In the second step, imitating the click reaction used in the experimental process, azide terminal groups were replaced by the photochromic compound in its closed form. Since the IND unit is bulkier than the azide unit of the non photoresponsive SAM, only a fraction of azides was replaced, yielding to three samples with different relative IND to total SAM molecule ratios, namely 1/4, 1/2 and 3/4, corresponding to IND coverages of 1.13, 2.26 and 3.38 molecules/nm<sup>2</sup>, respectively. The samples were first equilibrated for 30 ns, before we focused on the most dense SAM for which simulation was extended up to 150 ns. Finally, to obtain the open form layer for the highest coverage sample, the force field parameters were switched from the ones optimized for the CF to the ones optimized for the OF for all chromophores simultaneously, and the resulting OF system was equilibrated for further 85 ns.

## 7.2.2 Quantum Chemical Calculations

Individual molecular structures were extracted from the SAM with the highest relative coverage (3/4), at regular intervals along the MD trajectories, and their NLO responses subsequently calculated. Preliminary investigations demonstrated that, in addition to the photoresponsive IND unit, the triazole moiety, and to a lesser extent the alkyl chain, should be explicitly included in the calculations for an accurate evaluation of the hyperpolarizabilities, while the Si(OH)<sub>2</sub>O anchoring unit can be omitted (see Appendix D for details). A total of 900 structures were then used to sample the multiple geometrical conformations adopted by the NLO switches, in both their closed and open forms.

The static and dynamic components of the molecular first hyperpolarizability tensor ( $\beta$ ) were calculated using time-dependent (TD) DFT with the M06-2X [19] exchange-correlation functional (XCF) and the 6-311G(d) basis set. As demonstrated in previous theoretical reports, M06-2X is reliable to calculate hyperpolarizabilities of conjugated organic dyes, [20–22] including indolino-oxazolidine deriva-

tives, [16] owing to its substantial amount (54%) of long-range Hartree-Fock exchange. An incident wavelength of 1064 nm, typical of Nd:YAG laser sources, was used in frequency-dependent SHG calculations. The interfacial NLO responses were analyzed by considering the norm of the first hyperpolarizability vector:

$$\|\vec{\beta}\| = \beta = \sqrt{\beta_x^2 + \beta_y^2 + \beta_z^2} \quad (7.1)$$

where the  $i^{\text{th}}$  component of the  $\beta$  vector is defined from the  $\beta$  tensor elements:

$$\beta_i = \beta_{iii} + \frac{1}{3} \sum_{j \neq i} (\beta_{ijj} + \beta_{jij} + \beta_{jji}) \quad (7.2)$$

As in the previous work of Tegeder and co., [12] the anisotropy of the NLO response was also characterized using the component of the  $\beta$  vector normal to the surface plane ( $\beta_z$ ), and the corresponding in-plane ones:

$$a = \frac{|\beta_z|}{\sqrt{\beta_x^2 + \beta_y^2}} \quad (7.3)$$

All calculations were performed using the Gaussian09 package. [23] All  $\beta$  values are reported assuming a Taylor series expansion of the induced dipole with respect to the applied electric field (T convention), [24, 25] and are given in atomic units (1 au of  $\beta = 3.6310^{-42} \text{ m}^4\text{V}^{-1} = 3.2063 \times 10^{-53} \text{ C}^3\text{m}^3\text{J}^{-2} = 8.641 \times 10^{-33} \text{ esu}$ ).

## 7.3 Results and Discussion

### 7.3.1 Morphology of the Self-Assembled Monolayers

The equilibrated morphology of the non photoresponsive SAM (*i.e.* the surface functionalized with azidoalkyl chains only, see Scheme 7.1), as well as the morphology of the SAM functionalized with the photochromic units in their closed and open forms (for a 3/4 coverage), are represented by the snapshots in Figure 7.2. The supramolecular organization of the non photoresponsive SAM is characterized by a thickness of  $15 \pm 2 \text{ \AA}$ , an average tilt angle of  $26 \pm 7^\circ$ , a nematic order parameter  $\langle P_2 \rangle$  of 0.901 and a roughness of  $0.86 \text{ \AA}$ . To verify the extent of positional order in all SAMs, we used the 2D radial distribution function (RDF) in the  $(x, y)$  plane, which gives a measure of the probability of finding a molecule at a given position with respect to a reference central molecule (Figure 7.3). The 2D RDF of the non photoresponsive SAM clearly evidences a hexagonal positional order in the sample (with a lattice parameter  $d = 4.96 \text{ \AA}$ ), as already observed for H-terminated alkylsiloxane SAMs. [26] Comparing the top panels of Figure 7.3 reveals that the hexagonal organization of the azidoalkyl layer is globally maintained after functionalization with the photochromic dyes, although it induces a non negligible broadening of the

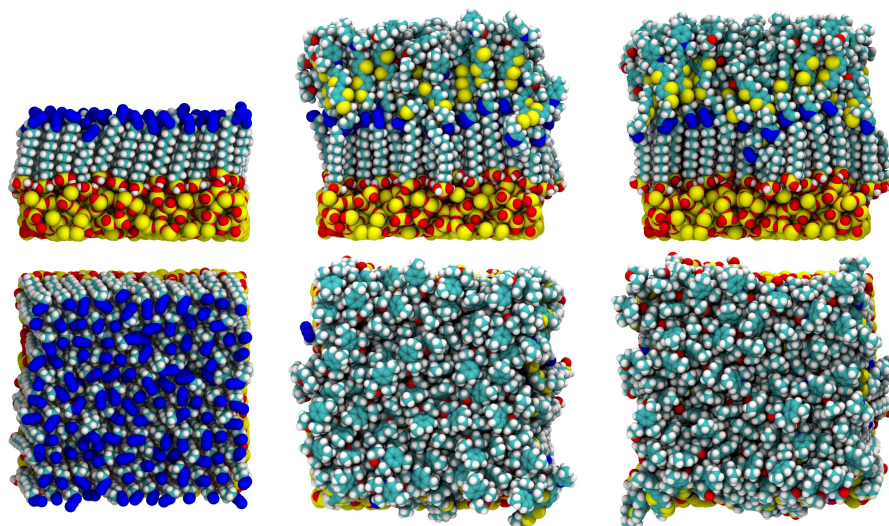


Figure 7.2: Left: side and top views of the non photoresponsive SAM. Middle: side and top views of the SAM functionalized with the photochromic units in their closed form. Right: in their open form.

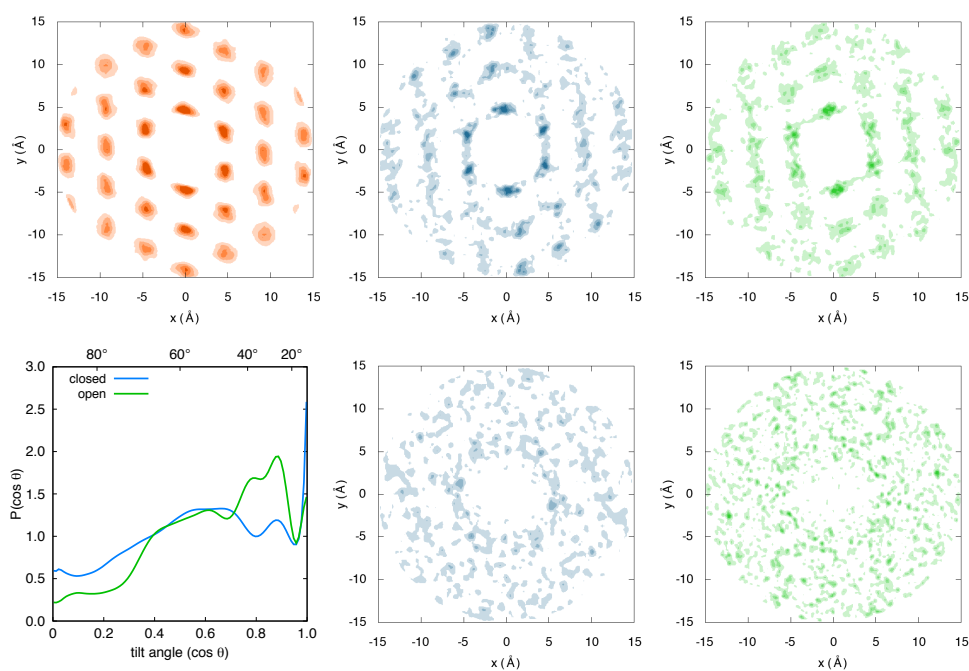


Figure 7.3: Top: 2D RDF of the centers of mass of the SAM alkyl chains in the non photoresponsive SAM (left), in the photoresponsive SAM in closed form (middle) and in open form (right). Bottom: distribution of the cosine of the tilt angle  $\theta$  between the double C=C bond of the vinyl bridge and the axis normal to the surface plane (left), and 2D RDF of the centers of mass of the triazole-indolino-oxazolidine units in the closed and open form SAMs (middle and right panels).

RDF peaks. On the contrary, a visual inspection of the morphology of the photoresponsive SAM (Figure 7.2) does not evidence any positional order in the top-half sublayer, as confirmed by the 2D RDFs reported in the bottom panels of Figure 7.3 for the closed and open layers. The distribution of the tilt angle of the dyes with respect to the surface normal (bottom left of Figure 7.3) reveals that even if a few units are vertically oriented, the distribution is overall almost isotropic. Conversely, the azido-alkyl chains have a uniform, nearly vertical orientation, which is not tilted, unlike that found in the non photoresponsive SAM (cf. top panels of Figure 7.2).

Decreasing the relative coverage induces a decrease of the SAM thickness, from 40.4 Å (3/4 coverage) to 34.0 Å (1/2 coverage) and 26.7 Å (1/4 coverage). Substantiated by a corresponding increase of the tilt (Table D.1), this demonstrates how NLO molecules bend at low coverage ratio, while they adopt more elongated conformations in the denser layer. On the other hand, the CF to OF photoconversion does not significantly change the thickness of the SAM (40.4 *vs.* 40.6 Å for CF and OF, respectively). Reversely, the roughness slightly increases when decreasing the coverage, from 1.32 to 3.15 Å.

Focusing on the SAM with higher IND density (3/4 coverage), we investigated more closely the geometrical conformations spanned by the photochromic molecules onto the surface. Consistently with the DFT geometries used for the force field parameterization, the average BLA of the open forms is three times smaller ( $0.089 \pm 0.061$  Å) than that of closed forms ( $0.288 \pm 0.061$  Å). The distributions of the torsional angles adopted by the molecules within the SAM, plotted with respect to the corresponding rotational potentials of isolated molecules (Figures D.8 and D.9), are also informative. Due to high rotation barriers (varying from 3.2 to 13.0 kcal/mol), the population of the  $\theta_4 - \theta_{10}$  and  $\gamma'$  dihedrals (Scheme 7.1) concentrate around the minima of the potential energy curves of the isolated molecules. Reversely, the  $\theta_1 - \theta_3$  and  $\gamma$  dihedrals exhibit very broad distributions due to low energy barriers ( $\sim 1$  kcal/mol or smaller). Interestingly, the maxima of the distributions of these torsional angles do not always correspond exactly to minima of the potential energy curve, suggesting that the most probable values are dictated by intermolecular interactions.

### 7.3.2 Commutation of the Nonlinear Optical Responses

The statistical distributions of the static and dynamic first hyperpolarizabilities ( $\beta$ , eq. 7.1), of their  $z$ -component ( $\beta_z$ ), and of the anisotropy factors ( $a$ , eq. 7.3) are illustrated in Figure 7.4, while average values and standard deviations ( $\sigma$ ) are collected in Table 7.1. The interquartile ranges (IQR), which provide a robust measure of the dispersion of statistical distributions, are also reported.

Considering first the static responses, dynamical geometry fluctuations and steric interactions lead to broad  $\beta$  and  $\beta_z$  distributions, characterized by large  $\sigma$  and IQR

values. It also clearly appears from Figure 7.4 that the distributions of open forms are much broader than those of closed forms, as confirmed by IQR values about four times larger. Moreover for both forms the component normal to the surface plane,  $\beta_z$ , dominates the static hyperpolarizability, as indicated by average anisotropy ratios  $\langle a \rangle$  lying between 3.6 and 4.2. Interestingly, a similar  $\langle a \rangle$  value ( $5.70/\sqrt{2} = 4.03$ ) was deduced from recent experimental measurements and DFT calculations for the *trans*-configuration of azobenzene-based SAMs. [12] However, while the *trans-cis* isomerization in azobenzene derivatives was shown to strongly reduce the anisotropy of the NLO response owing to the realignment of the upper phenyl ring parallel to the surface, the oxazolidine ring opening in IND derivatives hardly changes the anisotropy of the SHG response, consistently with the invariance of the SAM thickness mentioned above. One also notes that, contrary to the absolute NLO responses, the distribution of the anisotropy ratios is slightly less dispersed for the open form, even if in both cases a considerable fraction of molecules has very low anisotropy, consistently with the broad distributions of tilt angles shown in Figure 7.3.

The commutation between the closed and open forms induces a large enhancement of the static first hyperpolarizability, as shown by the shift of the  $\beta$  distributions. The OF/CF NLO contrast, evaluated as the ratio between the mean values of the distributions (Table 7.1), is equal to  $\sim 7$ . Strikingly, this contrast is only slightly smaller than the one calculated for the isolated molecule in its equilibrium geometry ( $\beta(\text{POF})/\beta(\text{CF}) = 8.93$ ). This result indicates that, despite the close molecular packing induces strong geometrical distortions, the high degree of disorder of the SAM is not detrimental to the average NLO contrast, which is of crucial importance for device efficiency. This also confirms and extends to amorphous morphologies the conclusions previously deduced from periodic self-consistent charge density functional tight binding calculations, that single IND units anchored through silanol linkers onto a  $\text{SiO}_2$  surface maintain their NLO activities and contrasts. [27]

Table 7.1: Averaged values, standard deviations ( $\sigma$ ), and interquartile range (IQR) of the average static ( $\lambda = \infty$ ) and dynamic ( $\lambda = 1064$  nm) hyperpolarizabilities ( $\beta$ ), of their  $z$ -component ( $\beta_z$ ), and of the anisotropy factor ( $a$ ). The two last lines report the OF/CF enhancement ratios of the NLO responses.

Property	$\lambda = \infty$		$\lambda = 1064$ nm	
	CF	OF	CF	OF
$\langle \beta \rangle \pm \sigma_\beta$	$2624 \pm 1655$	$19473 \pm 11410$	$5699 \pm 3942$	$(146337 \pm 70035)^a$
$\langle \beta_z \rangle \pm \sigma_{\beta_z}$	$-2311 \pm 1765$	$-16725 \pm 11322$	$-4960 \pm 4176$	$(-59100 \pm 123161)^a$
$\langle a \rangle \pm \sigma_a$	$4.20 \pm 5.18$	$3.56 \pm 4.19$	$4.18 \pm 5.22$	$(3.54 \pm 11.09)^a$
IQR( $\beta$ )	2765	12036	6309	275013
IQR( $\beta_z$ )	2770	11940	6359	188310
IQR( $a$ )	3.62	3.25	3.66	2.38
$\langle \beta(\text{OF}) \rangle / \langle \beta(\text{CF}) \rangle$	$7.42 \pm 9.03$		$25.68 \pm 30.05$	
$\langle \beta_z(\text{OF}) \rangle / \langle \beta_z(\text{CF}) \rangle$	$7.24 \pm 10.43$		$11.92 \pm 34.86$	

<sup>a</sup>Calculated by excluding all the molecules with  $\beta$  values outside the IQR.

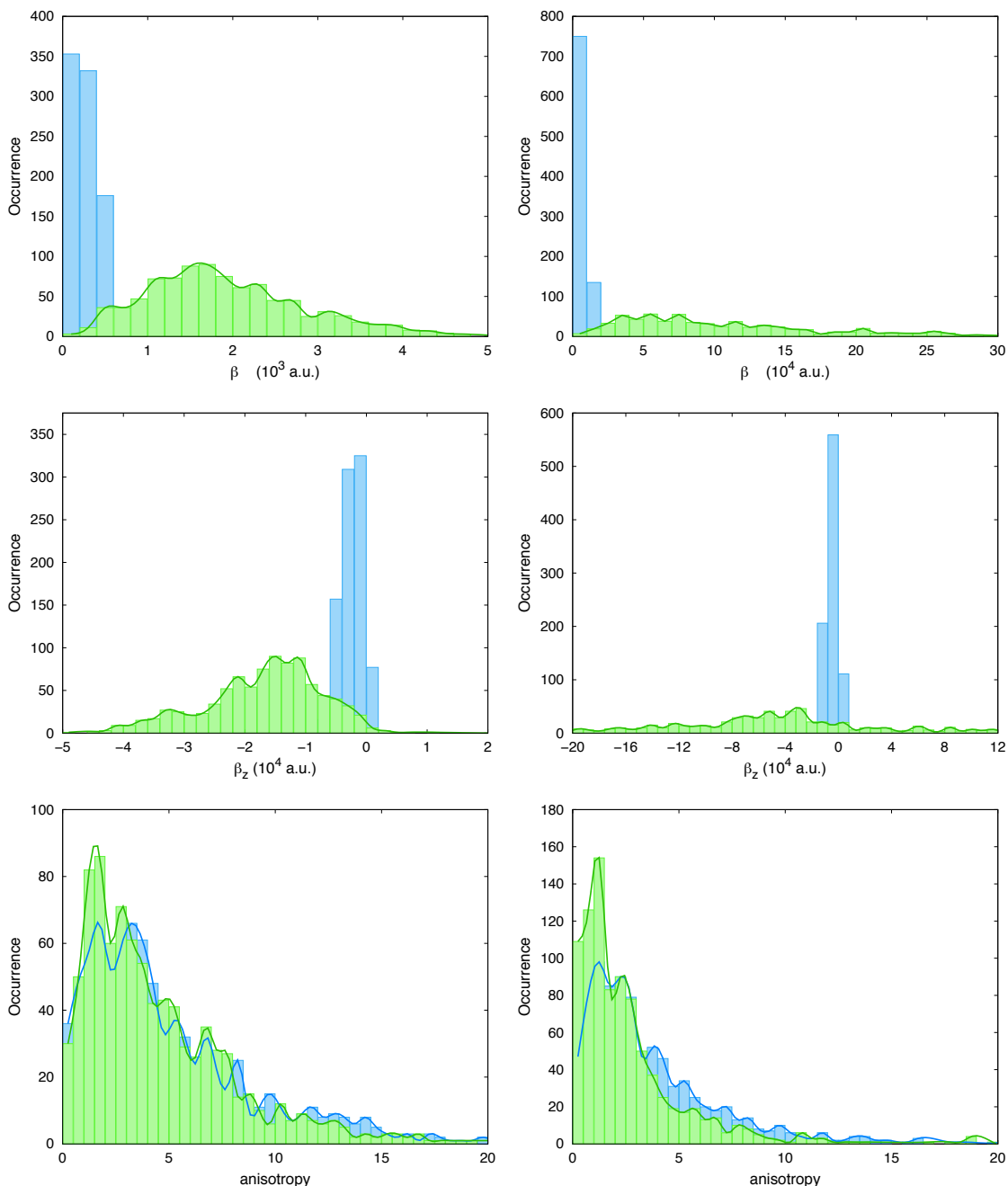


Figure 7.4: Distributions of the static (left) and dynamic (right) values of  $\beta$  (top),  $\beta_z$  (middle) and  $a$  (bottom), for closed (blue) and open (green) forms.

Considering the dynamic NLO responses, the average values of  $\beta$  and  $\beta_z$  computed for the closed forms are enhanced by a factor 2.2 compared to their static analogues. The dynamical distributions are also more dispersed than the static ones, with IQR values about two times larger. In the case of open forms, the dynamic  $\beta$  values are spread over a very broad range, the NLO responses of a few set of structures being strongly contaminated by electronic excitation resonances. These resonance phenomena give rise to numerical instabilities, which make the calculated dynamic  $\beta$  values of the OF less reliable. To partially circumvent this problem, the averages of the dynamic NLO properties of the OF were estimated by considering only the molecules with  $\beta$  values within the interquartile range. For

the open form, the enhancement due to frequency dispersion effects, defined as the ratio between the dynamic and static responses, amounts to 7.5 and 3.5 for  $\beta$  and  $\beta_z$ , respectively. Interestingly, the anisotropy of the NLO responses is not impacted by frequency resonance, the average anisotropy ratio  $\langle a \rangle$  being identical to that calculated considering the static responses. Finally, the dynamic  $\beta(\text{OF})/\beta(\text{CF})$  NLO contrast amounts to  $\sim 26$ , *i.e.* more than 3 times the static one, while it is reduced to  $\sim 12$  when considering the  $z$ -component only.

### 7.3.3 Relationships Between Geometrical Structures and NLO Responses

To gain a deeper understanding on the impact of the geometrical distortions on the intrinsic (static) NLO properties of the photochromes, correlations between the calculated  $\beta$  responses and molecular structural parameters were further analyzed. The variations of  $\beta$  with torsional angles around single bonds are reported in Appendix D, while Figure 7.5 illustrates the variations of  $\beta$  with respect to  $\gamma$ , as well as to the BLA along the vinyl bridge connecting the indolino-oxazolidine and the bithiophene. As already observed for molecules in solution, [16] Figure 7.5 (top panel) clearly evidences that the difference in the magnitude of the  $\beta$  response between open and closed forms is mainly driven by the BLA along the central part of the photochromes, whose average value decreases from 0.288 to 0.089 Å. Consid-

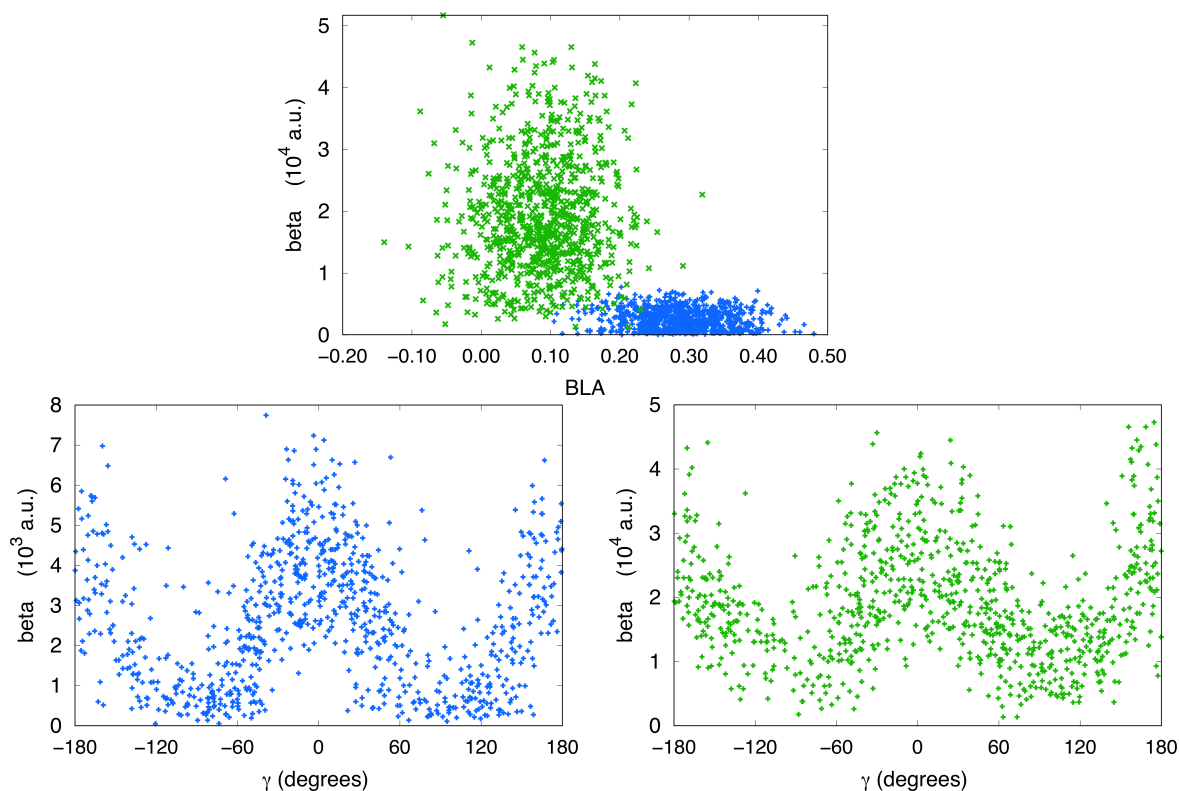


Figure 7.5:  $\beta$  values plotted versus the BLA and  $\gamma$  torsion angle in closed (blue) and open (green) forms.

ering CF and OF separately, it turned out quite unexpectedly that the amplitude of  $\beta$  in both forms is strongly correlated with the value of the torsion angle  $\gamma$  (see Scheme 7.1). As illustrated in Figure 7.5 (bottom panels), large first hyperpolarizabilities are obtained for planar conformations with respect to  $\gamma$  (*i.e.* when  $\gamma = 0^\circ$  or  $180^\circ$ ), while  $\beta$  is much smaller when the S-C bond of the thiomethylene group is perpendicular to the thiophene ring. Further analyses detailed in the Appendix D revealed that upon photoexcitation, planar conformations allow the conjugation of one lone pair of the sulfur atom of the thiopropylene, giving rise to an important charge transfer between the sulfur and the dithiophene. This effect is at the origin of the enhancement of the first hyperpolarizability compared to perpendicular conformations. On the contrary, the distributions of  $\beta$  with respect to  $\theta_2$  and  $\theta_3$  (see Appendix D) revealed that the amplitude of the NLO responses is not correlated to rotations around these two dihedrals, which also assume all possible values due to low rotational energy barriers. The other dihedrals ( $\theta_4 - \theta_{10}$ ) adopt instead specific values due to conjugation effects and steric constraints.

The striking correlation between the NLO response and the  $\gamma$  torsional angle reveals a crucial effect for the chemical engineering of 2D NLO materials. Owing to the low rotational energy barrier for the rotation around  $\gamma$  ( $\sim 0.8$  kcal/mol, see Appendix D), the conformations adopted are mostly driven by intermolecular contacts. Since these packing effects are very difficult to control, it emerges that the best strategy to maximize the NLO responses of dye-functionalized SAMs consists in designing rigid molecules with geometry constrained to their highest hyperpolarizability conformation.

## 7.4 Conclusions

In this work, we have used a sequential multiscale approach combining atomistic MD simulations and DFT calculations to evaluate the second harmonic generation responses of photoresponsive SAMs based on indolino-oxazolidine derivatives. MD simulations revealed that photoresponsive regions of the SAMs exhibit a high degree of orientational and positional disorder due to the flexibility of the photoresponsive units (in particular that of the thioalkyl group), which on the one hand is detrimental for crystalline packing, and on the other hand makes the chromophore conformation highly sensitive to intermolecular interactions. Quite interestingly, DFT calculations carried out on a large selection of simulated molecular structures evidence that, despite large geometrical distortions of the photochromic molecules and the lack of orientational order, IND-based SAMs are expected to display a good contrast in first hyperpolarizability upon the photochromic conversion, of the same order of magnitude as that observed in the isolated molecule.

As already known from previous studies, [16] the large NLO enhancement from

the closed to the open configuration can be attributed to the increase of the  $\pi$ -electron conjugation between the indolino-oxazolidine and bithiophene moieties, as described by the strong decrease of the bond length alternation along the vinyl linker connecting these two units. More surprising was the correlation found between the magnitude of the first hyperpolarizability in both forms and the torsional angle  $\gamma$  around the single bond between bithiophene and thioalkyl groups. Since this rotation is quasi barrierless in the isolated molecule, the statistical distribution of this dihedral angle is very broad for both forms of the SAMs studied here. In such a case, only controlling by chemical design the shape of this distribution in newly synthesized indolino-oxazolidine derivatives would allow maximizing their NLO responses. More generally, these results tell us that calculations of the NLO properties of isolated molecules allows a reliable screening of the most effective compounds for subsequent integration in 2D materials, but also highlight that optimizing the NLO responses of devices requires a fine control of the intermolecular interactions, which induce significant distortions in the molecular structure. Reducing the flexibility of the photoresponsive molecular units, together with variations of the coverage rate or the use of bulky separators, appear as promising strategies.

Mutual polarization effects, not considered in this first study, might also significantly impact the NLO responses of the SAMs. Future investigations, carried out on a representative set of molecular aggregates, are expected to provide design rules to effectively exploit the collective effects for optimizing the amplitude of the NLO responses of the system, as well as their contrast upon commutation. The sequential MD-QM approach implemented here promises to be a highly useful computational tool to explore these different alternatives. Finally, since the MD simulations were conducted on SAMs with fully closed or open forms, assuming therefore the switching of 100% of the chromophores, it would also be interesting to investigate the light-induced dynamic effects. These investigations should provide key information on the switching efficiency in these densely packed systems.

# Bibliography

---

- [1] B. L. Feringa and W. R. Browne, editors. *Molecular switches, second edition*. Wiley-VCH, Weinheim, 2011.
- [2] E. Orgiu and P. Samori. 25th anniversary article: organic electronics marries photochromism: generation of multifunctional interfaces, materials, and devices. *Adv. Mater.*, **26**(12):1827–1845, 2014.
- [3] J. Andréasson and U. Pischel. Molecules with a sense of logic: a progress report. *Chem. Soc. Rev.*, **44**(5):1053–1069, 2015.
- [4] W. R. Browne and B. L. Feringa. Light switching of molecules on surfaces. *Annu. Rev. Phys. Chem.*, **60**(1):407–428, 2009.
- [5] S. Casalini, C. A. Bortolotti, F. Leonardi, and F. Biscarini. Self-assembled monolayers in organic electronics. *Chem. Soc. Rev.*, **46**:40–71, 2017.
- [6] T. Lummerstorfer and H. Hoffmann. Click chemistry on surfaces: 1,3-dipolar cycloaddition reactions of azide-terminated monolayers on silica. *J. Phys. Chem. B*, **108**(13):3963–3966, 2004.
- [7] C. Haensch, S. Hoepfener, and U. S. Schubert. Chemical modification of self-assembled silane based monolayers by surface reactions. *Chem. Soc. Rev.*, **39**:2323–2334, 2010.
- [8] C. Nicosia and J. Huskens. Reactive self-assembled monolayers: from surface functionalization to gradient formation. *Mater. Horiz.*, **1**:32–45, 2014.
- [9] B. J. Coe. Molecular materials possessing switchable quadratic nonlinear optical properties. *Chem. Eur. J.*, **5**(9):2464–2471, 1999.
- [10] I. Asselberghs, K. Clays, A. Persoons, Michael D. Ward, and J. McCleverty. Switching of molecular second-order polarizability in solution. *J. Mater. Chem.*, **14**:2831–2839, 2004.

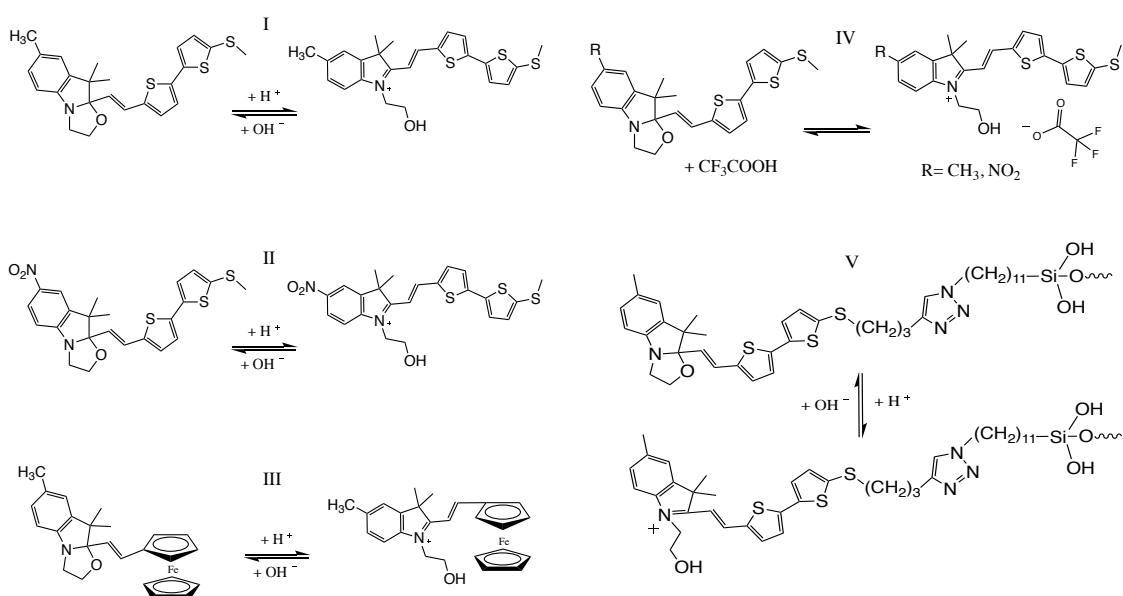
- 
- [11] F. Castet, V. Rodriguez, J.-L. Pozzo, L. Ducasse, A. Plaquet, and B. Champagne. Design and characterization of molecular nonlinear optical switches. *Acc. Chem. Res.*, **46**(11):2656–2665, 2013.
- [12] M. Schulze, M. Utecht, T. Moldt, D. Przyrembel, C. Gahl, M. Weinelt, P. Saalfrank, and P. Tegeder. Nonlinear optical response of photochromic azobenzene-functionalized self-assembled monolayers. *Phys. Chem. Chem. Phys.*, **17**:18079–18086, 2015.
- [13] M. Schulze, M. Utecht, A. Hebert, K. Ruck-Braun, P. Saalfrank, and P. Tegeder. Reversible photoswitching of the interfacial nonlinear optical response. *J. Phys. Chem. Lett.*, **6**(3):505–509, 2015.
- [14] L. Sanguinet, J.-L. Pozzo, V. Rodriguez, F. Adamietz, F. Castet, L. Ducasse, and B. Champagne. Acido- and photo-triggered NLO properties enhancement. *J. Phys. Chem. B*, **109**(22):11139–11150, 2005.
- [15] F. Mançois, J.-L. Pozzo, J. Pan, F. Adamietz, V. Rodriguez, L. Ducasse, F. Castet, A. Plaquet, and B. Champagne. Two-way molecular switches with large nonlinear optical contrast. *Chem.–Eur. J.*, **15**(11):2560–2571, 2009.
- [16] K. Pielak, F. Bondu, L. Sanguinet, V. Rodriguez, B. Champagne, and F. Castet. Second-order nonlinear optical properties of multiaddressable indolinoxazolidine derivatives: joint computational and hyper-Rayleigh scattering investigations. *J. Phys. Chem. C*, **121**(3):1851–1860, 2017.
- [17] J. Wang, R. M. Wolf, J. W. Caldwell, P. A. Kollman, and D. A. Case. Development and testing of a general amber force field. *J. Comput. Chem.*, **25**(9):1157–1174, 2004.
- [18] A. Pizzirusso, M. E. Di Pietro, G. De Luca, G. Celebre, M. Longeri, L. Muccioli, and C. Zannoni. Order and conformation of biphenyl in cyanobiphenyl liquid crystals: a combined atomistic molecular dynamics and 1h nmr study. *ChemPhysChem*, **15**(7):1356–1367, 2014.
- [19] Y. Zhao and D. G. Truhlar. The M06 suite of density functionals for main group thermochemistry, thermochemical kinetics, noncovalent interactions, excited states, and transition elements: two new functionals and systematic testing of four M06-class functionals and 12 other functionals. *Theor. Chem. Acc.*, **120**:215–241, 2008.
- [20] M. de Wergifosse and B. Champagne. Electron correlation effects on the first hyperpolarizability of push-pull  $\pi$ -conjugated systems. *J. Chem. Phys.*, **134**(7):074113, 2011.

- 
- [21] L. E. Johnson, L. R. Dalton, and B. H. Robinson. Optimizing calculations of electronic excitations and relative hyperpolarizabilities of electrooptic chromophores. *Acc. Chem. Res.*, **47**(11):3258–3265, 2014.
- [22] K. Garrett, X. Sosa Vazquez, S. B. Egri, J. Wilmer, L. E. Johnson, B. H. Robinson, and C. M. Isborn. Optimum exchange for calculation of excitation energies and hyperpolarizabilities of organic electro-optic chromophores. *J. Chem. Theory Comput.*, **10**(9):3821–3831, 2014.
- [23] M. J. Frisch, G. W. Trucks, H. B. Schlegel, G. E. Scuseria, M. A. Robb, J. R. Cheeseman, G. Scalmani, V. Barone, B. Mennucci, G. A. Petersson, H. Nakatsuji, M. Caricato, X. Li, H. P. Hratchian, A. F. Izmaylov, et al. Gaussian 09 revision d01. Gaussian Inc. Wallingford CT 2009.
- [24] A. Willetts, J. E. Rice, D. M. Burland, and D. P. Shelton. Problems in the comparison of theoretical and experimental hyperpolarizabilities. *J. Chem. Phys.*, **97**(10):7590–7599, 1992.
- [25] H. Reis. Problems in the comparison of theoretical and experimental hyperpolarizabilities revisited. *J. Chem. Phys.*, **125**(1):014506, 2006.
- [26] O. M. Roscioni, L. Muccioli, A. Mityashin, J. Cornil, and C. Zannoni. Structural characterization of alkylsilane and fluoroalkylsilane self-assembled monolayers on  $\text{SiO}_2$  by molecular dynamics simulations. *J. Phys. Chem. C*, **120**(27):14652–14662, 2016.
- [27] S. Nénon and B. Champagne. Scc-dftb calculation of the static first hyperpolarizability: From gas phase molecules to functionalized surfaces. *J. Chem. Phys.*, **138**(20):204107, 2013.



# Summary, General Conclusions, and Outlook

This thesis has employed theoretical chemistry methods and experimental techniques to study the second harmonic generation (SHG) responses of indolinoxazolidine derivatives in different environments. These systems exhibit versatile switching properties and interconvert between a colorless closed form and a colored open form in a trimodal way, *i.e.* under light irradiation, pH variations, and redox potential variations. In this thesis, the commutation has been triggered by trifluoroacetic acid. The studied switches are composed of an indolinoxazolidine switchable acceptor bearing either a methyl or a nitro group, linked by an ethylenic bridge to a bithiophene or a ferrocene donor moiety (Scheme 8.1).



Scheme 8.1: Structure of the molecular switches that have been investigated and their equilibrium between closed and open forms.

---

Experimental characterizations of the linear optical properties have been carried out using UV-vis absorption spectroscopy, while the nonlinear optical (NLO) properties have been characterized by means of the hyper-Rayleigh scattering (HRS) method as well as the electric-field induced second harmonic generation (EFISHG) technique. In the case of EFISHG, since the target system has to be neutral, the measurements have been achieved in chloroform solution because the protonated open form is associated with its trifluoroacetate counterion.

In parallel, quantum chemical calculations have been performed in order to optimize the molecular geometries, to highlight the different conformers, and to predict their populations at room temperature. These structures have then been used to evaluate the linear and nonlinear optical properties. This has been carried out at different levels of approximation including density functional theory (DFT) and its time-dependent form (TDDFT), using several exchange-correlation functionals (XCFs) and basis sets to analyze their effect in view of selecting the best. Methods including 'explicit' electron correlation have also been employed, such as the Møller-Plesset Perturbation theory. Solvent effects have been taken into account by using the polarizable continuum model in its integral equation formalism (IEF-PCM). This approach corresponds to the most conventional scheme to investigate structure - NLO property relationships in molecular switches. To go beyond these stationary states characterization and account for the dynamical behavior of the system, a two-step multiscale method has been developed and employed. It has been used for investigating the dynamical behavior of the ion pairs. In that case, structures of explicitly chloroform-solvated ion pairs were first generated using classical molecular dynamics (MD) simulations and, in a second step, extracted at regular time steps of the trajectories to calculate their EFISHG and HRS responses by means of DFT method. Then, the same MD-then-QM approach has been followed to study self-assembled monolayers (SAMs) of grafted indolinooxazolidine.

The results of the study showed that considering different torsion angles along the structure and Maxwell-Boltzmann statistical populations, several possible geometrical conformations of the compounds can exist. The averaged bond length alternation (BLA) along the conjugated chain of the open form is smaller by 1-3 times (1, 2 and 3 in case of bithiophene donor, ferrocene donor and SAM, respectively) than that of the closed forms, since opening of the oxazolidine ring strengthens the  $\pi$ -electron conjugation along the molecule. In the case of closed form, the influence of the nitro versus methyl substituent is negligible, while for the open form the presence of a nitro group decreases the value of BLA. For switches grafted on functionalized surfaces several physical properties have been calculated in order to characterize the morphology of the surfaces, such as the thickness, the tilt angle, the order parameter, and the roughness. These results show that, decreasing the relative coverage induces a lowering of the SAM thickness, as a consequence of the bending of the

---

NLO molecules on surfaces.

Experimental and theoretical results of the linear optical properties have been performed on the IND compounds in solution with respect to the nature of donor-acceptor groups. Consistently, they evidence that the nitro substitution has a negligible impact on the UV-vis absorption spectrum of the closed form, while it induces a bathochromic shift of the lowest-energy band of the open form. IND compound with bithiophene moiety showed  $\pi - \pi^*$  transition between the HOMO and LUMO, which is associated with an intermolecular charge transfer (ICT). In the case of ferrocene, the closed form exhibits one weak maximum, which is assigned to a metal-to-ligand charge transfer (MLCT) transition (*i.e.* from the Fe atom to the cyclopentadienyl rings), while the protonated open form possesses two absorption bands, the less intense band at larger wavelength is attributed to a MLCT transition, while the most intense one, located at smaller wavelength corresponds to a delocalized  $\pi - \pi^*$  charge transfer transition. For all systems, opening of the indolinooxazolidine ring induces a large increase of the charge transfer distance upon photo-excitation, which translates into large dipole moment differences  $\Delta\mu_{ge}$  between the ground and excited states, and into a significant enhancement of the  $\beta$  response of the open form. In the literature, various compounds including indolinooxazolidine have been described [1] and in their closed form they all present a similar UV-vis absorption spectrum ( $\lambda \sim 330$  nm), while for their open forms it is strongly correlated with the nature of the aryl groups ( $\lambda \sim 401 - 573$  nm). For the ferrocene compound the absorption spectrum presents the signature of both IND and ferrocene.

For all studied compounds, the HRS response is smaller for closed than open forms. Still, the nitro group increases the first hyperpolarizability of both forms. Such enhancement is associated with an increase of the DR, which is very close to the value of 5 typical of ideal one-dimensional (1D) systems, *i.e.* with a single nonzero diagonal component in the  $\beta$  tensor. The reinforcement of the 1D character of the NLO chromophore is also characterized by a decrease of the anisotropy ratio. The first hyperpolarizability contrasts measured upon commutation between the closed and open forms are large and demonstrate that the two compounds act as highly efficient NLO switches. Also, we can observe that the  $\beta$  contrast of the nitro-substituted derivative is smaller than the methylated one, due to the concomitant exaltation of the HRS response of the closed form. In the case of the ferrocene compound, the experimental  $\beta$  contrast is  $\sim 8$  times smaller than for IND switches with bithiophene donor. The agreement between the calculated and experimental  $\beta_{HRS}$  values is good for the open form, while for the closed form the comparison is made difficult owing to strong resonance effects. Similar to the previous compounds, the DR values of ferrocene are close to those of 1D NLOphores. In case of EFISHG, we have demonstrated the qualitative agreement between the calculated responses and the measured ones. That allows trustfully exploiting the calculations in order

---

to shed light on the experimental data. The MD-then-QM approach shows the huge effects of thermal fluctuations on the SHG responses, as evidenced by large standard deviations on both the HRS and EFISHG responses. Moreover, for this compound there is no simple relationship between the EFISHG  $\beta_{//}$  and HRS  $\beta_{HRS}$  amplitudes, as a result of the strong impact of the substituent on the relative orientation of the dipole moment with respect to the vector component of the first hyperpolarizability. Calculations have also showed that the second- and third-order contributions to  $\gamma_{EFISHG}$  vary over a broad scale and that  $\mu\beta_{//}$ , and therefore the global EFISHG response, can change sign along the dynamics. Moreover, they demonstrate that the inclusion of the third-order contribution to  $\gamma_{EFISHG}$  always improves the agreement with experiment. Indeed, the third-order contribution to EFISHG ( $\gamma_{//}$ ), which is often neglected in both calculations and experimental data analysis, should not be omitted because it can be large, or even dominant, with respect to its second-order counterpart ( $\mu\beta_{//}/3k_B T$ ) and, for the purpose of optimizing NLO switches, it can strongly influence the POF/CF contrast ratios. Then, both experiments and calculations demonstrate consistently an increase of the EFISHG responses when substituting the Me group on the indoline moiety by a  $\text{NO}_2$  acceptor group, *i.e.* when going from the protonated open form with a  $-\text{CH}_3$  to a  $-\text{NO}_2$  substituent, as well as for the closed forms.

In case of SAM, DFT calculations carried out on a large selection of molecular structures extracted from MD simulations suggested that, despite the large geometrical distortions, the photochromic molecules are expected to display a first hyperpolarizability contrast upon photochromic conversion of the same order of magnitude as that observed for the isolated molecule. The results further indicate that the close molecular packing induces strong geometrical distortions and that the high degree of disorder of the SAM is not detrimental to the NLO contrast, which is of crucial importance for the device efficiency. Furthermore, the distribution of the  $\beta$  value is similar to the molecules in solution. Moreover, for both forms, we have demonstrated a strong correlation between the magnitude of the first hyperpolarizability and the torsion angle between the bithiophene and the thioalkyl group.

Experimental and computational approaches of SHS responses of indolinoxazolidine derivatives, studied in this thesis showed that those multi-addressable switches display similarly high NLO responses in comparison to related systems from the literature [1–9], substantiating their potential to be successfully applied in optoelectronics, such as in molecular-scale memory devices with non-destructive read-out capacity. Moreover, the sequential MD-then-QM approach implemented in this thesis appears as a useful computational tool to explore new dynamical NLO molecules and materials and it calls for further applications to other complex systems. In particular, since we have showed that the NLO switching potential is kept upon grafting on oxide surfaces, further studies on NLO-active surfaces are needed to

---

highlight their structure-property relationships.

# Bibliography

---

- [1] L. Sanguinet, J.-L. Pozzo, V. Rodriguez, F. Adamietz, F. Castet, L. Ducasse, and B. Champagne. Acido- and photo-triggered NLO properties enhancement. *J. Phys. Chem. B.*, **109**(22):11139–11150, 2005.
- [2] M. Sliwa, S. Létard, I. Malfant, M. Nierlich, P. G. Lacroix, T. Asahi, H. Masuhara, P. Yu, and K. Nakatani. Design, synthesis, structural and nonlinear optical properties of photochromic crystals: Toward reversible molecular switches. *Chem. Mater.*, **17**(18):4727–4735, 2005.
- [3] S. De, M. Ray, Pati Y. A., and Das K. P. Base triggered enhancement of the first hyperpolarizability of a Keto-Enol tautomer. *J. Phys. Chem. B.*, **117**:15086–15092, 2013.
- [4] A. J. Garza, O. I. Osman, N. A. Wazzan, S. B. Khan, G. E. Scuseria, and A. M. Asiri. Photochromic and nonlinear optical properties of fulgides: A density functional theory study. *Comput. Theor. Chem.*, **1022**:82–85, 2013.
- [5] I. Asselberghs, Y. Zhao, K. Clays, A. Persoons, A. Comito, and Y. Rubin. Reversible switching of molecular second-order nonlinear optical polarizability through proton-transfer. *Chem. Phys. Lett.*, **364**(3-4):279–283, 2002.
- [6] F. Mançois, L. Sanguinet, J. L. Pozzo, M. Guillaume, B. Champagne, V. Rodriguez, F. Adamietz, L. Ducasse, and F. Castet. Acido-triggered nonlinear optical switches: Benzazolo-oxazolidines. *J. Phys. Chem. B*, **111**(33):9795–9802, 2007.
- [7] V. Aubert, V. Guerschais, E. Ishow, K. Hoang-Thi, I. Ledoux, K. Nakatani, and Le Bozec H. Efficient photoswitching of the nonlinear optical properties of dipolar photochromic zinc(II) complexes. *Angew. Chem., Int. Ed.*, **47**:577–580, 2008.
- [8] F. Mançois, J. L. Pozzo, J. Pan, F. Adamietz, V. Rodriguez, L. Ducasse, F. Castet, A. Plaquet, and B. Champagne. Two-way molecular switches with large nonlinear optical contrast. *Chem. Eur. J*, **15**(11):2560–2571, 2009.

- [9] S. van Bezouw, J. Campo, S. H. Lee, O. P. Kwon, and W. Wenseleers. Organic compounds with large and high-contrast pH-switchable nonlinear optical response. *J. Phys. Chem. C*, **119**(37):21658–21663, 2015.

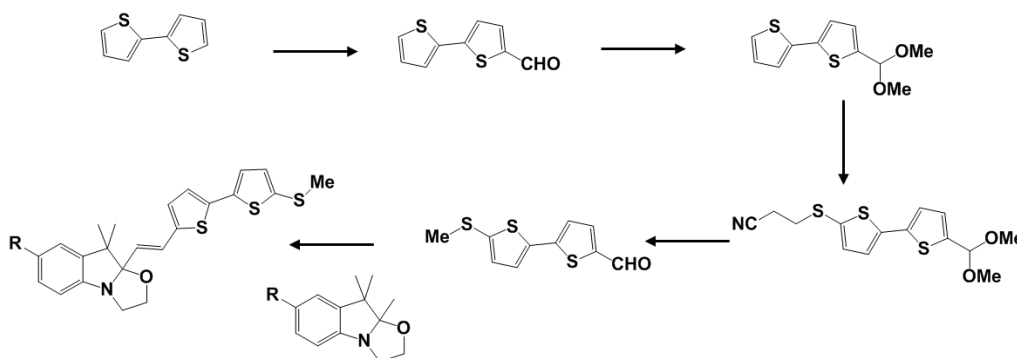


# Appendix A

## Synthesis of the Compounds

**General methods and materials:** Commercially available (Aldrich, Alfa Aesar and abcr) chemicals were used as received. For flash chromatography silica gel (Fluka, 60 Å pore size, 230-400 Å mesh) was used for all of the described compounds. For characterization NMR analysis was carried out using Bruker AVANCE 300 and Bruker AVANCE II 400 spectrometers in CDCl<sub>3</sub> at 25 °C. Chemical shifts are reported in ppm relative to the solvent (CDCl<sub>3</sub>) residual value:  $\delta = 7.26$  for <sup>1</sup>H NMR,  $\delta = 77.16$  for <sup>13</sup>C NMR. Coupling constants are reported in Hz and rounded to the nearest 0.1 Hz.

**Synthesis of the compounds:** The synthetic pathway is described in the scheme below.



**2,2'-Bithiophene-5-carboxaldehyde. (6)** This compound was obtained by a modification of the procedure described in Ref. To a solution of 2,2'-bithiophene (5.0g, 30mmol) in dry THF (100 ml) cooled at -78 °C, under argon 18 ml of 1.6 M nBuLi in hexane was added. After maintained 1 hour, dimethylformamide (6 ml, 78 mmol) was added dropwise. The temperature was allowed to increase to room temperature and agitation was maintained overnight. The reaction mixture was quenched by addition of 20 ml of water, then acidified using an aqueous HCl solution (1M) and extracted with AcOEt. The organic layer was dried over magnesium sulfate, the solvent evaporated and the product was purified by flash chromatography to produce 4.93g of desired compound as as white powder (25.4mmol; 88%). <sup>1</sup>H NMR (300 MHz, CDCl<sub>3</sub>):  $\delta = 9.79$  (1H, s); 7.60 (1H, d,  $J = 3.9$ ) 7.29 (2H, d,  $J = 4.4$ ), 7.18 (1H, d,  $J = 4.0$ ), 7.01(1H, dd,  $J = 4.4$ ;  $J' = 3.9$ ), RMN-<sup>13</sup>C (125 MHz, CDCl<sub>3</sub>)  $\delta = 182.6$ ; 147.2; 141.8; 137.3; 136.1; 128.4; 127.1; 126.2; 124.3. IR  $\bar{\nu} = 3086, 1641, 1447, 1230, 1047, 841, 706 \text{ cm}^{-1}$ .

**5-dimethoxymethyl-2,2'-bithiophene. (5)** was obtained according to the procedure described in Ref. <sup>1</sup>H NMR (300 MHz, CDCl<sub>3</sub>):  $\delta = 7.21$  (1H, dd,  $J = 5.1$ ;  $J' = 1.0$ ); 7.16 (1H, dd,  $J = 3.6$ ;  $J' = 1.0$ ); 7.07 (1H,d,  $J = 3.7$ ); 7.01 (1H, dd,  $J = 5.1$ ;  $J' = 3.6$ ); 6.97 (1H, dd,  $J = 3.6$ ;  $J' = 1.0$ );

5.61( 1H,s); 3.39(6H, s). IR  $\bar{\nu}$  = 3112; 2922; 2796; 1653; 1448; 1228; 1055; 798  $\text{cm}^{-1}$ .

**3-((5'-dimethoxymethyl-[2,2'-bithiophen]-5-yl)thio)propanenitrile. (4)** To a solution of 5-dimethoxymethyl-2,2'-bithiophene (1.0g, 4.2 mmol) in dry THF (20 ml) cooled at  $-78\text{ }^{\circ}\text{C}$ , under argon 2 ml of 2.5 M nBuLi in hexane was added. After maintained 30 min, elemental sulfur (0.133 g, 4.2mmol) was added in small portions and the mixture was stirred for 30 min at room temperature. The reaction was cooled to  $0\text{ }^{\circ}\text{C}$ , and a large excess of 3-bromopropionitrile (2ml) was slowly added and agitation is maintained overnight at room temperature. The reaction mixture was quenched by addition of 20 ml of water, and extracted with AcOEt. The organic layer was dried over magnesium sulfate, the solvent evaporated and the product was purified by flash chromatography to produce 0.6g of desired compound (1.8mmol, 43%).  $^1\text{H}$  NMR (300 MHz,  $\text{CDCl}_3$ ):  $\delta$  = 7.12 (1H, d,  $J$  = 3.7); 7.06 (1H, d,  $J$  = 3.7); 7.04 (1H, d,  $J$  = 3.7); 6.98 (1H, d,  $J$  = 3.7); 5.60 (1H, s); 3.38 (6H, s); 2.99 (2H, t,  $J$  = 7.2); 2.65 (2H, t,  $J$  = 7.2). RMN- $^{13}\text{C}$  (125 MHz,  $\text{CDCl}_3$ )  $\delta$  = 142.8; 141.6; 136.9; 129.9; 126.4; 124.2; 117.9; 117.1; 99.9; 52.8; 33.9; 24.0; 21.9. IR = 3112, 2922, 2796, 1653, 1448, 1228, 1055, 798  $\text{cm}^{-1}$ . IR  $\bar{\nu}$  = 2243, 1651, 1448, 1222, 1048, 807  $\text{cm}^{-1}$ .

**5'-thiomethyl-[2,2'-bithiophen]-5-carboxaldehyde. (3)** In round bottom flask, 0.183 g (0.56 mmol) of 3-((5'-dimethoxymethyl-[2,2'-bithiophen]-5-yl)thio)propanenitrile was dissolved in DMF (10mL) and carefully degassed by flushing nitrogen during 45 min. A solution of cesium hydroxide monohydrate (0.187g, 1.12 mmol) in MeOH (3 mL) was slowly added. After 1 hour at room temperature, large excess of methyl iodide (3mL) is added and reaction mixture was stirred for an additional hour. The reaction mixture was poured into water and extracted with DCM. The organic layer was dried over magnesium sulfate, the solvent evaporated and the product was purified by flash chromatography to produce 0.081 g of desired compound (0.34mmol, 61%).  $^1\text{H}$  NMR (300 MHz,  $\text{CDCl}_3$ ):  $\delta$  = 9.85 (1H, s); 7.65 (1H, d,  $J$  = 4.0); 7.20 (1H, d,  $J$  = 4.0); 7.18 (1H, d,  $J$  = 3.8); 6.99 (1H, d,  $J$  = 3.8); 2.55 (3H,s). RMN- $^{13}\text{C}$  (125 MHz,  $\text{CDCl}_3$ )  $\delta$  = 182.6; 146.8; 141.8; 140.6; 137.5; 137.3; 131.0; 126.5; 124.1; 21.6. IR  $\bar{\nu}$  = 2811; 1643; 1420; 1224; 1048; 874; 781  $\text{cm}^{-1}$ .

**Me-bTBox (1):** A solution of 5'-thiomethyl-[2,2'-bithiophen]-5-carboxaldehyde (120mg, 0.5 mmol) and 2,3,3,5-tetramethylindolino[1,2-b]oxazolidine (120mg, 0.55 mmol, 1.1 equiv.) in EtOH (15 mL) was refluxed for 4 days. Then the solvent was removed under reduced pressure and the crude material was purified by flash column chromatography (PE/EtOAc, 95/5) to give the desired compound product (60 mg, 27%) as a reddish oil.  $^1\text{H}$  NMR (300 MHz,  $\text{CDCl}_3$ ):  $\delta$ = 6.89-7.03 (7H, m); 6.71 (1H, d,  $J$  = 7.9); 6.10 (1H, d,  $J$  = 15.6); 3.83-3.37 (4H, m); 2.52 (3H, s); 2.32 (3H, s); 1.43 (3H, s); 1.17 (3H, s).  $^{13}\text{C}$  NMR (75 MHz)  $\delta$ = 148.4; 141.1; 140.0; 139.7; 137.0; 136.4; 132.0; 131.5; 128.4; 127.6; 126.5; 125.6; 124.2; 124.1; 123.4; 112.1; 110.2; 64.0; 50.8; 48.4; 28.7; 22.6; 21.4; 20.6. IR  $\bar{\nu}$  = 3409, 2960, 2918, 1658, 1489  $\text{cm}^{-1}$ .

**Nitro-bTBox (2):** A solution of 5'-thiomethyl-[2,2'-bithiophen]-5-carboxaldehyde (80mg, 0.32 mmol) and 5-nitro-2,3,3-trimethylindolino[1,2-b]oxazolidine (80mg, 0.33 mmol, 1.0 equiv.) in EtOH (15 mL) was refluxed for 4 days. Then the solvent was removed under reduced pressure and the crude material was purified by flash column chromatography (PE/EtOAc, 95/5) to give the desired compound product (21 mg, 14%) as a blueish oil.  $^1\text{H}$  NMR (300 MHz,  $\text{CDCl}_3$ ): 8.14 (1H, dd,  $J$  = 8.7;  $J'$  = 3.8); 7.95 (1H, d,  $J$  = 2.3); 7.01(1H, d,  $J$  = 3.7); 6.97 (1H, d,  $J$  = 8.7); 6.93 (1H, d,  $J$  = 15.6); 6.92 (1H, d,  $J$  = 3.7); 6.79 (1H, d,  $J$  = 8.7); 6.01 (1H, d,  $J$  = 15.6); 3.93-3.51 (4H, m); 2.52 (3H, s); 1.47 (3H, s); 1.21(3H, s).  $^{13}\text{C}$  NMR (75 MHz)  $\delta$ =157.0; 142.9; 141.0; 140.1; 139.2; 137.2; 136.8; 131.8; 128.1; 126.4; 125.3; 124.2; 124.1; 124.0; 119.0; 111.3; 109.8; 63.8; 49.6; 28.2; 22.1; 20.4. IR  $\bar{\nu}$  = 2922; 1719; 1601; 12981116; 794  $\text{cm}^{-1}$ .

# Linear Optical Properties

Table A.1: Transition wavelengths ( $\lambda_{ge}$ , nm), energies ( $\Delta E_{ge}$ , eV), oscillator strengths ( $f_{ge}$ ), dipole moment variations ( $\Delta\mu = |\vec{\mu}_e - \vec{\mu}_g|$ , D), charge transfers ( $q^{CT}$ , |e|), charge transfer distances ( $d^{CT}$ , Å) and HOMO-LUMO gap (eV), calculated for  $S_0 \rightarrow S_1$  transition of both comp. (CF and POF), as calculated at the M06-2X/6-311G(d) level in  $\text{CH}_3\text{CN}$ . Average values deduced from Maxwell-Boltzmann statistics distribution.

<i>Conf.</i>	$\lambda_{ge}$	$\Delta E_{ge}$	$f_{ge}$	$\Delta\mu$	$q^{CT}$	$d^{CT}$	H-L
CF 1: R=CH <sub>3</sub>							
I	364	3.406	1.353	4.316	0.451	1.991	5.504
II	354	3.503	1.364	0.678	0.391	0.361	5.650
III	347	3.575	1.347	0.816	0.393	0.432	5.720
IV	352	3.526	1.149	0.614	0.391	0.327	5.673
V	346	3.579	1.352	0.675	0.393	0.357	5.722
VI	364	3.402	1.170	4.504	0.458	2.049	5.498
VII	357	3.474	1.222	0.380	0.392	0.202	5.624
<b>Average</b>	<b>357</b>	<b>3.478</b>	<b>1.237</b>	<b>0.444</b>	<b>0.392</b>	<b>0.234</b>	<b>5.627</b>
CF 2: R=NO <sub>2</sub>							
I	365	3.396	1.410	5.045	0.462	2.275	5.158
II	355	3.488	1.446	0.277	0.389	0.148	5.462
III	360	3.445	1.419	5.152	0.466	2.301	5.172
IV	352	3.519	1.225	0.672	0.390	0.359	5.528
V	346	3.583	1.474	0.645	0.389	0.345	5.511
VI	366	3.384	1.223	5.037	0.467	2.246	5.189
VII	357	3.478	1.296	0.347	0.390	0.185	5.513
<b>Average</b>	<b>356</b>	<b>3.481</b>	<b>1.316</b>	<b>0.437</b>	<b>0.391</b>	<b>0.226</b>	<b>5.501</b>
POF 1: R=CH <sub>3</sub>							
I	585	2.119	2.006	10.800	0.612	3.677	3.905
II	572	2.169	1.981	10.820	0.613	3.672	3.960
III	577	2.149	2.018	10.192	0.600	3.535	3.940
IV	588	2.108	2.016	11.008	0.611	3.750	3.940
V	560	2.213	1.918	10.975	0.616	3.712	4.026
VI	551	2.249	1.839	10.972	0.619	3.690	4.077
VII	570	2.176	1.888	10.165	0.608	3.480	3.984
VIII	574	2.159	1.847	9.559	0.596	3.338	3.967
IX	580	2.139	1.827	9.590	0.598	3.340	3.949
<b>Average</b>	<b>565</b>	<b>2.193</b>	<b>1.869</b>	<b>10.364</b>	<b>0.609</b>	<b>3.535</b>	<b>4.006</b>
POF 2: R=NO <sub>2</sub>							
I	629	1.973	2.116	10.896	0.584	3.887	3.733
II	612	2.025	2.079	11.379	0.595	3.979	3.786
III	614	2.019	2.117	10.472	0.579	3.765	3.785
IV	631	1.965	2.124	10.635	0.577	3.835	3.725
V	603	2.056	2.046	11.124	0.591	3.917	3.834
VII	609	2.037	1.997	10.865	0.591	3.828	3.915
VIII	612	2.028	1.964	9.950	0.575	3.603	3.810
IX	618	2.007	1.927	9.748	0.574	3.537	3.790
<b>Average</b>	<b>608</b>	<b>2.044</b>	<b>2.005</b>	<b>10.926</b>	<b>0.592</b>	<b>3.845</b>	<b>3.869</b>

# Nonlinear Optical Properties

Table A.2:  $\beta_{HRS}$  and  $\beta_J$  values, as well as  $\rho$  and DR calculated for **1**: R=CH<sub>3</sub> and **2**: R=NO<sub>2</sub> in its closed form, as calculated at the M06-2X/6-311+G(d) level in acetonitrile, using wavelengths of 1064 and 1907 nm and in the static limit ( $\lambda = \infty$ ). The last column reports the average values deduced from a Maxwell-Boltzmann statistics using the standard temperature and pressure conditions (298.15 K, 1 atm)

CF 1: R=CH <sub>3</sub>									CF 2: R=NO <sub>2</sub>							
	I	II	III	IV	V	VI	VII	average	I	II	III	IV	V	VI	VII	average
$\lambda = 1064$ nm									$\lambda = 1064$ nm							
$\beta_{HRS}$	4128	405	475	546	454	4060	361	<b>394</b>	7682	3126	7284	3598	3130	7020	2406	<b>2653</b>
<b>D.R.</b>	4.96	4.17	2.94	3.69	2.80	5.40	3.15	<b>3.28</b>	5.09	4.72	5.17	4.81	4.45	5.87	4.63	<b>4.66</b>
$ \beta_{J=1} $	7705	713	704	915	650	7763	558	<b>629</b>	14449	5743	13762	6653	5643	13715	4396	<b>4865</b>
$ \beta_{J=3} $	6354	732	1102	1087	1086	5697	803	<b>835</b>	11513	5062	10730	5718	5347	8864	3960	<b>4318</b>
$\rho$	0.82	1.03	1.57	1.19	1.67	0.73	1.44	<b>1.39</b>	0.80	0.88	0.78	0.86	0.95	0.65	0.90	<b>0.89</b>
$\lambda = 1907$ nm									$\lambda = 1907$ nm							
$\beta_{HRS}$	2251	207	303	407	295	2261	283	<b>290</b>	4374	1992	4204	2336	2012	4053	2235	<b>2238</b>
<b>D.R.</b>	4.88	3.87	2.74	3.79	2.63	5.58	3.47	<b>3.53</b>	4.95	4.47	5.07	4.63	4.23	5.89	4.60	<b>4.59</b>
$ \beta_{J=1} $	4180	354	427	689	403	4360	460	<b>478</b>	8158	3595	7898	4266	3562	7925	4075	<b>4080</b>
$ \beta_{J=3} $	3526	397	735	795	730	3048	589	<b>589</b>	6751	3392	6328	3850	3593	5092	3702	<b>3705</b>
$\rho$	0.84	1.12	1.72	1.15	1.81	0.70	1.28	<b>1.26</b>	0.83	0.94	0.80	0.90	1.00	0.64	0.91	<b>0.91</b>
$\lambda = \infty$									$\lambda = \infty$							
$\beta_{HRS}$	2606	285	448	552	426	2648	366	<b>376</b>	5206	2511	4989	3010	2585	5042	2831	<b>2832</b>
<b>D.R.</b>	4.82	2.96	2.64	3.97	2.54	5.43	3.84	<b>3.75</b>	4.92	4.30	5.06	4.53	4.05	6.18	4.51	<b>4.49</b>
$ \beta_{J=1} $	4820	424	615	953	566	5069	623	<b>636</b>	9689	4472	9368	5458	4499	9970	5127	<b>5125</b>
$ \beta_{J=3} $	4133	659	1108	1039	1075	3694	706	<b>727</b>	8093	4423	7525	5060	4788	5919	4777	<b>4783</b>
$\rho$	0.86	1.56	1.80	1.09	1.90	0.73	1.13	<b>1.18</b>	0.84	0.99	0.80	0.93	1.06	0.59	0.93	<b>0.94</b>

Table A.3:  $\beta_{HRS}$  and  $\beta_J$  values, as well as  $\rho$  and DR calculated for **1**: R=CH<sub>3</sub> in its protonated open form, as calculated at the M06-2X/6-311+G(d) level in acetonitrile, using wavelengths of 1064 and 1907 nm and in the static limit ( $\lambda = \infty$ ). The last column reports the average values deduced from a Maxwell-Boltzmann statistics using the standard temperature and pressure conditions (298.15 K, 1 atm)

POF 1: R=CH <sub>3</sub>										
	I	II	III	IV	V	VI	VII	VIII	IX	average
$\lambda = 1064$ nm										
$\beta_{HRS}$	2111669	2095114	4429239	1558452	710318	493892	23030383	4536393	25009529	<b>1179784</b>
<b>D.R.</b>	5.04	5.04	5.01	5.04	5.00	5.00	4.96	4.86	4.85	<b>4.94</b>
$ \beta_{J=1} $	3960034	3928746	8292239	2922947	1329251	924329	42981442	8416424	46357672	<b>2196476</b>
$ \beta_{J=3} $	3198438	3174064	6748908	2359446	1083974	753456	35476394	7126962	39409287	<b>1832036</b>
$\rho$	0.81	0.81	0.81	0.81	0.82	0.82	0.83	0.85	0.85	<b>0.83</b>
$\lambda = 1907$ nm										
$\beta_{HRS}$	39450	36108	35801	40080	34191	36977	41020	38194	32588	<b>32560</b>
<b>D.R.</b>	4.92	4.92	4.97	4.92	4.97	4.95	4.91	4.96	4.97	<b>4.91</b>
$ \beta_{J=1} $	73456	67241	66862	74633	63860	68977	76312	71301	60848	<b>60611</b>
$ \beta_{J=3} $	61248	56036	55015	62213	52526	57052	63867	58777	50114	<b>53025</b>
$\rho$	0.83	0.83	0.82	0.83	0.82	0.83	0.84	0.82	0.82	<b>0.83</b>
$\lambda = \infty$										
$\beta_{HRS}$	48322	43141	44052	49541	41155	43533	49826	46610	40747	<b>39560</b>
<b>D.R.</b>	4.86	4.86	4.94	4.86	4.95	4.88	4.84	4.95	4.94	<b>4.86</b>
$ \beta_{J=1} $	89603	80005	82127	91881	76744	80864	92316	86913	75973	<b>73384</b>
$ \beta_{J=3} $	76050	67874	68107	77923	63570	68126	78631	72010	62969	<b>62184</b>
$\rho$	0.85	0.85	0.83	0.85	0.83	0.84	0.85	0.83	0.83	<b>0.85</b>

Table A.4:  $\beta_{HRS}$  and  $\beta_J$  values, as well as  $\rho$  and DR calculated for **2**: R=NO<sub>2</sub> in its protonated open form, as calculated at the M06-2X/6-311+G(d) level in acetonitrile, using wavelengths of 1064 and 1907 nm and in the static limit ( $\lambda = \infty$ ). The last column reports the average values deduced from a Maxwell-Boltzmann statistics using the standard temperature and pressure conditions (298.15 K, 1 atm)

POF <b>2</b> : R=NO <sub>2</sub>										
$\lambda = 1064$ nm										
$\beta_{HRS}$	384768	539273	508382	367891	683105	1011401	571543	492217	390457	<b>6337367</b>
<b>D.R.</b>	4.98	4.99	4.94	4.98	5.01	4.98	4.95	4.79	4.78	<b>4.95</b>
$ \beta_{J=1} $	718852	1008247	947407	687504	1278920	1889420	1065823	909056	720619	<b>1181719</b>
$ \beta_{J=3} $	590546	825585	787015	564121	1040744	1552742	882794	784657	623786	<b>979019</b>
$\rho$	0.82	0.82	0.83	0.82	0.81	0.82	0.83	0.86	0.87	<b>0.83</b>
$\lambda = 1907$ nm										
$\beta_{HRS}$	59455	56120	52531	58588	53924	49179	52973	49159	46870	<b>52369</b>
<b>D.R.</b>	4.97	5.00	5.10	4.97	4.95	5.04	4.86	4.88	5.16	<b>4.94</b>
$ \beta_{J=1} $	111023	104976	98829	109379	100593	92202	98282	91274	88482	<b>97574</b>
$ \beta_{J=3} $	91410	85768	78643	90142	83192	74555	83225	77040	69272	<b>81110</b>
$\rho$	0.82	0.82	0.80	0.82	0.83	0.81	0.85	0.84	0.78	<b>0.83</b>
$\lambda = \infty$										
$\beta_{HRS}$	73300	67266	64730	72857	65099	58872	64312	61047	60511	<b>63593</b>
<b>D.R.</b>	4.92	4.95	5.09	4.91	4.91	5.00	4.77	4.80	5.33	<b>4.87</b>
$ \beta_{J=1} $	136441	125453	121770	135569	121146	110150	118592	112828	115301	<b>117987</b>
$ \beta_{J=3} $	113916	103855	96931	113362	101255	89894	103014	97095	86181	<b>99867</b>
$\rho$	0.83	0.83	0.80	0.84	0.84	0.82	0.87	0.86	0.75	<b>0.85</b>

Table A.5:  $\beta_{HRS}$  and  $\beta_J$  values, as well as  $\rho$  and DR calculated for **1**: R=CH<sub>3</sub> and **2**: R=NO<sub>2</sub> in its closed form, as calculated at the CAM-B3LYP/6-311+G(d) level in acetonitrile, using wavelengths of 1064 and 1907 nm and in the static limit ( $\lambda = \infty$ ). The last column reports the average values deduced from a Maxwell-Boltzmann statistics using the standard temperature and pressure conditions (298.15 K, 1 atm)

	CF <b>1</b> : R=CH <sub>3</sub>								CF <b>2</b> : R=NO <sub>2</sub>							
	I	II	III	IV	V	VI	VII	average	I	II	III	IV	V	VI	VII	average
$\lambda = 1064$ nm																
$\beta_{HRS}$	3721	577	579	543	539	3636	359	<b>408</b>	7645	3316	7237	3859	3381	6945	2523	<b>2785</b>
<b>D.R.</b>	4.96	4.53	3.40	3.39	3.19	5.44	2.72	<b>2.94</b>	5.11	4.70	5.17	4.70	4.40	5.89	4.52	<b>4.57</b>
$ \beta_{J=1} $	6943	1046	933	872	839	6965	504	<b>613</b>	14393	6084	13675	7082	6071	13579	4572	<b>5073</b>
$ \beta_{J=3} $	5737	970	1223	1148	1185	5059	875	<b>919</b>	11413	5394	10661	6269	5836	8731	4249	<b>4621</b>
$\rho$	0.83	0.93	1.31	1.32	1.41	0.73	1.74	<b>1.64</b>	0.79	0.89	0.78	0.89	0.96	0.64	0.93	<b>0.92</b>
$\lambda = 1907$ nm																
$\beta_{HRS}$	2053	289	344	395	327	205	4 246	<b>265</b>	4364	2081	4184	2466	2135	4030	2339	<b>2339</b>
<b>D.R.</b>	4.86	4.41	3.04	3.46	2.89	5.62	2.76	<b>2.96</b>	4.96	4.45	5.06	4.53	4.18	5.87	4.50	<b>4.50</b>
$ \beta_{J=1} $	3810	519	520	641	479	3971	348	<b>395</b>	8146	3751	7854	4470	3762	7873	4230	<b>4235</b>
$ \beta_{J=3} $	3226	498	781	823	768	2744	592	<b>601</b>	6721	3553	6318	4151	3850	5089	3962	<b>3949</b>
$\rho$	0.85	0.96	1.51	1.28	1.60	0.69	1.70	<b>1.61</b>	0.83	0.95	0.80	0.93	1.02	0.65	0.94	<b>0.94</b>
$\lambda = \infty$																
$\beta_{HRS}$	2408	347	461	534	442	2474	327	<b>347</b>	5215	2675	5010	3199	2770	4894	3006	<b>3002</b>
<b>D.R.</b>	4.81	3.33	2.74	3.67	2.65	5.71	3.15	<b>3.19</b>	4.89	4.30	5.03	4.44	4.04	5.92	4.42	<b>4.42</b>
$ \beta_{J=1} $	4450	552	650	892	608	4799	505	<b>544</b>	9689	4761	9391	5761	4818	9579	5403	<b>5397</b>
$ \beta_{J=3} $	3829	742	1117	1069	1090	3244	726	<b>751</b>	8155	4716	7602	5476	5139	6115	5175	<b>5162</b>
$\rho$	0.86	1.34	1.72	1.20	1.79	0.68	1.44	<b>1.42</b>	0.84	0.99	0.81	0.95	1.07	0.64	0.96	<b>0.96</b>

Table A.6:  $\beta_{HRS}$  and  $\beta_J$  values, as well as  $\rho$  and DR calculated for **1**: R=CH<sub>3</sub> in its protonated open form, as calculated at the CAM-B3LYP/6-311+G(d) level in acetonitrile, using wavelengths of 1064 and 1907 nm and in the static limit ( $\lambda = \infty$ ). The last column reports the average values deduced from a Maxwell-Boltzmann statistics using the standard temperature and pressure conditions (298.15 K, 1 atm)

POF 1: R=CH <sub>3</sub>										
	I	II	III	IV	V	VI	VII	VIII	IX	average
$\lambda = 1064$ nm										
$\beta_{HRS}$	3728159	749450	957183	11440696	402956	275026	551502	637616	1103304	<b>675317</b>
<b>D.R.</b>	5.04	5.04	5.02	5.04	5.01	5.00	4.94	4.81	4.85	<b>4.93</b>
$ \beta_{J=1} $	6990706	1405434	1792573	21455302	754320	514325	1028109	1179076	2045487	<b>1259965</b>
$ \beta_{J=3} $	5649011	1135201	1456831	17327342	614212	420688	852799	1012408	1737448	<b>1041106</b>
$\rho$	0.81	0.81	0.81	0.81	0.81	0.82	0.83	0.86	0.85	<b>0.83</b>
$\lambda = 1907$ nm										
$\beta_{HRS}$	34656	31790	31491	35292	30225	27913	29413	27792	28760	<b>28777</b>
<b>D.R.</b>	4.91	4.91	4.97	4.92	4.97	4.93	4.85	4.89	4.96	<b>4.89</b>
$ \beta_{J=1} $	64497	59165	58811	65686	56438	51992	54534	51652	53665	<b>53497</b>
$ \beta_{J=3} $	53891	49433	48399	54867	46478	43281	46308	43418	44330	<b>44909</b>
$\rho$	0.84	0.84	0.82	0.84	0.82	0.83	0.85	0.84	0.83	<b>0.84</b>
$\lambda = \infty$										
$\beta_{HRS}$	42866	38350	39049	44061	36712	33726	36053	34869	36361	<b>35289</b>
<b>D.R.</b>	4.84	4.84	4.93	4.85	4.64	4.87	4.76	4.83	4.94	<b>4.82</b>
$ \beta_{J=1} $	79427	71048	72760	81657	68420	62593	66440	64565	67771	<b>65316</b>
$ \beta_{J=3} $	67627	60533	60480	69467	56821	52929	57863	55132	56260	<b>55870</b>
$\rho$	0.85	0.85	0.83	0.85	0.83	0.85	0.87	0.85	0.83	<b>0.85</b>

Table A.7:  $\beta_{HRS}$  and  $\beta_J$  values, as well as  $\rho$  and DR calculated for **2**: R=NO<sub>2</sub> in its protonated open form, as calculated at the CAM-B3LYP/6-311+G(d) level in acetonitrile, using wavelengths of 1064 and 1907 nm and in the static limit ( $\lambda = \infty$ ). The last column reports the average values deduced from a Maxwell-Boltzmann statistics using the standard temperature and pressure conditions (298.15 K, 1 atm)

POF 2: R=NO <sub>2</sub>										
	I	II	III	IV	V	VI	VII	VIII	IX	average
$\lambda = 1064$ nm										
$\beta_{HRS}$	461943	734758	685108	439684	1161910	3992836	865395	702253	505218	1409579
<b>D.R.</b>	4.97	4.98	4.94	4.97	5.02	4.98	4.94	4.80	4.79	4.94
$ \beta_{J=1} $	862515	1373328	1276777	821202	2176266	7462272	1613630	1297730	933082	2630674
$ \beta_{J=3} $	710474	1126009	1060522	675535	1767595	6120943	1337163	1117409	805340	2171258
$\rho$	0.82	0.82	0.83	0.82	0.81	0.82	0.83	0.86	0.86	0.83
$\lambda = 1907$ nm										
$\beta_{HRS}$	53132	50090	46997	52510	48437	44004	47545	44394	42204	46962
<b>D.R.</b>	4.97	5.00	5.11	4.96	4.95	5.04	4.84	4.85	5.19	4.93
$ \beta_{J=1} $	99208	93703	88495	98024	90330	82527	88079	82301	79804	87434
$ \beta_{J=3} $	81707	76535	70133	80820	74803	66632	75061	69920	61983	72918
$\rho$	0.82	0.82	0.79	0.82	0.83	0.81	0.85	0.85	0.78	0.83
$\lambda = \infty$										
$\beta_{HRS}$	65899	60459	58180	65704	58815	52978	58131	55445	53201	57392
<b>D.R.</b>	4.91	4.94	5.11	4.91	4.90	5.00	4.73	4.77	5.20	4.85
$ \beta_{J=1} $	122632	112735	109534	122219	109393	99133	106940	102207	100698	106330
$ \beta_{J=3} $	102511	93416	86873	102345	91644	80868	93796	88903	77838	90537
$\rho$	0.84	0.83	0.79	0.84	0.84	0.82	0.88	0.87	0.77	0.85

Table A.8:  $\beta_{HRS}$  and  $\beta_J$  values, as well as  $\rho$  and DR calculated for **1**: R=CH<sub>3</sub> and **2**: R=NO<sub>2</sub> in its closed form, as calculated at the HF/6-311+G(d) level in acetonitrile, using wavelengths of 1064 and 1907 nm and in the static limit ( $\lambda = \infty$ ). The last column reports the average values deduced from a Maxwell-Boltzmann statistics using the standard temperature and pressure conditions (298.15 K, 1 atm)

	CF 1: R=CH <sub>3</sub>								CF 2: R=NO <sub>2</sub>							
	I	II	III	IV	V	VI	VII	average	I	II	III	IV	V	VI	VII	average
	$\lambda = 1064$ nm								$\lambda = 1064$ nm							
$\beta_{HRS}$	1324	545	501	380	481	1395	296	<b>332</b>	2903	1192	2778	1687	1368	2766	1207	<b>1257</b>
<b>D.R.</b>	4.84	4.48	3.89	3.85	3.80	5.71	3.18	<b>3.35</b>	4.77	3.65	4.88	4.06	3.43	5.64	3.80	<b>3.81</b>
$ \beta_{J=1} $	2452	984	858	647	817	2706	459	<b>534</b>	5354	1984	5160	2938	2211	5351	2046	<b>2138</b>
$ \beta_{J=3} $	2089	926	961	732	937	1827	653	<b>639</b>	4646	2394	4349	3120	2871	3680	2352	<b>2432</b>
$\rho$	0.85	0.94	1.12	1.13	1.15	0.68	1.42	<b>1.36</b>	0.87	1.21	0.84	1.06	1.30	0.69	1.15	<b>1.15</b>
	$\lambda = 1907$ nm								$\lambda = 1907$ nm							
$\beta_{HRS}$	881	334	322	282	311	960	182	<b>205</b>	2017	928	1949	1287	1042	1957	1152	<b>1141</b>
<b>D.R.</b>	4.73	4.37	3.63	3.80	3.58	5.85	2.84	<b>3.04</b>	4.55	3.49	4.69	3.92	3.30	5.49	3.78	<b>3.76</b>
$ \beta_{J=1} $	1619	598	535	478	514	1875	264	<b>314</b>	3663	1513	3574	2211	1651	3758	1948	<b>1927</b>
$ \beta_{J=3} $	1422	580	649	548	634	1218	432	<b>456</b>	3378	1925	3176	2447	2244	2696	2253	<b>2232</b>
$\rho$	0.88	0.97	1.21	1.15	1.23	0.65	1.64	<b>1.55</b>	0.92	1.27	0.89	1.11	1.36	0.72	1.16	<b>1.17</b>
	$\lambda = \infty$								$\lambda = \infty$							
$\beta_{HRS}$	1054	398	417	388	405	1195	221	<b>249</b>	2457	1239	2387	1704	1397	2430	1502	<b>1491</b>
<b>D.R.</b>	4.62	3.54	3.13	4.18	3.12	5.90	3.00	<b>3.09</b>	4.34	3.25	4.54	3.79	3.12	5.36	3.64	<b>3.61</b>
$ \beta_{J=1} $	1923	654	641	684	622	2337	331	<b>384</b>	4387	1948	4332	2886	2147	4639	2500	<b>2473</b>
$ \beta_{J=3} $	1740	817	931	701	907	1496	505	<b>549</b>	4298	2694	4007	3324	3118	3437	3020	<b>3007</b>
$\rho$	0.90	1.25	1.45	1.02	1.46	0.64	1.53	<b>1.49</b>	0.98	1.38	0.92	1.15	1.45	0.74	1.21	<b>1.23</b>

Table A.9:  $\beta_{HRS}$  and  $\beta_J$  values, as well as  $\rho$  and DR calculated for **1**: R=CH<sub>3</sub> in its protonated open form, as calculated at the HF/6-311+G(d) level in acetonitrile, using wavelengths of 1064 and 1907 nm and in the static limit ( $\lambda = \infty$ ). The last column reports the average values deduced from a Maxwell-Boltzmann statistics using the standard temperature and pressure conditions (298.15 K, 1 atm)

	POF 1: R=CH <sub>3</sub>									
	I	II	III	IV	V	VI	VII	VIII	IX	average
	$\lambda = 1064$ nm									
$\beta_{HRS}$	66944	55787	58954	70475	49879	39446	48071	48398	52840	<b>46208</b>
<b>D.R.</b>	4.96	4.96	5.00	4.96	5.01	4.98	4.88	4.87	4.99	<b>4.92</b>
$ \beta_{J=1} $	124927	104136	110279	131533	93353	73726	89278	89815	98791	<b>86028</b>
$ \beta_{J=3} $	103154	85875	90092	108547	76083	60454	75274	75979	80898	<b>71762</b>
$\rho$	0.83	0.82	0.82	0.83	0.82	0.82	0.84	0.85	0.82	<b>0.83</b>
	$\lambda = 1907$ nm									
$\beta_{HRS}$	18680	16863	17142	19215	16165	14259	15879	15598	16012	<b>15353</b>
<b>D.R.</b>	4.81	4.82	4.93	4.81	4.91	4.86	4.66	4.72	4.96	<b>4.76</b>
$ \beta_{J=1} $	34542	31199	31942	35529	30073	26453	29069	28672	29881	<b>28352</b>
$ \beta_{J=3} $	29660	26728	26547	30520	25167	22408	25993	25228	24670	<b>24671</b>
$\rho$	0.86	0.86	0.83	0.86	0.84	0.85	0.89	0.88	0.83	<b>0.87</b>
	$\lambda = \infty$									
$\beta_{HRS}$	24141	21348	22462	25069	20655	17868	20229	20487	21277	<b>19660</b>
<b>D.R.</b>	4.69	4.69	4.85	4.69	4.84	4.74	4.47	4.57	4.88	<b>4.61</b>
$ \beta_{J=1} $	44265	39147	41635	45973	38264	32889	36520	37251	39514	<b>35857</b>
$ \beta_{J=3} $	39334	34775	35398	40835	32611	28782	34420	34191	33322	<b>32519</b>
$\rho$	0.89	0.89	0.85	0.89	0.85	0.88	0.94	0.92	0.84	<b>0.91</b>

Table A.10:  $\beta_{HRS}$  and  $\beta_J$  values, as well as  $\rho$  and DR calculated for **2**: R=NO<sub>2</sub> in its protonated open form, as calculated at the HF/6-311+G(d) level in acetonitrile, using wavelengths of 1064 and 1907 nm and in the static limit ( $\lambda = \infty$ ). The last column reports the average values deduced from a Maxwell-Boltzmann statistics using the standard temperature and pressure conditions (298.15 K, 1 atm)

POF <b>2</b> : R=NO <sub>2</sub>										
	I	II	III	IV	V	VI	VII	VIII	IX	average
$\lambda = 1064$ nm										
$\beta_{HRS}$	132292	106444	102240	135303	94856	72557	88779	85985	92203	<b>89852</b>
<b>D.R.</b>	4.96	4.97	5.00	4.96	5.02	5.03	4.89	4.84	5.01	<b>4.94</b>
$ \beta_{J=1} $	246873	198837	191352	252490	177628	135954	164991	159291	172613	<b>167394</b>
$ \beta_{J=3} $	203847	163453	155947	208496	144412	110224	138704	135742	140504	<b>139224</b>
$\rho$	0.83	0.82	0.81	0.83	0.81	0.81	0.84	0.85	0.81	<b>0.83</b>
$\lambda = 1907$ nm										
$\beta_{HRS}$	26890	24891	23650	26836	24054	21256	23826	22773	21906	<b>23438</b>
<b>D.R.</b>	4.84	4.88	5.03	4.83	4.87	4.95	4.63	4.65	5.11	<b>4.76</b>
$ \beta_{J=1} $	49825	46232	44332	49697	44636	39644	43531	41648	41246	<b>43169</b>
$ \beta_{J=3} $	42420	38961	35877	42417	37768	32816	39233	37393	32697	<b>376357</b>
$\rho$	0.85	0.84	0.81	0.85	0.85	0.83	0.90	0.90	0.79	<b>0.87</b>
$\lambda = \infty$										
$\beta_{HRS}$	36153	32573	32056	36490	31726	27249	31211	30762	30028	<b>30805</b>
<b>D.R.</b>	4.73	4.77	4.96	4.72	4.79	4.84	4.45	4.49	5.03	<b>4.62</b>
$ \beta_{J=1} $	66504	60049	59833	67080	58582	50472	56249	55599	56282	<b>56154</b>
$ \beta_{J=3} $	58342	52219	49359	59002	50608	43041	53345	52185	45567	<b>51005</b>
$\rho$	0.88	0.87	0.82	0.88	0.86	0.85	0.95	0.94	0.81	<b>0.91</b>

Table A.11: Static  $\beta_{HRS}$  and DR calculated for compound **1** and **2** in their closed forms at the HF/6-311+G(d) and MP2/6-311+G(d) levels in acetonitrile.

	I	II	III	IV	V	VI	VII	average
HF method, CF <b>1</b> : R=CH <sub>3</sub>								
$\beta_{HRS}$	1053	399	417	387	405	1194	221	<b>249</b>
<b>D.R.</b>	4.62	3.55	3.12	4.19	3.11	5.91	3.00	<b>3.09</b>
HF method, CF <b>2</b> : R=NO <sub>2</sub>								
$\beta_{HRS}$	2458	1237	2389	1704	1397	2427	1503	<b>1491</b>
<b>D.R.</b>	4.34	3.25	4.54	3.79	3.13	5.36	3.64	<b>3.61</b>
MP2 method, CF <b>1</b> : R=CH <sub>3</sub>								
$\beta_{HRS}$	2300	201	270	508	272	2359	418	<b>409</b>
<b>D.R.</b>	4.99	2.63	2.25	4.11	2.19	5.91	3.95	<b>3.82</b>
MP2 method, CF <b>2</b> : R=NO <sub>2</sub>								
$\beta_{HRS}$	5078	2796	4902	3214	2823	4754	3115	<b>3104</b>
<b>D.R.</b>	5.07	4.53	5.23	4.77	4.41	6.16	4.72	<b>4.71</b>

Table A.12: Static  $\beta_{HRS}$  and DR calculated for compound **1** and **2** in their protonated open forms at the HF/6-311+G(d) and MP2/6-311+G(d) levels in acetonitrile.

	I	II	III	IV	V	VI	VII	VIII	IX	average
HF method, POF <b>1</b> : R=CH <sub>3</sub>										
$\beta_{HRS}$	24141	21348	22460	25070	20655	17865	20230	20493	21275	19660
<b>D.R.</b>	4.69	4.69	4.85	4.69	4.84	4.74	4.47	4.57	4.88	4.61
HF method, POF <b>2</b> : R=NO <sub>2</sub>										
$\beta_{HRS}$	36156	32576	32054	36489	31717	27249	31216	30764	30029	30808
<b>D.R.</b>	4.73	4.77	4.96	4.72	4.79	4.84	4.45	4.49	5.03	4.62
MP2 method, POF <b>1</b> : R=CH <sub>3</sub>										
$\beta_{HRS}$	61976	53968	57512	64375	50654	44098	49585	49945	52898	48424
<b>D.R.</b>	4.97	4.97	5.02	4.96	5.02	5.03	4.98	5.09	5.13	5.02
MP2 method, POF <b>2</b> : R=NO <sub>2</sub>										
$\beta_{HRS}$	92937	82604	81860	93164	79472	69156	77355	75419	75610	77049
<b>D.R.</b>	4.97	5.00	5.10	4.97	4.97	5.06	4.86	4.90	5.21	4.95

## Experimental Results

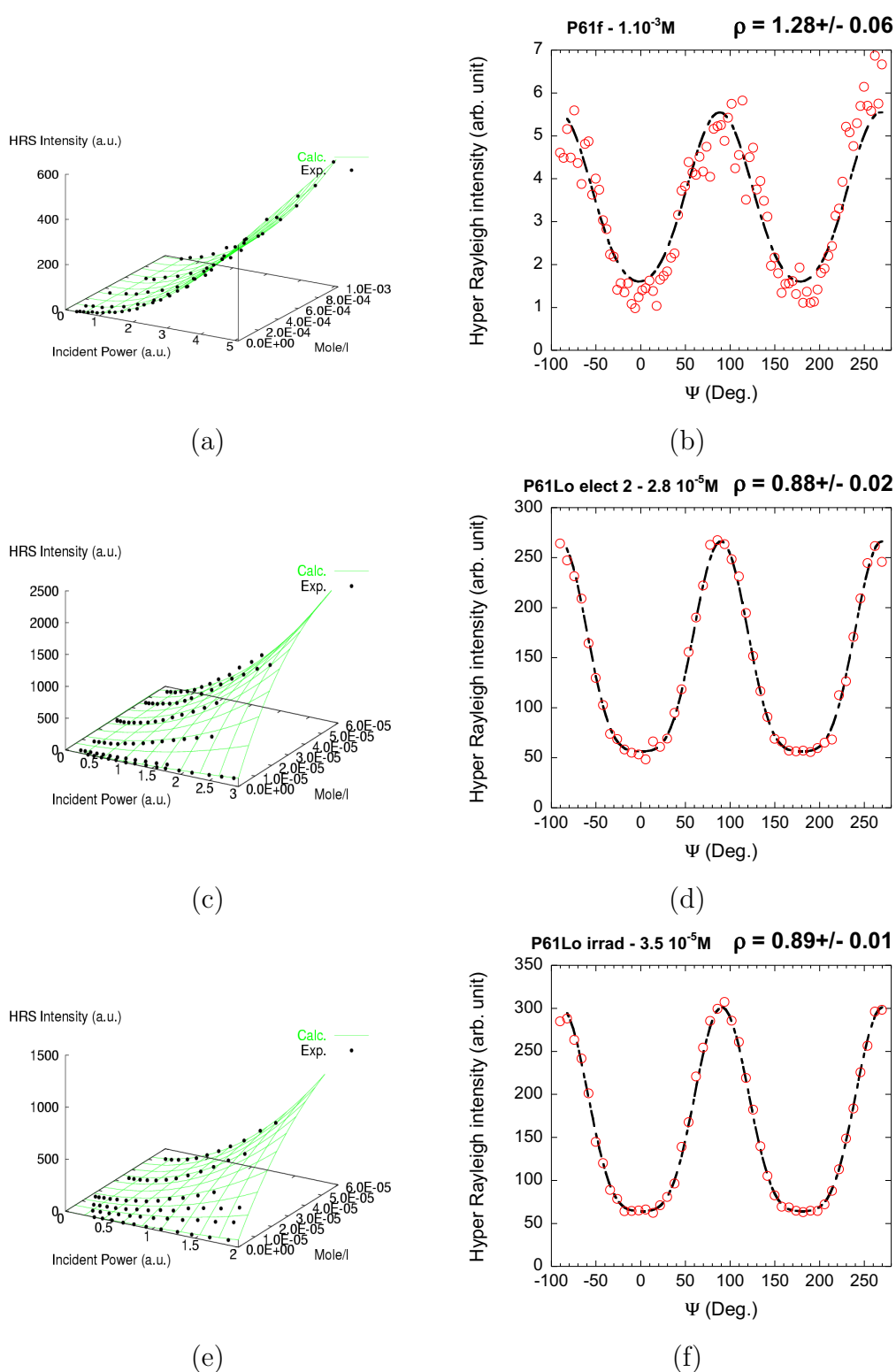
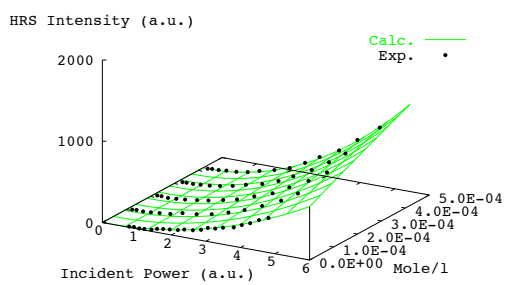
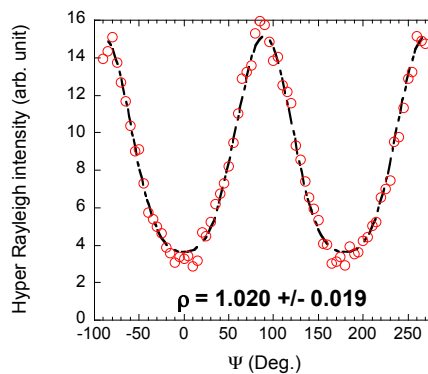


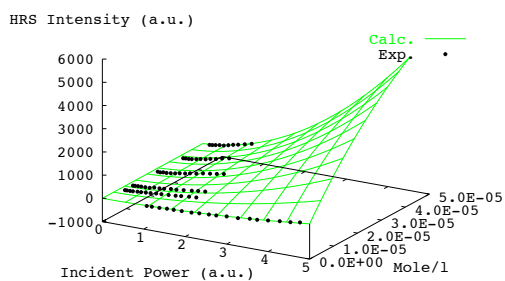
Figure A.1: HRS response of compound **1** in its closed and protonated open forms in acetonitrile: 3D representation as a function of the incident power and concentration (left) and extracted plot of the polarization curve (right). (a-b) CF, (c-d) POF by oxidation, (e-f) POF by irradiation.



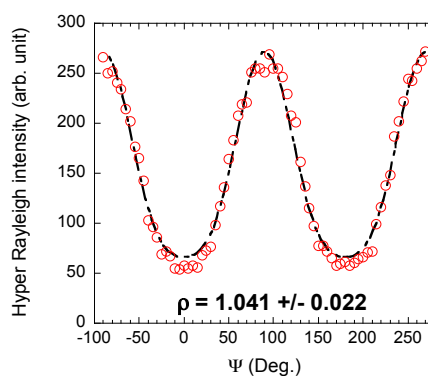
(a)



(b)



(c)



(d)

Figure A.2: HRS response of compound **2** in its closed and protonated open forms in acetonitrile: 3D representation as a function of the incident power and concentration (left) and extracted plot of the polarization curve (right). (a-b) CF, (c-d) POF.

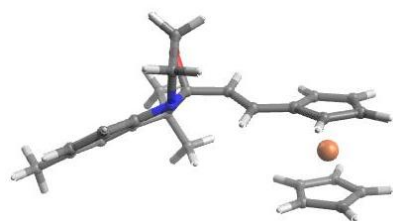
## Synthesis and Analysis of 10-[2-(Ferrocenyl)ethylene]-7,9,9-trimethyl-indolino[2,1-b]oxazolidine

To 2 g of silica, 2,3,3,5-tetramethylindolinoxazolidine (500 mg, 2.34 mmol) and ferrocenecarboxaldehyde (508 mg, 2.34 mmol) were added and the heterogeneous mixture was homogenized by the addition of minimal amount (ca 10 mL) of DCM. The solvent was removed under reduced pressure at ambient temperature and the powder was heated to 100 °C during 10 min under normal atmosphere in a 50 mL sealed tube. For better homogenization of the solid reaction mixture, continuous stirring was applied. The crude product was purified by flash column chromatography using DCM to DCM/MeOH systems (9/1) as eluent to give the desired compound as green solid (340 mg, 35%).

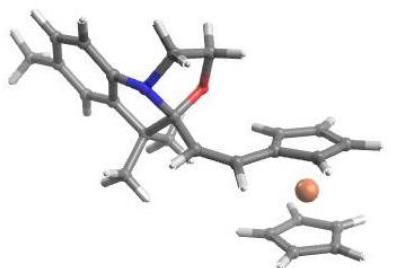
m.p.: 129-131 °C; <sup>1</sup>H NMR (300 MHz) δ 1.18 (3H, s), 1.45 (3H, s), 3.423.80 (4H, m), 4.12 (5H, s), 4.25 (2H, t, J = 1.8 Hz), 4.40 (2H, m), 5.85 (1H, d, J = 15.8 Hz), 6.63 (1H, d, J = 15.8, CH), 6.69 (1H, d, J = 7.9 Hz), 6.90 (1H, s), 6.97 (1H, d, J = 7.7 Hz); <sup>13</sup>C NMR (75 MHz) δ 20.4 (CH<sub>3</sub>), 21.2 (CH<sub>3</sub>), 28.6 (CH<sub>3</sub>), 47.6 (C), 50.4 (CH<sub>2</sub>), 63.5 (CH<sub>2</sub>), 67.2 (CH), 69.1 (CH), 69.2 (CH), 82.4 (C), 110.4 (C), 111.9 (CH), 122.5(CH), 123.3(CH), 128.1(CH), 130.4(CH), 131.2 (C), 139.9 (C), 148.4(C); IR  $\nu$  = 3091, 2957, 2923, 2882 cm<sup>-1</sup>; HRMS (FAB+): m/z calcd. for C<sub>25</sub>H<sub>27</sub>FeNO: 413.1442 [M + H]<sup>+</sup>; found: 414.1515.

---

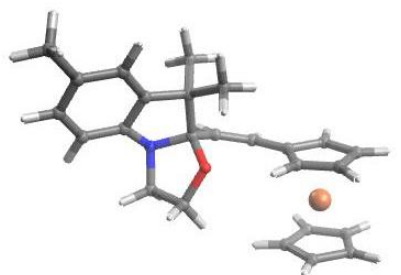
## Structural Properties



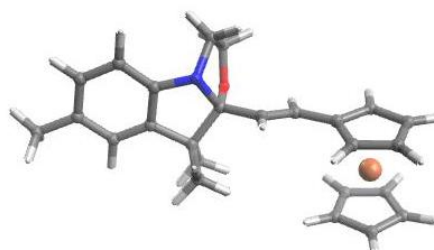
CF: conformer I



CF: conformer II



CF: conformer III



CF: conformer IV

Figure B.1: Different conformers of the closed form, as optimized at the IEF-PCM/B3LYP/6-311G(d) level in acetonitrile. Left and right figures correspond to side and top views, respectively

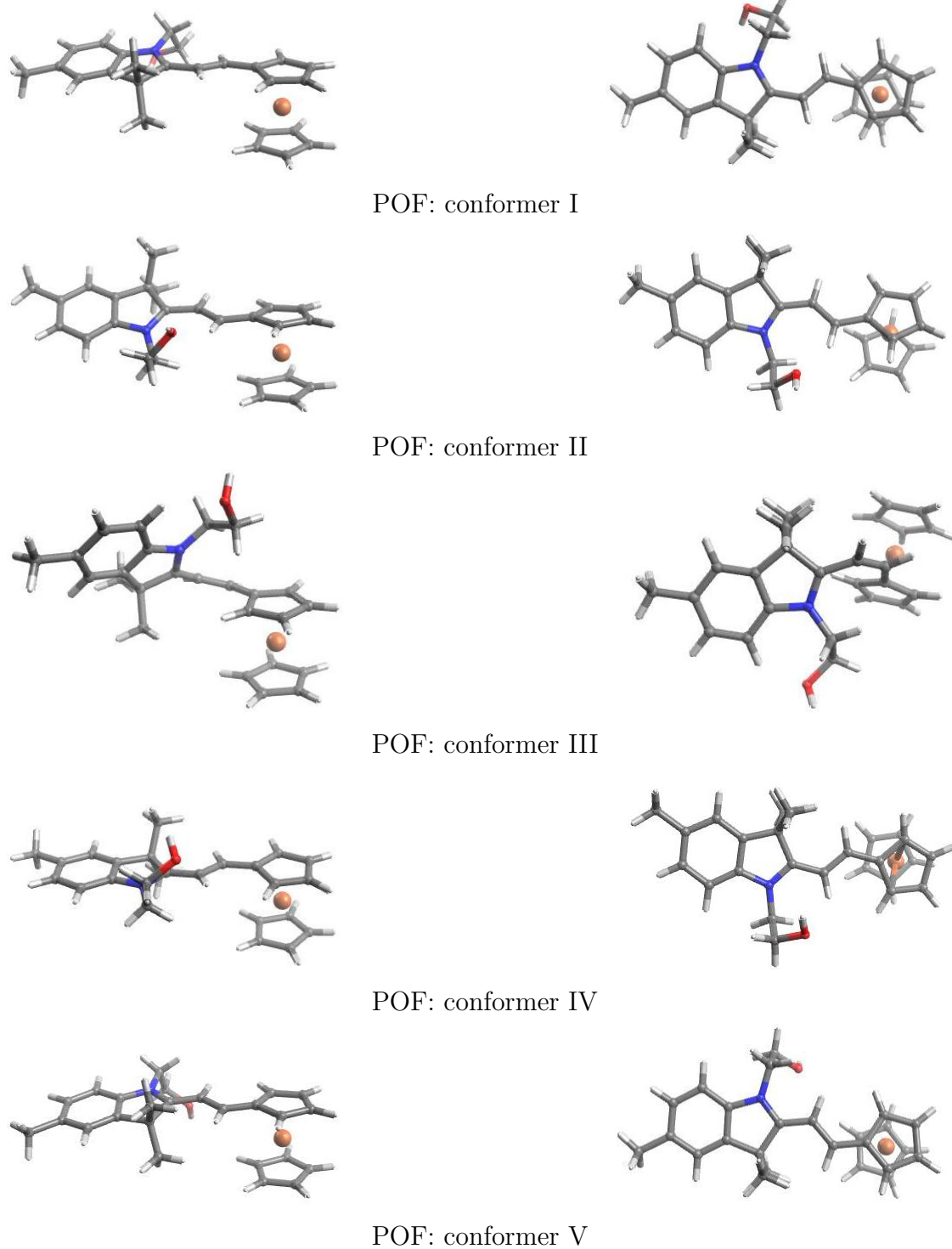


Figure B.2: Different conformers of the protonated open form, as optimized at the IEF-PCM/B3LYP/6-311G(d) level in acetonitrile. Left and right figures correspond to side and top views, respectively

# Linear Optical Properties

Table B.1: Transition wavelengths ( $\lambda_{ge}$ , nm) and energies ( $\Delta E_{ge}$ , eV), oscillator strengths ( $f_{ge}$ ), dipole moment variation ( $\Delta\mu_{ge} = |\vec{\mu}_e - \vec{\mu}_g|$ , D), charge transferred ( $q^{CT}$ , |e|) and charge transfer distance ( $d^{CT}$ , Å), calculated for the low-energy optically active  $S_0 \rightarrow S_N$  transition for the different conformers of **closed and protonated open forms**, as calculated at the **B3PW91/6-311G(d)** level in acetonitrile, using the B3LYP/6-311G(d) geometry. Last lines (in bold) present the average values.

<i>Conf.</i>	$\lambda_{ge}$	$\Delta E_{ge}$	$f_{ge}$	$\Delta\mu_{ge}$	$q^{CT}$	$d^{CT}$	<i>Conf.</i>	$\lambda_{ge}$	$\Delta E_{ge}$	$f_{ge}$	$\Delta\mu_{ge}$	$q^{CT}$	$d^{CT}$
<b>Closed Form</b>													
I. $S_0 \rightarrow S_2$	560	2.216	0.003	0.601	0.492	0.254	I. $S_0 \rightarrow S_3$	495	2.504	0.002	0.741	0.569	0.271
II. $S_0 \rightarrow S_2$	559	2.218	0.003	0.310	0.475	0.136	II. $S_0 \rightarrow S_3$	495	2.505	0.001	0.362	0.547	0.138
III. $S_0 \rightarrow S_2$	563	2.203	0.004	0.484	0.497	0.203	III. $S_0 \rightarrow S_3$	498	2.491	0.002	0.563	0.551	0.213
IV. $S_0 \rightarrow S_2$	559	2.218	0.003	0.360	0.483	0.155	IV. $S_0 \rightarrow S_3$	495	2.505	0.002	0.476	0.551	0.180
<b><math>S_0 \rightarrow S_2</math></b>	<b>559</b>	<b>2.219</b>	<b>0.003</b>	<b>0.398</b>	<b>0.485</b>	<b>0.170</b>	<b><math>S_0 \rightarrow S_3</math></b>	<b>495</b>	<b>2.506</b>	<b>0.002</b>	<b>0.517</b>	<b>0.554</b>	<b>0.194</b>
<b>Protonated Open Form</b>													
I. $S_0 \rightarrow S_2$	681	1.820	0.122	7.432	0.770	2.011	I. $S_0 \rightarrow S_7$	437	2.839	1.018	2.386	0.541	0.917
II. $S_0 \rightarrow S_2$	663	1.870	0.115	7.507	0.764	2.046	II. $S_0 \rightarrow S_7$	424	2.922	1.053	1.071	0.533	0.589
III. $S_0 \rightarrow S_2$	625	1.983	0.068	7.753	0.809	1.996	III. $S_0 \rightarrow S_7$	415	2.987	0.359	5.657	0.686	1.717
IV. $S_0 \rightarrow S_2$	677	1.833	0.127	7.439	0.748	2.069	IV. $S_0 \rightarrow S_7$	434	2.857	1.101	1.812	0.526	0.718
V. $S_0 \rightarrow S_2$	672	1.846	0.122	7.002	0.755	1.932	V. $S_0 \rightarrow S_7$	431	2.877	1.093	2.029	0.529	0.798
<b><math>S_0 \rightarrow S_2</math></b>	<b>675</b>	<b>1.843</b>	<b>0.124</b>	<b>7.207</b>	<b>0.753</b>	<b>1.995</b>	<b><math>S_0 \rightarrow S_7</math></b>	<b>433</b>	<b>2.872</b>	<b>1.097</b>	<b>1.923</b>	<b>0.528</b>	<b>0.761</b>

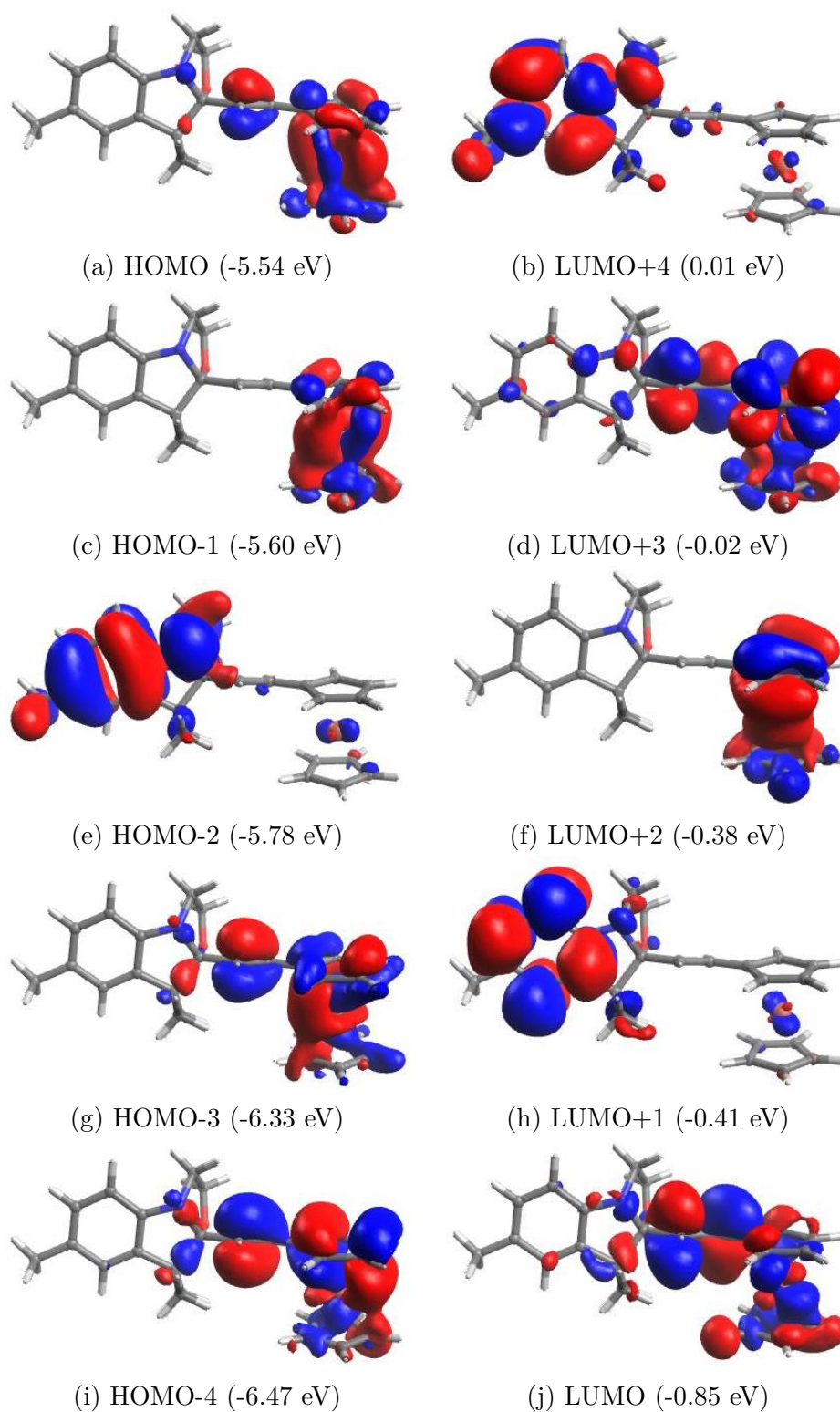


Figure B.3: Shape of frontier molecular orbitals in the most stable closed form, calculated at the B3PW91/6-311G(d) level in acetonitrile.

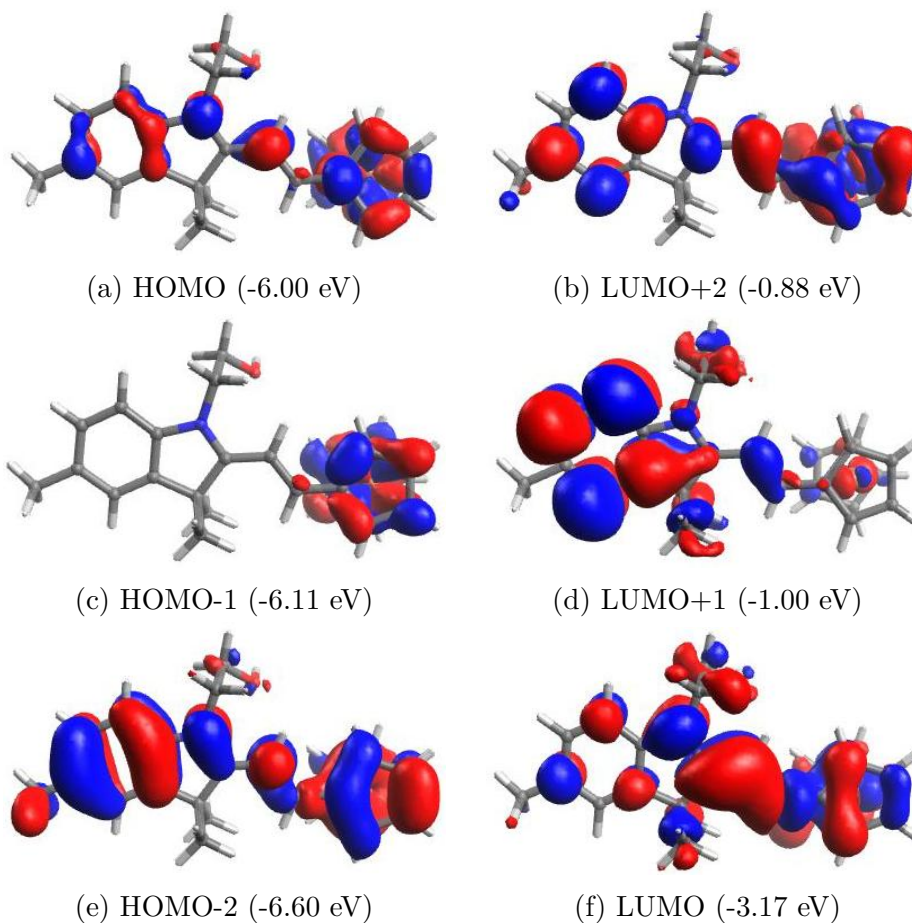


Figure B.4: Shape of frontier molecular orbitals in the most stable protonated open form, calculated at the B3PW91/6-311G(d) level in acetonitrile.

# Nonlinear Optical Properties

Table B.2: Static and dynamic ( $\lambda = 1064$  and  $1907$  nm) HRS hyperpolarizabilities ( $\beta_{HRS}$ ), dipolar ( $\beta_{J=1}$ ) and octupolar ( $\beta_{J=3}$ ) contributions, as well as depolarization ratios (DR) and nonlinear anisotropy factors ( $\rho$ ) for the different conformers of the closed (left) and protonated open (right) forms as calculated at the CAM-B3LYP/6-311+G(d) level in acetonitrile. The last columns report the average values (in bold).

	Closed Form					Protonated Open Form					
	I	II	III	IV	Average	I	II	III	IV	V	Average
$\lambda = 1064$ nm											
$\beta_{HRS}$	451	418	450	459	<b>458</b>	37864	12693	3241	52200	23073	<b>32246</b>
<i>D.R.</i>	5.54	5.49	5.78	4.90	<b>5.00</b>	4.84	4.79	4.21	4.82	4.79	<b>4.80</b>
$ \beta_{J=1} $	868	802	876	853	<b>865</b>	70157	23439	5727	96557	42595	<b>59604</b>
$ \beta_{J=3} $	613	574	580	716	<b>701</b>	59741	20241	5811	82802	36826	<b>51269</b>
$\rho$	0.71	0.71	0.66	0.84	<b>0.80</b>	0.85	0.86	1.01	0.86	0.86	<b>0.86</b>
$\lambda = 1907$ nm											
$\beta_{HRS}$	370	341	361	378	<b>378</b>	3541	3523	1570	3453	3331	<b>3422</b>
<i>D.R.</i>	5.74	5.68	5.95	5.03	<b>5.15</b>	4.65	4.74	3.94	4.58	4.65	<b>4.62</b>
$ \beta_{J=1} $	720	660	708	709	<b>712</b>	6477	6482	2701	6283	6094	<b>6249</b>
$ \beta_{J=3} $	482	450	448	573	<b>559</b>	5811	5681	2973	5752	5464	<b>5646</b>
$\rho$	0.67	0.68	0.63	0.81	<b>0.78</b>	0.90	0.88	1.10	0.92	0.90	<b>0.90</b>
$\lambda = \infty$											
$\beta_{HRS}$	472	455	482	475	<b>475</b>	4375	4337	2055	4247	4236	<b>4243</b>
<i>D.R.</i>	5.88	6.2	6.58	5.51	<b>5.56</b>	4.58	4.69	3.85	4.44	4.54	<b>4.49</b>
$ \beta_{J=1} $	922	901	967	914	<b>915</b>	7961	7952	3504	7644	7688	<b>7674</b>
$ \beta_{J=3} $	595	531	509	651	<b>642</b>	7287	7069	3963	7281	7107	<b>7182</b>
$\rho$	0.65	0.59	0.53	0.71	<b>0.70</b>	0.92	0.89	1.14	0.95	0.92	<b>0.93</b>

## Effect of the Level of Approximation

Table B.3: Averaged static and dynamic ( $\lambda = 1064$  and  $1907$  nm)  $\beta_{HRS}$  and  $\beta_J$  values, as well as  $\rho$  and DR calculated for the **closed form** using different XC functionals and methods (HF, MP2) together with the **6-311+G(d)** basis set in acetonitrile and employing the B3LYP/6-311G(d) optimized geometry. All  $\beta$  values are given in a.u. .

	<i>B3LYP</i>	<i>CAM-B3LYP</i>	<i>BPW91</i>	<i>M06-2X</i>	<i>HF</i>	<i>MP2</i>
$\lambda = 1064$ nm						
$\beta_{HRS}$	520	458	1285	484		
<i>D.R.</i>	4.86	5.00	5.49	4.98		
$ \beta_{J=1} $	966	865	2469	904		
$ \beta_{J=3} $	817	701	1762	741		
$\rho$	0.85	0.80	0.71	0.81		
$\lambda = 1907$ nm						
$\beta_{HRS}$	449	378	531	407		
<i>D.R.</i>	5.12	5.15	5.04	5.18		
$ \beta_{J=1} $	846	712	996	770		
$ \beta_{J=3} $	670	559	803	598		
$\rho$	0.80	0.78	0.80	0.77		
$\lambda = \infty$						
$\beta_{HRS}$	562	475	652	483	331	428
<i>D.R.</i>	5.52	5.56	5.41	5.40	5.18	6.30
$ \beta_{J=1} $	1080	915	1249	924	625	397
$ \beta_{J=3} $	767	642	910	676	486	158
$\rho$	0.71	0.70	0.72	0.72	0.77	

Table B.4: Averaged static and dynamic ( $\lambda = 1064$  and  $1907$  nm)  $\beta_{HRS}$  and  $\beta_J$  values, as well as  $\rho$  and DR calculated for the **protonated open form** using different XC functionals and methods (HF, MP2) together with the **6-311+G(d)** basis set in acetonitrile and employing the B3LYP/6-311G(d) optimized geometry. All  $\beta$  values are given in a.u. .

	<i>B3LYP</i>	<i>CAM-B3LYP</i>	<i>BPW91</i>	<i>M06-2X</i>	<i>HF</i>	<i>MP2</i>
$\lambda = 1064$ nm						
$\beta_{HRS}$	6757	32246	31046	4348		
<i>D.R.</i>	4.64	4.80	5.31	4.33		
$ \beta_{J=1} $	12305	59604	34223	7767		
$ \beta_{J=3} $	11109	51269	44283	7600		
$\rho$	0.90	0.86	1.26	0.97		
$\lambda = 1907$ nm						
$\beta_{HRS}$	4197	3422	6608	1275		
<i>D.R.</i>	4.35	4.62	3.77	2.89		
$ \beta_{J=1} $	7505	6249	11174	2022		
$ \beta_{J=3} $	7319	5646	12927	2621		
$\rho$	0.97	0.90	1.15	1.29		
$\lambda = \infty$						
$\beta_{HRS}$	4080	4243	3258	3533	2214	5108
<i>D.R.</i>	3.93	4.49	2.79	4.53	3.84	4.82
$ \beta_{J=1} $	7059	7674	29560	6407	3771	4648
$ \beta_{J=3} $	7741	7182	7792	5937	4277	2118
$\rho$	1.10	0.93	1.17	0.92	1.14	

---

## Force Field Derivation

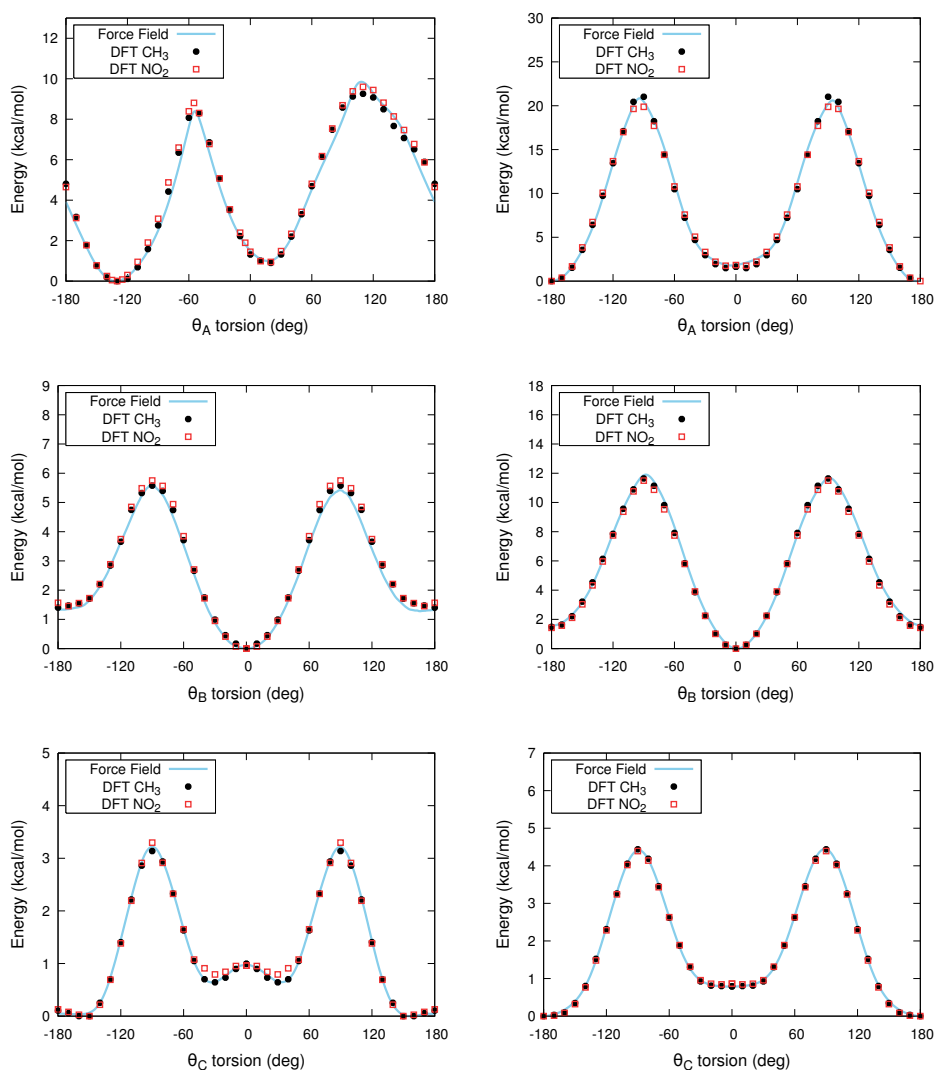


Figure C.1: Dihedral potentials obtained from constrained optimizations at the M06/6-311G(d) level for compounds **1** (R = CH<sub>3</sub>) and **2** (R = NO<sub>2</sub>) in their closed (left) and protonated open (right) forms, and fitted potential used in the classical force field. The definition of the dihedrals is given in the main text, Scheme 6.1.

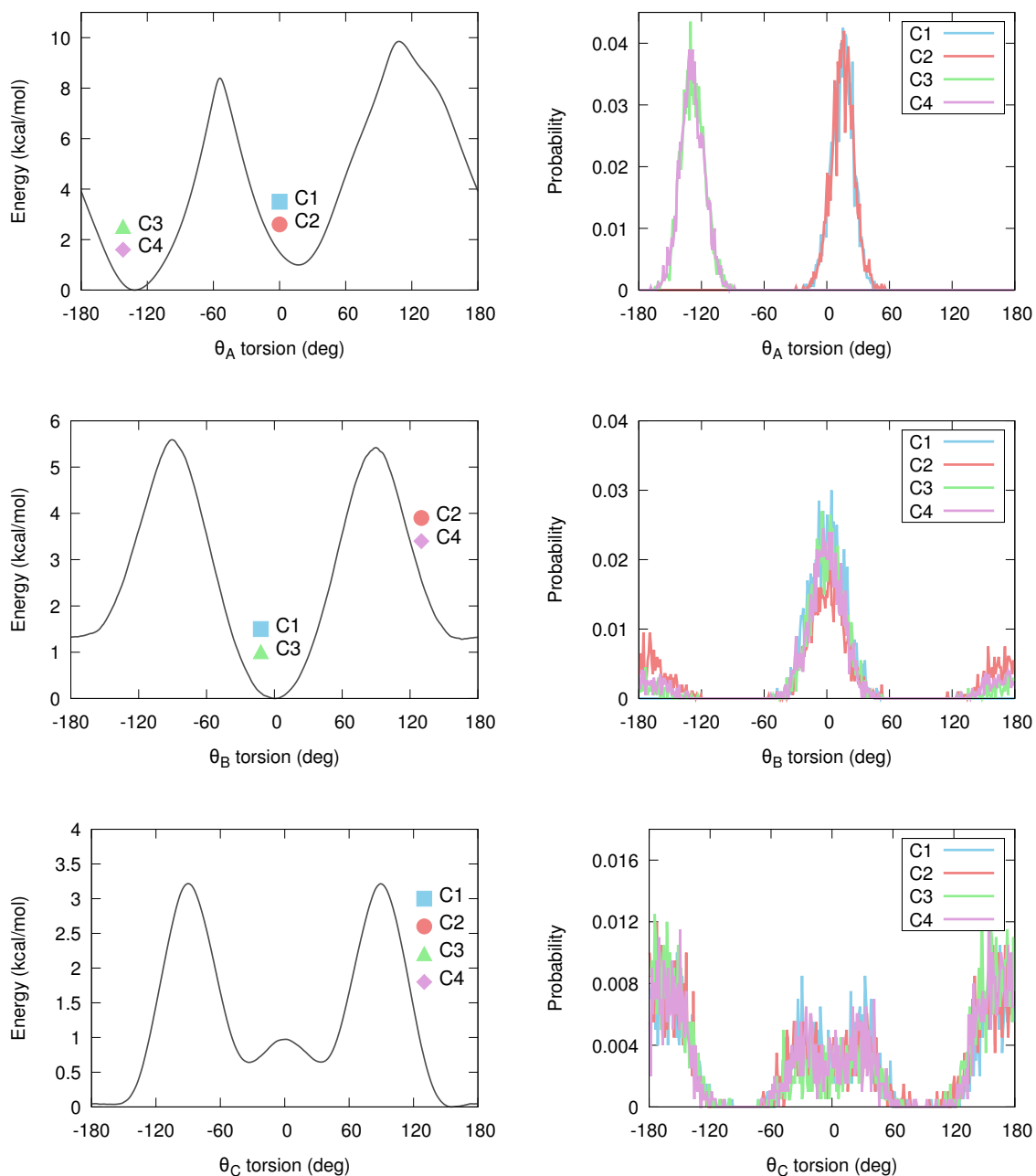


Figure C.2: Potential energy curves associated to the rotation around the  $\theta_{A-C}$  dihedral angles (kcal/mol) (left) and probability distributions ( $\text{deg}^{-1}$ ) of the dihedral angles over the 20 000 frames extracted from MD simulations (right) for compound **1** ( $R=\text{CH}_3$ ) in its closed form. Points on the dihedral potentials plots indicate the starting geometries/conformers, denoted C1-C4.

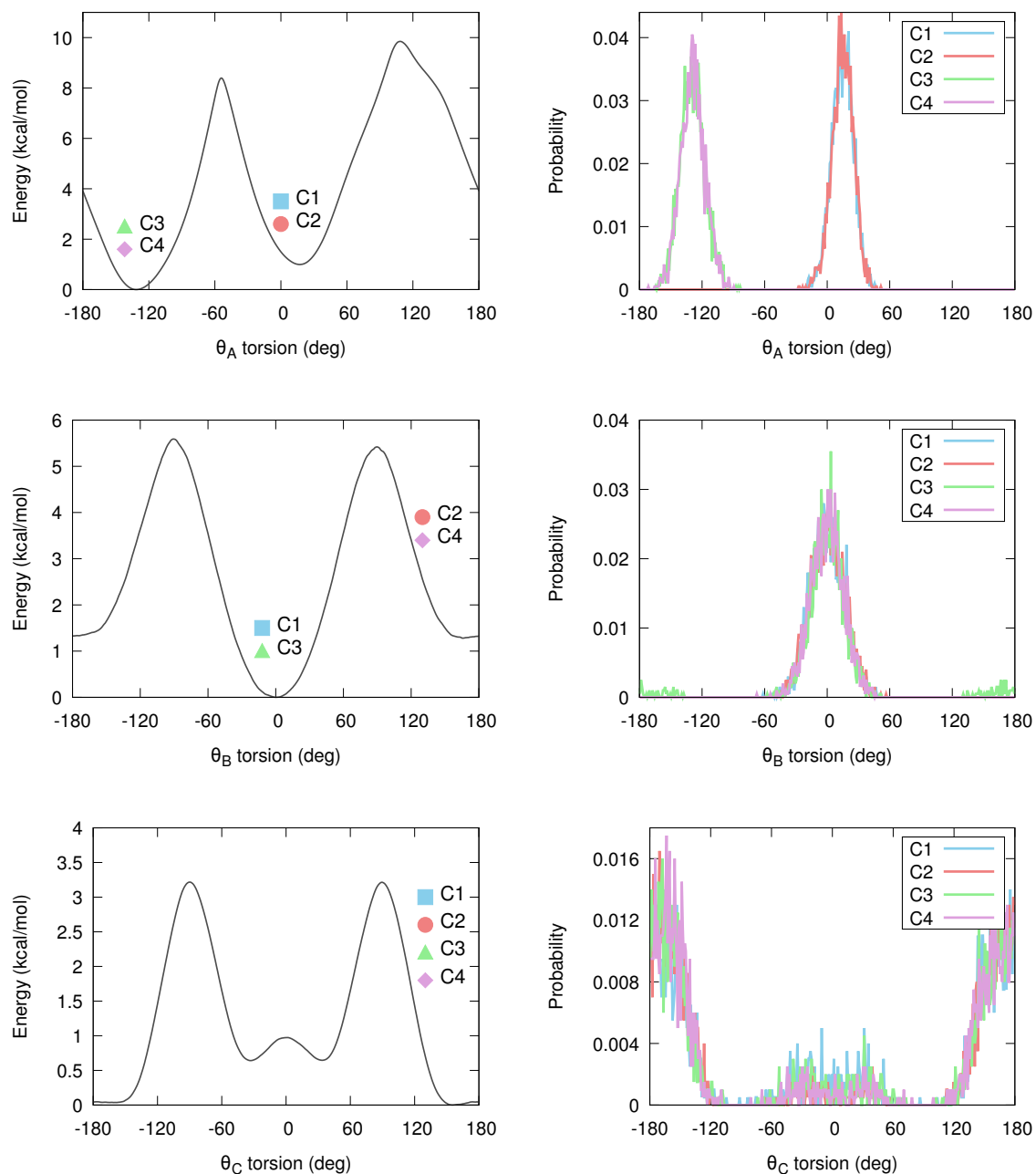


Figure C.3: Potential energy curves associated to the rotation around the  $\theta_{A-C}$  dihedral angles (kcal/mol) (left) and probability distributions ( $\text{deg}^{-1}$ ) of the dihedral angles over the 20 000 frames extracted from MD simulations (right) for compound **2** ( $R=\text{NO}_2$ ) in its closed form. Points on the dihedral potentials plots indicate the starting geometries/conformers, denoted C1-C4.

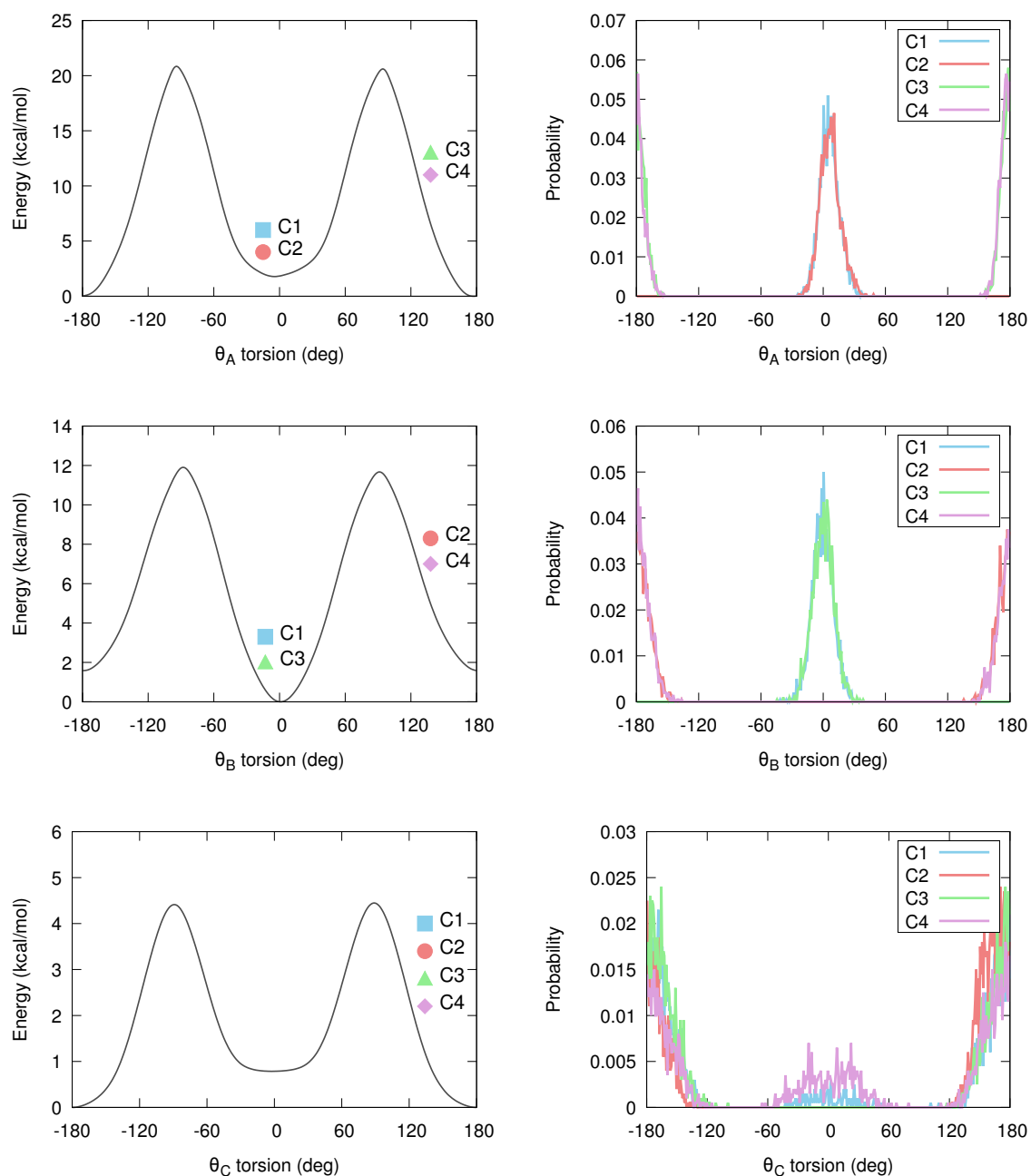


Figure C.4: Potential energy curves associated to the rotation around the  $\theta_{A-C}$  dihedral angles (kcal/mol) (left) and probability distributions ( $\text{deg}^{-1}$ ) of the dihedral angles over the 20 000 frames extracted from MD simulations (right) for compound **1** ( $R=\text{CH}_3$ ) in its open form. Points on the dihedral potentials plots indicate the starting geometries/conformers, denoted C1-C4.

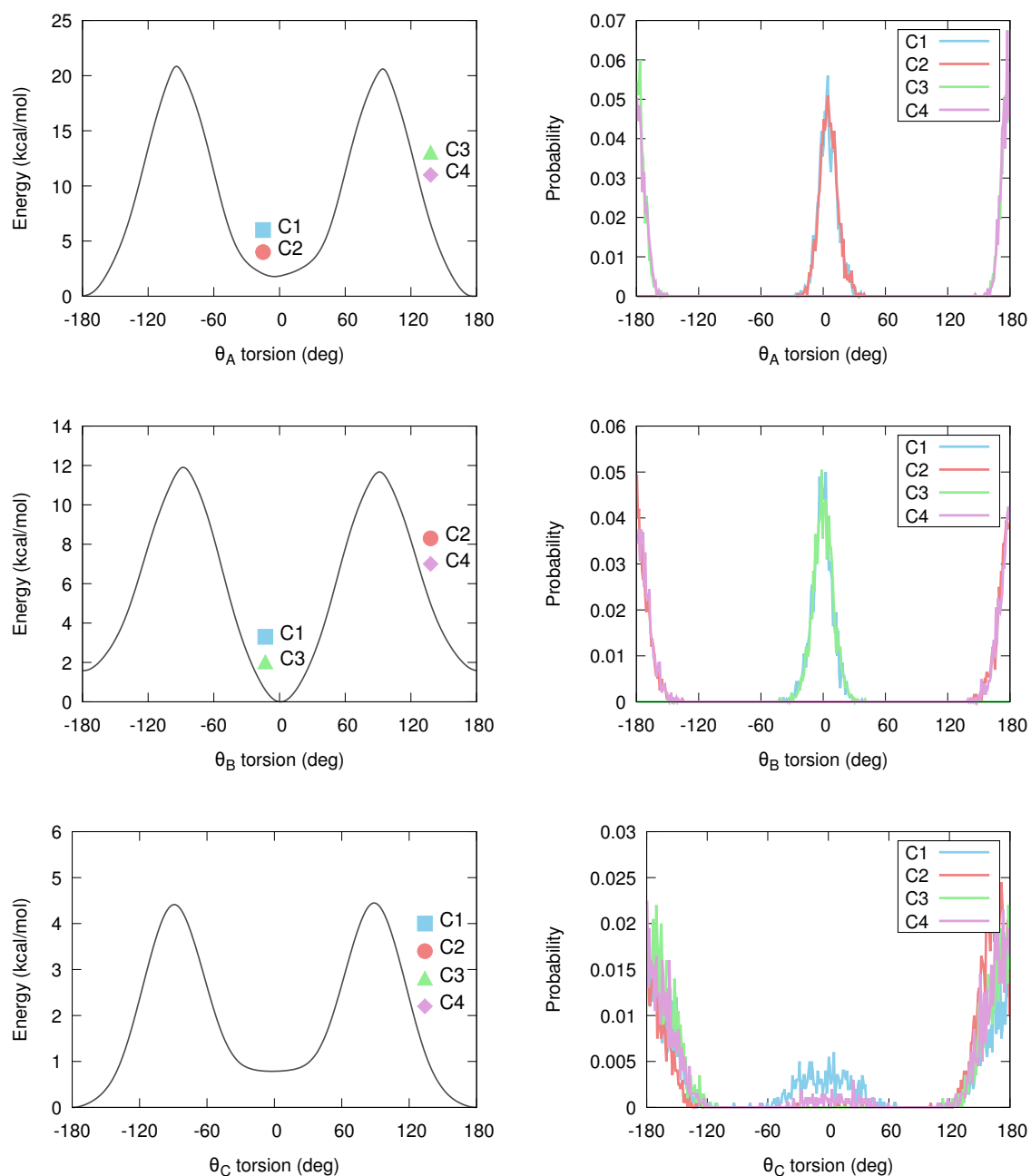


Figure C.5: Potential energy curves associated to the rotation around the  $\theta_{A-C}$  dihedral angles (kcal/mol) (left) and probability distributions ( $\text{deg}^{-1}$ ) of the dihedral angles over the 20 000 frames extracted from MD simulations (right) for compound **2** (R=NO<sub>2</sub>) in its open form. Points on the dihedral potentials plots indicate the starting geometries/conformers, denoted C1-C4.

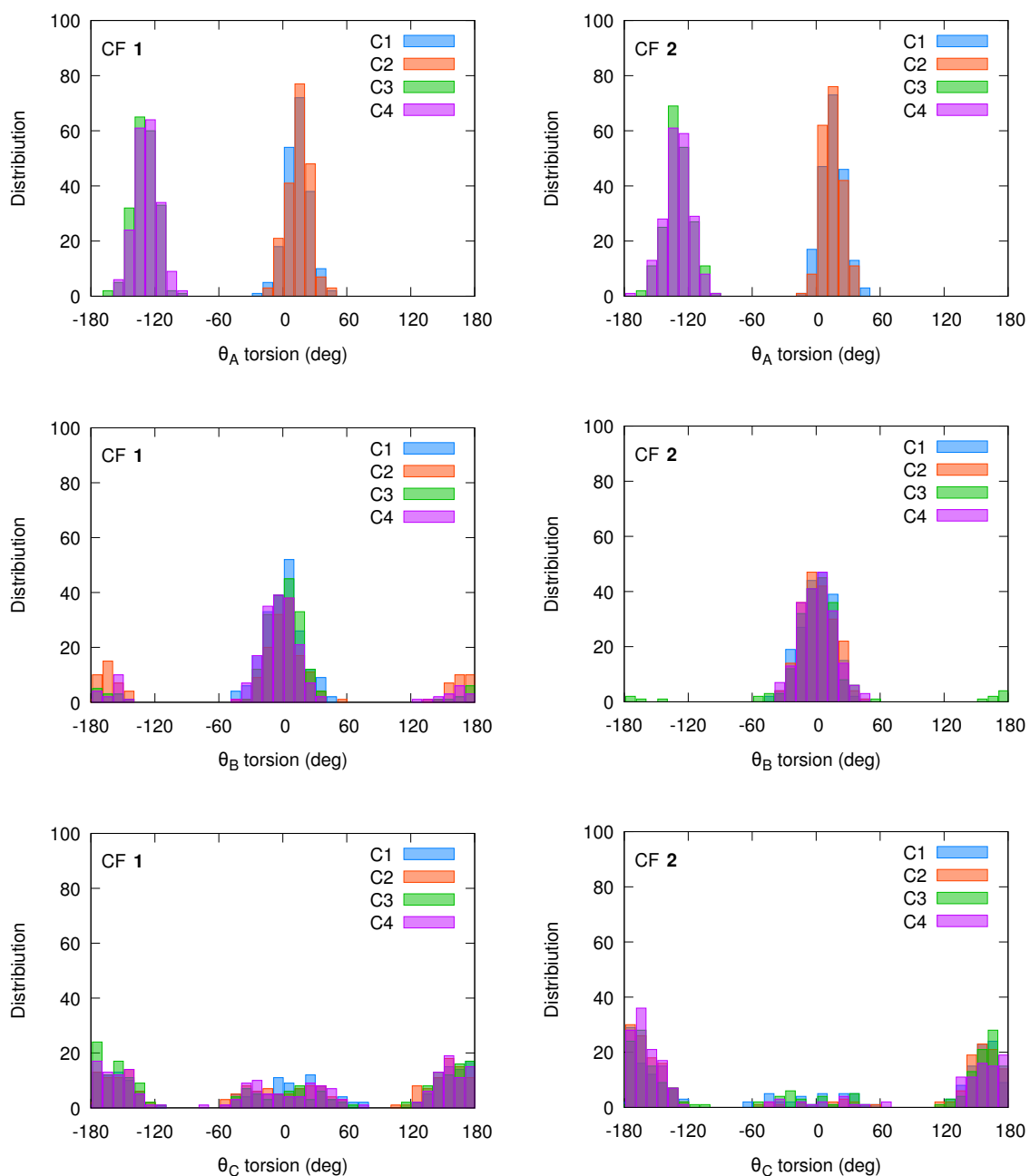


Figure C.6: Distributions of the dihedral angles over the 200 snapshots selected from MD simulations for compound **1** (R=CH<sub>3</sub>) (left) and compound **2** (R=NO<sub>2</sub>) (right) in their closed forms.

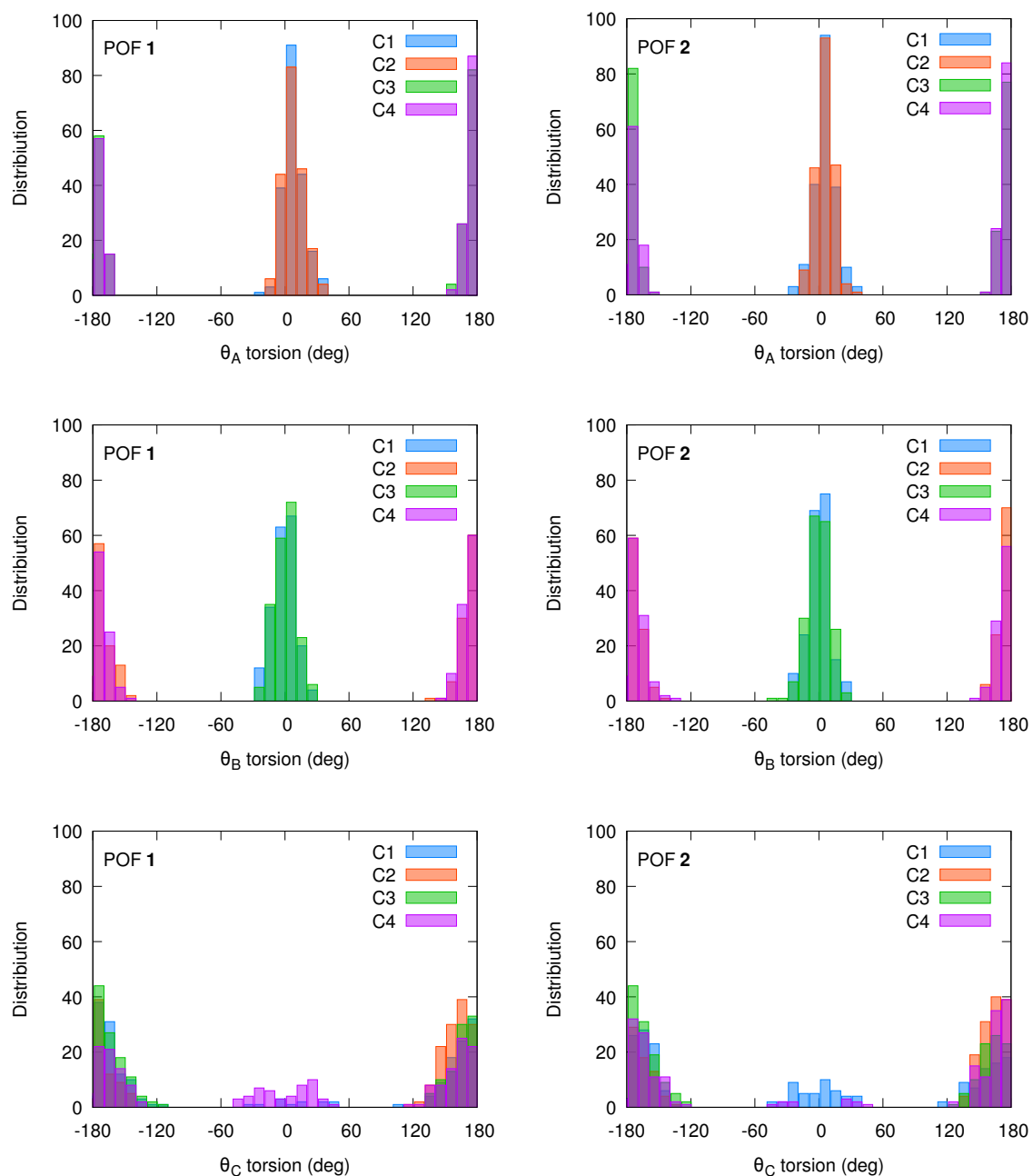


Figure C.7: Distributions of the dihedral angles over the 200 snapshots selected from MD simulations for compound **1** (R=CH<sub>3</sub>) (left) and compound **2** (R=NO<sub>2</sub>) (right) in their open forms.

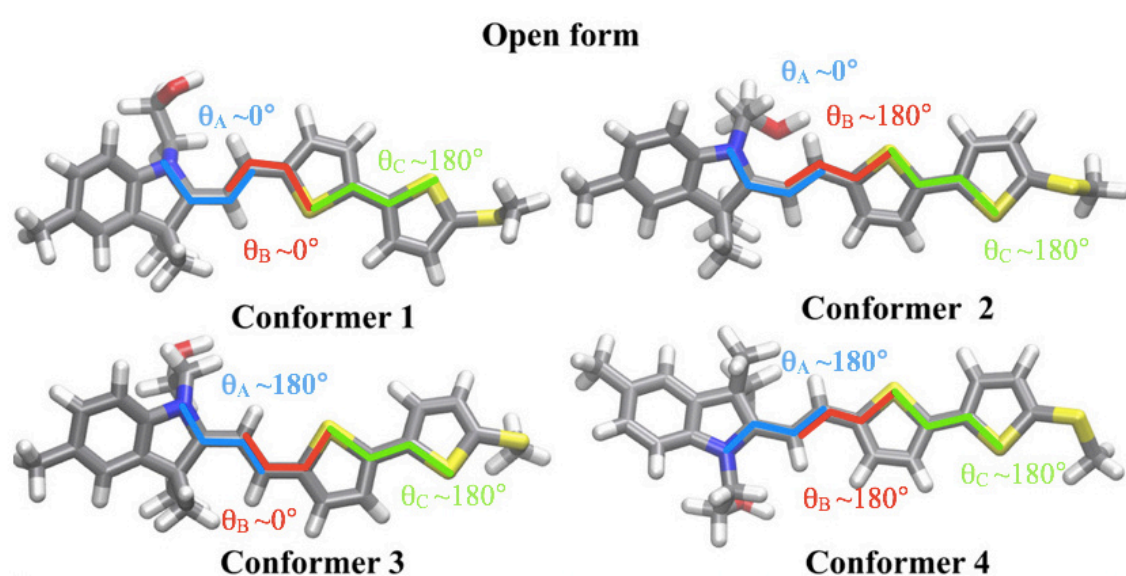


Figure C.8: Conformers 1-4 (C1-C4) for closed and protonated open forms used as starting geometries in MD simulations.

## Average Internal Energies

Table C.1: Total internal energies ( $E_{tot}$ , kcal/mol), intra- and intermolecular contributions ( $E_{intra}$  and  $E_{inter}$ , kcal/mol), and relative energies ( $\Delta E$ , kcal/mol), averaged over the 200 snapshots produced by the various MD simulations, as well as populations of each conformer evaluated using Boltzmann statistics at 298.15 K.

	Closed Forms							
	C1	C2	C3	C4	C1	C2	C3	C4
	1: R=CH <sub>3</sub>				2: R=NO <sub>2</sub>			
$E_{tot}$	-16.8	-16.6	-18.9	-18.5	39.1	38.7	37.7	38.4
$E_{intra}$	44.1	44.8	42.7	42.9	107.1	106.1	105.8	105.9
$E_{inter}$	-60.9	-61.4	-61.6	-61.4	-70	-67.4	-68	-67.6
$\Delta E$	2.2	2.3	0.0	0.4	1.4	1	0.0	0.6
Population %	1.7	1.2	64.3	32.8	5.7	11.4	61.4	21.5
	Open Forms							
	C1	C2	C3	C4	C1	C2	C3	C4
	1: R=CH <sub>3</sub>				2: R=NO <sub>2</sub>			
$E_{tot}$	-11.4	-11.3	-11.6	-11.3	60.7	61.8	61.2	61.4
$E_{intra}$	80	77.3	79.6	77.3	156.8	159.2	155.3	156.3
$E_{inter}$	-91.4	-88.5	-91.2	-88.5	-96.1	-97.4	-94.1	-94.9
$\Delta E$	0.1	0.3	0.0	0.3	0.0	1.1	0.6	0.7
Population %	26.2	20.2	33.4	20.2	54.1	8.5	21.0	16.4

# Average Structural Parameters

## Bond Length Alternation

Table C.2: Average bond length alternations (BLA, Å) and their standard deviations for closed and open forms of compounds **1** and **2** issued from the various MD simulations, as well as their Boltzmann averages.

	Closed Forms		Open Forms	
	<b>1</b> : R=CH <sub>3</sub>	<b>2</b> : R=NO <sub>2</sub>	<b>1</b> : R=CH <sub>3</sub>	<b>2</b> : R=NO <sub>2</sub>
C1	0.136 ± 0.030	0.135 ± 0.030	0.033 ± 0.033	0.011 ± 0.032
C2	0.141 ± 0.032	0.139 ± 0.030	0.040 ± 0.029	0.012 ± 0.030
C3	0.143 ± 0.030	0.139 ± 0.029	0.041 ± 0.033	0.016 ± 0.030
C4	0.144 ± 0.030	0.138 ± 0.031	0.033 ± 0.029	0.014 ± 0.031
<b>Average</b>	<b>0.141 ± 0.022</b>	<b>0.138 ± 0.019</b>	<b>0.038 ± 0.019</b>	<b>0.012 ± 0.019</b>

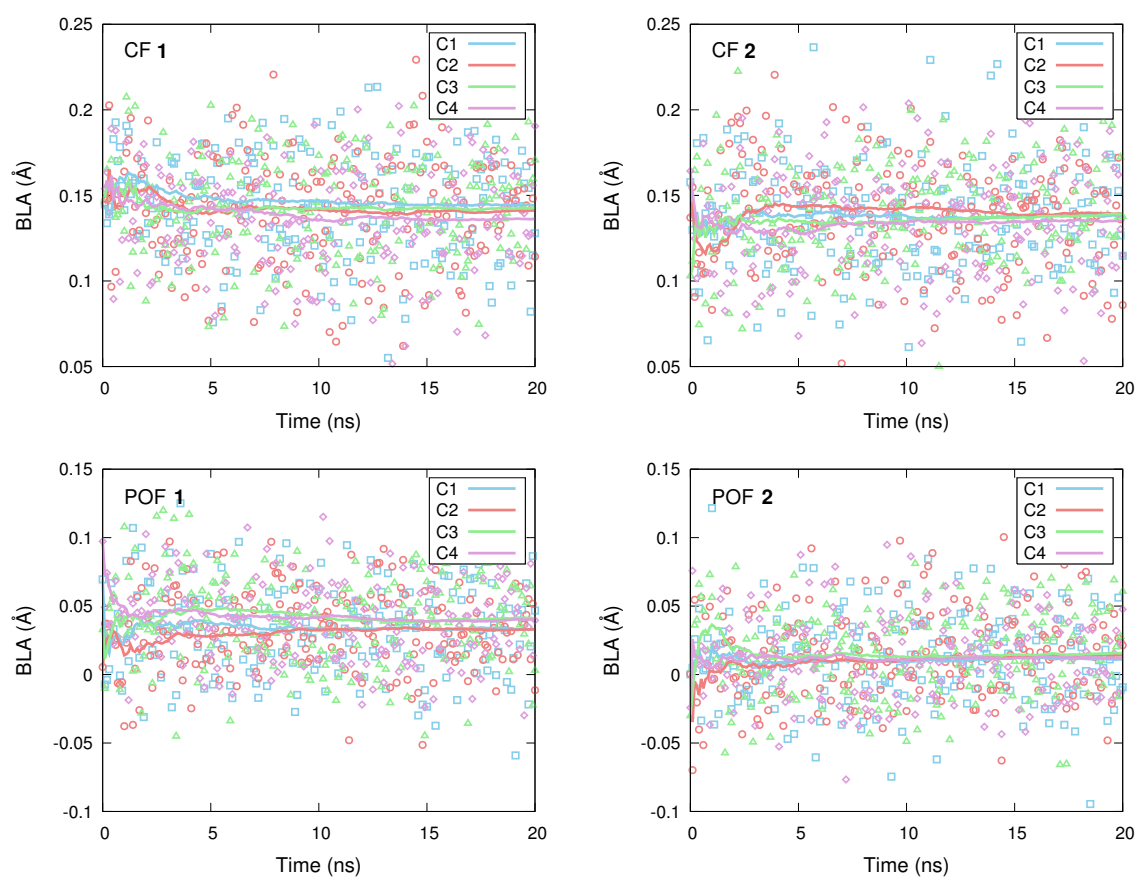


Figure C.9: Time evolution of the bond length alternation along the vinyl bridge (BLA, Å) in compounds **1** (left) and **2** (right), in their closed (top) and open (bottom) forms. Lines correspond to running averages.

## Hydrogen Bond Length

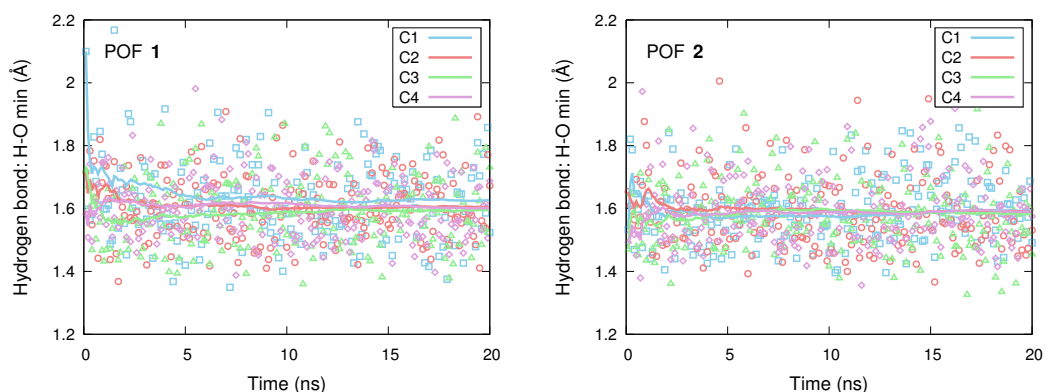


Figure C.10: Time evolution of the length of the hydrogen bond between the perfluoroacetate anion and the protonated open form of compounds **1** (left) and **2** (right). Lines correspond to running averages.

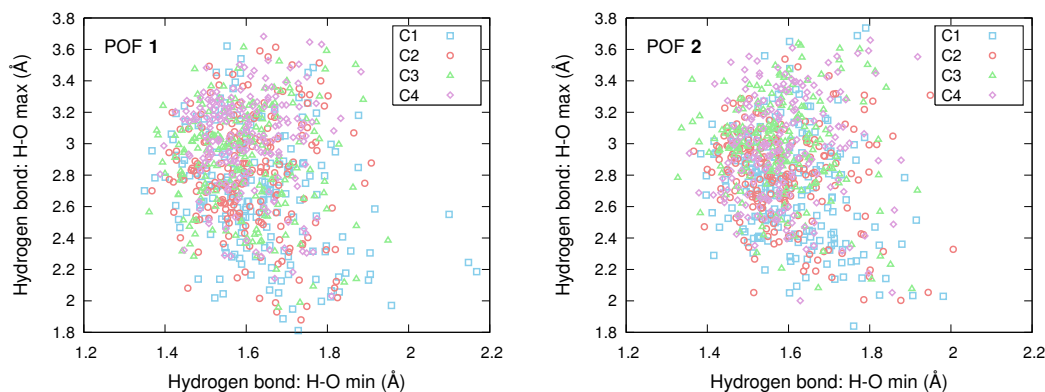


Figure C.11: Global distribution of the  $\text{O}^- \dots \text{H}$  distances (Å) between the oxygen atoms of the perfluoroacetate anion and the terminal hydroxyl group of the protonated open form of compound **1** (left) and **2** (right).

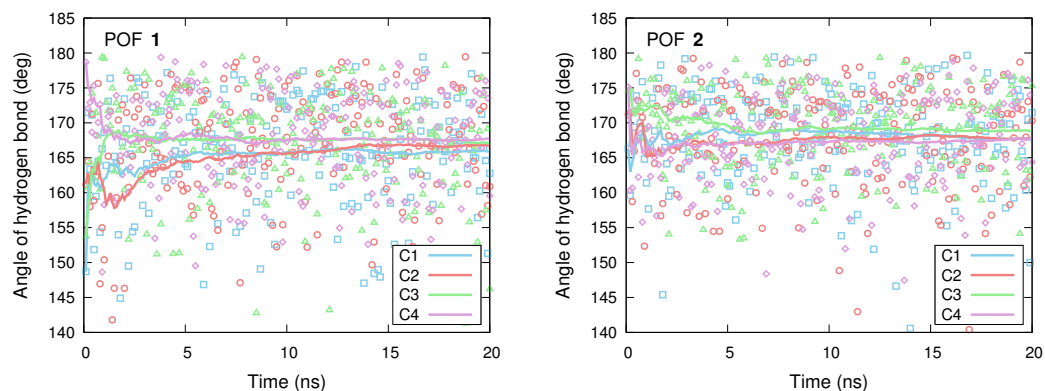


Figure C.12: Time evolution of the angle of the hydrogen bond between the perfluoroacetate anion and the protonated open form of compounds **1** (left) and **2** (right). Lines correspond to running averages.

Table C.3: Average and standard deviations of the lengths ( $\text{\AA}$ ) and angles ( $^\circ$ ) of the hydrogen bond between the perfluoroacetate anion and the protonated open form of compounds **1** and **2**, issued from the various MD simulations as well as their Boltzmann averages.

	1: R=CH <sub>3</sub>		2: R=NO <sub>2</sub>	
	O-H	angle	O-H	angle
C1	1.626 $\pm$ 0.135	165.9 $\pm$ 7.835	1.605 $\pm$ 0.110	167.6 $\pm$ 7.020
C2	1.601 $\pm$ 0.097	167.7 $\pm$ 6.694	1.590 $\pm$ 0.106	167.8 $\pm$ 6.141
C3	1.596 $\pm$ 0.113	167.0 $\pm$ 7.330	1.581 $\pm$ 0.108	168.9 $\pm$ 6.530
C4	1.605 $\pm$ 0.106	166.7 $\pm$ 7.866	1.589 $\pm$ 0.118	167.8 $\pm$ 7.686
<b>Average</b>	<b>1.603 <math>\pm</math> 0.068</b>	<b>166.4 <math>\pm</math> 4.4</b>	<b>1.596 <math>\pm</math> 0.067</b>	<b>167.9 <math>\pm</math> 4.3</b>

## Anion-Cation Distance

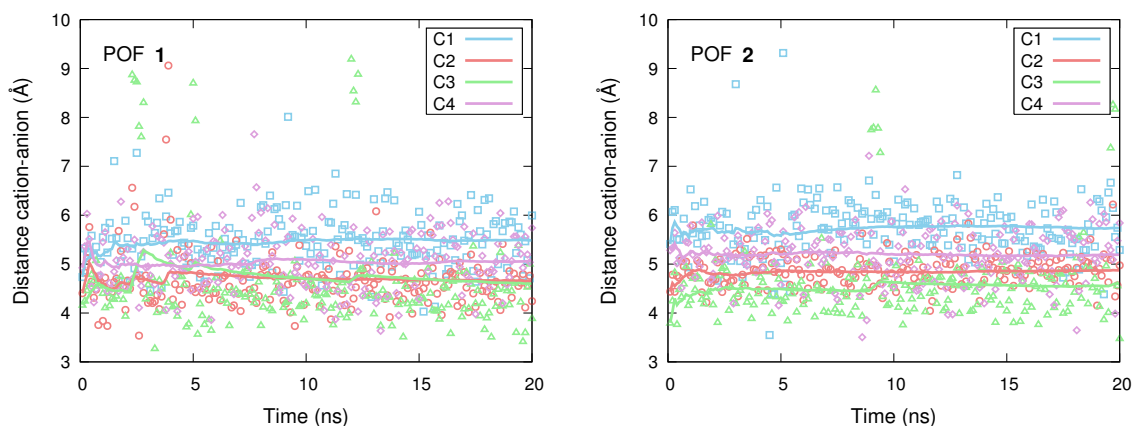


Figure C.13: Time evolution of the distance ( $\text{\AA}$ ) between the centers of mass of the anion and of the open form of compounds **1** (left) and **2** (right). Distances larger than  $7 \text{\AA}$  correspond to accidental changes in the orientation of the hydroxylated arm of the POF, as illustrated on figure C.14. Lines correspond to running averages.

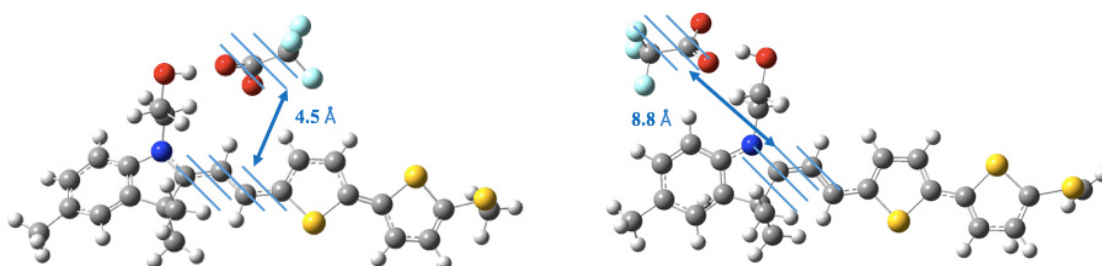


Figure C.14: Snapshots of the anion/cation pair with different orientation of the hydroxylated arm of the POF for compound **1**.

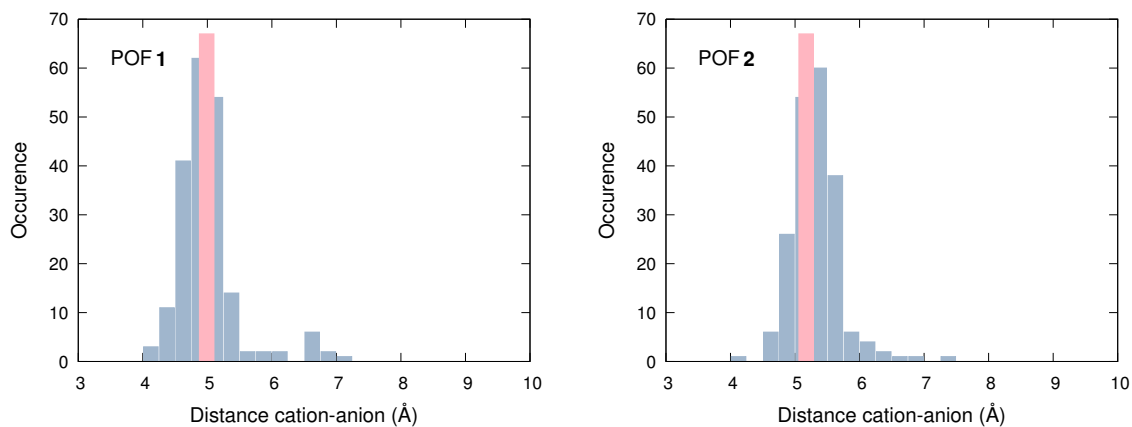


Figure C.15: Distributions (out of the 200 snapshots) of the distance between the centers of mass of the anion and of the open form of compounds **1** (left) and **2** (right).

Table C.4: Average and standard deviations of the lengths ( $\text{\AA}$ ) and angles ( $^\circ$ ) of the hydrogen bond between the perfluoroacetate anion and the protonated open form of compounds **1** and **2**, issued from the various MD simulations as well as their Boltzmann averages.

	<b>1: R=CH<sub>3</sub></b>	<b>2: R=NO<sub>2</sub></b>
C1	5.487 $\pm$ 0.562	5.435 $\pm$ 0.638
C2	5.061 $\pm$ 0.582	5.190 $\pm$ 0.547
C3	4.598 $\pm$ 1.062	4.595 $\pm$ 0.773
C4	4.657 $\pm$ 0.579	4.887 $\pm$ 0.322
<b>Average</b>	<b>4.990 <math>\pm</math> 0.491</b>	<b>5.172 <math>\pm</math> 0.393</b>

# NLO Responses

## Time Evolution and Average NLO Responses Calculated with the QM Approach

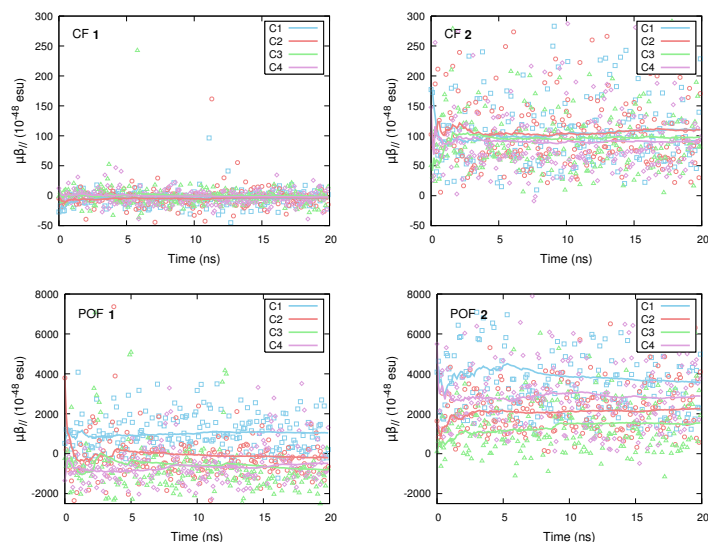


Figure C.16: Time evolution of the  $\mu\beta_{//}$  ( $10^{-48}$  esu = 45.539 a.u.) values (dots) and of their cumulative averages (lines) for compounds **1** (left) and **2** (right) in their closed form (top) and for the POF/TFA pair (bottom), as determined at the IEFPCM(solvent=chloroform)/M06-2X/6-311+G(d) level of approximation for a wavelength of 1907 nm. The results correspond to a total of 200 snapshots equally distributed over the 20 ns production time. Lines correspond to running averages.

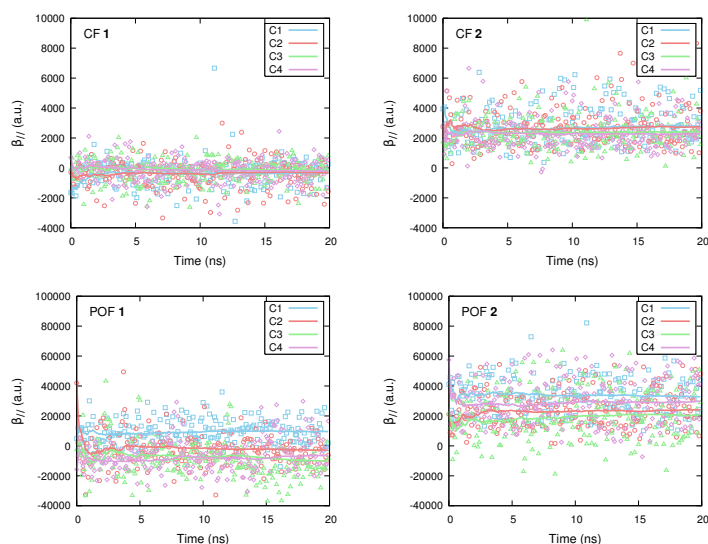


Figure C.17: Time evolution of the  $\beta_{//}$  (a.u.) values (dots) and of their cumulative averages (lines) for compounds **1** (left) and **2** (right) in their closed form (top) and for the POF/TFA pair (bottom), as determined at the IEFPCM(solvent=chloroform)/M06-2X/6-311+G(d) level of approximation for a wavelength of 1907 nm. The results correspond to a total of 200 snapshots equally distributed over the 20 ns production time. Lines correspond to running averages.

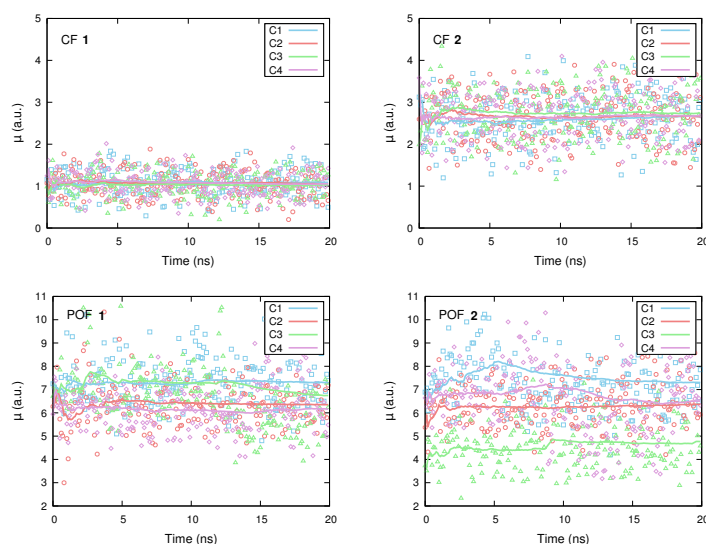


Figure C.18: Time evolution of the dipole moments  $\mu$  (a.u.) and of their cumulative averages (lines) for compounds **1** (left) and **2** (right) in their closed form (top) and for the POF/TFA pair (bottom), as determined at the IEFPCM(solvent=chloroform)/M06-2X/6-311+G(d) level of approximation. The results correspond to a total of 200 snapshots equally distributed over the 20 ns production time. Lines correspond to running averages.

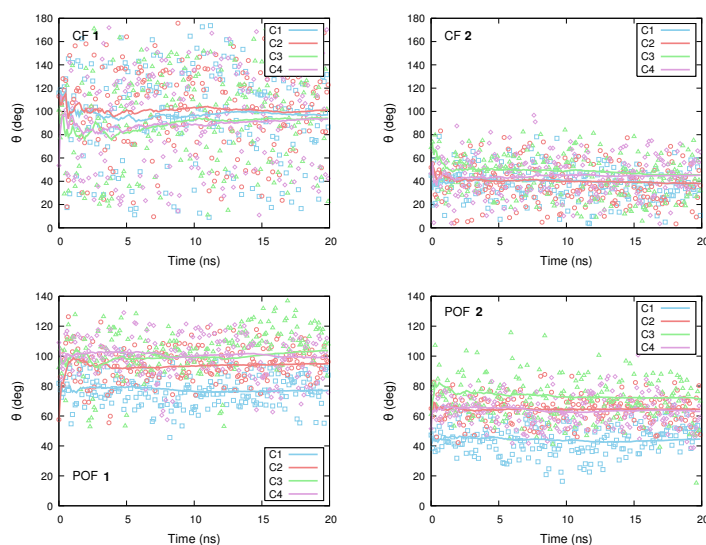


Figure C.19: Time evolution of the angle values ( $^{\circ}$ , dots) between the dipole moment and vector component of  $\beta$ ,  $\theta(\mu, \beta)$ , and of their cumulative averages (lines) for compounds **1** (left) and **2** (right) in their closed form (top) and for the POF/TFA pair (bottom), as determined at the IEFPCM(solvent=chloroform)/M06-2X/6-311+G(d) level of approximation for a wavelength of 1907 nm. The results correspond to a total of 200 snapshots equally distributed over the 20 ns production time. Lines correspond to running averages.

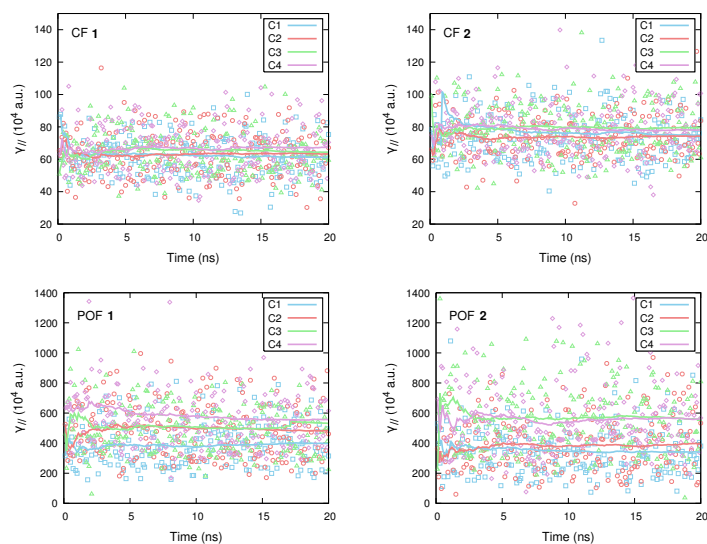


Figure C.20: Time evolution of the  $\gamma_{//}$  (a.u.) values (dots) and of their cumulative averages (lines) for compounds **1** (left) and **2** (right) in their closed form (top) and for the POF/TFA pair (bottom), as determined at the IEFPCM(solvent=chloroform)/M06-2X/6-311+G(d) level of approximation for a wavelength of 1907 nm. The results correspond to a total of 200 snapshots equally distributed over the 20 ns production time. Lines correspond to running averages.

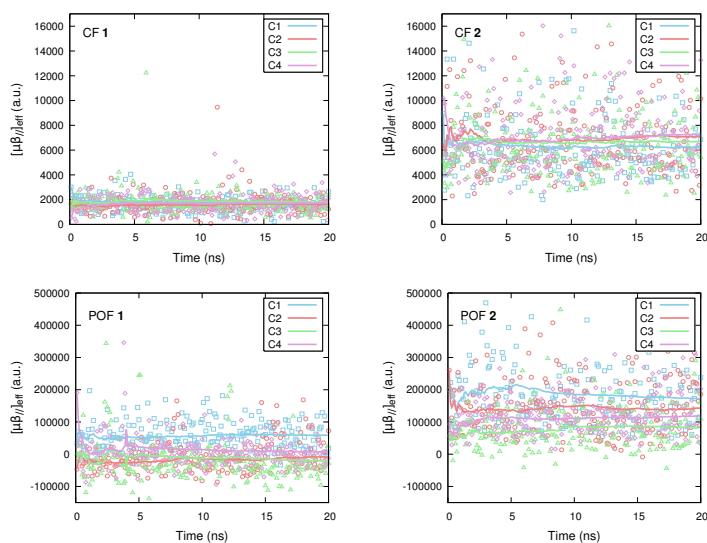


Figure C.21: Time evolution of the  $[\mu\beta_{//}]_{eff}$  (in a.u.;  $10^{-48}$  esu = 45.539 a.u.) values (dots) and of their cumulative averages (lines) for compounds **1** (left) and **2** (right) in their closed form (top) and for the POF/TFA pair (bottom), as determined at the IEFPCM(solvent= chloroform)/M06-2X/6-311+G(d) level of approximation for a wavelength of 1907 nm. The results correspond to a total of 200 snapshots equally distributed over the 20 ns production time. Lines correspond to running averages.

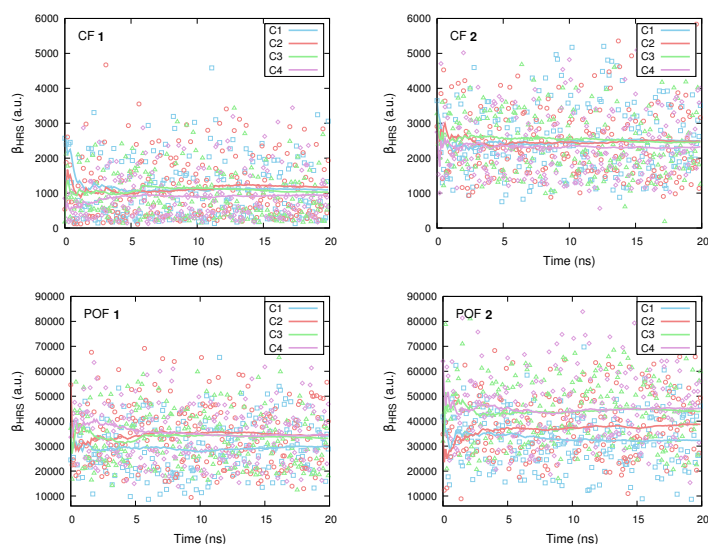


Figure C.22: Time evolution of the  $\beta_{HRS}$  (a.u.) values (dots) and of their cumulative averages (lines) for compounds **1** (left) and **2** (right) in their closed form (top) and for the POF/TFA pair (bottom), as determined at the IEFPCM(solvent=chloroform)/M06-2X/6-311+G(d) level of approximation for a wavelength of 1907 nm. The results correspond to a total of 200 snapshots equally distributed over the 20 ns production time. Lines correspond to running averages.

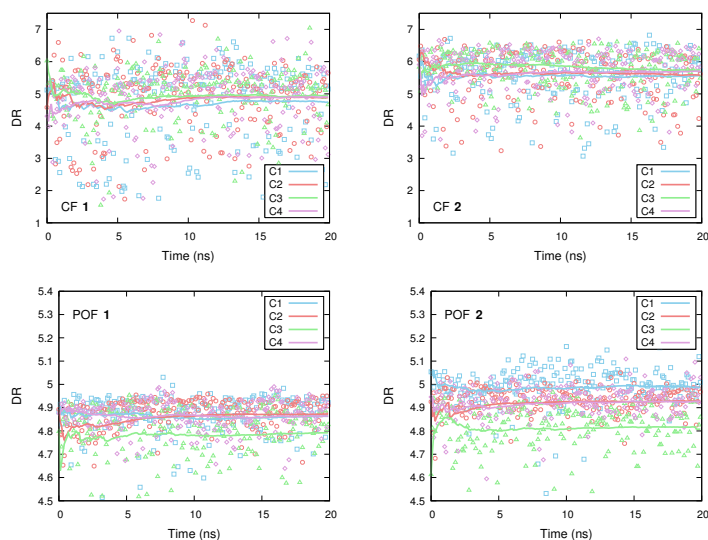


Figure C.23: Time evolution of the DR values (dots) and of their cumulative averages (lines) for compounds **1** (left) and **2** (right) in their closed form (top) and for the POF/TFA pair (bottom), as determined at the IEFPCM(solvent=chloroform)/M06-2X/6-311+G(d) level of approximation for a wavelength of 1907 nm. The results correspond to a total of 200 snapshots equally distributed over the 20 ns production time. Lines correspond to running averages.

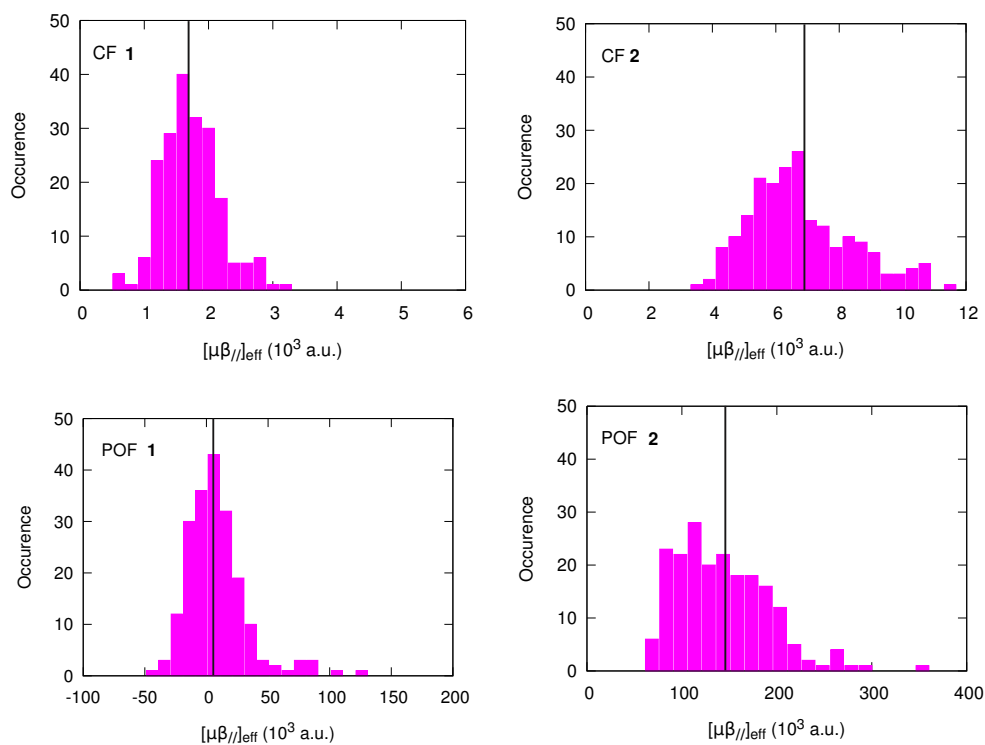


Figure C.24: Statistical distributions of  $[\mu\beta_{//}]_{eff}$  and their averages (black vertical lines). Results are given for compounds **1** (left) and **2** (right) in their closed form (top) and for the POF/TFA pair (bottom).

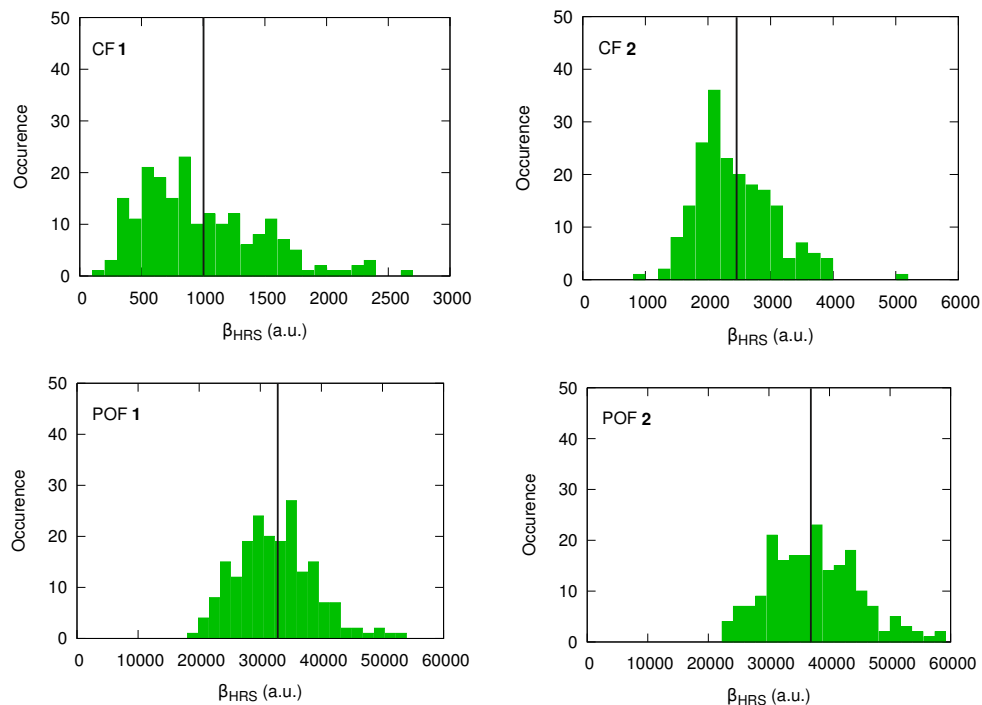


Figure C.25: Statistical distributions of  $\beta_{HRS}$  (a.u.) and their averages (black vertical lines). Results are given for compounds **1** (left) and **2** (right) in their closed form (top) and for the POF/TFA pair (bottom).

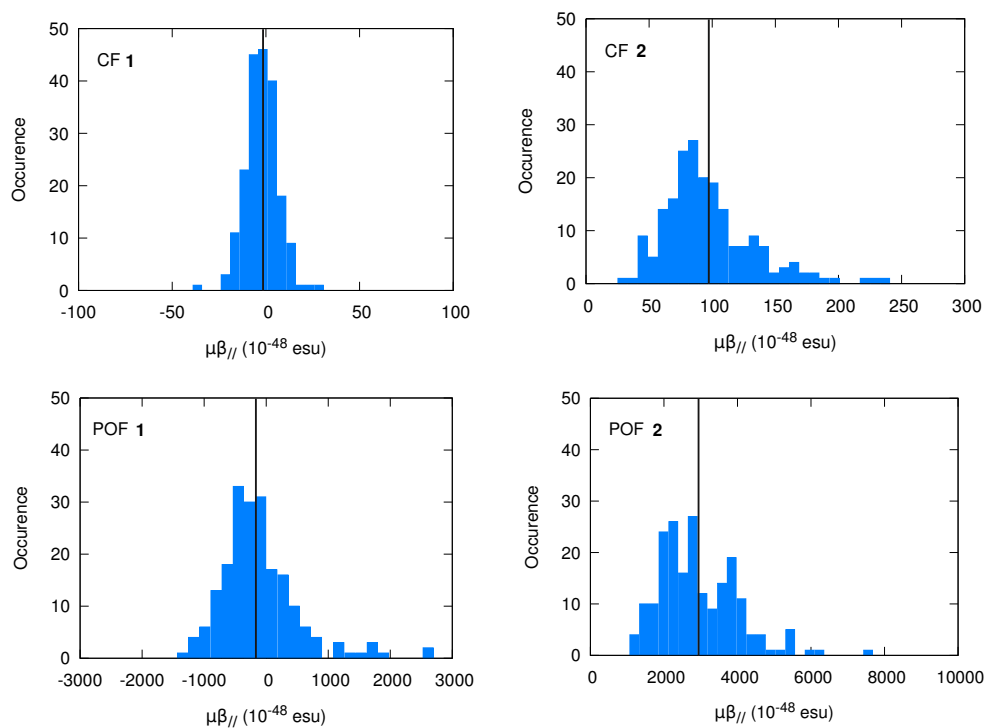


Figure C.26: Statistical distributions of  $\mu\beta_{//}$  ( $10^{-48}$  esu) and their averages (black vertical lines). Results are given for compounds **1** (left) and **2** (right) in their closed form (top) and for the POF/TFA pair (bottom).

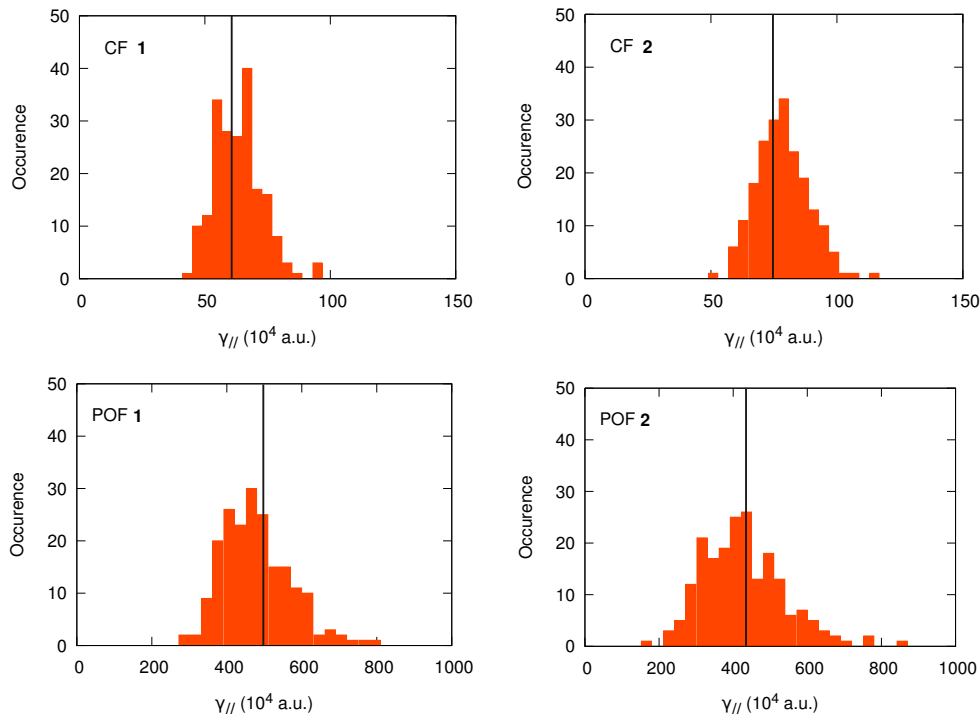


Figure C.27: Statistical distributions of  $\gamma_{//}$  ( $10^4$  a.u.) and their averages (black vertical lines). Results are given for compounds **1** (left) and **2** (right) in their closed form (top) and for the POF/TFA pair (bottom).

## Experimental Data

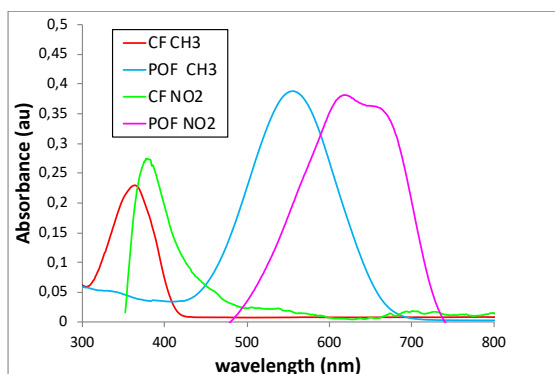


Figure C.28: UV/visible absorption spectra of the **1**(CH<sub>3</sub>) and **2**(NO<sub>2</sub>) in CHCl<sub>3</sub> solutions before (CF) and after (POF) exposure to CF<sub>3</sub>COOH vapor.

Table C.5: EFISHG results. Experimental  $[\mu\beta_{//}]_{eff}$  values ( $10^{-48}$  esu = 45.54 a.u.) for **1** and **2** in closed (CF) and protonated open (POF) forms. The protonation is triggered by the addition of trifluoroacetic acid so that the  $[\mu\beta_{//}]_{eff}$  values of the POF correspond to that of the ion pair formed with the trifluoroacetate anion. Results are provided for different chromophore concentrations.

	$C = 10^{-3}$ M	$C = 5 \times 10^{-4}$ M	Average
CF <b>1</b>	$108 \pm 143$	$105 \pm 492$	$107 \pm 256$
POF <b>1</b>	$197 \pm 124$	$285 \pm 417$	$227 \pm 218$
POF/CF Contrast	1.82	2.71	2.12
	$C = 5 \times 10^{-4}$ M	$C = 4.4 \times 10^{-4}$ M	Average
CF <b>2</b>	$284 \pm 166$	$203 \pm 103$	$243 \pm 98$
POF <b>2</b>	$628 \pm 335$	$544 \pm 100$	$585 \pm 175$
POF/CF Contrast	2.21	3.38	2.40

---

## Force Field Parameterization

Torsional potentials around the  $\theta_1 - \theta_{10}$  dihedrals (Figure D.1) were derived from DFT calculations performed at the M06/6-311G(d) level. The DFT and re-parameterized molecular mechanics torsional potentials are displayed in Figure D.2.

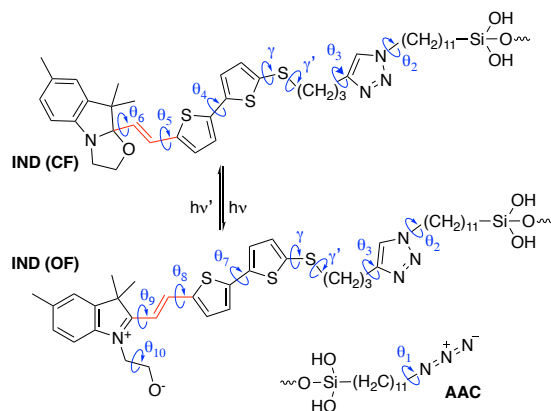


Figure D.1: Scheme of the photochromic switchable closed form (CF) and open form (OF) of the indolino-oxazolidine (IND) derivative, and azido-undecylsilane chain (AAC). Force field parameters have been re-calculated for torsions  $\theta_1$  to  $\theta_{10}$ . The dihedrals are defined as follows:  $\theta_1$ =NNCC,  $\theta_2$ =CCNC,  $\theta_3$ =NCCC,  $\theta_4$ =SCCS,  $\theta_5$ =SCCC,  $\theta_6$ =CCCN,  $\theta_7$ =SCCS,  $\theta_8$ =SCCC,  $\theta_9$ =CCCN,  $\theta_{10}$ =NCCO,  $\gamma$ =CSCC,  $\gamma'$ =CSCC.

## Preparation of the SiO<sub>2</sub> Surface

Simulations were carried out using Clay force field [1] to describe amorphous silica. A bulk sample was prepared following a procedure similar to the one reported by Della Valle *et al.* [2] and described hereafter. A box of dimensions  $52.044 \times 51.119 \times 30.000 \text{ \AA}^3$  was filled with 1745 Si atoms and 3490 O atoms randomly distributed (using Packmol [3]) to achieve the experimental density [4] of vitreous silica at room temperature ( $2.2 \text{ g}\cdot\text{cm}^{-3}$ ). An energy minimization was performed to avoid possible steric clashes or irregularities in the input structure, applying 3D periodic boundary conditions. The sample was then heated up to 4000 K (i) for the first 100 ps, a 0.2 fs timestep was used and velocities rescaled every step, (ii) for additional 80 ps, time step was increased to 0.4 fs and put in contact with a heat bath simulated using Lowe-Andersen thermostat with a collision rate of  $1 \text{ fs}^{-1}$ . To obtain an amorphous silica glass, the sample was subsequently gradually cooled

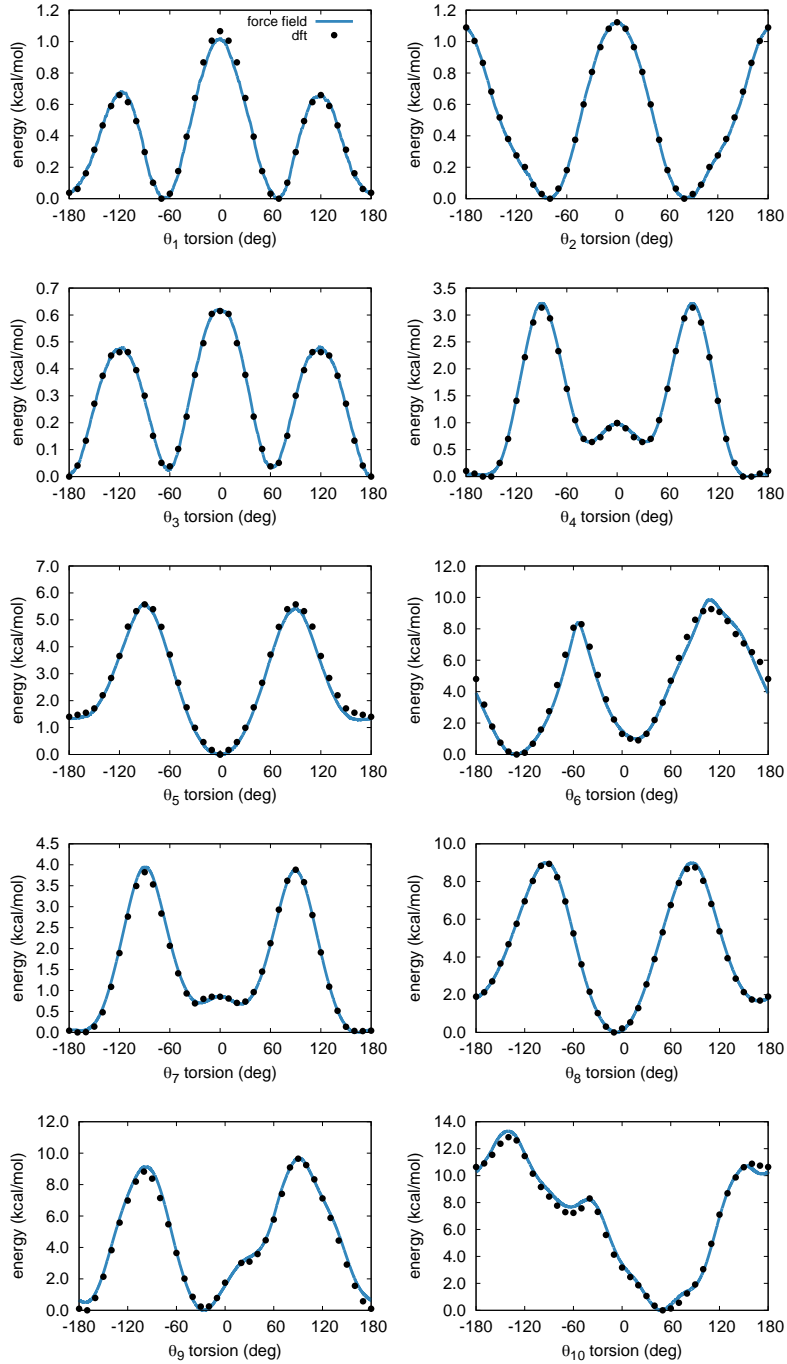


Figure D.2: DFT and re-parameterized molecular mechanics torsional potentials around dihedrals  $\theta_1 - \theta_{10}$  (see Scheme D.1).

down to 300 K at a rate of 0.01 K/0.5 fs for 185 ps and equilibrated for additional 100 ps at 300 K. A 10 ns equilibration was performed before a production run of 1 ns for subsequent characterization of the amorphous sample.

The pair radial distribution functions  $g_{ij}(r)$  were computed and are in close agreement with the X-Ray diffraction measurements (in orange) from Mozzi *et al.* [4], as shown in Figure D.3. From the integral to the first minimum of  $g_{ij}(r)$  one can determine a coordination number of 3.93 and 1.96 for the Si and O atoms, respectively (expected 4 and 2, respectively).

A glass surface was then obtained using an approach similar to that described by Feuston and Garofalini [5]. The simulation box was extended to 150 Å in the  $z$  direction, rendering the

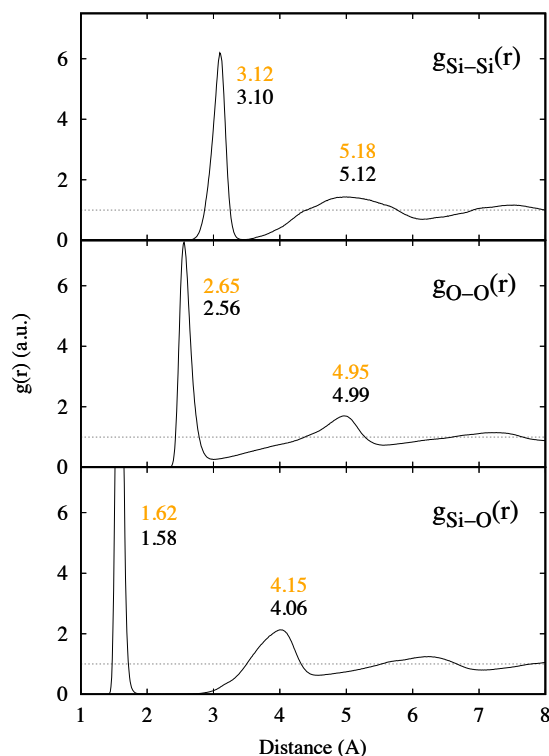


Figure D.3: Radial distribution functions  $g(r)$  for Si-Si pairs (top), O-O pairs (middle) and Si-O pairs (bottom), computed at 300 K for amorphous silica. Experimental (orange) distances [4] are shown for each peak together with theoretical values (black).

periodic boundary conditions effective only in the  $x$  and  $y$  directions for the resulting  $\text{SiO}_2$  slab and a 20 Å-thick layer of atoms was kept immobile at the bottom (Figure D.4). The free surface was annealed at 1000 K for 1 ns to mimic the spontaneous heating during the fracture, as well as to help the local surface reconstruction and structure relaxation. The sample was then gradually cooled down to 300 K at a rate of 0.02 K/fs and further relaxed for 5 ns.

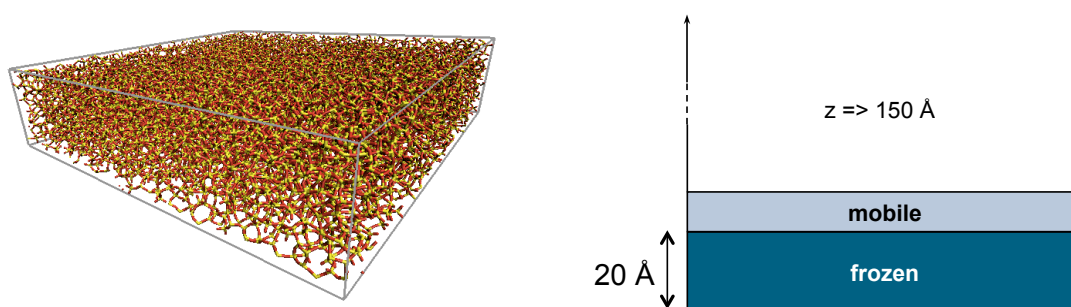


Figure D.4: Equilibrated bulk of amorphous  $\text{SiO}_2$  (left), and sketch of the simulation box used for the  $\text{SiO}_2$  surface (right).

Based on the assumption that the grafted molecules link to the surface via a Si-O single bond, one hydroxyl hydrogen of the  $-\text{Si}(\text{OH})_3$  group was removed and its charge summed to the one of the corresponding oxygen atom. The surface was prepared for grafting as follows: oxygen atoms with coordination number of 1 located at  $z > 27$  Å were removed from the slab and the corresponding total charge redistributed over the atoms of the frozen layer ( $z \leq 20$  Å). A specific Lennard-Jones interaction ( $\epsilon = -0.1554$  kcal/mol,  $r = 1.64$  Å) was then added between alkylsilane

grafting oxygens and 'reactive' silicon atoms from the surface (the ones previously bonded to monocoordinate oxygen atoms), providing an effective bond without explicit grafting. [6]

## Functionalized Surfaces with Various Coverage Rates

After the preparation of a fully covered azidoalkyl SAM, only a fraction of the azide groups was substituted by chromophore units, with the rationale of avoiding a too close packing of the chromophores onto the surface that could hamper the efficiency of the switching process. Three samples with different relative chromophore fraction (1/4, 1/2 and 3/4) were generated, corresponding to coverages of 1.13, 2.26 and 3.38 molecules/nm<sup>2</sup>, respectively. As can be seen in Figure D.5, decreasing the coverage induces a decrease of the SAM thickness, evaluated as the average difference between the height of the complete system and that of the SiO<sub>2</sub> surface alone. The numerical data are collected in Table D.1.

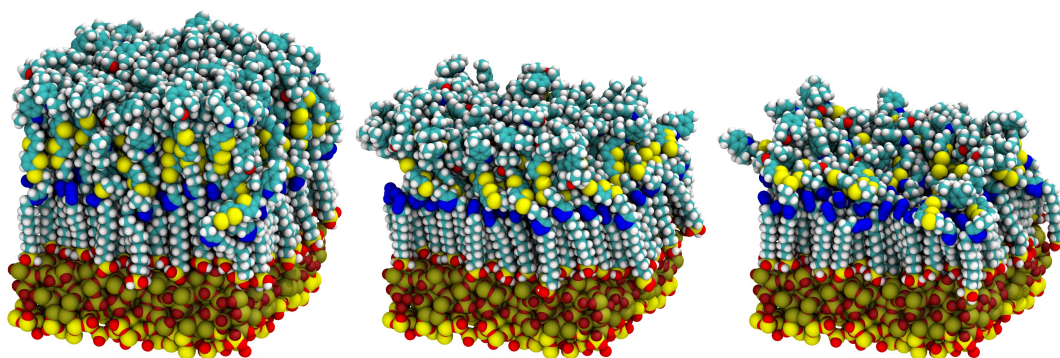


Figure D.5: From left to right: SAMs functionalized with the closed IND molecule, with relative grafting ratios of 1/4, 1/2 and 3/4.

Table D.1: Average value of the cosine of the tilt angle,  $\theta_{tilt}$ , defined as the angle between the double C-C bond of the vinyl bridge (red segment in Fig. D.1) and the axis normal to the surface plane. Thickness and roughness (both in Å) of the SAM in its closed form (CF) and in its open form (OF), with respect to the relative coverage (1/4, 1/2 or 3/4).

Property	CF (1/4)	CF (1/2)	CF (3/4)	OF (3/4)
$\cos^2(\theta_{tilt})$	0.220	0.396	0.362	0.448
Thickness	26.68	33.96	40.40	40.56
Roughness	3.15	2.03	1.32	1.44

## Choice of the Relevant Molecular Fragment for NLO Calculations

Before running NLO calculations on molecular structures extracted from MD simulations, preliminary tests were carried out to define the size of the fragments that should be considered. The complete reference molecule (IND1 in Figure D.6), including from the indolino-oxazolidine photoresponsive part to the terminal Si(OH)<sub>3</sub> anchoring unit was first optimized at the M06/6-311G(d) level, and its first hyperpolarizability  $\beta$  subsequently calculated at the M06-2X/6-311G(d)

level. Then, the NLO properties of the simplified fragments illustrated in Figure D.6 were calculated at the same level of theory, without performing any further geometrical relaxation. So, in the IND2 fragment, the  $\text{Si}(\text{OH})_3$  anchor was removed and replaced by an hydrogen atom; starting from IND2, the alkyl chain was removed in IND3 and replaced by a simple methyl group; finally, the triazole moiety as well as the central  $(\text{CH}_2)_3$  chain were removed and replaced by a methyl group in IND4.

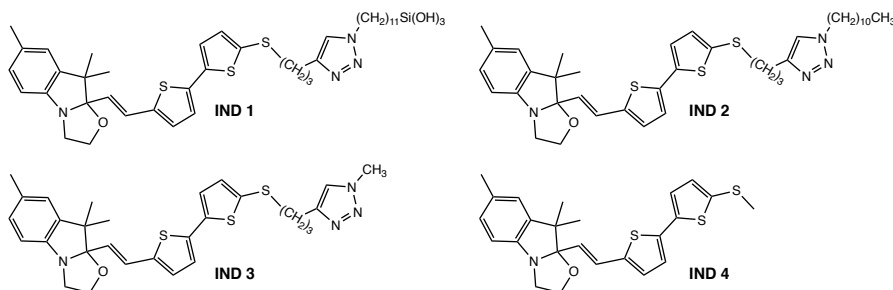


Figure D.6: Molecular fragments considered in DFT calculations of the NLO properties.

The geometries of the reference open and closed conformers are illustrated in Figure D.7, and the relevant geometrical parameters are gathered in Table D.2. The  $\beta$  values calculated for the four IND 1-4 systems in both their closed and open forms are collected in Table D.3. According to a previous study on indolino-oxazolidine molecules in solution (corresponding to the IND4 system), [7] one single conformer exists at room temperature for the closed form, while three conformers differing by the values of the  $\theta_7$  and  $\theta_9$  dihedrals exhibit non negligible populations for the open form. The corresponding three conformers were therefore considered as starting structures for geometry optimizations of the OF in the present study.

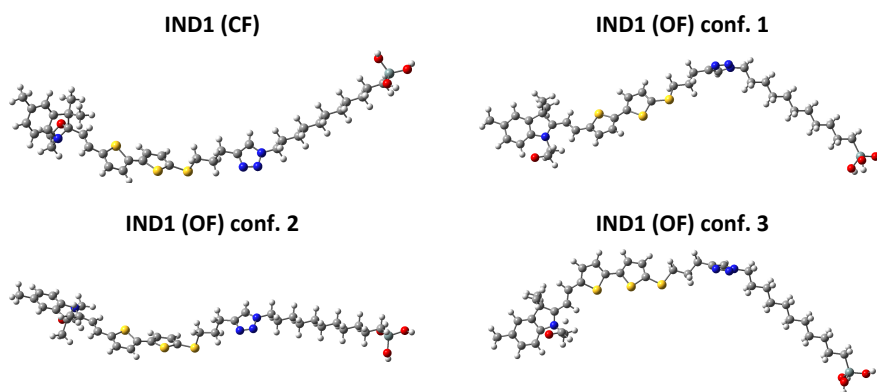


Figure D.7: Geometry of the reference IND1 molecules optimized at the M06/6-311G(d) level.

The static and dynamic hyperpolarizabilities of the closed form (CF) and open form (OF) of the four systems defined in Figure D.6 are collected in Table D.3, while the  $\beta(\text{OF})/\beta(\text{CF})$  contrast ratios are reported in Table D.4. The results lead to similar conclusions for the static and dynamic cases. With the exception of the relatively large  $\sim 10\%$  error obtained for the dynamic  $\beta$  of the conformer 3 (IND2 OF), removing the terminal  $\text{Si}(\text{OH})_3$  anchoring unit neither impacts the  $\beta$  values, which deviate from the reference ones by  $< 4\%$  for the CF and  $< 1\%$  for the OF, nor the OF/CF contrasts, for which the errors are smaller than 5%. Removing the alkyl chain induces slightly larger errors on the  $\beta$  values of both CF and OF, but the latter remain lower than 10%, again with the exception of the dynamic value of conformer 3 (IND3 OF), which reaches

22%. Finally, the most simplified IND4 system leads to large errors on  $\beta$ , of the order of 60% for the CF and ranging from 22% to 47% for OF; in addition OF/CF contrasts are significantly overestimated. On the basis of these results, the IND2 fragment was selected as the best trade-off between accuracy and calculation time for all further DFT calculations of the NLO properties of the photochromic molecules extracted from the MD simulation trajectory.

Table D.2: Bond Length Alternation (BLA, Å) along the vinyl bridge of the indolino-oxazolidine moiety (red segment in Fig. D.1, and torsional angles ( $\theta_{5-9}$  and  $\gamma$ , degrees) calculated at the M06/6-311G(d) level for the reference system (IND1) defined in Figure D.6 in its closed and open form (CF, OF). Three different conformers are considered for the OF.

System (form)	Conf.	BLA	$\theta_4$	$\theta_5$	$\theta_6$	$\gamma$
IND1 (CF)	1	-0.135	158.1	1.2	-17.7	101.7
System (form)	Conf.	BLA	$\theta_7$	$\theta_8$	$\theta_9$	$\gamma$
IND1 (OF)	1	-0.051	-167.1	-5.9	-24.9	-16.4
IND1 (OF)	2	-0.055	158.5	2.5	-174.6	99.8
IND1 (OF)	3	-0.053	-25.8	3.3	-173.2	7.1

Table D.3: Static ( $\lambda = \infty$ ) and dynamic ( $\lambda = 1064$  nm) hyperpolarizabilities ( $\beta$ , a.u.) calculated at the M06-2X/6-311G(d) level for the four systems defined in Figure D.6 in their closed and open form. Three conformers (Conf.) are considered for the open forms. The relative differences (% Diff.) between the  $\beta$  values calculated for the IND2-4 systems and the reference IND1 system are also reported. All  $\beta$  values are given in atomic units ( $1$  au of  $\beta = 3.6310^{-42} \text{ m}^4\text{V}^{-1} = 3.2063 \times 10^{-53} \text{ C}^3\text{m}^3\text{J}^{-2} = 8.641 \times 10^{-33} \text{ esu}$ ).

System (form)	Conf.	$\lambda = \infty$		$\lambda = 1064$ nm	
		$\beta$	% Diff.	$\beta$	% Diff.
IND1 (CF)	1	846	/	1306	/
IND2 (CF)	1	878	3.66	1325	1.45
IND3 (CF)	1	797	-5.90	1193	-8.65
IND4 (CF)	1	334	-60.57	468	-64.17
System (form)	Conf.	$\beta$	% Diff.	$\beta$	% Diff.
IND1 (OF)	1	13668	/	114016	/
IND2 (OF)	1	13572	-0.70	113328	-0.60
IND3 (OF)	1	12766	-6.60	109830	-3.67
IND4 (OF)	1	8967	-34.39	89040	-21.91
IND1 (OF)	2	3961	/	27787	/
IND2 (OF)	2	3965	0.10	25094	-9.69
IND3 (OF)	2	3941	-0.50	21669	-22.02
IND4 (OF)	2	4974	25.57	14777	-46.82
IND1 (OF)	3	13731	/	49260	/
IND2 (OF)	3	13778	0.34	48435	-1.67
IND3 (OF)	3	13147	-4.25	45833	-6.96
IND4 (OF)	3	9547	-30.47	33966	-31.05

Table D.4:  $\beta(OF)/\beta(CF)$  contrast ratios for the static ( $\lambda = \infty$ ) and dynamic ( $\lambda = 1064$  nm) first hyperpolarizabilities, calculated at the M06-2X/6-311G(d) level for the four systems defined in Figure D.6 (considering three different conformers (Conf.) for the OF). The relative differences (% Diff.) between the contrast values calculated for the IND2-4 systems and the reference IND1 system are also reported.

System	Conf.	$\lambda = \infty$		$\lambda = 1064$ nm	
		$\beta(OF)/\beta(CF)$	% Diff.	$\beta(OF)/\beta(CF)$	% Diff.
IND1	1	16.14	/	87.30	/
IND2	1	15.46	-4.21	85.53	-2.03
IND3	1	16.02	-0.74	92.06	5.45
IND4	1	26.85	66.37	190.26	117.93
IND1	2	4.68	/	21.28	/
IND2	2	4.52	-3.43	18.94	-10.99
IND3	2	4.94	5.74	18.16	-14.63
IND4	2	14.89	218.45	31.57	48.40
IND1	3	16.21	/	37.72	/
IND2	3	15.69	-3.20	36.55	-3.08
IND3	3	16.50	1.75	38.42	1.86
IND4	3	28.58	76.32	72.58	92.42

## Probability Distributions of Dihedrals

Figures D.8 and D.9 report the potential energy curves associated to torsions within the isolated molecule around the  $\theta_1 - \theta_{10}$  and  $\gamma - \gamma'$  dihedrals, respectively. The plots also show the probability distributions of the dihedral angles for the subset of molecular geometries extracted from the MD trajectories. The distributions indicate that the  $\theta_2$  and  $\theta_3$  (and in a lesser extent  $\theta_1$ ) dihedrals assume all possible values due to low rotational energy barriers, while all other dihedrals ( $\theta_4 - \theta_{10}$ ) adopt specific values due to larger energy barriers associated to steric and conjugation constraints.

## Relationships Between Geometrical Structures and NLO Responses

Figures D.10 and D.11 report the scatter plots of  $\beta$  with respect to torsions around  $\theta_1 - \theta_{10}$  and  $\gamma - \gamma'$  dihedrals, respectively. These graphs evidence how the amplitude of the NLO responses of the molecules within the SAM is strongly correlated to the value of the  $\gamma$  dihedral: large  $\beta$  values are obtained when  $\gamma$  is close to  $0^\circ$  or  $180^\circ$ , while  $\beta$  is much weaker when  $\gamma$  is close to  $90^\circ$ . To gain further insights on the  $\gamma - \beta$  relationship, we focused on the three open-form conformers of IND2, since this molecular fragment was selected for the statistical sampling of the NLO properties. As reported in Table D.3, conformers 1 and 3 display very similar static  $\beta$  values associated to quasi planar conformations with respect to  $\gamma$ , while conformer 2 exhibits a much lower  $\beta$  value associated to a perpendicular conformation. Within the two-state approximation (TSA), the static first hyperpolarizability of these conformers can be expressed as:

$$\beta^{TSA} = 6 \times \frac{\mu_{ge}^2 \Delta\mu_{ge}}{\Delta E_{ge}} = 9 \times \frac{f_{ge} \Delta\mu_{ge}}{\Delta E_{ge}^2} \quad (\text{D.1})$$

in which  $\Delta E_{ge}$  is the excitation energy between the ground state ( $g$ ) and the dipole-allowed excited state ( $e$ ),  $\mu_{ge}$  is the transition dipole associated to the excitation,  $f_{ge} = \frac{2}{3} \Delta E_{ge} \mu_{ge}^2$  is the

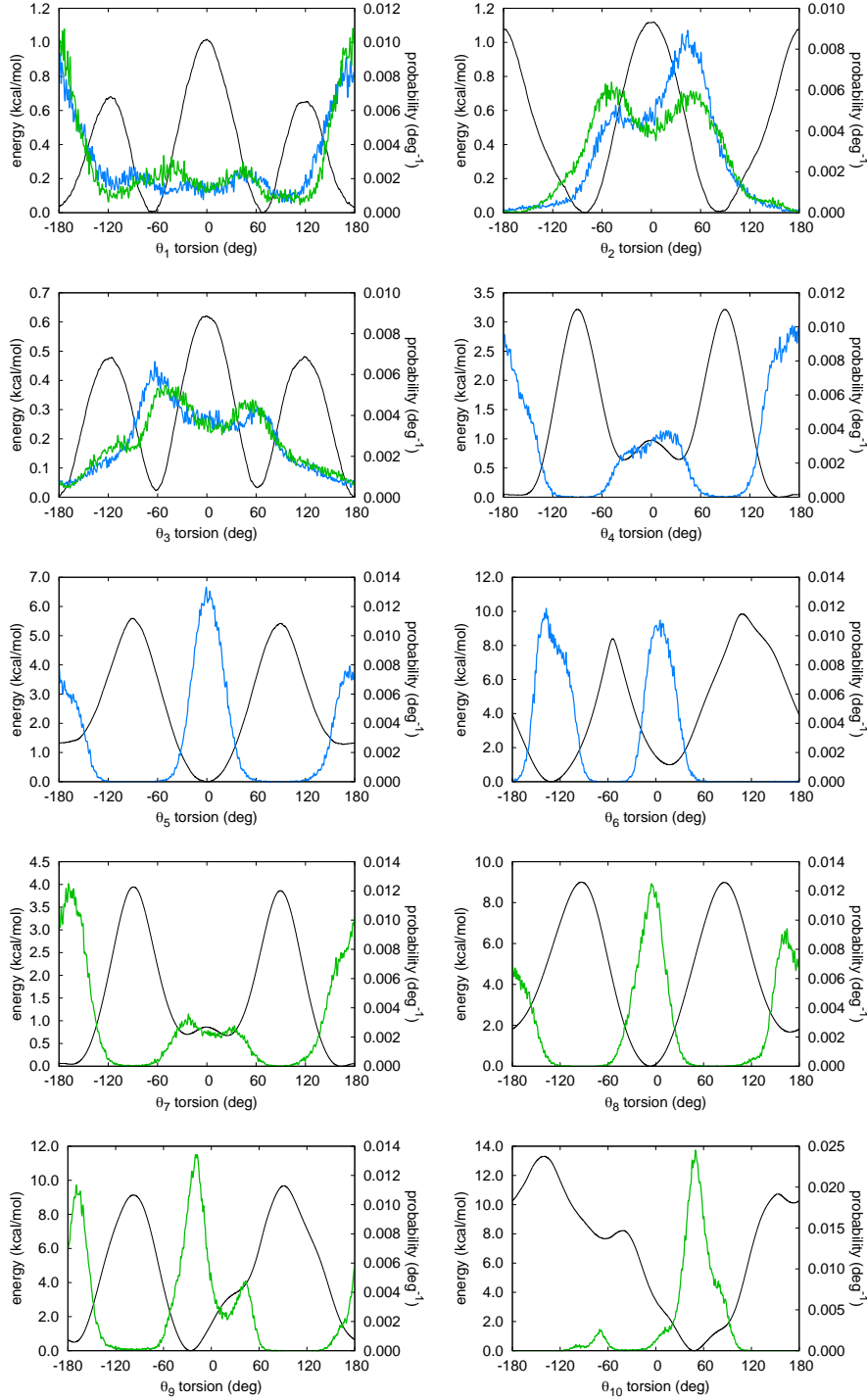


Figure D.8: Potential energy curves associated to torsions  $\theta_1 - \theta_{10}$  (black line) and probability distributions of the dihedral angles of molecules in the SAM, in the closed (blue) and open (green) forms.

oscillator strength, and  $\Delta\mu_{ge} = |\vec{\mu}_e - \vec{\mu}_g|$  is the change in dipole moment between the two electronic states. This latter quantity can be factorized into two contributions:

$$\Delta\mu_{ge} = \Delta q \times \Delta r \quad (\text{D.2})$$

where  $\Delta q$  is the amount of charge transferred during the excitation, and  $\Delta r$  is the average distance over which this charge transfer occurs. The quantities involved in equations D.1 and D.2 were calculated for the two lowest-energy optically-allowed excitations ( $S_0 \rightarrow S_2$  and  $S_0 \rightarrow S_3$ )

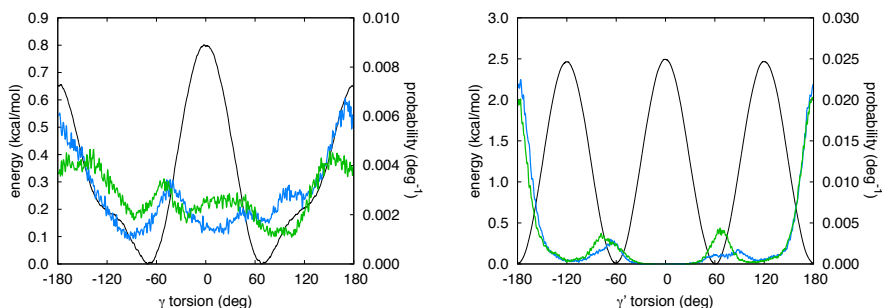


Figure D.9: Potential energy curves associated to torsions  $\gamma$  and  $\gamma'$  (black line) and probability distributions of the dihedral angles of molecules in the SAM, in the closed (blue) and open (green) forms.

of the three IND2 open-form conformers using time-dependent DFT at the M06-2X/6-311G(d) level, and are collected in Table D.5. The differences in the total densities of the excited and ground states are reported in Figure D.12. The results show that the lowest-energy  $S_0 \rightarrow S_2$  transition is localized on the indolino-oxazolidine moiety and the closest thiophene ring, with no contribution of the central sulfur atom. The most intense  $S_0 \rightarrow S_3$  transition is more delocalized and induces an electronic redistribution impacting both the indolino-oxazolidine and bithiophene units. Moreover, in conformers 1 and 3 (showing quasi planar conformations with respect to  $\gamma$ ), the charge transfer extends to the central sulfur atom, while this latter does not contribute to the density reorganization in conformer 2 (showing a perpendicular conformation with respect to  $\gamma$ ). Therefore, the excitation-induced charge transfer is much more pronounced in planar conformers 1 and 3, with dipole moment variations  $\Delta\mu_{ge}$  two times larger than that of conformer 2, mainly due to an increase of the charge transfer distance  $\Delta r$ . In addition, the  $S_0 \rightarrow S_3$  transition energies of conformers 2 and 3 are lower than that of conformer 1, which also contributes to increase the  $\beta$  values of these two conformers with respect to conformer 1. The dependence of  $\beta$  on the value of the dihedral angle  $\gamma$  is then explained in terms of the sizable participation of the sulfur atom of the thioalkyl group to the brightest  $S_3$  excitation in the case of planar conformers, as highlighted in Figure D.12.

Table D.5: Excitation energies ( $\Delta E_{ge}$ , eV), oscillator strengths ( $f_{ge}$ ), dipole moment variation ( $\Delta\mu_{ge}$ , D), charge transfer ( $\Delta q$ , |e|) and charge transfer distance ( $\Delta r$ , Å) for the two lowest-energy excitations of the three IND2 open-form conformers.

System (form)	Conf.	Transition	$\Delta E_{ge}$	$f_{ge}$	$\Delta\mu_{ge}$	$\Delta q$	$\Delta r$
IND2 (OF)	1	$S_0 \rightarrow S_2$	1.7878	0.3598	3.203	0.470	1.418
		$S_0 \rightarrow S_3$	2.8953	1.2107	7.289	0.538	2.822
IND2 (OF)	2	$S_0 \rightarrow S_2$	1.9202	0.4573	1.548	0.383	0.841
		$S_0 \rightarrow S_3$	3.1123	1.1350	3.774	0.478	1.644
IND2 (OF)	3	$S_0 \rightarrow S_2$	1.8864	0.4223	1.628	0.388	0.874
		$S_0 \rightarrow S_3$	2.9850	1.0865	7.735	0.559	2.879

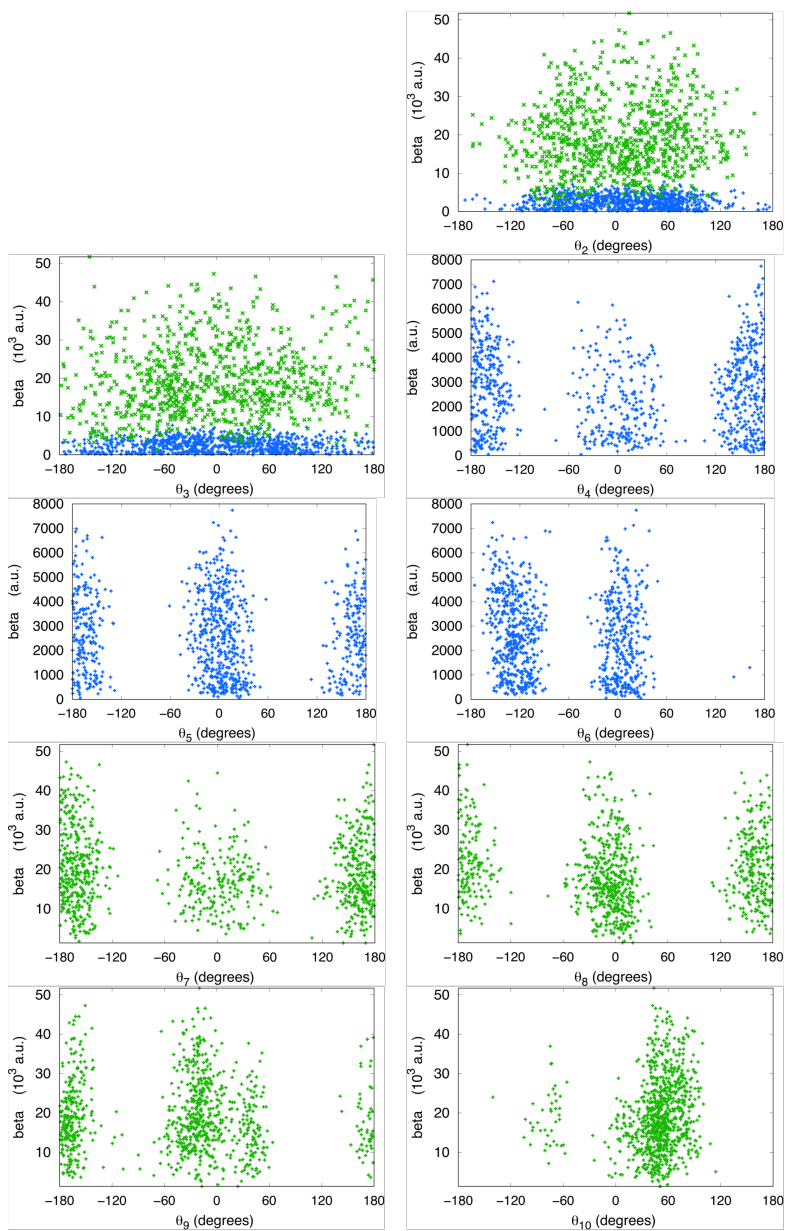


Figure D.10: Scatter plots of individual values of  $\beta$  with respect to torsion angles  $\theta_2 - \theta_{10}$  for molecules in closed (blue) and open (green) forms.

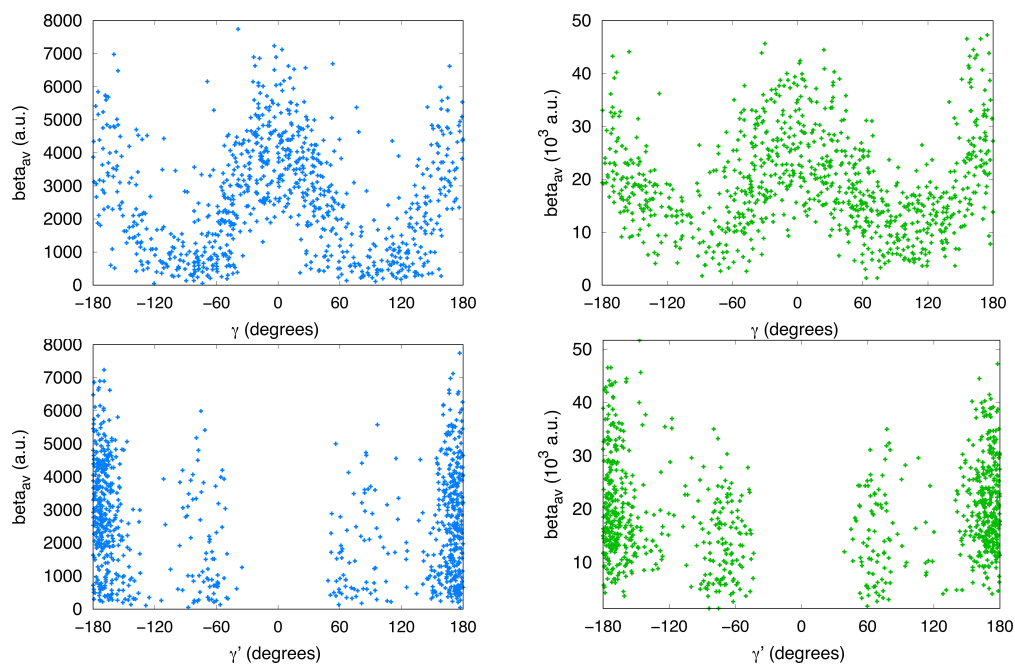


Figure D.11: Scatter plots of individual values of  $\beta$  with respect to torsion angles  $\gamma$  and  $\gamma'$  for molecules in closed (blue) and open (green) forms.

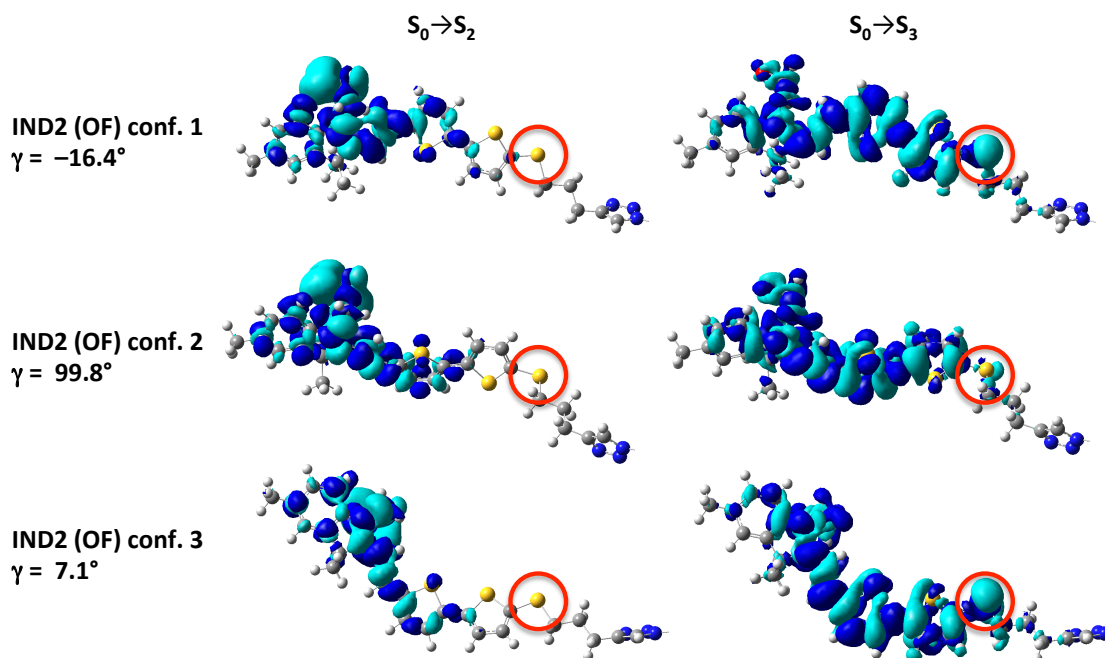


Figure D.12: Density difference maps calculated at the M06-2X/6-311G(d) for the three IND2 open-form conformers (isovalues = 0.0004). Light (dark) blue lobes are associated with negative (positive) values. The terminal alkyl chains are hidden for clarity. The red circles highlight the contribution of the thioalkyl sulfur atom in the electronic redistribution.

# Bibliography

---

- [1] R. T. Cygan, J.-J. Liang, and A. G. Kalinichev. Molecular models of hydroxide, oxyhydroxide, and clay phases and the development of a general force field. *J. Phys. Chem. B*, **108**(4):1255–1266, 2004.
- [2] R. G. Della Valle and H. C. Andersen. Molecular dynamics simulation of silica liquid and glass. *J. Chem. Phys.*, **97**(4):2682–2689, 1992.
- [3] L. Martinez, R. Andrade, E. G. Birgin, and J. M. Martinez. Packmol: A package for building initial configurations for molecular dynamics simulations. *J. Comput. Chem.*, **30**(13):2157–2164, 2009.
- [4] R. L. Mozzi and B. E. Warren. The structure of vitreous silica. *J. Appl. Crystallogr.*, **2**(4):164–172, Oct 1969.
- [5] B. P. Feuston and S. H. Garofalini. Topological and bonding defects in vitreous silica surfaces. *J. Chem. Phys.*, **91**(1):564–570, 1989.
- [6] A. Mityashin, O. M. Roscioni, L. Muccioli, C. Zannoni, V. Geskin, J. Cornil, Di. Janssen, S. Steudel, J. Genoe, and P. Heremans. Multiscale modeling of the electrostatic impact of self-assembled monolayers used as gate dielectric treatment in organic thin-film transistors. *ACS Appl. Mater. Interfaces*, **6**(17):15372–15378, 2014.
- [7] K. Pielak, F. Bondu, L. Sanguinet, V. Rodriguez, B. Champagne, and F. Castet. Second-order nonlinear optical properties of multiaddressable indolinooxazolidine derivatives: joint computational and hyper-Rayleigh scattering investigations. *J. Phys. Chem. C*, **121**(3):1851–1860, 2017.

